Exploring the stability of tailing pond embankments and stabilization of tailing materials through alkali activation for various field applications

Thesis

submitted in partial fulfilment of the requirement for degree of

Doctor of Philosophy

by

Surender Singh

(186104105)

under the supervision of

Dr. Abhishek Kumar

&

Prof. T.G. Sitharam

Department of Civil Engineering

Indian Institute of Technology (IIT) Guwahati, Assam, India.

July 2024

Certificate

This is to certify that the thesis entitled *"Exploring the stability of tailing pond embankments and stabilization of tailing materials through alkali activation for various field applications"* submitted by Surender Singh (186104105), a research scholar in the Department of Civil Engineering, Indian Institute of Technology Guwahati, for the award of the degree of Doctor of Philosophy, is a record of an original research work carried out by him under my supervision and guidance. The thesis has fulfilled all requirements as per the regulations of the institute and in my opinion has reached the standard needed for submission. The results presented in this thesis have not been submitted to any other university or institute for the award of any degree or diploma.

Dr. Abhishek Kumar
Associate Professor, Geotechnical Division
Department of Civil Engineering
Indian Institute of Technology Guwahati

Prof. T.G. Sitharam
Chairman, AICTE, New Delhi and
Former director
Indian Institute of Technology Guwahati

Acknowledgements

I would like to sincerely express my deep gratitude to my supervisors, **Dr. Abhishek Kumar** and **Prof. T.G. Sitharam,** for their invaluable guidance and support throughout my doctoral studies. Their unwavering dedication and insightful supervision have been instrumental in shaping my academic and research endeavours. I am especially thankful for their encouragement in allowing me the autonomy to delve into new and unexplored areas within my field of study. Their mentorship has not only fostered my intellectual growth but has also instilled in me a profound passion for academic research.

I wholeheartedly thank my doctoral committee panel members **Prof. Sreedeep S.**, **Prof. Rajan Choudhary** and **Prof. Poonam Kumari** for the valuable feedback provided during various annual progress seminars. Their insightful input has not only helped in refining my research direction but also contributed significantly to the advancement of my academic pursuits.

I extend my gratitude to the **Ministry of Education** for their financial assistance and to the **Indian Institute of Technology Guwahati** for providing all the necessary facilities for the successful completion of this work. Additionally, I acknowledge the **International Society for Soil Mechanics and Geotechnical Engineering (ISSMGE)** for granting me the travel assistance to attend the 9th International Congress on Environmental Geotechnics held in Chania, Greece.

Lastly, I express my heartfelt appreciation to **my parents and elder brother** for their unwavering moral support throughout my doctoral studies. Their belief in me has been instrumental in enabling me to successfully complete my PhD journey.

Table of contents

Abstract

A substantial quantity of mine tailings (MT) is generated as a byproduct during the extraction of minerals and metals from their respective ores. Due to their hazardous nature, MT are commonly disposed of in large impoundments known as tailings ponds (TP). However, challenges arise with the disposal of MT in TP, as these ponds pose safety risks due to potential breaches and contribute to soil degradation and groundwater contamination. Moreover, the stability of TP is significantly reduced by the excess pore water pressure (EPWP) developed during the frequent raising of embankments, which may lead to the ultimate collapse of such geo-structures. This thesis presents a detailed stability analysis for the embankments of an existing TP, the height of which was increased twice utilizing downstream (D/S) and upstream (U/S) construction techniques. A rigorous two-dimensional transient-fully-coupled-stress-pore pressure analysis is performed in the finite element-based package RS2 to examine the build-up of EPWP during different stages of construction. Furthermore, an attempt is made to investigate the feasibility of future height raising, with due consideration given to the influence of embankment raising rates. The study reveals that the development of EPWP is highly affected by the rate at which embankments of TP are being raised. A higher rate of embankment-raising results in the development of greater EPWP in comparison to a lower embankment-raising rate, which may lead to the ultimate collapse of TP. Furthermore, based on the stability analysis, the height of existing TP can be further raised by 4 m (two lifts of 2 m height) utilizing the U/S construction technique.

MT can be effectively utilized in various raw material intensive applications thereby reducing the volume of MT that would otherwise need to be stored in TP. Given their mineralogy and chemical composition, MT present themselves as suitable materials for alkali activated applications. This thesis also presents the potential utilization of three distinct MT i.e. red mud (RM), iron tailings (FeT), and zinc tailings (ZT) in three different field

applications. Firstly, the applicability of RM, FeT and ZT stabilized through alkali activation is investigated for use as TP embankment material. A series of laboratory experiments including unconfined compressive strength (UCS), direct shear test (DST), alternate wetting-drying tests and permeability tests are performed to evaluate the strength, durability and hydraulic properties of alkali activated MT. While doing so, the influence of alkali activator concentration, curing conditions and curing period is also investigated. Furthermore, the overall performance of alkali activated MT as TP embankment material is compared with that of pozzolana Portland cement (PPC) stabilized MT. Based on the experimental findings, the 28-day UCS of untreated RM, FeT and ZT is enhanced from 1.49 MPa to 10.55 MPa, 1.15 MPa to 2.65 MPa and 0.07 MPa to 4.24 MPa respectively through alkali activation. Furthermore, the study reveals that the compressive strength of RM and ZT increases with increasing NaOH concentrations. Of all stabilized MT specimens, RM display the highest weathering resistance followed by ZT and FeT. Permeability tests reveal that the hydraulic conductivity of untreated MT (RM, ZT, FeT) is reduced by an order of two magnitude using alkali activation technique.

Secondly, this thesis explores the feasibility of RM, FeT and ZT as geopolymer binder for stabilizing the soil for road subgrade. The performance of soil amended with various MT geopolymers is evaluated through various tests including UCS, California bearing ratio (CBR), wetting-drying, permeability, and leachability tests. Based on the experimental findings, the compressive strength of untreated soil is increased significantly from 0.39 MPa to 5.24 MPa, 5.13 MPa and 3.78 MPa with the use of RM, FeT, and ZT-based geopolymers respectively. The study further shows a 26-fold, 19-fold, and 15.8-fold increase in the soaked CBR values of soil when it is stabilized with RM, FeT, and ZT-based geopolymers respectively. In contrast to untreated soil, soil treated with MT-based geopolymers exhibit excellent weathering resistance to alternate wetting and drying cycles indicating its exceptional durability under

adverse environmental conditions. Irrespective of the MT content, curing conditions, and the alkali activator concentrations, soil treated with MT-based geopolymers is found to satisfy both the strength (i.e. UCS = 0.75-1.5 MPa and CBR > 5%) and durability criteria (i.e. % loss in mass < 10%) as specified by Indian Road Congress for the subgrade soil.

Finally, this thesis explores the potential utilization of alkali activated RM, FeT, and ZT as paste backfill materials for underground mine cavities. A series of experiments including tests for UCS, drying shrinkage, workability, and setting time are conducted to assess the suitability of alkali-activated paste backfills (AAPB) for filling mine cavities. Furthermore, a comparison is also drawn between AAPB and conventional cemented paste backfills (CPB) in terms of their performance and production costs. The experimental study reveals that at a given w/s ratio and alkali activator concentration, AAPB exhibit a far better UCS, workability and shrinkage performance as compared to untreated paste backfills (UPB). The study further demonstrates that the addition of GBFS not only enhances the UCS but also reduces the setting time of AAPB mixtures. In contrast to UPB, the volumetric shrinkage, V_s (%) in RM, FeT and ZT based AAPB is reduced by 95-fold, 90-fold and 81-fold respectively with the inclusion of GBFS. Overall, this thesis not only discusses the stability aspects of TP but also provides alternative methods for utilizing MT in various field applications through alkali activation. This approach not only reduces the volume of MT that would otherwise require TP storage but also facilitates the environmentally sustainable disposal of MT.

Keywords: *Mine tailings; tailings pond stability; alkali activation; soil stabilization; mine paste backfills; unconfined compressive strength, shear strength, durability.*

List of Figures

List of Tables

Abbreviations

AAPB	Alkali activated paste backfills
AC	Ambient curing
CBR	California bearing ratio
CL	Low plastic clay
CPB	Cemented paste backfill
UCS	Unconfined compressive strength
D/S	Downstream
DC	Dry curing
DST	Direct shear test
ECS	Effective confining stress
EDS	X-ray Energy Dispersive Spectroscopy
EPWP	Excess pore water pressure
FEM	Finite element method
FESEM	Field emission scanning electron microscope
FeT	Iron tailings
FST	Final setting test
GBFS	Granulated blast furnace slag
INR	Indian rupee
IRC	Indian rod congress
IST	Initial setting time
KOH	Potassium hydroxide
LEM	Limit equilibrium method
MDU	Maximum dry unit weight
ML	Low plastic silt
MT	Mine tailings
Na_2SiO_3	Sodium silicate
NaOH	Sodium hydroxide
OMC	Optimum moisture content
PPC	Pozzolana Portland cement
PVC	Poly Vinyl Chloride
RM	Red mud

SRF	Strength reduction factor
SSA	Specific surface area
TCLP	Toxicity Characteristics Leaching Procedure
TP	Tailings pond
U/S	Upstream
UPB	Untreated paste backfills
USCS	Unified soil classification system
w/s	Water to solid ratio
WHC	Water holding capacity
XRD	X-ray diffraction technique
XRF	X-ray fluorescence spectrometer
ZT	Zinc tailings

Chapter 1

Introduction

1.1 Mine tailings (MT)

The demand for mineral products has increased substantially in the recent years due to rise in the economic development. Due to this reason, a large quantity of rock mass is mined out by the mining industries to extract metal and other mineral concentrate from their respective ore. While recovering the metal concentrate, the excavated rock mass is crushed, ground and processed, leaving behind a significant volume of waste residue referred as "tailings" (EPA, 1994). The overall sequence of various operations performed to obtain metal/mineral concentrates is outlined in Fig. 1.1.

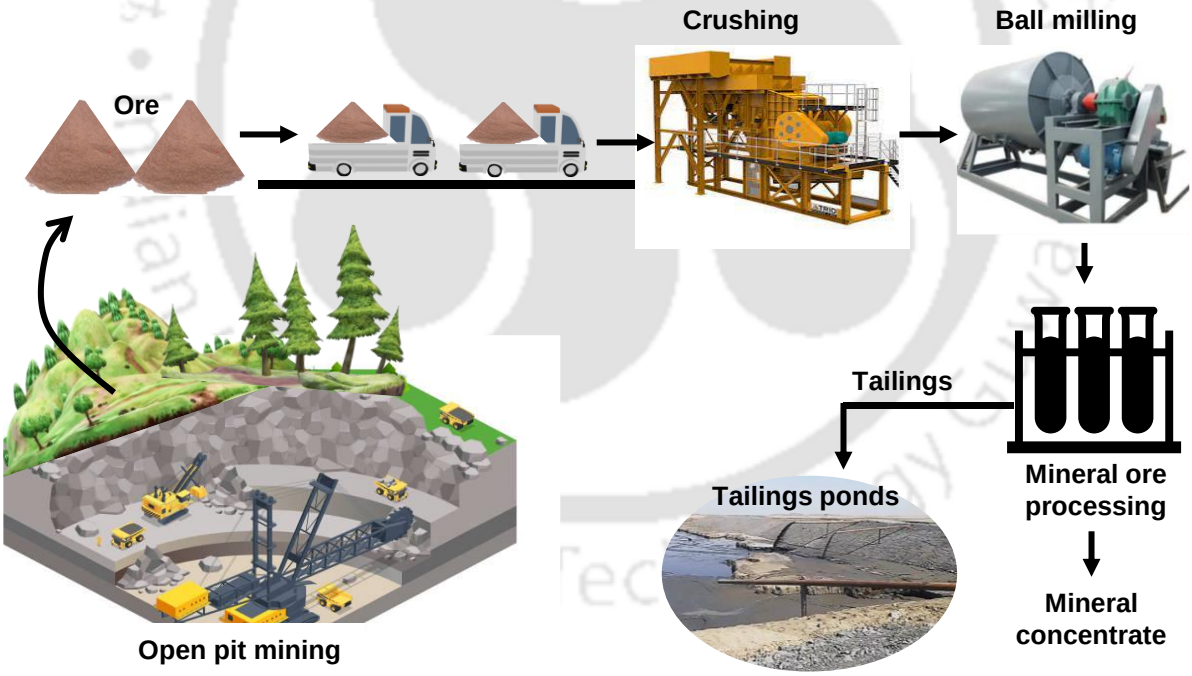

Fig. 1. 1 Illustration of various operations performed during mineral extraction

In general, the ratio of metal concentrate to tailings residue can reach up to 1:200 (Kossoff et al, 2014) depending on the type of ore being extracted. Table 1.1 highlight the fraction of tailings produced during the extraction of various minerals. It is evident from Table

1.1 that extracting a small fraction of pure mineral may generate a significant volume of tailings waste. On a global scale, approximately 5-7 billion tons of tailings are produced annually worldwide (Qi and Fourie, 2019) with the majority attributed to iron tailings (i.e. 1.4 billion tons as per Wu et al., 2023). Tailings often contain harmful substances such as heavy metals and chemicals that can pollute soil, water and air if not handled properly. Hence, it is crucial to effectively manage these tailings waste to mitigate their environmental contamination.

Table 1. 1 Tailings generated during the extraction of various minerals

Minerals	Tailings generated	References
Alumina	1-2 tons of red mud per ton of alumina product	Qi and Fourie, (2019)
Copper	128-196 tons of tailings per ton of copper	Gordon et al, (2002)
Coal	70-120 kg of dry tailings per ton of coal	Wang et al, (2014)
Manganese	6-9 tons of tailings per ton of manganese	Duan et al, (2010)
Iron	10-25 wt. % of tailings from total iron ore mined	Das et al, (2000)

1.2 Disposal of MT

Various methods are used for the disposal of MT including subaqueous disposal, riverine disposal, backfilling mine cavities and open pits, stockpiling dry and thickened tailings. However, the most widely used method for tailings disposal involves storing them behind impoundments commonly known as tailings ponds (TP). The construction of TP embankments typically follows a staged process. Initially, a starter dike is constructed forming the initial pond which is then filled with MT. As the capacity of the starter dike is reached, subsequent embankments are built to raise the height of TP. To increase the height of existing TP embankments, three primary construction methods are commonly employed: upstream (U/S) method, downstream (D/S) method, and centreline method. Each method has its own distinct characteristics and considerations.

In U/S method, the embankments in subsequent stages are lifted towards the U/S side of TP (refer to Fig. 1.2a) whereas embankments in D/S method are raised towards the D/S side of TP (refer to Fig. 1.2b). In case of centreline method, material is deposited evenly on both sides of the centreline of the starter dike gradually building up the embankment (refer to Fig. 1.2c). Table 1.2 briefly summarizes the comparison between various aspects of TP raised by different construction technique. The choice between U/S and D/S construction techniques for TP development involves careful consideration of environmental impacts, stability, and long-term performance. While U/S construction offers simplicity and flexibility in initial design, D/S construction may provide better environmental stewardship and enhanced stability over the life of the structure. Ultimately, site-specific factors, regulatory requirements, and engineering considerations should guide the selection of the most appropriate construction technique for TP projects.

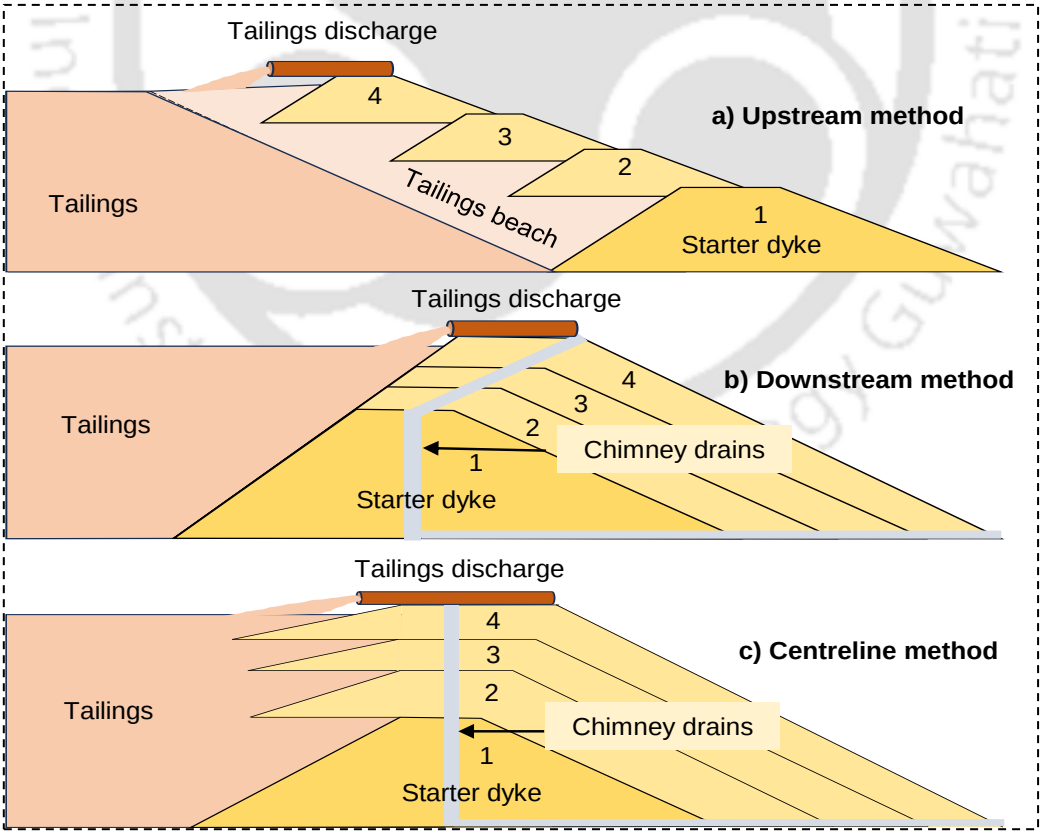

Fig. 1. 2 Different types of construction method a) upstream method, b) downstream method, and c) centreline method

Table 1. 2 Comparison of different construction techniques adopted for TP construction (as per Vick 1990)

Aspect	U/S method	D/S method	Centreline method
Discharge requirements	Peripheral discharge, well-controlled beach required	Depends on design details	Peripheral discharge with nominal beach widths
Long term stability	Lower due to use of deposited tailings	Higher as embankment is built independently	Moderate, may vary with construction pace
Construction material used	Native soil, sand tailings, waste rock	Sand tailings, waste rock, native soils	Sand tailings, waste rock, native soils
Relative cost of construction	Low	High	Moderate
Raising rate requirements	4.5m/year to 9 m/year	None	height restrictions for individuals raises
Seismic resistance	Poor	Good	Acceptable
Drainage system	Not possible	Can be installed	Can be installed

1.3 Failures of TP

While intended to securely store MT, the failures of TP represent a persistent and concerning risk that has garnered significant attention due to its potential for catastrophic environmental and social consequences. The rate of failure in TP can range in between 1 in 700 and 1 in 1750 (Kosoff et al, 2014) which is way more than that observed in water retention dams (i.e. 1 in 10000) (Davies, 2001). Furthermore, it has been observed that U/S type tailings ponds are more susceptible to failure when compared to those constructed using the D/S and centreline construction methods (refer to Fig. 1.3). In the recent years, several high-profile TP failures including the catastrophic breach of the Mount Polley mine in British Columbia, Canada (2014) and the devastating collapse of the Brumadinho dam in Brazil (2019) have emphasized the urgent need for enhanced regulatory oversight, improved engineering standards, and more sustainable tailings management practices within the mining industry. These incidents have prompted a reassessment of the inherent risks associated with tailings storage facilities and

sparked calls for greater transparency, accountability, and environmental stewardship across the mining sector.

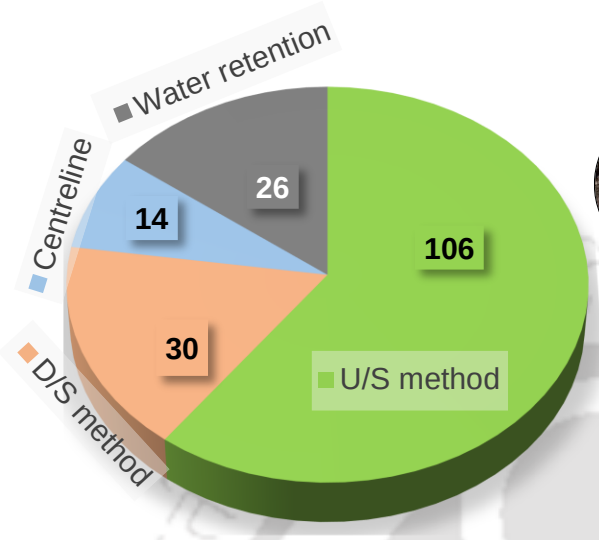

Fig. 1. 3 Distribution of failures event based on construction method (data from Lyu et al, 2019)

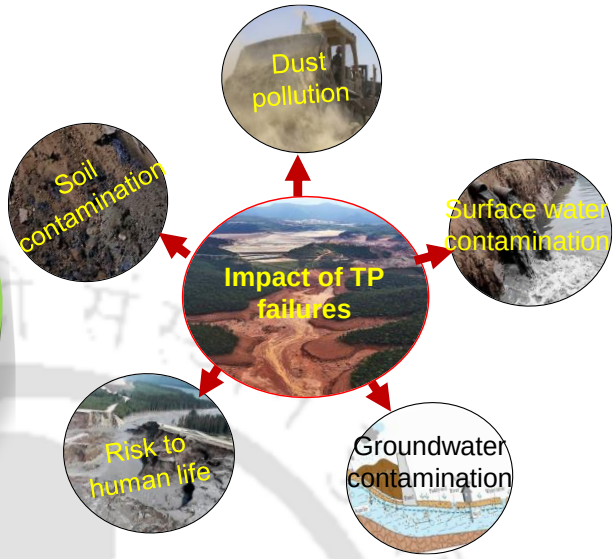

Fig. 1. 4 Various environmental impacts of TP failures

The failure of TP can stem from several factors including foundation failure, slope instability, liquefaction, overtopping, piping or seepage, structural issues and other contributing factors such as snow melt or mine subsidence (Lyu et al., 2008). When these ponds breach or collapse, they unleash torrents of toxic slurry into surrounding ecosystems, contaminating water bodies, disrupting habitats, and posing substantial risks to human health and safety. Fig. 1.4 illustrates various environmental impacts caused by the failures of TP. The environmental fallout from such failures can endure for decades, leaving irreversible scars on landscapes and ecosystems while precipitating profound social and economic upheaval in affected communities.

1.4 Motivation for the current study

The motivation behind exploring the stability aspects of TP and the utilization potential of alkali-activated MT arises from several pressing concerns and opportunities. Firstly, TP though represents critical components of mining operations, their stability and safety yet remain

paramount challenges. Understanding the factors influencing their stability is essential to mitigate risks associated with potential failures, safeguarding both human lives and the environment. Secondly, the exploration of alkali-activated MT opens avenues for sustainable waste management and resource utilization within the mining industry. By transforming MT into value-added products through alkali activation, one can reduce environmental burdens associated with traditional disposal methods while creating opportunities for resource recovery and circular economy practices. Moreover, the utilization potential of alkali-activated MT spans multiple fields including road subgrade construction, geotechnical engineering, and environmental remediation. Investigating their applicability in these diverse contexts holds promising for enhancing infrastructure development, soil stabilization and pollution mitigation efforts. In summary, the motivation behind this study lies in addressing critical challenges related to TP stability while simultaneously exploring innovative solutions for waste valorisation and sustainable resource management in the mining industry. By advancing the understanding of these interconnected issues, one can strive towards a more resilient, resource-efficient, and environmentally responsible mining sector.

1.5 Organization of thesis

The current thesis is organized chapter wise as follows:

- Chapter 1 provides an introduction to MT and explores how mining companies manage them. Additionally, this chapter briefly discusses the challenges associated with their disposal.
- Chapter 2 delves into a comprehensive literature review focusing on two interconnected topics addressed in this thesis i.e. stability of TP embankments, and the utilization of alkali activated MT in various field applications. Based on the literature review, this chapter also identifies research gaps and subsequently formulates the objectives for the present thesis.

- Chapter 3 analyse the stability of a TP considering the effect of staged construction and embankment raising rate.
- Chapter 4 investigates the applicability of three different alkali-activated MT i.e. red mud, iron tailings and zinc tailings as a construction material for TP embankment application.
- Chapter 5 examines the utilization potential of red mud, iron tailings and zinc tailings based geopolymers in soil stabilization for road subgrade applications.
- Chapter 6 investigates the utilization potential of alkali activated MTs as paste backfills for underground mine stopes.
- Chapter 7 finally summarizes the major conclusions, limitations and possible future scope of this study.

Chapter 2

Literature review

2.1 General

This chapter presents an in-depth literature review on two interrelated topics covered in the present thesis namely; 1) stability aspects of TP embankments and 2) stabilization of MT through alkali activation process for various field applications. Through a holistic examination of the existing literature, this chapter not only seeks to provide a thorough understanding of factors affecting the stability of TP embankments but also to elucidate the state-of-the-art practices in alkali activation for the tailings material. Moreover, by critically assessing existing knowledge, the review endeavours to identify research gaps and formulate the objectives for this thesis. This dual focus on stability and innovative reuse reflects a holistic approach to address the current challenges associated with MT, emphasizing both the safe containment of waste and the sustainable utilization of this resource in diverse applications.

2.2 Stability aspects of TP embankments

The stability of the entire TP facility primarily depends on the structural stability of its embankments. As highlighted earlier in section 1.3, TP constructed using U/S method are more prone to failures as compared to D/S and centerline methods. Therefore, literature review carried out in this section is primarily focused on investigating the stability aspects of U/S type TP. Typically, limit equilibrium method (LEM) and finite element method (FEM) based approach have been utilized to evaluate the stability of TP embankments. While mining companies have frequently employed LEM to evaluate the stability of TP, it falls short in accurately assessing TP stability due to inherent limitations. Firstly, the LEM disregards the stress-strain behaviour of materials when determining the FOS values on the embankment slope. Secondly, it relies on arbitrary assumptions about inter-slice forces to maintain static

determinacy (Krahn, 2003). On the other hand, FEM allows for more accurate modelling of material behaviour, loading, and boundary conditions, making it more suitable for analysing the stability of TP (Saad and Mitri, 2011).

The structural stability of TP embankments is influenced by various factors including the strength and hydraulic properties of embankment material, seepage flow within the TP facility which is controlled by the beach area (EPA, 1994; Yin et al., 2011), development of excess pore water pressure (EPWP) during staged construction (Saad and Mitri, 2011; Orman et al., 2013), rate at which embankments are raised (Do et al., 2021). In general, the stability of TP is usually examined for three limiting conditions namely: 1) stability at the end of construction (prior to pond filling), 2) stability considering the steady-state seepage flow condition, and 3) stability of TP under sudden drawdown condition (Sitharam and Hegde, 2017). Due to the presence of a beach area (which keeps the ponded water away from the embankments of TP), scenarios involving sudden drawdown conditions are rare in TP (EPA, 1994). The most critical condition for the stability of TP occurs when it is filled with tailings and the seepage takes place at full rate. The water flowing within the embankments exert seepage pressure to the soil mass consequently decreasing its effective stress and thus the shear strength. This in turn reduces the overall stability of TP. The amount of water seeping through the embankments primarily depends on the position of phreatic line within the TP facility. Ideally, the phreatic surface should be kept as low as possible near the D/S face of TP embankments (EPA, 1994). The location of phreatic surface (within the TP facility) is governed by various factors including the hydraulic properties of embankment material, installed drainage system, and the beach area provided towards the U/S of TP (Vick, 1990). The subsequent sections provide a concise overview of the diverse factors that predominantly influence the seepage pathway within the TP facility and their impact on its overall stability.

2.2.1 Effect of beach length

Beach in TP refers to the exposed surface of the tailings between the point of discharge and the supernatant pond, which defines the interface between the sub-aerial and sub-aqueous region within TP (Vick, 1990; EPA, 1994). In general, the beach area comprises of a coarser fraction of tailings which promotes rapid water drainage thereby lowering the phreatic line within the embankments of the TP. Furthermore, the extent of this beach region influences the seepage pattern within TP facility. A longer beach length typically results in a lower phreatic surface within TP embankments, consequently enhancing their stability (refer to Fig. 2.1) (Zhang et al., 2020). Moreover, the presence of the beach area helps to dissipate wave energy and reduce erosive forces along the embankments of the TP. Till date, limited studies have been conducted to clearly demonstrate the impact of beach length on the location of the phreatic surface and therefore, on the overall stability of the TP. Hence, there is a necessity for a thorough study that explores the influence of beach length on the seepage dynamics within a TP facility.

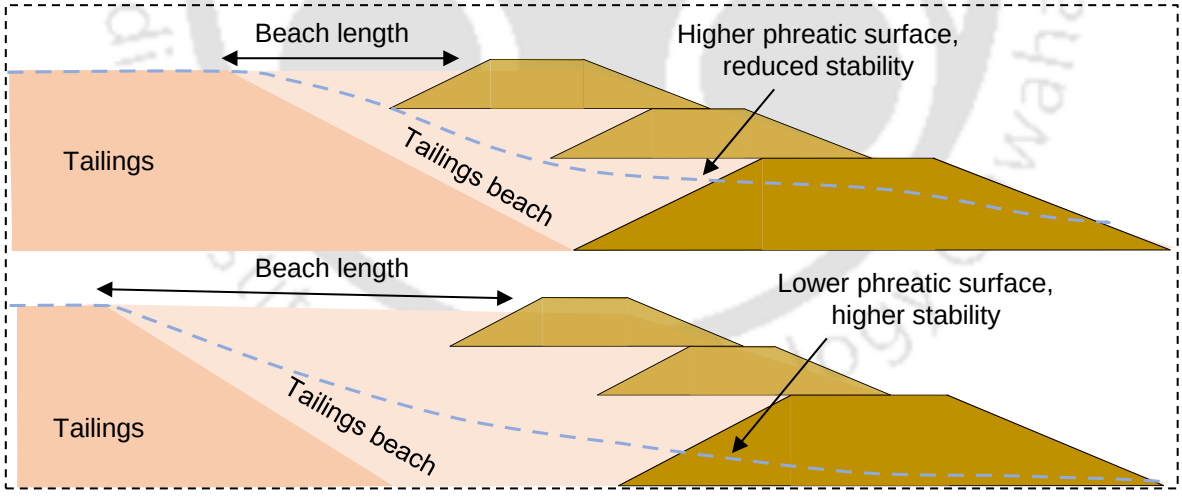

Fig. 2. 1 Location of phreatic surface with varying beach length

2.2.2 Effect of EPWP and embankment raising rates

In general, steady state-seepage analysis is performed while examining the stability of TP (Coulibaly et al., 2017; Sitharam and Hedge, 2017). However, flow occurring within the TP may take several years to reach a steady-state condition (Zandarín et al., 2009). Prior to the

steady state, transient flow exists within TP facility for the initial several years. The classical seepage analysis (which assumes steady-state seepage condition) does not consider the transient flow condition which is induced due to the self-weight-consolidation of the tailings (Saad and Mitri, 2011).

Since the construction of TP embankments is carried out in a staged manner, the consolidation behavior of tailings plays a crucial role while analyzing the stability of TP particularly for those constructed by U/S method. EPWP may develop within the tailing beach region when embankments are constructed over it during the height raising operation. Moreover, a rapid rate of embankment raising can result in faster building-up of EPWP leading to the potential collapse of TP facility (Ormann et al., 2013; Do et al., 2021). The EPWP developed during height raising operations dissipates gradually throughout the consolidation process, increasing the effective stress and subsequently the shear strength of tailings (Ormann et al., 2013). This indicates that the stability of a TP is most vulnerable immediately after the construction of a new dyke. Moreover, the time required for the consolidation process to conclude also influences the EPWP profile within the TP facility. If new embankments are built before the completion of consolidation process, EPWP will remain, and it will further escalate with subsequent raises of TP embankments. In such scenarios, it is imperative to allow sufficient time for the consolidation process to conclude before building of new embankments.

Till date, only one study (Do et al., 2021) has been conducted which comprehensively investigate the influence of embankment raising rate on the stability of TP. Therefore, detailed research is required to examine the overall stability of TP, considering the influence of embankment raising rate and EPWP developed during the height raising operations.

2.2.3 Strengthening of TP embankments

Mining companies have implemented various techniques in the past to enhance the structural stability of TP embankments. Fig. 2.2 illustrates different approaches employed to enhance the structural stability of TP embankments. For instance, Ormann et al. (2013) examined the stability of U/S type TP by employing rockfill buttresses on the D/S side of the embankments. The study concluded that apart from enhancing the overall stability of TP, the inclusion of rockfill berms aids in dissipating EPWP generated during height-raising operations. Similarly, in a related study, Do et al. (2021) performed a numerical analysis to assess the stability of U/S type TP, reinforced by the addition of rockfill berms on the D/S side during height-raising operations.

An alternative approach employed to enhance the stability of TP embankments is the incorporation of geosynthetic reinforcements throughout its height. These reinforcements may consist of geogrids, geotextile bags, geotextile tubes, or a combination of these materials. Numerous studies have been conducted in the past which employed geosynthetic reinforcements to improve the stability of TP embankments (Wei et al., 2009; Yang et al., 2019; Li et al., 2023; Du et al., 2024). For instance, Wei et al. (2009) combined geogrid with a reinforced terraced field method to enhance the stability of U/S type TP constructed with fine tailings materials. More recently, Du et al. (2024) investigated the impact of geogrid reinforcements on the seepage field, and consequently on the overall stability of TP embankments. The study revealed that the use of geogrid reinforcements not only lowered the phreatic surface by up to 5 m but also increased the factor of safety value by 43%. Likewise, Yang et al. (2019) conducted a case study on the feasibility of employing geotextile tubes for building TP dykes, concluding that the stability of TP can be significantly improved using geotextile tubes. While several studies have showcased the effectiveness of geosynthetic reinforcements in improving the structural stability of TP, further research is necessary to

explore the broader applicability of geosynthetics as reinforcing materials for TP embankments.

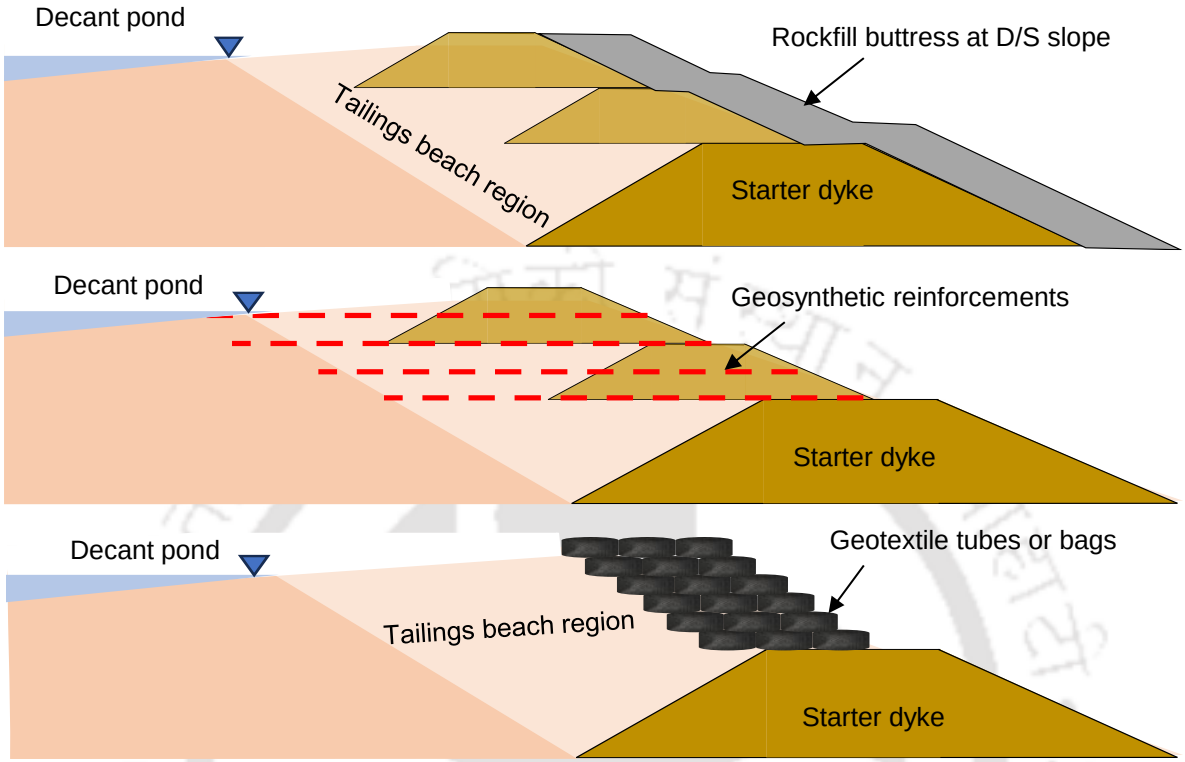

Fig. 2. 2 Various methods adopted to enhance the structural stability of TP embankments

2.3 Utilization potential of MT

The storage of MT in TP presents a significant risk to ecosystems and human health due to their frequent collapse. Consequently, in an effort to reduce dependence on TP, mining industries are investigating practices which are primarily focused on the sustainable utilization of MT in various raw material-intensive applications. So far, the utilization of MT encompasses four key aspects namely; a) extracting valuable metals/ minerals from stored tailings, b) employing them as fillers to refill mined-out areas, c) incorporating them as raw materials in building materials, and d) restoring tailings disposal sites for tree or crop cultivation (Cheng et al., 2016). However, the most common and cost-effective method for MT utilization has been centred around incorporating them as raw materials in building construction.

Numerous researchers have examined the utilization potential of MT in a wide array of applications, encompassing their viability as raw materials for cement, concrete, mortar, bricks, ceramic tiles, road subgrade etc. For instance, Gou et al. (2019) provided a summary of previous research regarding the utilization of various types of MT including iron tailings, copper tailings, and red mud, as raw materials for cement clinker production. The study concluded that MT not only lowers the sintering temperature by 100-150°C but also promotes the formation of C_3S gel thereby improving the mechanical properties of cement (Luo et al., 2016). Likewise, several researchers have explored the potential of red mud, iron tailings, and copper tailings as filler materials to replace conventional sand in cement mortar (Anirudh et al., 2021; Arunachalam et al., 2023; Huang et al., 2023; Kong et al., 2023). These studies revealed that incorporation of MT at proportions ranging from 10% to 50% (by weight of the total mix) not only improves the structural integrity of cement mortar but also enhances its resistance to chemical attacks (Arunachalam et al., 2023). MT, particularly red mud and iron tailings have been employed as fine aggregate in concrete mixes (Kuranchie et al., 2015; Liu and Poon, 2016; Tang et al., 2018; Gou et al., 2019; Hou et al., 2021). These studies suggest that while the addition of MT adversely affects fresh properties like workability and setting time of concrete mixes, it improves the mechanical properties of hardened concrete mixes. Nonetheless, excessive use of MT as fine aggregates can detrimentally affect both fresh and hardened properties due to the presence of heavy metals (Gou et al., 2019). Besides their application in cement mortar and concrete mixes, MTs have also been utilized as raw materials for manufacturing bricks (Weishi et al., 2018; Luo et al., 2020; Wei et al., 2021) and ceramics tiles (Wang et al., 2018; Fontes et al., 2019).

In recent times, there has been a growing interest in exploring the potential of MT as geopolymer binders. Geopolymers are the inorganic binders derived from aluminosilicate source through the process of geopolymerization. In geopolymerization, raw materials which

are rich in alumina (Al_2O_3) and silica (SiO_2), are activated with suitable alkaline solution (called as alkali activator) to form a new 3D tetrahedrally-interlinked-chain structure of aluminosilicate (refer to Fig. 2.3). Typically, NaOH, KOH, Na_2SiO_3 or a combination of these are employed as alkali activators to dissolve the aluminosilicate rich source material. The synthetic inorganic polymer thus formed has a chemical formula of $M_n\{-(SiO_2)_q - AlO_2\}_n$ where, M is alkali cations (Na^+, K^+ etc.), n is degree of polycondensation, and q is Si/ Al ratio. Geopolymer binders offer numerous advantages over conventional binders (such as cement and lime) including rapid strength development, excellent durability, immobilization of hazardous/ toxic elements and low greenhouse gas emissions (Zhuang et al., 2016; Hassan et al., 2019; Wan et al., 2019).

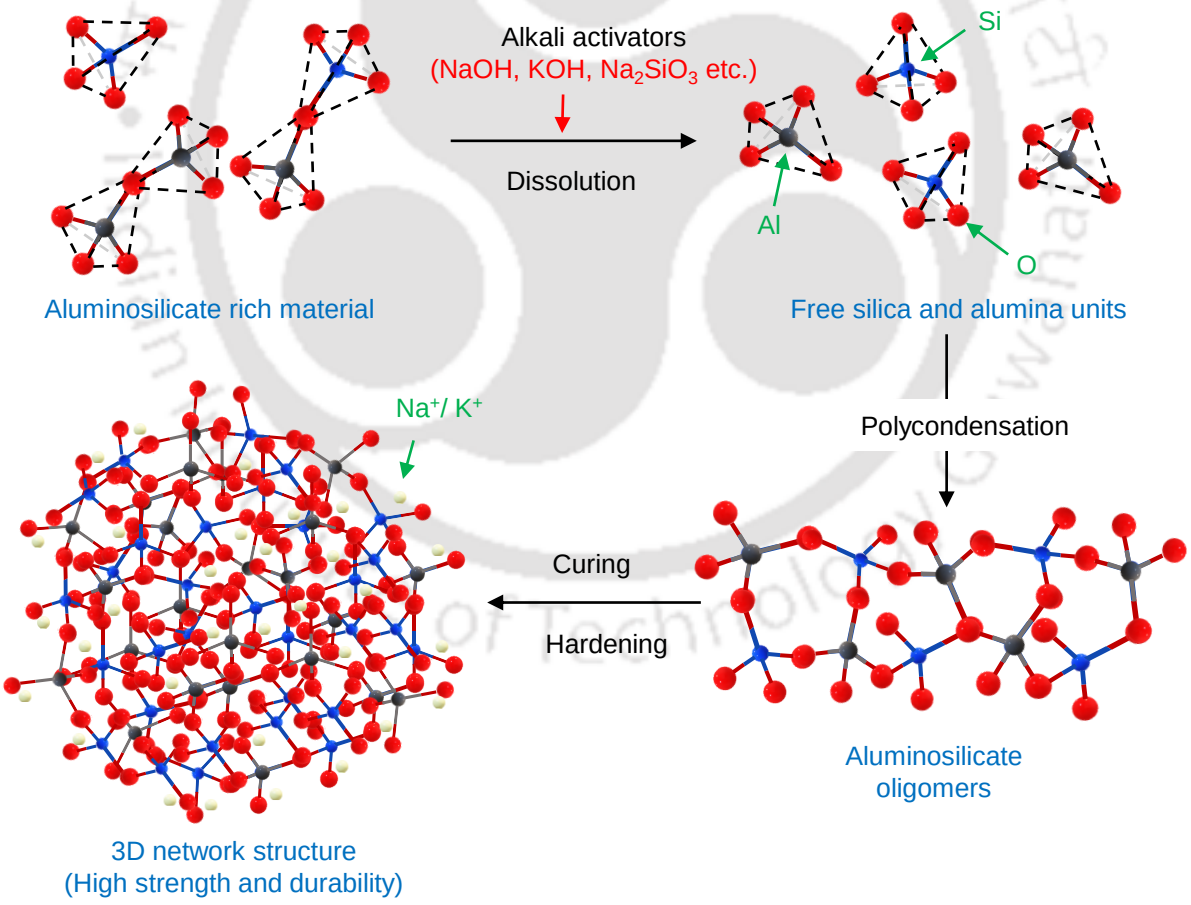

Fig. 2. 3 Various steps involved during the geopolymerization process

Since most of the MT contains a significant proportion of SiO_2 and Al_2O_3, they can be utilized as a potential aluminosilicate source to form geopolymer binders. Till date, several studies have been carried out to investigate the potential of MT as a geopolymer binder for a variety of geotechnical applications. The subsequent section provides a comprehensive overview of previous studies conducted on the potential utilization of MT geopolymers in various civil engineering projects. While doing so, the section will also highlight the practical applications of MT geopolymers in areas that have not been previously explored by researchers.

2.3.1 Potential applications of MT geopolymers

MT geopolymers find diverse applications across various fields including brick and ceramics manufacturing, utilization as fine aggregates in mortars and concretes, serving as adsorbents etc. (see Fig. 2.4). Table 2.1 compiles earlier research efforts focused on exploring the potential applications of MT geopolymers.

Table 2. 1 Overview of previous investigations conducted on the application prospects of MT geopolymers

MT type	Additional binder	Alkali activators	Applications	Reference
Copper tailings	-	NaOH	Bricks	Ahmari and Zhang (2012)
Iron tailings	-	Na_2SiO_3	Bricks	Kuranchie et al. (2016)
Red mud	Slag and fly ash	NaOH+Na_2SiO_3	Bricks	Singh et al. (2020)
Slate tailings	Metakaolin and fly ash	NaOH+Na_2SiO_3	Bricks	Kang et al. (2021)
Gold tailings	Slag	NaOH+Na_2SiO_3	Mine backfill material	Jiang et al. (2022, 2023)
High sulphide mill tailings	Slag	NaOH+Na_2SiO_3	Mine backfill material	Cihangir et al. (2012)
Copper tailings	-	NaOH	Road base	Manjarrez and Zhang (2018)
Red mud	Fly ash	NaOH+Na_2SiO_3	Road subgrade	Chandra et al. (2021)
Jarofix	Slag	NaOH+Na_2SiO_3	Road sub-base	Singh et al. (2023)
Iron tailings	Fly ash	NaOH+Na_2SiO_3	Mortar	Sharath et al. (2018)
Sulfidic tailings	-	Na_2SiO_3	Mortar	Niu et al. (2022)
Gold tailings	Copper-zinc tailings	Na_2SiO_3	Concrete	Yliniemi et al. (2017)
Iron tailings	Fly ash	NaOH+Na_2SiO_3	Adsorbent	Duan et al. (2016)
Gold tailings	-	NaOH+Na_2SiO_3	Adsorbent	Demir and Derun (2019)
Gold tailings	Ferrodirome slag	NaOH+Na_2SiO_3	Adsorbent	Falayi and Ikotun (2021)

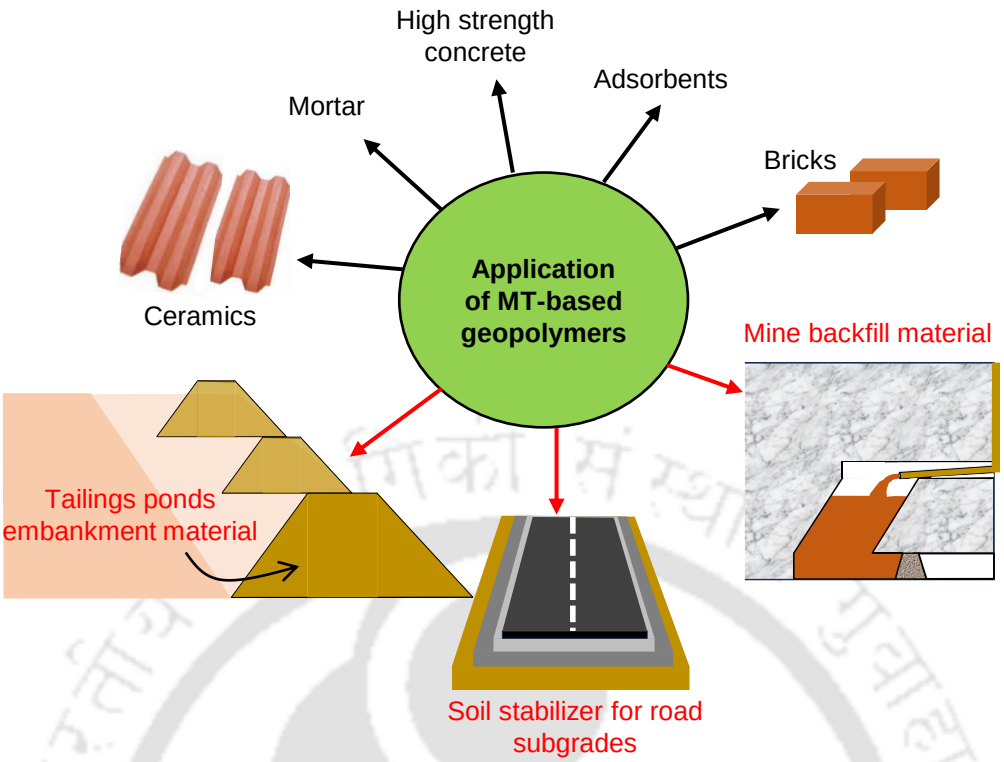

Fig. 2. 4 Utilization potentials of MT based geopolymers

a) Brick manufacturing

Bricks are widely utilized as construction and building material. Traditional bricks, commonly made from clay and shale, necessitate high-temperature kiln firing (900-1000 ˚C) for production. This process not only consumes considerable energy but also emits substantial greenhouse gases. In recent times, the geopolymerization technique has emerged as an alternative method for producing bricks using MT instead of clay. Fig. 2.5 outlines the procedures involved in the manufacturing of bricks utilizing natural clay and MT geopolymers. Several recent studies have explored the feasibility of manufacturing bricks from MT through geopolymerization (Ahmari and Zhang, 2012; Kuranchie et al., 2016; Singh et al., 2020; Kang et al., 2021). For instance, Ahmari and Zhang (2012) examined the feasibility of copper MT to produce eco-friendly bricks using geopolymerization technique. While doing so, the study also explored the influence of NaOH concentration, curing temperature, and water content on the physical and mechanical properties of the geopolymer bricks. Experimental results revealed

that unlike conventional bricks, which require high kiln firing temperatures, geopolymer bricks can be manufactured at lower temperatures ranging from 60 ˚C to 120 ˚C. The prepared geopolymer brick showed a compressive strength of 33.7 MPa satisfying the minimum strength criteria (20.7 MPa) set by ASTM standard for building bricks.

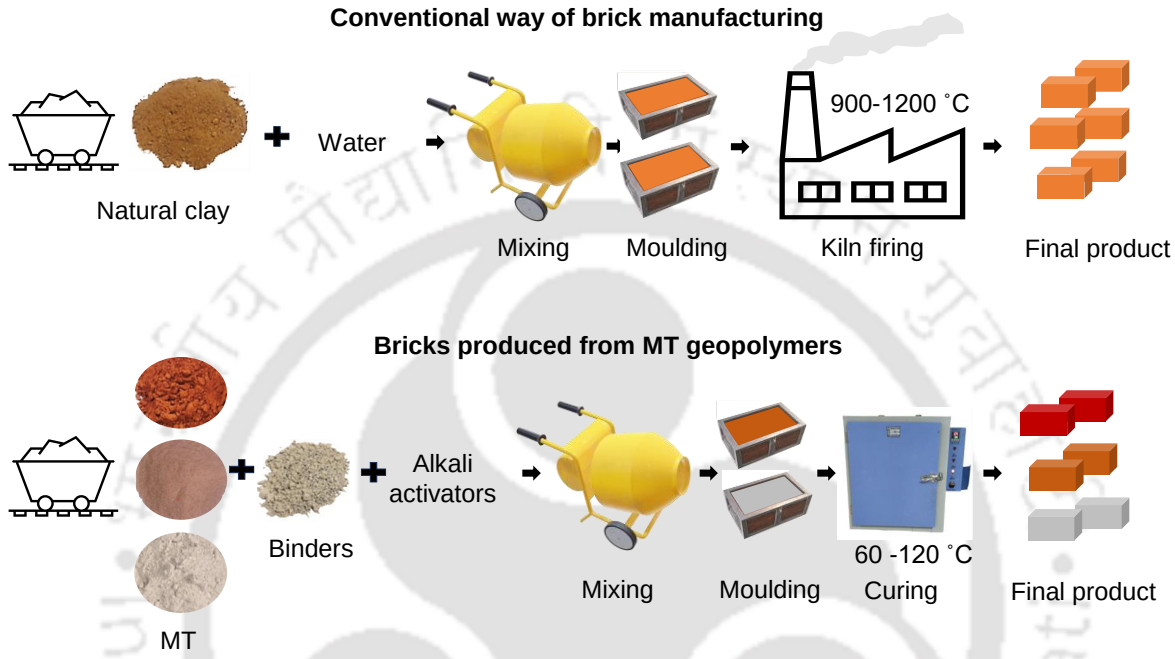

Fig. 2. 5 Manufacturing of bricks using natural clay and MT geopolymers

Another significant study by Kuranchie et al. (2016) examined the feasibility of iron tailings as a raw material to prepare geopolymer bricks. Apart from achieving a high compressive strength of 50.35 MPa, the developed geopolymer bricks were found to be more cost-effective with a 36.8% reduction in production costs compared to fired clay bricks. On a similar note, Singh et al. (2020) investigated the physical and mechanical characteristics of geopolymer bricks made from a blend of red mud, fly ash, sand, and ground granulated blast furnace slag. Their findings indicated that incorporating up to 30% red mud by dry weight yielded optimal compressive strength and water absorption values. Moreover, the inclusion of slag allowed for the utilization of red mud up to 50% without compromising the strength properties. More recently, Kang et al. (2021) investigated the viability of using slate tailings,

metakaolin, and fly ash as raw materials for synthesizing bricks via geopolymerization. The research concluded that geopolymer bricks composed of 50% slate tailings exhibited a compressive strength of 20.37 MPa and a water absorption rate of 13.4%, meeting the Chinese standards for building construction.

In summary, these studies indicate the substantial potential of employing MT in the preparation of bricks through geopolymer technology. Nevertheless, the scope of these studies is confined to the use of a few MT types such as red mud, copper MT, iron tailingss as raw material. Further research can explore the utilization of other MT such as zinc tailings, gold tailings, and other MT with high SiO_2 content in the production of geopolymer bricks.

b) Mortars and concretes

MT geopolymers have emerged as a promising alternative to conventional cement-based materials in the production of mortar and concrete. Geopolymers derived from MT offer a unique opportunity to repurpose industrial by-products, mitigate environmental degradation associated with traditional cement production, and improve the overall sustainability of construction practices. Numerous studies have explored the potential of various MT to serve as a cementitious binder for mortar and concrete manufacturing (Kastiukas et al., 2017; Yliniemi et al., 2017; Sharath et al., 2018; Akinyemi et al., 2022; Niu et al., 2022). For example, Yliniemi et al. (2017) investigated the suitability of lightweight geopolymer aggregates derived from gold MT, copper-zinc MT, and fly ash combined with sodium silicate as an alkali activator, for use in mortar and concrete. The resulting mortar and concrete displayed higher mechanical strength, greater dynamic modulus of elasticity, and improved density compared to concrete made from natural aggregates. In another study, Niu et al. (2022) utilized bioleached sulfidic MT to develop slag-based geopolymer mortar. The resultant mortar made from 20% sulfidic MT exhibited exceptional mechanical performance with a compressive strength of 91.1 MPa after 90 days of curing. The findings of Akinyemi et al. (2022) indicate that addition of

MT in geopolymer concrete reduces both its workability and porosity which is attributed to the smaller particle size of MT.

c) Mine backfill material

Mine backfilling is a mining technique used to fill underground voids created by extracting valuable ore deposits. In general, cemented paste backfill (CPB) technology is utilized to fill the mined-out areas to provide support and stability to the surrounding rock mass. CPB technology not only facilitates the safe disposal of MT but also minimizes surface subsidence, offers ground support, reduces water infiltration, and stabilizes heavy metals (Yilmaz et al., 2014, 2015; Qi and Fourie, 2019; Jiang et al., 2023). In CPB technology, a paste of MT (70-85% solids by weight), water (fresh or processed) and binder (3-10% by weight) is prepared and pumped from the surface to the underground mine cavities (mine stopes) (see Fig. 2.6). Typically, cement has been the preferred choice as a binding material for the preparation of CPB (Thompson et al., 2012; Yilmaz et al., 2014, 2015; Qi and Fourie, 2019; Qin et al., 2023). However, there are several challenges associated with the use of cement as the sole binder in CPB design. Firstly, the high-water content (>20%) used in CPB preparation yields a comparatively slower rate of strength development (Jiang et al., 2023). Secondly, CPB made from cement are vulnerable to chemical attack by sulphide minerals. Thirdly, the utilization of cement is regarded as environmentally unfriendly due to the substantial emission of CO_2 during its production (Duxson et al., 2007). Given these limitations, significant efforts have been made by researchers to seek alternative binders to cement. Lately, alkali activated binders prepared with an alkaline solution and aluminosilicate-rich materials have gained the attention of mining industries as an alternative to cement. These binders not only offer superior strength and flowability properties compared to cement but also exhibit enhanced resistance to chemical attacks (Ercikdi et al., 2009; Cihangir et al., 2012).

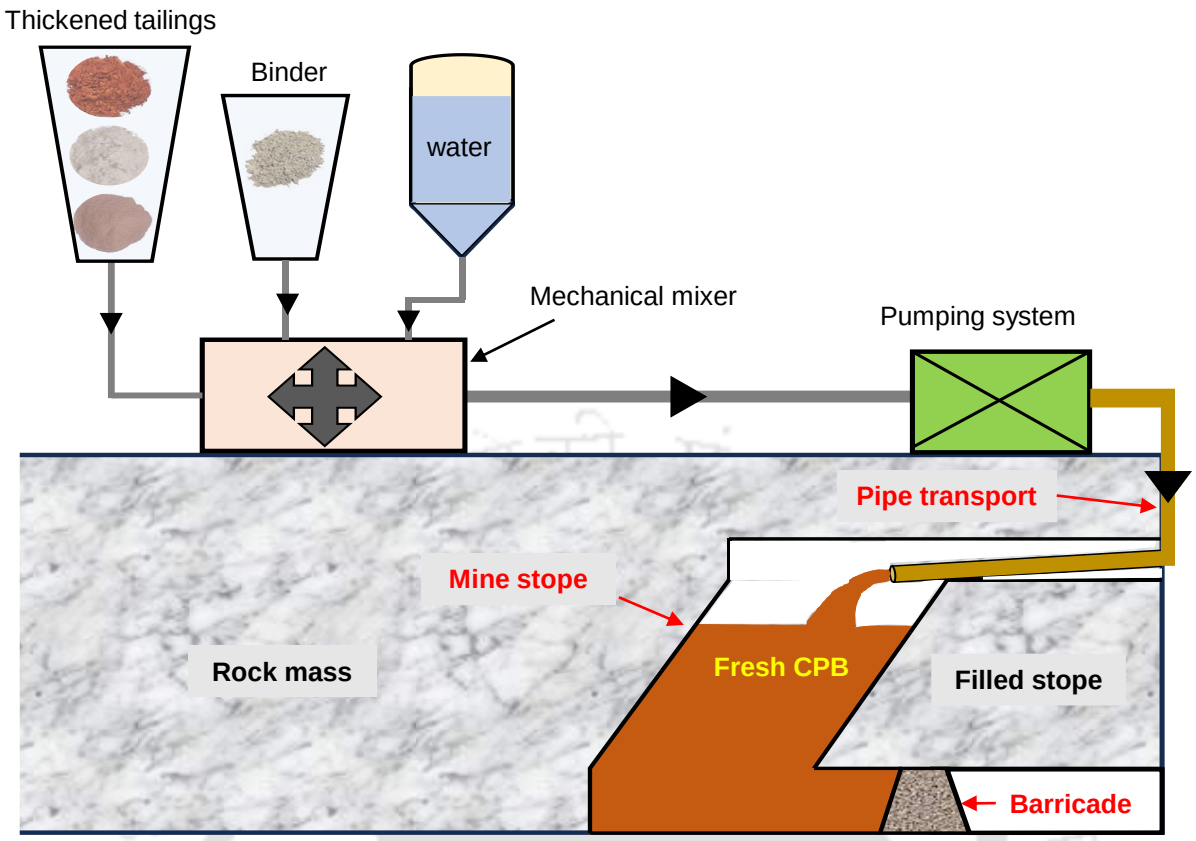

Fig. 2. 6 Schematic diagram showing the mixing, transportation and deposition of paste backfills

Several studies have been carried out in the recent past which explored the potential of alkali activated paste backfills (AAPB) for underground mine stopes and cavities (Cihangir et al., 2015; Jiang et al., 2019; Ouffa et al., 2020; Jiang et al., 2022; Yang et al., 2022; Yin et al., 2022; Ouffa et al., 2022, Jiang et al., 2023). Typically, the performance of paste backfills is examined in terms of various parameters viz. compressive strength, workability, shrinkage and setting time. A minimal compressive strength for AAPB is essential to resist the pressure from the overlying rock mass and prevent ground subsidence. Simultaneously, the workability of AAPB is crucial for efficiently transporting the slurry through pipes from the surface to the underground cavities. Mostly slag has been utilized as an alternative binder to enhance the strength and workability performance of AAPB (Cihangir et al., 2015; Jiang et al., 2019; Ouffa et al., 2020; Jiang et al., 2022; Yang et al., 2022; Yin et al., 2022; Ouffa et al., 2022, Jiang et al., 2023). For instance, Jiang et al. (2019) examined the strength and workability properties of

paste backfills made from alkali-activated slag for underground cavities. The study revealed that under specific binder dosage and curing conditions, AAPB prepared with slag binder demonstrated a far superior strength and workability compared to cement-based CPB. Similarly, Cihangir et al. (2015) delved into the impact of alkali activator type (NaOH and Na_2SiO_3) and concentration on the strength development of AAPB derived from sulphide mill tailings and slag. The study unveiled that NaOH imparts high early strength to AAPB matrix whereas Na_2SiO_3 was responsible for the long-term strength of paste backfills. In a related study, Jiang et al. (2023) investigated the synergistic effect of activator type and curing temperature on the rheological behaviour of paste backfills prepared from alkali-activated slag. The study found that higher curing temperatures led to a decrease in the fluidity of paste backfills which adversely affected the workability of AAPB.

It is evident from the preceding discussion that the majority of studies concentrated on assessing the impact of individual factors on the strength and rheology (flowability) of paste backfills. However, it is crucial to acknowledge that the setting properties of paste backfill plays a significant role in pipe transport and influence the overall construction timeline (Cavusoglu et al., 2021; Yin et al., 2022). A rapid setting of the backfill slurry hinders its ease of pouring and transportation through pipes whereas a slow setting of the backfill slurry extends the demoulding time, thus delaying the overall construction at mine site (Yin et al., 2022).

Apart from setting properties, the shrinkage behaviour of paste backfills is also a crucial parameter in the design of CPB mix. Excessive shrinkage may result in undesirable settlement of the backfill slurry, creating a gap between the stope roof and the deposited CPB (Qin et al., 2021). Consequently, this reduces the volume of CPB that was initially required to ensure the close contact between the backfilled slurry and the stope roof. To date, no study has been conducted which comprehensively investigated the setting performance of AAPB. Moreover,

there is a scarcity of research that extensively examines the shrinkage behaviour of CPB (particularly of AAPB).

d) Adsorbents and porous materials

The utilization potential of MT geopolymers as adsorbents has gained attention for their ability to address environmental challenges associated with water and soil contamination. The unique surface properties of geopolymers derived from the aluminosilicate-rich composition of MT make them effective adsorbents for different classes of pollutants. Typically, MT geopolymers have been utilized for the removal of various heavy metals such as Cu^{+2}, Pb^{+2}, Ni^{+2}, Mn^{+2}, Cr^{+6} etc. from wastewater/water bodies (Zhang et al., 2008; Duan et al., 2016; Demir and Derun, 2019; Falayi and Ikotun, 2021). For instance, Duan et al. (2016) examined the feasibility of geopolymer made from a combination of iron tailings and fly ash to remove Cu^{+2}. The resulting geopolymer exhibited a Cu^{+2} removal efficiency of 90.7% attributed to its well-defined pore size distribution induced during the geopolymerization. In another study, Demir and Derun (2019) utilized gold MT geopolymer for the removal of Pb^{+2} from water. The prepared geopolymer increased the surface area of gold MT from 3.8 m^2/g to 74.9 m^2/g contributing to its higher adsorption efficiency of 94%. Overall, the utilization of MT geopolymers as adsorbents holds great promise for addressing environmental challenges and advancing sustainable resource management practices in the mining industry. Continued research and development in this field are essential to unlock the full potential of MT geopolymers and facilitate their widespread adoption in environmental remediation applications.

e) Potential future applications

As mentioned earlier, the applications of MT geopolymers span various sectors, including the production of mortars, concrete, bricks, ceramics, and more. Given the escalating volume of MT generated by the mining industry, it is imperative to explore additional avenues for their

substantial utilization. One promising alternative involves using MT as a geopolymer binder for soil stabilization replacing the conventional use of cement and lime for road application. Another viable option is employing MT in the construction of TP embankments effectively reducing the overall burden on tailings storage facilities.

Road pavement material: Several studies have investigated the use of MT for road pavement applications. In these studies, MT are incorporated either by adding stabilizers such as cement and lime (Gupta and Prasad, 2017; Manjarrez and Zhang, 2018; Mukiza et al., 2019; Sinha et al., 2021; Nigam et al., 2023; Shanmugasundaram and Shanmugam, 2023) or in combination with soil to prepare road subgrades (Etim et al., 2017; Mukiza et al., 2019). For instance, Gupta and Prasad (2017) examine the strength and durability characteristics of lime treated jarosite (zinc smelter residue) for its use as a sub-base and subgrade material for road pavements. The study concluded that the addition of 10% lime to jarosite imparts sufficient strength and durability properties making it suitable for sub-base material. Similarly, Sinha et al. (2021) used jarofix mixed with cement to enhance the strength and stiffness properties of the sub-base and base layer of road pavement. On a similar note, Mukiza et al. (2019) conducted a review on the potential use of red mud in road base and subgrade materials. Their study revealed that when red mud is employed for subgrade, it reduces the thickness of road pavement compared to natural soil. Additionally, red mud stabilized with other waste materials such as slag and fly ash proved to be more suitable as road material than red mud alone. More recently, Shanmugasundaram and Shanmugam (2023) investigated the potential use of magnesite tailings stabilized with cement as road subgrade material. The resulting mixture prepared with 10% cement and magnesite tailings was found to satisfy the strength, durability, and leaching criteria set by the Indian Road Congress (IRC) for potential use as subgrade material. The majority of the work discussed above utilized cement and lime to stabilize MT for its use as pavement material. However, the use of lime and cement for MT stabilization is not regarded

as an environmentally friendly approach since their production emits a significant amount of CO_2 into the atmosphere (Hoy et al. 2016).

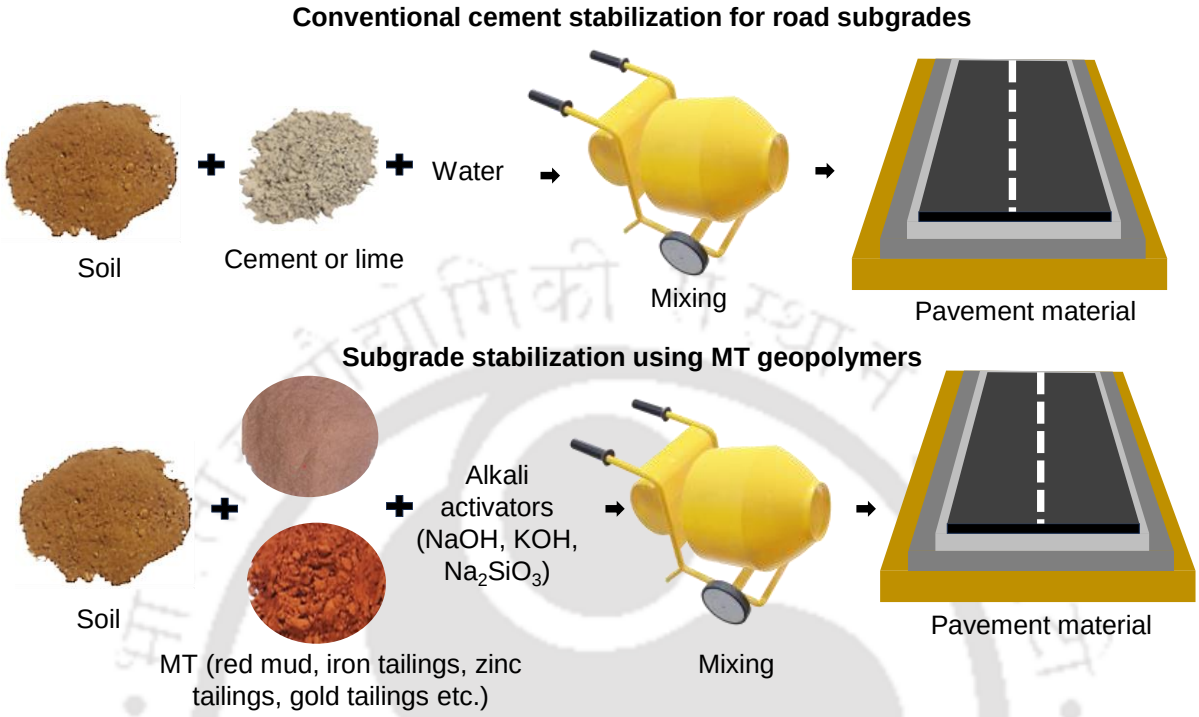

Fig. 2. 7 Utilization of MT geopolymers for subgrade soil stabilization

To eliminate the shortcoming of cement and lime stabilization, geopolymer technology is utilized more recently to stabilize MT and soil for their use in road applications (Manjarrez and Zhang, 2018; Chandra et al., 2021). For instance, Manjarrez and Zhang, (2018) examined the potential of copper MT for its use as road base construction material using geopolymerization. The study revealed that the compressive strength of copper MT could be improved from 0.60 MPa to 5.35 MPa when it is activated with 11M NaOH solution making it suitable for road base. In another study, Chandra et al. (2021) developed a geopolymer composite made from red mud and fly ash for its potential use as road subgrade material. The developed geopolymer composite exhibited a maximum California bearing ratio (CBR) and unconfined compressive strength (UCS) of 12% and 2.7 MPa which are suitable for road subgrades.

The above discussion underscores the scarcity of research utilizing MT-based geopolymers, particularly for soil stabilization in road construction. Additionally, most of the aforementioned studies focused solely on evaluating the compressive strength of geopolymer composites. However, the durability of pavement materials, especially under wetting and drying environmental conditions, is crucial as it can ultimately lead to the overall disintegration of a pavement. Additionally, there is a lack of research examining the hydraulic and toxicity performance of soil stabilized with geopolymer binders. Therefore, future research should be conducted to investigate the strength, durability, hydraulic behaviour, and geo-environmental attributes of soils stabilized with various MT-based geopolymers.

TP embankment material: Another possible application of MT could be to utilize them as an embankment material in the construction of TP. In general, the embankments of TP are constructed with locally available soil at pond site or from mine spoils released during mineral extraction. Due to the scarcity of land, use of natural soil in the construction of TP embankments (during height raising operations) is difficult these days. As a result, MT has been utilized as a construction material in the construction of TP embankments (EPA, 1994; Karim et al., 2023). However, these structures are frequently prone to failure due to low shear strength and poor durability properties of MT. This can be understood from the fact that the failure of Fandao tailings dam occurred due to clogging of drainage systems, resulting in the collapse of dam embankments constructed with iron tailings (Carmo et al., 2017; Vick et al., 2016). Hence, MT must be stabilized in terms of its strength and integrity before being used in the construction of TP embankments.

The strength and durability of MT can be improved with the addition of cement or lime. However, as previously highlighted, this conventional method of stabilization is not environment friendly as the manufacturing of cement and lime results in high CO_2 emissions (Duxson et al., 2007). In contrast, geopolymerization process provides comparable strength

improvement in comparison to cement stabilization that too with lower carbon footprint (Zhuang et al., 2016). To date, no study has been carried out in the past which utilizes alkali-activated MT (especially ZT) for the construction of TP embankments. Furthermore, the weathering resistance of MT against extreme environmental conditions (which an embankment material may be exposed to) has not been extensively studied in the past. In addition, past research have relied solely on UCS while assessing the mechanical response of geopolymerized MT (Ferreira et al., 2022; Li et al., 2019; Liu et al., 2022; Manjarrez et al., 2019). However, for a material to be used in TP construction, it must have sufficient shear strength to prevent slope failure of TP embankments, which cannot be assessed by UCS test. Furthermore, there is a scarcity of research that investigates the hydraulic performance of alkali activated MT, which plays a pivotal role in delineating the seepage path within TP embankments consequently influencing the overall stability of the TP. Hence, further studies should be conducted to explore the strength, durability, and hydraulic performance of various MT stabilized through geopolymerization for constructing TP embankments. The concept of employing MT as embankment material for constructing TP through the process of geopolymerization is shown in Fig. 2.8.

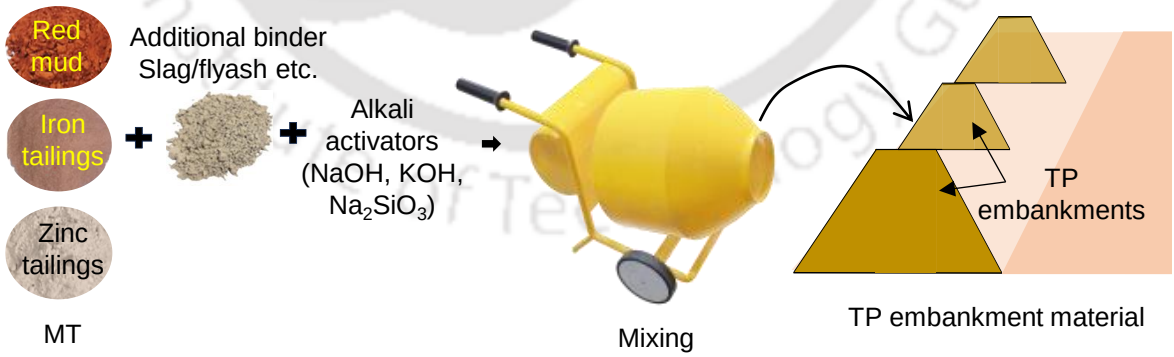

Fig. 2. 8 Utilization of alkali activated MT as TP embankment material

2.4 Research gaps

Based on the literature review performed above, following research gaps have been identified in the current study:

- While numerous studies have examined the stability of TP, taking into account various influencing factors such as EPWP effects, beach length effects, construction technique impact, etc., there is a lack of comprehensive research that examines the effect of embankment raising rate on the stability of TP embankments.
- Previous research does not explore the potential utilization of MT through geopolymerization as TP embankment material. Moreover, there is a gap in research that comprehensively investigates the strength, durability, hydraulic properties, and economic impact of alkali-activated MT as TP embankment material.
- There has been limited research conducted on stabilizing subgrade soil using MT geopolymers. Additionally, only a few studies have investigated the hydraulic and durability performance of soil stabilized with various MT geopolymers.
- While a few studies have delved into the strength and flowability characteristics of AAPB, there is a shortage of research exploring the shrinkage and setting properties of AAPB. Excessive shrinkage can result in ground subsidence issues, while the setting properties of AAPB are crucial for managing the construction timeline of mine backfilling operations.

2.5 Objectives

Considering the above-mentioned research gaps, this thesis aims to achieve the following four objectives:

- To analyse the stability of a TP considering the effect of staged construction and embankment raising rate.
- To investigate the applicability of alkali-activated MT as a construction material for TP embankment application.
- To examine the utilization potential of MT based geopolymers in soil stabilization for road subgrade applications.
- To investigate the utilization potential of alkali activated MT as paste backfills for underground mine stopes.

Chapter 3

Stability investigation of a typical tailings pond considering the effect of staged construction and embankment raising rates

3.1 General

The height of tailings pond (TP) embankments is frequently raised to accommodate the ever-increasing volume of tailings released by the mining industries. Excess pore water pressure (EPWP) may develop during the height-raising operations, which can affect the overall stability of TP. This chapter presents a detailed stability analysis for the embankments of an existing TP, the height of which was increased twice utilizing downstream (D/S) and upstream (U/S) construction techniques. A rigorous two-dimensional transient fully coupled stress-pore pressure analysis is performed in the finite element-based package RS2 to examine the build-up of EPWP during different stages of construction. Furthermore, an attempt is also made to investigate the feasibility of future height raising of existing TP embankments. Given the substantial impact of the rate at which embankments of TP are raised on the development of EPWP, thorough attention is given to the influence of embankment raising rates while conducting the stability analysis.

3.2 Site description and geometry of TP under consideration

TP considered in the present study is located at Debari in Udaipur district of Rajasthan (India) (refer to Fig. 3.1). It receives tailings from the nearby zinc smelter situated at Debari. The smelter produces high-grade zinc as its primary product whereas it recovers cadmium as a secondary by-product. Jarosite is the primary waste discharged after various hydro-metallurgical processes performed at the zinc smelter. Due to its hazardous nature, it is disposed into TP in an eco-friendly manner after stabilizing it with lime and cement. The bedrock at TP

site was found at a depth of 10 m which was overlain by a low permeable soil profile with hydraulic conductivity ranging from 0.8×10^{-8} to 1×10^{-8} m/s.

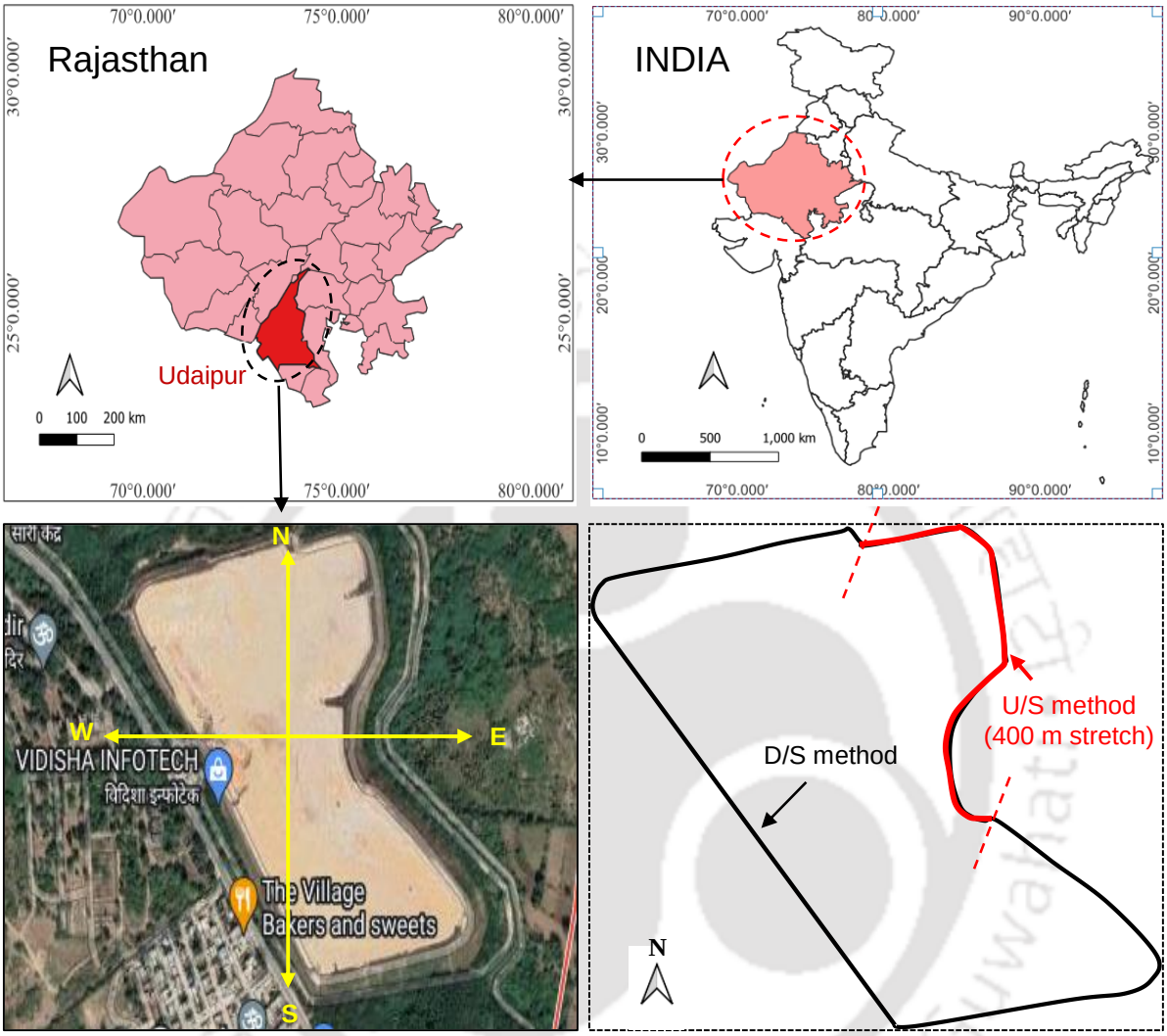

Fig. 3. 1 Location of TP site at Udaipur, Rajasthan (India)

The TP was originally intended to be built in two stages, with a total height of approximately 12 m. In the first stage of construction, the starter dyke was constructed with a height varying between 7 m to 9.5 m throughout the outer periphery. Embankments of the starter dyke (both D/S and U/S slope) were sloped at 2H: 1V with a crest width of 3 m. Within ten years of its service, the starter dyke's storage capacity was reached. Later, to increase the storage capacity, the overall height of the starter dyke was increased by 2 – 4 m (depending upon the cross-section) during stage 2 construction utilizing the D/S method of construction.

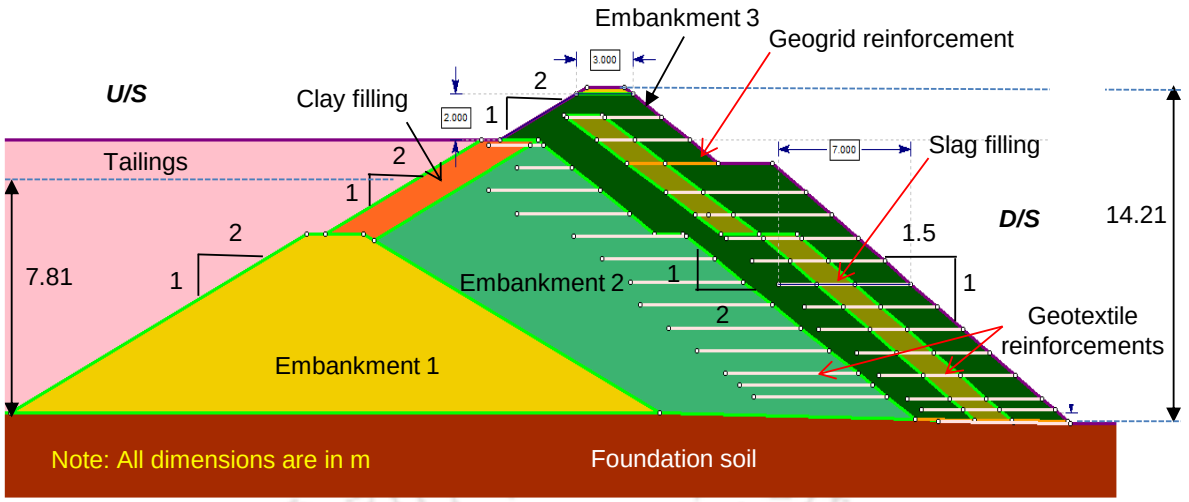

Fig. 3. 2 Geometry of TP embankments built by D/S method

The U/S face of the embankment in stage 2 was sloped at 2H: 1V with a 1 m bench, while the D/S face was sloped at 1.5H: 1V. Furthermore, a 1.5 m wide berm was provided on the D/S slope of embankment 2 while the crest width was maintained at 3 m (similar to that provided in embankment 1). In addition, a compacted clay cover of 1.5 m thickness was installed on the U/S slope of embankment 2 to prevent seepage within the TP embankments (refer to Figs. 3.2 and 3.3). Furthermore, geotextile reinforcements were installed throughout the height of embankment 2 to enhance the overall stability of TP as shown in Figs. 3.2 and 3.3. It must be mentioned here that the embankments built under stage 2 construction operates for a period of approximately 5 years.

Due to the continuous generation of tailings (approximately 750 m^3/day on a volume basis) by the Zn smelter, the rise provided in stage 2 was found to be insufficient to store the additional tailings. Hence, the height of the TP was further increased by 2 m under stage 3 construction. To raise the height in stage 3, both D/S and U/S construction technique was followed as shown in Fig. 3.1. In case of D/S method, the U/S face of the embankment 3 was sloped at 2H: 1V whereas a slope of 1.5H: 1V was provided on the D/S face of embankment 3. The top width of embankment 3 (at the end of stage 3 construction) was maintained at 3 m. In addition, geotextile and geogrid reinforcements were installed within embankment 3 to

enhance the overall stability of the TP. Geotextile reinforcements were provided throughout the height of embankment 3 whereas geogrid reinforcements were installed at the foundation level and the berm level of embankment 3 (refer to Fig. 3.2). Specifications of both geotextile and geogrid reinforcements installed within the embankment 3 are presented in Table 3.1.

In the case of U/S method, the height of TP (after stage 2) was increased by 2 m by constructing embankment 3 towards the U/S section (refer to Fig. 3.3). Before beginning the construction of embankment 3, tailings stored (in stage 2) under it, was replaced with the slag filling up to a depth of 2 m (refer to Fig. 3.3) to nullify the consolidation of previously settled tailings. In addition, geotextile and geogrid reinforcements were also installed within the slag-filled portion. The inclusion of these geosynthetic reinforcements offers numerous advantages. Firstly, these reinforcements aid in the effective distribution of loads originating from embankment 3 and tailings mitigating the stress concentration at the base of the embankment 3. Secondly, geosynthetic reinforcements improve the bearing capacity of the foundation soil (i.e. slag layer in this case) thereby enhancing its shear strength and stiffness properties. Thirdly, geosynthetic reinforcements are help in mitigating the potential for differential settlements across the base of the embankment 3 thereby ensuring the structural integrity over time. The U/S face of embankment 3 was built with a slope of 2H: 1V, while the D/S face was provided with a slope of 1.5H: 1V. Furthermore, geogrid reinforcements were provided across the height of embankment 3 to enhance the overall TP's stability. A description of various reinforcements used in stage 3 construction are summarized in Table 3.1. It should be noted that the total height of TP varies along its perimeter. However, in the current study, cross-sections with maximum height (for both D/S and U/S case) were used for the stability analysis to account for the worst-case scenario.

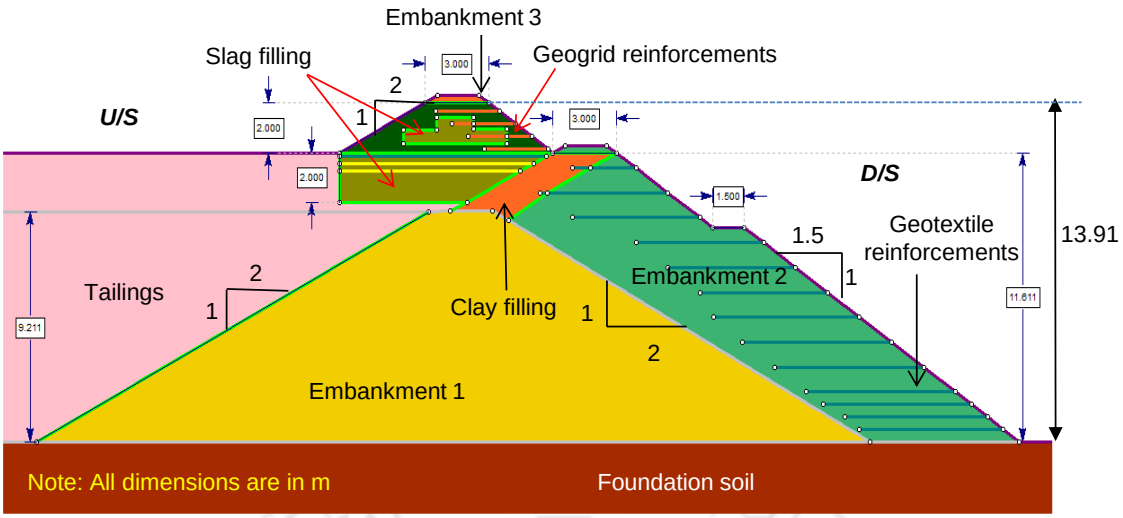

Fig. 3. 3 Geometry of TP embankments built by U/S method

Table 3. 1 Details of reinforcements used within the TP embankments constructed by D/S and U/S method

Construction method	Reinforcement type	Embankment 2			Embankment 3		
		Length (m)	No.	Spacing (m)	Length (m)	No.	Spacing (m)
D/S	Geotextile (PET 100/50)	7	3	0.5	7	3	0.5
		7	3	1	7	9	1
		6	5	1	5	2	1
		3	2	1			
	Geogrid (RE 40)	-	-	-	5	1	-
					8.2	1	-
U/S	Geotextile (PET 100/50)	7	5	0.5			
		6	5	1	-	-	-
		3	1	1			
	Geogrid (RE 40)	-	-	-	3	4	0.5
					8.5	1	-
					9.1	1	-

3.3 Methodology adopted for the stability analysis

In general, the stability of TP embankments is determined under three critical scenarios namely 1) stability at the end of construction, 2) stability considering the steady-state seepage flow

conditions, and 3) stability under sudden drawdown condition (Sitharam and Hegde, 2017). However, due to the presence of a beach region (which keeps the ponded water away from the TP embankments), the sudden drawdown scenario seldom occurs in the TP (Vick, 1990). Hence, in the present work, stability of TP is not assessed for the sudden drawdown scenario. At first, the stability of embankments is assessed at the completion of construction of each phase i.e., prior to the filling of tailings slurry. Subsequently, the stability of TP is investigated considering the transient seepage condition, once the embankments built in each phase are filled with liquid tailings.

Traditional seepage analysis overlooks the transient flow condition, which is caused by the self-weight consolidation of materials (both tailings and embankment) at different stages of TP construction. The preceding statement suggests that the flow occurring inside the TP system is unaffected by its mechanical response, which is in direct contradiction to the fundamental physical reality of porous media behaviour (Biot, 1941). To overcome the limitations of steady-state seepage analysis, two-dimensional transient fully coupled analysis is utilized in this study to model the soil-fluid interactions using Biot's consolidation theory (Biot, 1941). In Biot's theory, the soil skeleton is conceptualized as a porous elastic solid coupled with laminar pore fluid using the conditions of continuity and compressibility. For the analysis, following governing equation given by Biot (1941) is adopted to model the soil-fluid interaction.

$$\frac{K'}{\gamma_w}\left(K_x\frac{\partial^2 u_w}{\partial x^2}+K_y\frac{\partial^2 u_w}{\partial y^2}+K_z\frac{\partial^2 u_w}{\partial z^2}\right)=\frac{\partial u_w}{\partial t}-\frac{\partial p}{\partial t} \qquad (3.1)$$

where, K' (soil bulk modulus) $=1/m_v$, m_v= coefficient of volume compressibility, p = mean total stress, u_w = pore water pressure, K_x, K_y and K_z = hydraulic conductivities in x, y and z direction respectively.

To obtain the governing equation for the two-dimensional analysis, the gradient of effective stress is augmented with the gradient of pore water pressure as follows (Smith et al., 2013);

$$\frac{\partial \sigma_x'}{\partial x} + \frac{\partial \tau_{xy}}{\partial y} + \frac{\partial u_w}{\partial x} = 0 \tag{3.2}$$

$$\frac{\partial \sigma_y'}{\partial y} + \frac{\partial \tau_{xy}}{\partial x} + \frac{\partial u_w}{\partial y} = 0 \tag{3.3}$$

where, σ_x' = effective stress in x direction and σ_y' = effective stress in y direction

The constitutive law for the soil-solid in plane strain can be given as;

$$\begin{Bmatrix} \sigma_x' \\ \sigma_y' \\ \tau_{xy}' \end{Bmatrix} = \frac{E(1-\nu)}{(1+\nu)(1-2\nu)} \begin{bmatrix} 1 & \nu/1-\nu & 0 \\ \nu/1-\nu & \nu/1-\nu & 0 \\ 0 & 0 & 1-2\nu/2(1-\nu) \end{bmatrix} \begin{Bmatrix} \epsilon_x \\ \epsilon_y \\ \gamma_{xy} \end{Bmatrix} \tag{3.4}$$

where, E = elastic modulus of soil, ϵ_x and ϵ_y = axial strains in x and y directions respectively, ν = Poisson's ratio, τ_{xy}' and γ_{xy} = shear stresses and shear strains respectively.

Similarly, the constitutive law for the fluid present within the voids of soil in plane strain can be represented as follows:

$$\begin{Bmatrix} q_x \\ q_y \end{Bmatrix} = \frac{1}{\gamma_w} \begin{bmatrix} K_x & 0 \\ 0 & K_y \end{bmatrix} \begin{Bmatrix} \partial u_w/\partial x \\ \partial u_w/\partial y \end{Bmatrix} \tag{3.5}$$

where, q_x and q_y = volume flow rate per unit area into and out of the element in x and y directions respectively, u_w = pore water pressure, γ_w = unit weight of water.

To obtain the deformation at each of the discretised node, following strain-displacement relationship is used to eliminate the σ and ϵ (Smith et al., 2013);

$$\begin{Bmatrix} \epsilon_x \\ \epsilon_y \\ \gamma_{xy} \end{Bmatrix} = \begin{bmatrix} \partial/\partial x & 0 \\ 0 & \partial/\partial y \\ \partial/\partial y & \partial/\partial x \end{bmatrix} \begin{Bmatrix} u \\ v \end{Bmatrix} \tag{3.6}$$

where, u = displacement components in x direction and v = displacement components in y direction

Considering fully saturated soil and the condition of incompressibility, the total outflow from a soil element is equal to the total reduction in the volume of soil element, which results in the following equation (Smith et al., 2013);

$$\frac{\partial q_x}{\partial x} + \frac{\partial q_y}{\partial y} = -\frac{\partial}{\partial t}\left(\frac{\partial u}{\partial x} + \frac{\partial v}{\partial y}\right) \tag{3.7}$$

Similarly, using equation 5 and 7 collectively gives;

$$\frac{K_x}{\gamma_w}\frac{\partial^2 u_w}{\partial x^2} + \frac{K_y}{\gamma_w}\frac{\partial^2 u_w}{\partial y^2} + \frac{\partial}{\partial t}\left(\frac{\partial u}{\partial x} + \frac{\partial v}{\partial y}\right) = 0 \tag{3.8}$$

Equations 3.2 and 3.3 along with equation 3.8 leads to the following equilibrium and continuity equations;

$$KMr + Cu_w = f \tag{3.9}$$

$$C^T\frac{dr}{dt} - KPu_w = 0 \tag{3.10}$$

For 6 noded elements, r and u_w can be obtained as;

$$\boldsymbol{r} = \begin{bmatrix} u_1 \\ v_1 \\ u_2 \\ v_2 \\ u_3 \\ v_3 \end{bmatrix} \tag{3.11}$$

$$\boldsymbol{u_w} = \begin{bmatrix} u_{w1} \\ u_{w2} \\ u_{w3} \\ u_{w4} \\ u_{w5} \\ u_{w6} \end{bmatrix} \tag{3.12}$$

Further, *KM* and *KP* in equation 3.9 and 3.10 are the elastic and fluid stiffness matrices respectively; *f* is the external loading vector and *C* is a rectangular coupling matrix. After assembling into global matrices, equations 3.9 and 3.10 can be integrated in each time step to obtain the final solutions.

3.4 Numerical analysis in RS2

In this study, the RS2 software (Rocscience inc. 2020) is utilized to perform the stability analysis of TP during its staged construction. RS2 is a 2D finite element analysis-based software used for solving the problems of geotechnical structures such as tunnel and support design, underground excavations, surface excavation, slope stability, embankments, dynamic analysis, foundations, consolidation, groundwater seepage, etc. RS2 utilizes the shear strength reduction technique to analyse the stability of TP embankments. The shear strength reduction technique involves a systematic reduction of shear strength parameters such as cohesion and angle of internal friction by a factor known as strength reduction factor (SRF) until the failure of slope occurs. Failure of slopes in such cases is defined by the critical SRF value, which is similar to the factor of safety as used in limit equilibrium analysis.

3.4.1 Model setup, boundary conditions and loading conditions

The overall geometry of TP has three components namely; 1) pond embankments, 2) tailings deposit, and 3) foundation system. The embankments of TP (built in stages 1, 2, and 3) are drawn in RS2 modeler by utilizing the specifications discussed in section 3.2. The tailing deposit consists of a beach area with an average beach width equal to 3 times the height of TP provided at the end of each stage for both U/S and D/S cases. Additionally, a slope of 1% is

adopted for the beach portion formed on the U/S side of TP (Do et al., 2021). To avoid the boundary effects, the foundation of TP is extended to a depth of 20 m while the side boundaries are extended to 100 m and 20 m towards the U/S and D/S sides respectively (refer to Fig. 3.4).

To model the staged construction of TP, three stages are created in RS2. Stage 0 depicts the initial site condition prior to the construction of TP embankments (i.e., at t = 0 years), which is characterized by a saturated foundation system with steady-state seepage. The construction of each stage (i.e. stages 1, 2, and 3) comprises of 2 phases i.e. a) the raising phase, which includes both embankment construction and pond filling operations, and b) the consolidation phase, which includes the time given for the self-weight consolidation of tailings after pond filling operation. Accordingly, the time is provided for raising and consolidation phases of stages 1, 2 and 3 based on the available reports. For stage 1, 2 years' time is provided for the raising phase followed by 8 years of time for consolidation phase. Similarly for stages 2 and 3 each, 1 year time is provided for the raising phase followed by 4 years for the consolidation phase.

Once the time required for each construction stage is provided, both mechanical and hydraulic boundary conditions are invoked in the numerical model. The bottom boundary of the TP system is assigned with fixed supports to restrain the soil movement in both the x and y-direction. However, due to the decrease in overburden pressure, stiffness of the soil reduces from the bedrock (i.e., bottom boundary) towards the foundation level, allowing for the deformation of soil mass in y-direction. Accordingly, the side boundaries of the TP model are assigned with pinned roller support modelled to prevent soil deformations in the x-direction. Furthermore, the pressure exerted by the ponded water in RS2 is defined by the total head boundary condition where the value of total head (m) at each stage is given as per the height achieved at the end of that stage (refer to Fig. 3.4). For example, in D/S case of construction, a total head boundary condition of 7.81 m, 11.91 m, and 12.6 m are imposed at the end of stages

1, 2, and 3 respectively. Similarly, for the U/S case of construction, a total head boundary condition of 9.21 m, 11.61 m, and 12.37 m is applied at the end of stages 1, 2, and 3 respectively. To locate the exit point of the phreatic surface, the pressure p = 0 boundary condition is invoked within the beach area as well as on the D/S slope of the TP embankments as shown in Fig. 3.4.

Following the application of boundary conditions, the entire TP geometry is discretized into number of finite elements. Sensitivity analysis is performed beforehand to obtain the optimum meshing parameters used in the analysis. Several trials are carried out with 950, 1520, 2225, 3470, and 890, 1425, 1936, 3240 numbers of 6-noded triangular elements for D/S and U/S cases respectively. Results from the sensitivity analysis are examined in terms of the total head obtained at the D/S slope of TP embankments. Based on the sensitivity analysis results, the final discretization for the D/S and U/S cases utilize 2225 and 1936 numbers of 6-noded triangular elements respectively. Furthermore, a finer mesh is provided near the embankments of TP and tailings beach region to increase the accuracy of the analysis (refer to Fig. 3.4).

TP at the site is subjected to load due to self-weight of embankment material, load from tailings and load due to ponded water. The above pond site is situated in seismic zone-II as per IS 1893 (2002), which comes under a low seismicity zone. Hence, to incorporate the effect of seismic loading, the pseudo-static approach is followed in the analysis using the seismic coefficients (K_h) of 0.07 based on equation 3.13 provided in IS 1893 (2002).

$$K_h = \frac{Z}{2}\frac{I}{R}\frac{S_a}{g} \tag{3.13}$$

Where, Z is zone factor taken as 0.10, I is the importance factor considered as 1.5, R is the Response reduction factor for corresponding structures (considered as 2.5) and S_a/g is the design acceleration coefficient for different types of soils normalised with peak ground acceleration and corresponding to natural period of structure. For the present analysis, the value of S_a/g is considered as 2.5.

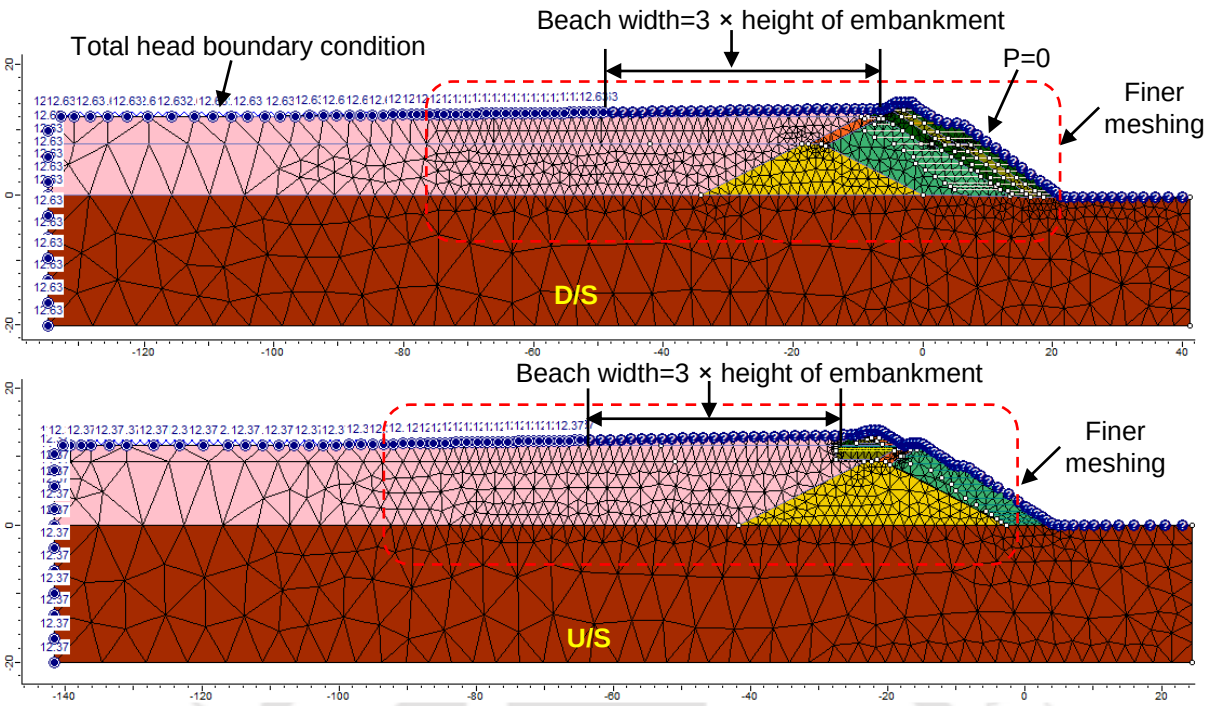

Fig. 3. 4 Finite element model utilized for the numerical analysis

3.4.2 Materials and constitutive laws

a) Soil and tailings

The TP embankments were constructed with the soil collected from the Udaisagar roadside, which is located close to the TP site. Basic geotechnical properties of various materials used in the construction of TP are obtained from the available reports provided by the concerned authority. Furthermore, the hydraulic conductivity, Young's modulus and coefficient of volume compressibility (m_v) of various materials are adopted from the relevant literatures (Ormann et al., 2013; Coulibaly et al., 2017; Hu et al., 2017; Naeini and Akhtarpour, 2018). The effect of anisotropy is prominent in the tailings deposit due to its layered nature caused by the phased disposal of tailings into the pond. As a result, to account for the anisotropy effect, a permeability ratio (K_y/K_x) of 0.1 is used for the tailings deposit, while K_y/K_x of 0.8 is considered for the embankment material (Vick, 1990; Saad and Mitri, 2011). Various geotechnical properties of the materials utilized in the present analysis are summarised in Table 3.2.

Table 3. 2 Geotechnical properties of various materials used in the numerical simulation

Material type	c' (kPa)	Φ' (Degree)	Saturated unit weight (kN/m^3)	Poisson's ratio, ν	m_v (MPa^{-1})	Hydraulic conductivity, K_x (m/s)
Embankment 1	5	28	18.60	0.30	0.10	10^{-5}
Embankment 2	32	20	17.70	0.30	0.10	10^{-5}
Embankment 3	25	22	21.00	0.30	0.10	10^{-5}
Foundation soil	30	19	21.00	0.30	0.20	10^{-9}
Tailings	24	0	18.00	0.30	0.15	10^{-7}
Clay layer	32	20	19.68	0.30	0.22	10^{-8}
Slag	0	32	13.00	0.30	0.18	10^{-7}

To simulate the behaviour of all materials, Mohr-Coulomb elastic-perfectly-plastic model is adopted which define the shear strength of soil as;

$$\tau = c' + \sigma' tan\emptyset' \tag{3.14}$$

Where, τ = shear strength of soil (kPa), c' = effective cohesion (kPa), σ'= effective normal stress (kPa) and $\emptyset'$= effective internal friction of soil (degree).

The effect of matric suction (force of attraction between unsaturated soil grains developed due to surface tension in water) on soil's shear strength is also considered in the current study by using the effective stress approach proposed by Bishop (1959).

$$\tau = c' + [(\sigma - u_a) + \chi\,(u_a - u_w)]\, tan\emptyset' \tag{3.15}$$

Where, τ = shear stress, u_a= air pressure, χ = matric suction coefficient.

The value of χ depends on the degree of saturation of soil (i.e. 1 for saturated soil and 0 for dry soil), which is determined from the soil water characteristic curve of soil or by suction-controlled triaxial shear test. Due to the unavailability of experimental data, the soil water characteristic curves of tailings and embankment soil are determined by using van Genuchten's

model (Van Genuchten, 1980). Furthermore, the van Genuchten - Mualem model is used to determine the hydraulic conductivity function of various materials using the following expression (Fredlund and Rahardjo, 1993);

$$K = K_s(\sqrt{S_e}\left[1-\left(1-S_e{}^{1/m}\right)^m\right]^2 \quad (3.16)$$

Where,

$$S_e = \frac{1}{[1+(\alpha h)^n]^m} \quad (3.17)$$

S_e = effective degree of saturation, K_s= saturated hydraulic conductivity, h = pressure head, m and n = curve fitting parameters

Values of parameters α, n and m for various materials are considered as per the default values given in RS2 which are referred from the work carried by Vogel et al. (2000). These values are also summarized in Table 3.3.

Table 3. 3 Values of α, n and , K_y/K_x used in the current study

Material type	α (m^{-1})	n	Anisotropy ratio, K_y/K_x
Embankment 1	14.5	2.68	0.8
Embankment 2	14.5	2.68	0.8
Embankment 3	14.5	2.68	0.8
Foundation soil	0.8	1.80	1.0
Tailings	1.6	1.37	0.1
Clay layer	0.8	1.80	0.8
Slag	1.6	1.37	0.8

b) Reinforcement properties

PET 100/50, a polyester woven multifilament geotextile with a tensile strength of 50 kN/m was utilized as reinforcement in both D/S and U/S case. Given that the geotextile strength degrades

with time because of creep and the chemicals present in tailings, the long-term design strength of geotextiles is determined based on the expression proposed by Berg et al. (2009):

Long-term design strength of geotextiles,

$$T = \frac{T_{ult}}{RF_{CR}.RF_{ID}.RF_{CD}} \tag{3.18}$$

Where, T_{ult} = ultimate tensile strength = 100 kN/m, RF_{CR} (reduction factor to account for creep effect) =1.67, RF_{ID} (installation damage factor) =1.4, RF_{CD} (chemical degradation factor) =1.10 are considered for PET 100/50 in the analysis, as available for the site. The values of RF_{CR} and RF_{CD} are obtained from the available reports, which are determined based on the laboratory creep and chemical tests as per IS 14739 (1999) and ASTM D 5322 (2017) standards respectively. Further, to obtain the value of RF_{ID}, the federal highway administration guidelines are referred (Berg et al., 2009), which account for the damage incurred during the installation of reinforcements. Utilizing the various reduction factors discussed above in equation 3.18, the long-term design tensile strength of geotextile is determined as 38.88 kN/m.

In addition to geotextile reinforcements, uniaxial geogrid 40RE with an ultimate strength of 52.80 kN/m was also used within embankment 3 (built in stage 3) in both U/S and D/S cases. Reduction factors for the geogrid reinforcements are considered as RF_{CR} =2.75, RF_{ID} =1.07, and RF_{CD} =1.0. In RS2, geosynthetic reinforcements are simulated by a structural interface element that has a sliding interface (joint) between either side of the support element (i.e., geotextiles and geogrid). The friction between the geosynthetic reinforcements and the embankment soil is determined by using equation 3.19, where the effective interface angle ($\emptyset'_{interface}$) is given as (Berg et al., 2009);

$$\emptyset'_{interface} = tan^{-1}\left(\frac{2}{3}tan\,\emptyset'\right) \tag{3.19}$$

Similarly, the effective unit adhesion (c_a') between the embankment soil and geosynthetic reinforcements (both geotextile and geogrid) is assumed as 0.5 times the soil-to-soil cohesion (Koerner et al., 1986).

Once the set of input parameters (i.e. material properties, loading, constitutive laws, meshing properties, etc.) are defined, transient coupled pore pressure analyses are conducted for both D/S and U/S cases. Results from the analyses are obtained in terms of EPWP, SRF, and the displacements observed during various stages of construction. Obtained results are discussed in the following section.

3.5 Results and discussion

3.5.1 Stability at the end of construction (prior to pond filling)

Two sets of analyses (one each for D/S and U/S case) are performed for the end of each phase of construction. It should be noted that the effect of seepage is not considered in the analyses performed at the end of construction as liquid tailings are not being stored at this point. Fig. 3.5 represents the critical SRF observed at the end of construction of each stage for both D/S and U/S cases. It can be seen from Fig. 3.5 that critical SRF (at the end of construction) in the D/S case decreases from 2.53 to 1.65 as the construction of embankments proceeds from stage 1 to stage 3. On the other hand, for the U/S case, the critical SRF observed at the end of construction drops initially from 2.33 (for stage 1) to 1.93 (in stage 2). However, due to the stabilization of the embankment 3 foundation with slag and geosynthetic materials (refer to Fig. 3.3), a minor increase in SRF is observed at the end of stage 3 construction. Nevertheless, the critical SRF observed at the end of construction of each stage (i.e., stages 1, 2, and 3) is found to be well within the permissible limits specified by IS 7894 (1975) (reaffirmed 1997).

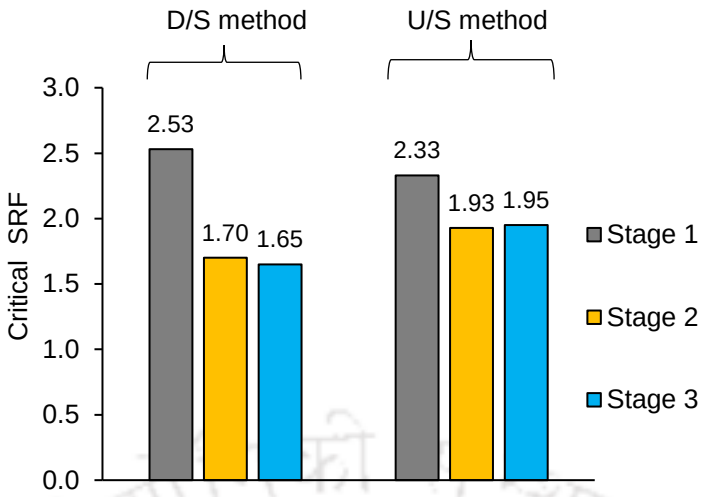

Fig. 3. 5 Critical SRF obtained at the end of construction (before pond filling) of each phase

3.5.2 Stability during staged construction (transient coupled stress-seepage analysis)

a) Development of EPWP during various stages of construction

Figs. 3.6 and 3.7 depict the contours of EPWP observed within the TP at the end of operation of stages 1, 2, and 3 respectively, for D/S and U/S cases respectively. The development of EPWP during various stages of construction is studied along a vertical profile through points A, B and C as marked in Figs. 3.6 and 3.7. Point A is considered at the middle (approximately 65 m away from the crest of embankment 3) of the minimum width of TP available at the end of stage 3 (refer to Figs. 3.6 and 3.7). Point B is selected close to the toe of the starter dyke whereas point C is located within the TP embankments. It can be observed from Fig. 3.6 that for the D/S case, EPWP at various locations within the TP (i.e., at A, B, and C) increases as the construction of embankments progresses from stage 1 to stage 3. Similarly, in the case of U/S method, EPWP is found to be increasing with increase in the stages of construction (refer to Fig. 3.7). This increase in EPWP is caused due to the application of additional construction load associated with each stage on the existing TP (built previously).

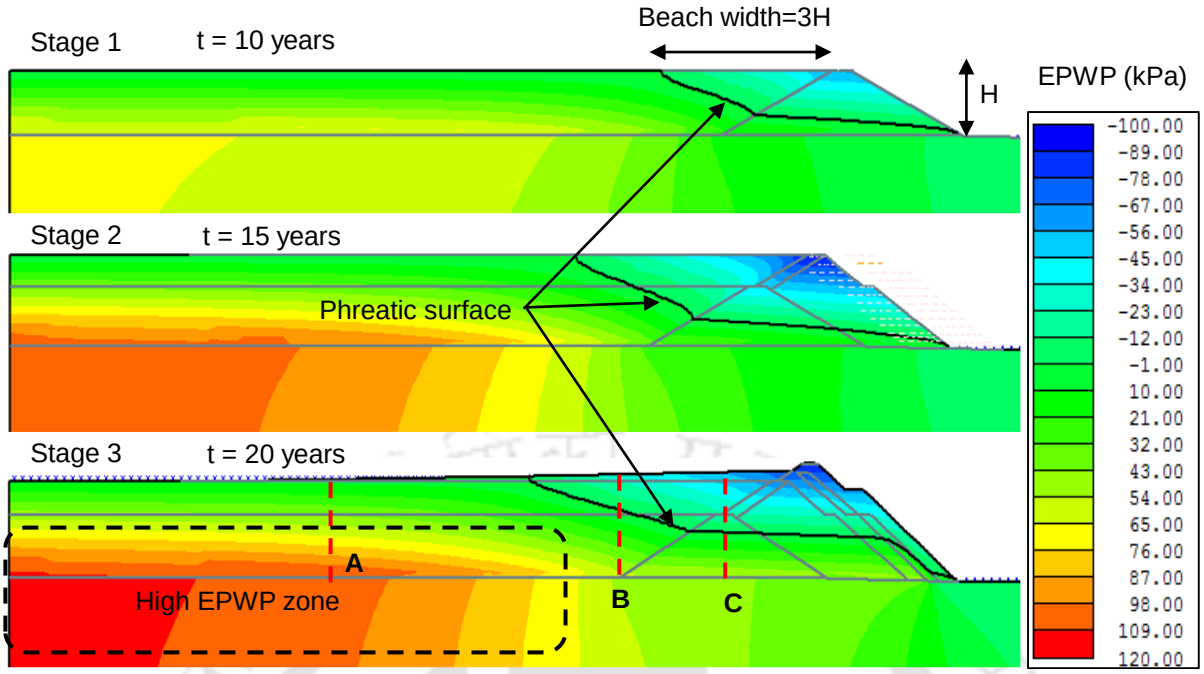

Fig. 3. 6 EPWP contours observed within TP constructed by D/S method

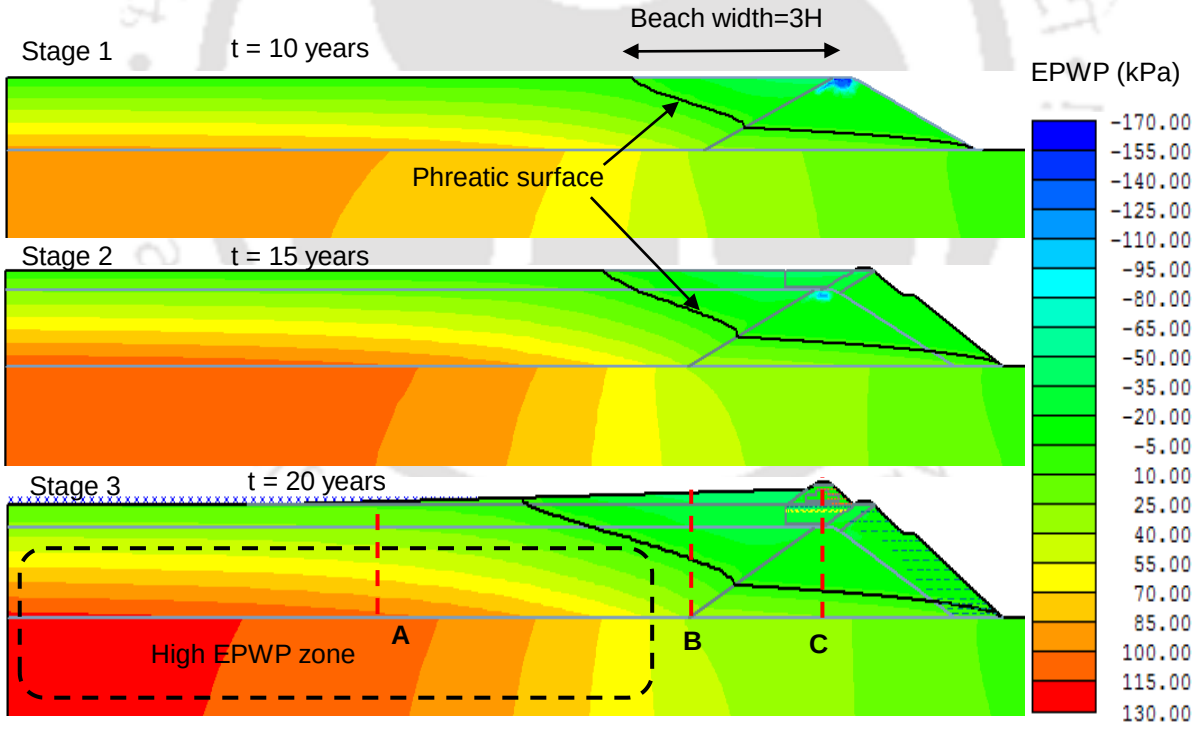

Fig. 3. 7 EPWP contours observed within TP constructed by D/S method

Furthermore, high EPWP is observed to be developed (due to the low hydraulic conductivity of tailings deposit and foundation soil) near the vicinity of point A, indicating the development of an undrained-like condition. However, EPWP decreases as one moves away

from point A towards the TP embankments as shown in Fig. 3.8 which happens due to following reasons:

a) higher hydraulic conductivity of embankment materials in comparison to the tailings.

b) availability of a shorter drainage path (as compared to zone neighbouring point A) adjacent to the TP embankments, allowing for the dissipation of pore water pressure.

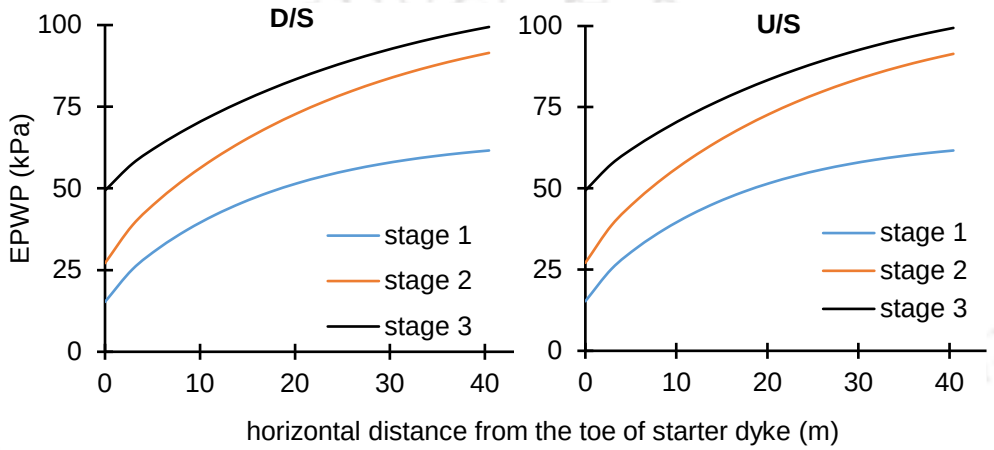

Fig. 3. 8 Variation of EPWP with horizontal distance from point B to A

Furthermore, a decrease in EPWP is observed with an increase in the height of TP built by both D/S and U/S method. This is because the length of drainage path decreases towards the surface of TP allowing the pore water pressure to dissipate easily. As highlighted earlier, a high rate of embankment rises results in the development of excessive EPWP which can trigger static liquefaction within the TP. Therefore, to investigate such a possibility, the development of EPWP at the end of the operational period of each stage is plotted against the initial effective confining stress. It can be seen from Figs. 3.9 (a-b) and 3.10 (a-b) that in none of the stages, EPWP is exceeding the initial effective confining stress at sections B and C respectively for D/S and U/S cases. This eliminates the risk of static liquefaction. However, a higher EPWP than the initial effective confining stress is observed (refer Figs. 3.11a-b) at point A making the area neighbouring point A vulnerable to static liquefaction. This observation is in accordance

with the actual condition prevailing at the site (during the operation of TP) where tailings stored near point A are in slurry form (i.e. already liquefied) thereby verifying the results of the current analysis.

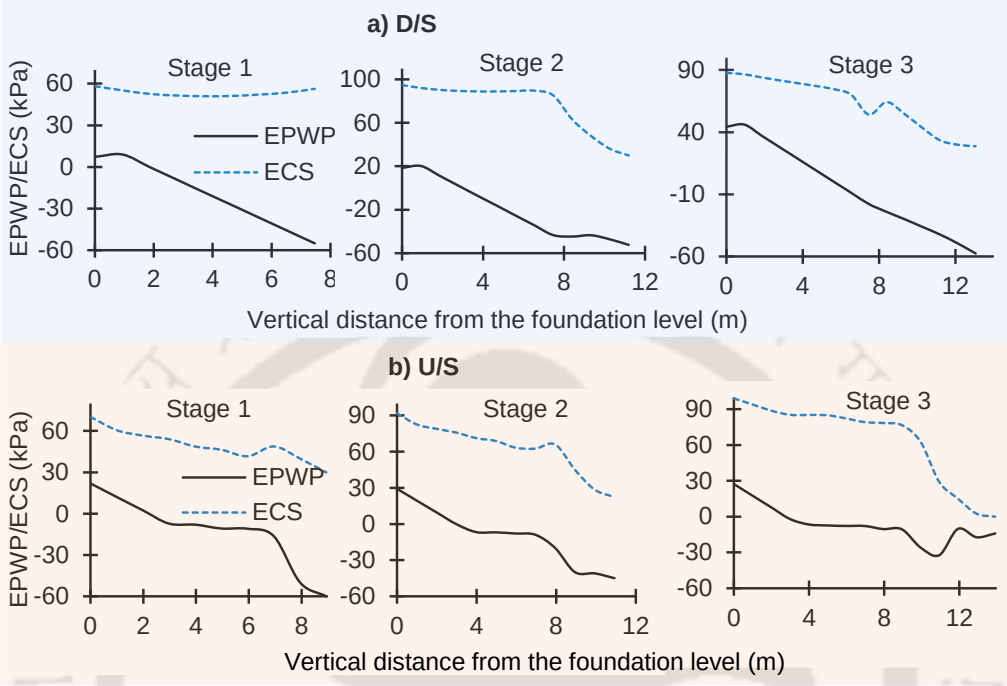

Fig. 3. 9 EPWP and initial effective confining stress (ECS) observed along vertical section at point B a) D/S case and b) U/S case

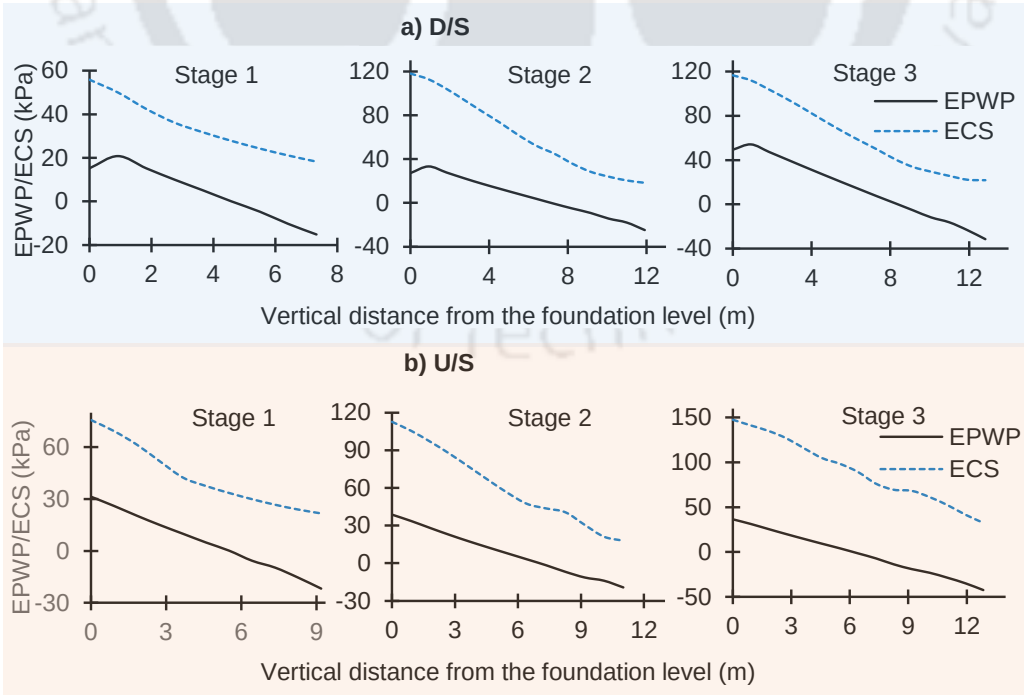

Fig. 3. 10 EPWP and initial ECS observed along vertical section at point C a) D/S case and b) U/S case

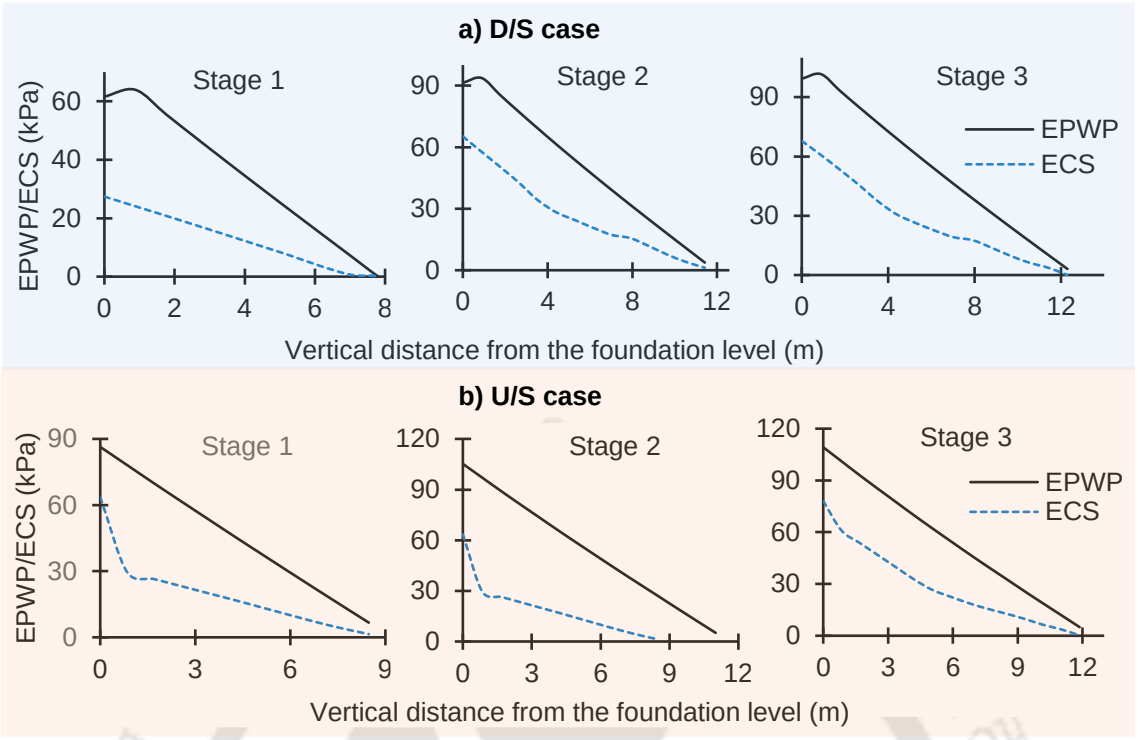

Fig. 3. 11 EPWP and initial ECS observed along vertical section at point A a) D/S case and b) U/S case

It must be highlighted here that the above findings regarding the development of EPWP within the TP cannot be found by using traditional steady seepage analysis. Hence, the results obtained from transient analysis substantiate the inappropriateness of steady-state analysis in inspecting the hydro-mechanical behaviour of TP during its staged construction.

b) Total displacements and maximum shear strain observed during staged construction

Horizontal displacements observed within the TP directly influence the stability of TP during its staged construction. Fig. 3.12 (a-b) shows the contours of horizontal displacements observed at the end of TP operation (i.e., t = 20 years) for the D/S and U/S cases respectively. It can be seen from Figs. 3.12 (a-b) that maximum horizontal displacement is observed near the toe of the embankment compared to any other region within the TP. This is because a considerable amount of flow exists near the toe region (due to the high hydraulic conductivity of embankment material) causing relatively large displacements. However, the maximum horizontal displacements observed (0.318 m and 0.289 m for D/S and U/S cases respectively)

at the end of the TP operation are found to be insignificant to make the slope of TP embankments unstable Saad and Mitri (2011).

To validate the horizontal displacements occurred within the TP, maximum shear strain observed at the end of operation of stage 3 is also analysed for both D/S and U/S cases. It can be noticed from Fig. 3.13a that the contours of maximum shear strain (i.e. failure slip surface) in D/S case follow a circular pattern initiating from the toe of embankment and ending at the tailings beach region. However, in case of U/S method, shape of failure slip surface is not entirely circular as a high shear strain get developed within the beach region due to the construction of embankment 3 (refer to Fig. 3.13b). Nevertheless, maximum shear strain obtained at the end of TP's design life is found to be 0.098 and 0.095 for D/S and U/S case respectively, which as per Saad and Mitri (2011) is negligible to induce instability in the TP.

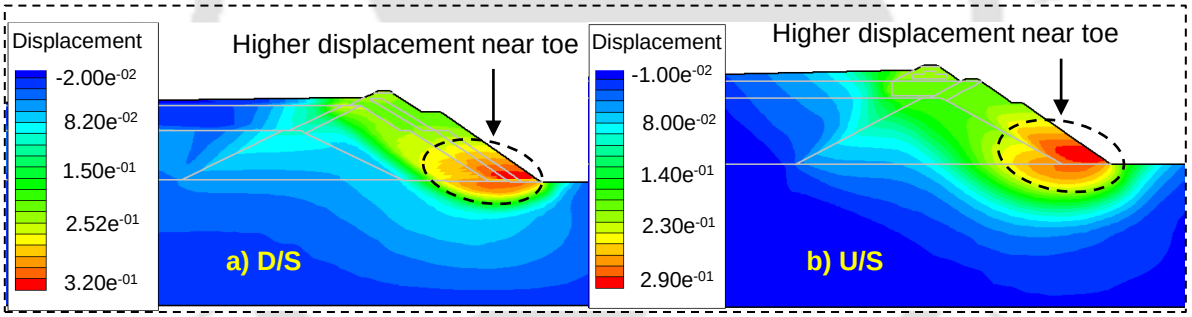

Fig. 3. 12 Contours of horizontal displacements at the end of TP operation (i.e. after t=20 years) a) D/S case and b) U/S case

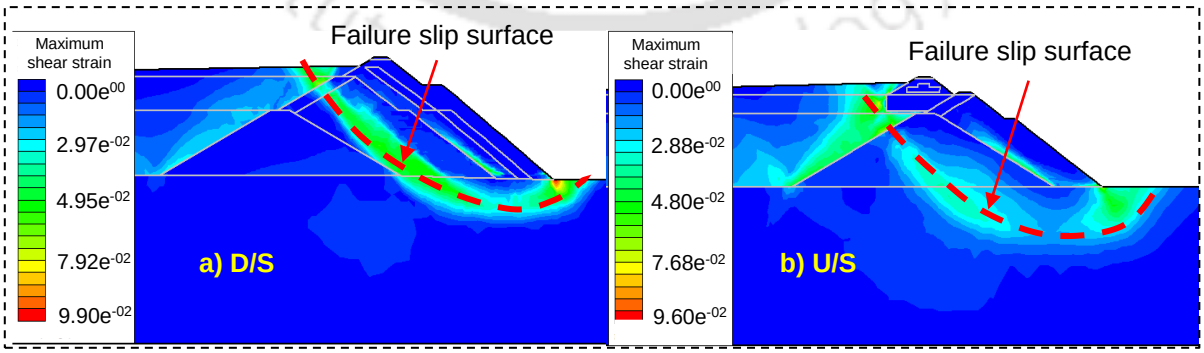

Fig. 3. 13 Maximum shear strain observed at the end of TP operation a) D/S case and b) U/S case

c) Critical SRF observed during various stages of construction

The overall stability of the entire TP at the end of the operation in each stage is assessed based on the critical SRF obtained for that stage. Fig. 3.14 illustrates the critical SRF obtained at the end of each stage (i.e., stages 1, 2, and 3) for both D/S and U/S cases. It can be seen from Fig. 3.14 that the critical SRF decreases with an increase in the stages of construction for the D/S case whereas the decrease in critical SRF is observed only at the end of stages 1 and 2 for the U/S case. However, the drop in the critical SRF (see Fig. 3.14) is not noticed for stage 3 construction (for the U/S case) since the base of embankment 3 and the embankment 3 were already stabilized with slag and geosynthetic reinforcements. The decrease in the critical SRF during the various stages of construction is due to the reason that EPWP developed within the TP increases with increase in the stages of construction, which in turn reduces the shear strength of embankment material (due to reduction in the effective stress). Nevertheless, the critical SRF (1.38 and 1.70 for D/S and U/S cases respectively) at the end of operation of stage 3 (i.e., in the present condition at the site) is found to be within the permissible limits (i.e., SRF > 1) recommended by IS 7894 (1975) (reaffirmed 1997).

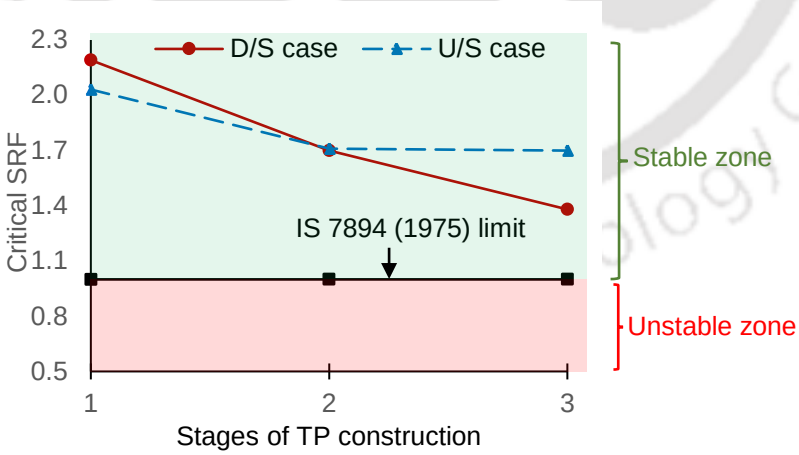

Fig. 3. 14 Critical SRF obtained at the end of various stages of TP construction

3.5.3 Scope for future expansion and effect of embankment raising rate on TP stability

The production of tailings (jarosite) is increasing at a rapid rate due to the continual extraction of zinc. Therefore, to accommodate extra tailings, the scope for the future expansion of TP is also investigated in the current study. In the present scenario, the heightening of TP embankments by D/S method is not practically feasible due to the unavailability of land around TP. As a result, the only alternative left is to investigate the viability of height raising by U/S method. Fig. 3.15 shows the proposed geometry of TP constructed by U/S method for its future expansion.

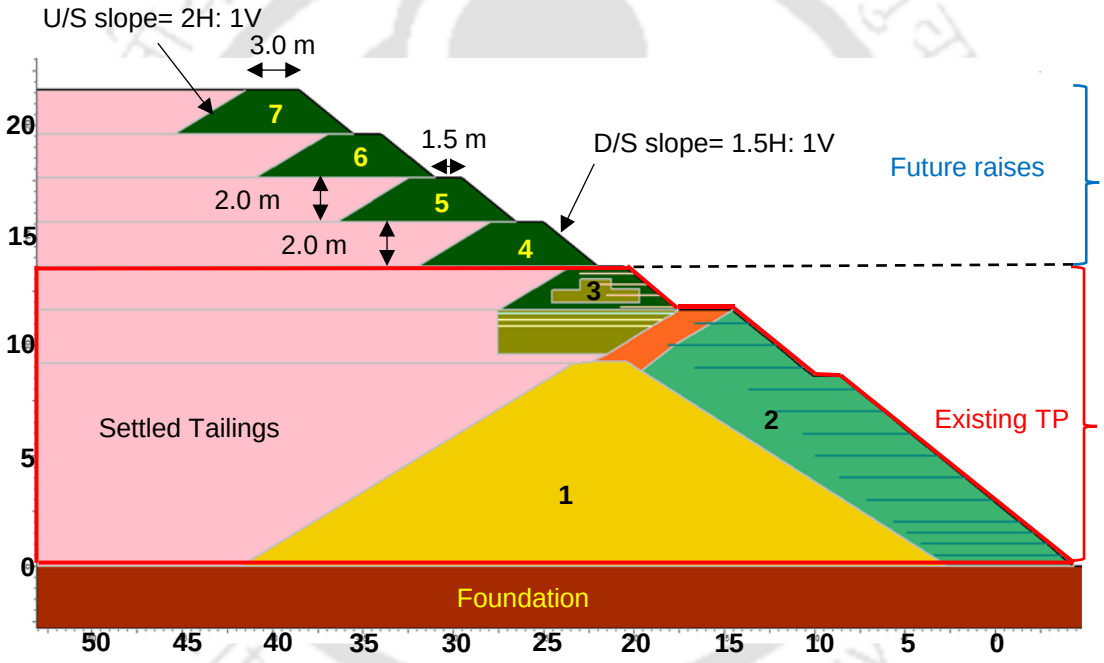

Fig. 3. 15 Geometry used for the future expansion of TP by U/S construction method

A total 4 raises of 2 m height are provided to increase the height of the existing TP as shown in Fig. 3.15. The dimensions of new embankments are kept the same as provided in the existing embankments of TP (refer to Fig. 3.15). For example, the U/S and D/S slopes of embankments are maintained at 2H: 1V and 1.5H: 1V respectively, while the crest width in each embankment is set at 3 m. In addition, a 1.5 m wide berm is also given to the embankment built in the previous stage before the construction of the new embankment. Stability analysis

is performed in RS2 software to examine the feasibility of the proposed TP discussed above. While doing so, the impact of embankment raising rate on the overall stability of TP is also assessed.

To investigate the influence of embankment raising rate, the geometry of TP is drawn in RS2 modeler as per the dimensions discussed above. 5 stages are created in RS2, 4 of which replicate the 4 lifts provided for height raising, whereas the remaining stage (i.e. initial stage) is provided to simulate the existing geometry of TP (after stage 3). The construction of each stage (i.e. stages 4, 5, 6, and 7) consists of 2 phases i.e. a) the raising phase, which includes both embankment construction and pond filling operations, and b) the consolidation phase, which includes the time given for the self-weight consolidation of tailings after pond filling operation. For the present study, the embankment raising rate is considered as the time required (in days) to raise the height of the embankment by 2 m. Therefore, to examine the impact of embankment raising rate on the stability of TP, the time required for each raising operation is considered as 10, 30, 60, 120, and 365 days. However, a constant time of 365 days is considered for each consolidation phase to account for the self-weight consolidation of tailings. Once the staged construction is simulated in RS2, various input parameters are defined, and the stability analysis is carried out. It is worth noting here that the input parameters used for the current analysis (such as material properties, constitutive laws, loading conditions, mechanical and hydraulic boundaries) are kept similar to those used in the stability analysis performed earlier. Finally, transient stress-pore pressure analysis is carried out for different embankment raising rates and the EPWP developed during different phases of construction are examined.

a) Development of EPWP with varying embankment raising rate

Fig. 3.16 depicts the contours of EPWP developed within the TP facility during different phases of height raising. It can be noted from Fig. 3.16 that a higher EPWP is developed beneath the embankment during each phase of height raising (i.e. R4, R5, R6, and R7). However, this

increased EPWP dissipates subsequently during each phase of consolidation (i.e. C4, C5, C6, and C7).

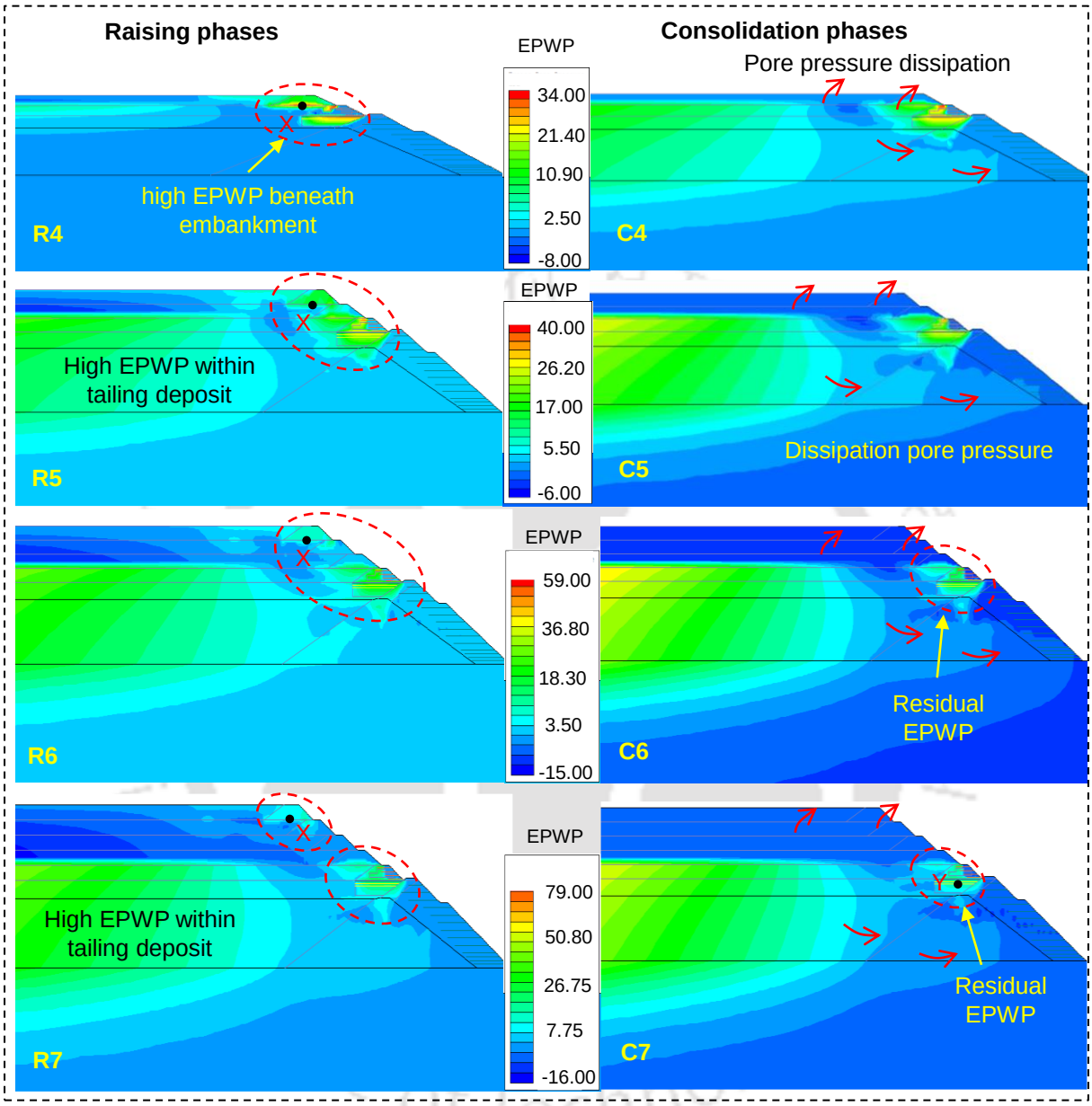

Fig. 3. 16 Contours of EPWP developed during various phases of construction with respect to an embankment raising rate of 10 days (R=Raising phase, C= Consolidation phase)

As illustrated in Fig. 3.16, a zone of high EPWP forms within the tailings deposit attributable to two potential reasons. Firstly, the tailings exhibit lower hydraulic conductivity than the embankment materials redistricting the dissipation of EPWP. Secondly, the drainage path within the midsection of the tailings deposit is notably longer compared to that near the

embankments requiring an extended period for EPWP dissipation. To further investigate the impact of embankment raising rate on the stability of TP, the evolution of EPWP with varying embankment raising rates is analysed at point X (refer to Fig. 3.16 for further details) which lies beneath the embankment which is being raised.

The variation of EPWP at point X with different rates of embankment rising is depicted in Fig. 3.17. It can be seen from Fig. 3.17 that EPWP increases significantly with increasing embankment raising rate. For instance, the maximum EPWP is found to develop when the embankments are raised in 10 days. On the other hand, a minimum EPWP is developed when the embankments of TP are raised in 365 days, which also corresponds to the field rate followed at the site. The development of high EPWP at a higher embankment-raising rate can be attributed to the availability of less time for the dissipation of EPWP during height-raising operations. On the other hand, at a lower embankment-raising rate sufficient time is available for the EPWP to dissipate (partially), resulting in the development of a smaller amount of EPWP. It should be noted here that the complete dissipation EPWP does not occur during the consolidation phases, which could be attributed to the lower hydraulic conductivity of tailings and embankment materials. In addition, the time allotted for each consolidation phase also influences the dissipation of EPWP, the effect of which is beyond the scope of this study. As depicted in Fig 3.16, a notable residual EPWP persists beneath the embankment raised during stage 3 compared to other locations along the embankments. This is because the area around the embankment raised in the third stage is encased by clay and slag materials, which possess relatively lower hydraulic conductivity. Consequently, the dissipation of EPWP becomes challenging leading to a higher residual EPWP. To further investigate the extent of this residual EPWP at varying raising rates, the residual EPWP is plotted at point Y situated within the high EPWP zone (see Fig. 3.16).

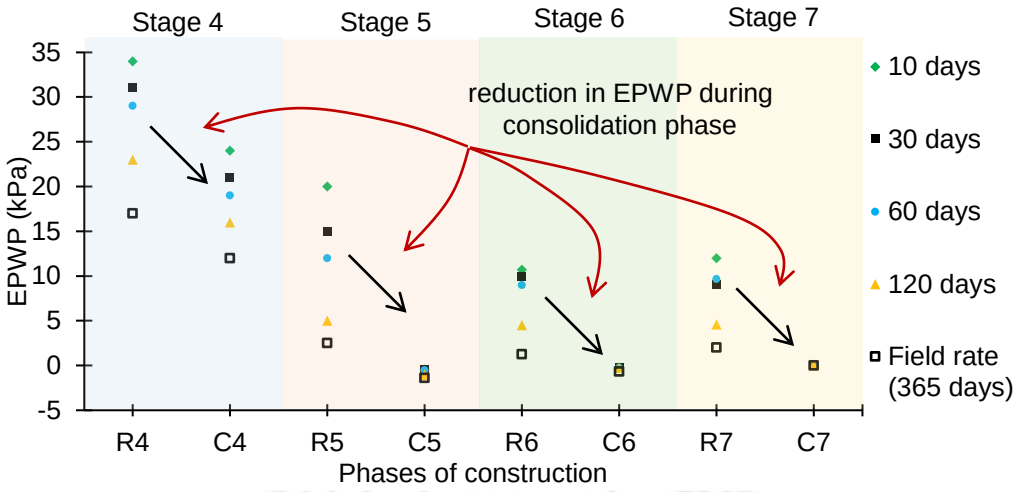

Fig. 3. 17 Variation of EPWP at point X (refer to Fig. 3.16) with respect to different embankment raising rate (R=Raising phase, C= Consolidation phase)

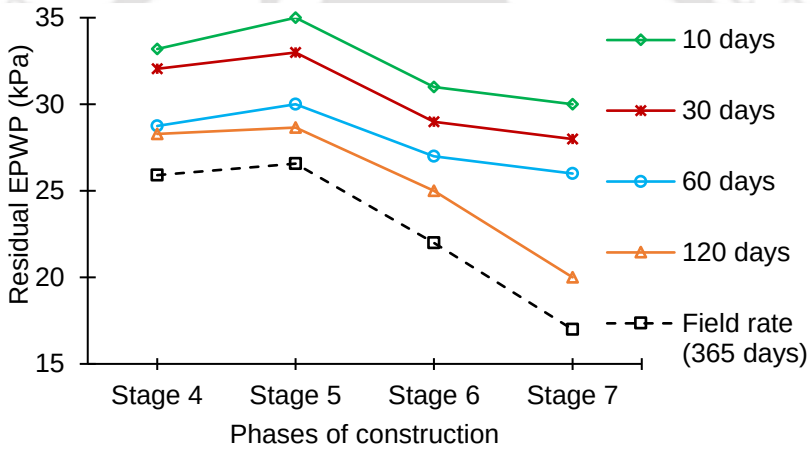

Fig. 3. 18 Residual EPWP remaining after each consolidation phase for different embankment raising rate

Fig. 3.18 shows the residual EPWP remaining (at point Y) after each consolidation phase with respect to different embankment-raising rates. A high residual EPWP remains after each phase of consolidation corresponding to a higher embankment-raising rate. For instance, the residual EPWP remaining after stage 4 with respect to 10 days of embankment raising is found to be 30.32 kPa in comparison to 17.20 kPa for 365 days of embankment raising. The residual EPWP has an impact on the overall stability of TP embankments, which is analysed in relation to the critical SRF as elaborated in the following section.

b) Impact on critical SRF

The stability of TP embankments is greatly influenced by the residual EPWP remaining after each stage of construction. Fig. 3.19 illustrates the critical SRF observed during various stages of TP construction with respect to different embankment raising rates.

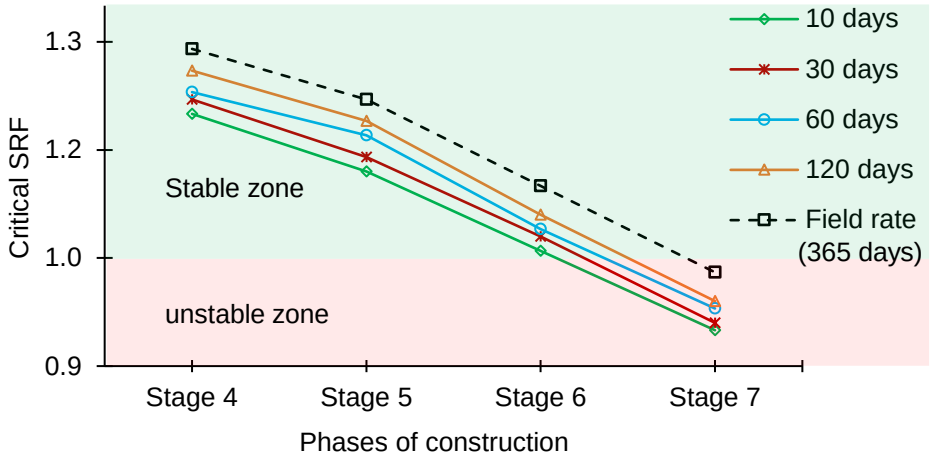

Fig. 3. 19 Variation of critical SRF with respect to different embankment raising rate

It can be observed from Fig. 3.19 that the critical SRF decreases with increasing rates of embankment raising. This is due to the larger residual EPWP left after each stage of construction at a higher embankment-raising rate, which reduces the effective stress and consequently the shear strength of tailings and embankment material. Furthermore, the critical SRF decreases with increase in the stages of construction as shown in Fig. 3.19. For instance, the critical SRF drops from 1.29 to 0.98 at the end of 4th raise when the embankments are raised at an embankment raising rate of 365 days. Similar observations can be also noticed with respect to other embankment raising rates, where critical SRF drops below 1 after 4th raise. Therefore, it can be inferred from the stability analysis that TP will be stable for a maximum of two rises at any given embankment raising rate. Providing more than 2 lifts will make the TP unstable as the critical SRF for those cases is close to 1 or less than 1 (minimum value specified in IS-7894, 1975). Since the width of TP at the central portion is very less (see Fig. 3.1), height raising by U/S method will further reduce the storage capacity of TP. This can make

the future expansion of TP practically infeasible and therefore any further raises are not recommended. The TP must therefore be decommissioned with an appropriate closure plan.

3.6 Closure of TP

Considering the stability analysis performed above, the embankments of TP (built using both U/S and D/S construction techniques) are deemed to be safe in their existing state. In the present condition, the TP has also reached its full capacity with no scope for further rise due to the non-availability of space. Hence, to avoid future environmental hazards from the contaminated stored tailings, dry closure of the TP must be done. Prior to the closure of TP, the settled tailings must be in dry condition to avoid excessive settlements during the capping of TP (Justo et al., 2019). It can be observed from Fig. 3.20a that the topmost surface of the tailings deposit (in its current state) is mostly dry at various locations within the TP. However, traces of water are also detected at certain locations within the TP (refer to Fig. 3.20b). Furthermore, growth of vegetation is noticed on the D/S slopes of embankments of TP (refer to Fig. 3.20c), which provides additional protection against the slope erosion. Thus, collectively based on the outcomes of the present stability analysis and actual site-based observations, the closure of TP can be done by providing an appropriate covering system.

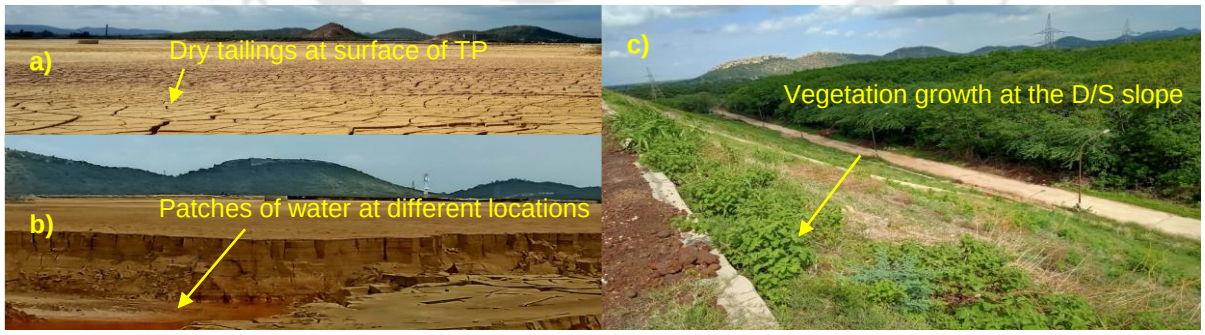

Fig. 3. 20 TP condition at site showing a) dry tailings at surface b) presence of water at certain locations and c) growth of vegetation on the D/S slope

3.7 Summary

This chapter investigated the stability of a TP by incorporating the effect of EPWP and embankment raising rate. Following major conclusions are drawn from the present study:

- A high EPWP zone is found to develop within the tailings deposit during each phase of construction which is attributable to the low hydraulic conductivities of tailings and foundation soil. However, a relatively smaller EPWP is found to develop within the TP embankments due to the higher hydraulic conductivity of the embankment materials.
- At no stage, EPWP is found to exceed the initial effective confining stress within the embankments of TP and tailings beach region eliminating the risk of static liquefaction. Overall, the critical SRFs obtained (in both D/S and U/S cases) during various stages of construction are found to be within the permissible limits specified by IS 7894 (1975). Therefore, TP in its current form can be considered safe.
- The rate of embankment raising is found to have a significant impact on the development of EPWP and thereby on the overall stability of TP. A greater EPWP is developed in the TP facility with an increasing embankment-raising rate, resulting in the reduction of critical SRF values.
- EPWP increases during each phase of height raising which subsequently decreases during the consolidation phases owing to the dissipation of EPWP. However, a residual EPWP remains after each consolidation phase which has a negative impact on the overall stability of TP.
- Overall, based on the site investigation and the stability analysis, future expansion of TP is not economically feasible (by any method), hence it must be decommissioned using a suitable closure system.

Chapter 4

Exploring the utilization potential of alkali activated MT as tailings pond embankment material

4.1 General

This chapter explores the feasibility of three different MT namely; red mud (RM), iron tailings (FeT) and zinc tailings (ZT) as construction materials for TP embankments through alkali activation. A series of unconfined compressive strength (UCS) tests and direct shear tests (DST) are carried out to assess the strength performance of alkali activated MT. While doing so, the influence of alkali activator concentration, curing period and curing conditions are also investigated. Furthermore, durability tests are conducted to examine the weathering resistance of stabilized MT specimens against 12 alternate wetting and drying cycles. To further improve the strength and durability performance of MT, granulated blast furnace slag (GBFS) is also added as a precursor to increase the effectiveness of geopolymerization. Moreover, specimens of MT are also prepared using Pozzolana Portland cement (PPC, grade 43) as a reference mix. Furthermore, permeability tests are conducted to evaluate the hydraulic performance of stabilized MT specimens, which has a direct impact on the overall stability TP embankments. Finally, cost analysis is also performed to compare the effectiveness of alkali activate MT as embankment material compared to cement stabilized MT. In the end, the suitability of alkali activated MT as an embankment material is further confirmed through a numerical analysis conducted on an existing TP, validating its appropriateness for the deployment in TP embankments.

4.2 Materials characterization

4.2.1 Geotechnical characterization of RM, FeT and ZT

Materials used in this study include RM, FeT, ZT, GBFS and PPC. RM and GBFS are obtained from Guru Corporation in Ahmadabad, Gujarat, India, while FeT is sourced from Gogga Minerals and Chemicals in Bellari, Karnataka, India. ZT samples are collected from the tailings disposal facility at Zawar mines in Udaipur, Rajasthan, India whereas PPC (grade 43) is procured from the local supplier. The specific gravity of various MT materials is determined using the pycnometer method following the guidelines outlined in ASTM D854 (2014). The particle size distribution of various materials is determined through a combination of sieve analysis and sedimentation (hydrometer) analysis following the procedure specified in ASTM D422-63 (2007) and ASTM D7928 (2021) respectively. In addition, the liquid limit and plastic limit are determined using Casagrande's apparatus, following the guidelines outlined in ASTM D4318 (2010).

Table 4.1 provides an overview of the various geotechnical properties of RM, FeT, and ZT. It is apparent from Table 4.1 that FeT exhibits the highest specific gravity (3.47) among all the three materials followed by RM (2.94), and ZT (2.65). The presence of high Fe_2O_3 content in FeT and RM (confirmed by the XRF results discussed subsequently) contributes to their higher specific gravity compared to ZT. Fig. 4.1 displays visual images along with grain size distribution curves of various materials employed in this study. As depicted in Fig. 4.1, RM and FeT exhibit a reddish-brown hue due to the presence of Fe_2O_3, whereas ZT displays a greyish appearance. According to the Unified Soil Classification System (USCS) (ASTM D2487, 2011), RM and FeT fall under the category of low plastic clay (CL), whereas ZT is classified as low plastic silt (ML).

Table 4. 1 Basic geotechnical properties of RM, FeT, ZT and GBFS used in the study

Properties	RM	FeT	ZT	GBFS
Specific gravity	2.94	3.47	2.65	2.80
Clay content (< 0.002 mm)	30.22	17.41	13.01	1.47
Silt content (0.075 – 0.002) mm	57.38	37.68	73.56	91.36
Sand fraction (4.75 – 0.075) mm	12.40	44.91	13.43	7.17
Liquid limit	40.30	31.37	23.45	-
Plastic limit	18.85	19.05	Non-plastic	-
Plasticity Index	21.45	12.32	Non-plastic	-
USCS classification	CL	CL	ML	-
pH	10.40	8.58	8.60	8.72
Specific surface area, SSA (m^2/g)	23.50	12.85	3.06	-
Average pore diameter (nm)	15.72	12.27	8.24	-
Water holding capacity, WHC (%)	149.08	139.36	128.56	129.20

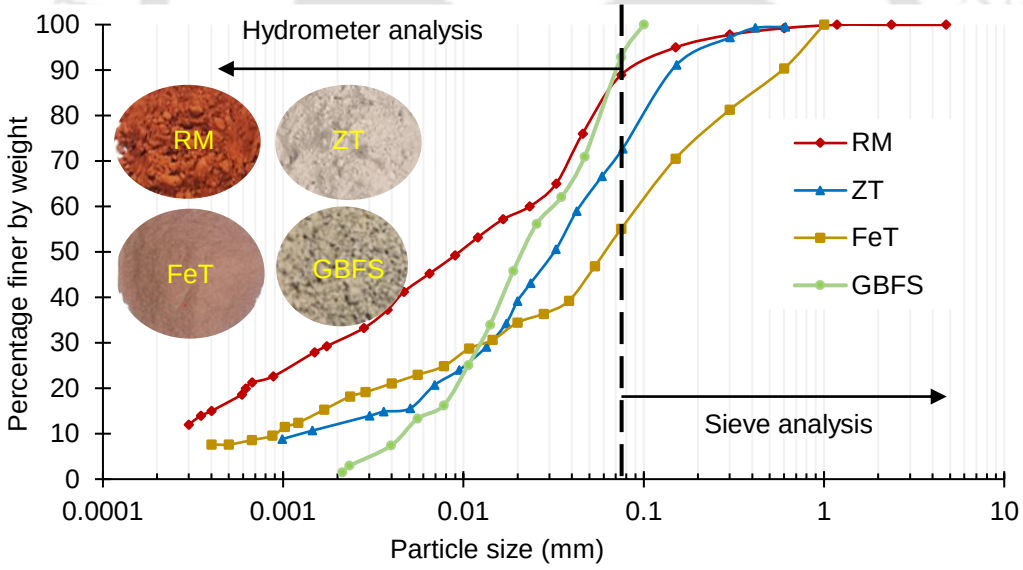

Fig. 4. 1 Particle size distribution curve of RM, FeT, ZT and GBFS

4.2.2 Physicochemical characterization

The pH value of various materials used in the current study is determined using the EUTECH PC2700 (Singapore). The samples for pH testing are prepared by maintaining a solid to water ratio (i.e. weight to volume ratio) of 1:5 as recommended by Hendershot et al. (1993). The experimental results reveal pH values of 10.40, 8.58, and 8.60 for RM, FeT, and ZT

respectively indicating their alkaline nature. The increased alkalinity of RM compared to other MT can be attributed to the digestion of bauxite with NaOH during the Bayer process, which raise the pH of RM.

Brunauer-Emmett-Teller (BET) surface area analysis is conducted to determine the specific surface area of various material through N_2 gas adsorption. As shown in Table 4.1, RM exhibits the highest specific surface area (23.50 m^2/g) followed by FeT (12.85 m^2/g) and then ZT (3.06 m^2/g). To determine the water holding capacity of various materials, a known quantity of oven-dried samples is submerged in deionized water for 48 h. Subsequently, the wet weight of the samples is measured after allowing them to drain by gravity for 2 h through Whatman grade-1 filter paper. The water holding capacity is then expressed as a percentage, calculated as the ratio of the wet weight to the initial dry weight of the sample (Patwa et al., 2021). Based on the experimental results, the water holding capacity of RM, FeT and ZT is measured as 149.08%, 139.36% and 128.56% respectively. The higher specific surface area of RM contributes to their greater water holding capacity content as compared to FeT and ZT.

4.2.3 Mineralogical and microstructural characterization

The mineralogy of various materials utilized in the current study is assessed through X-ray diffraction (XRD) using the Rigaku Micromax-007HF instrument (Tokyo). Figs. 4.2 (a-d) display the results of XRD analysis showcasing the peaks of various phase constituents specific to each material. It is evident from Figs. 4.2 (a-d) that quartz (SiO_2) emerges as a prominent phase constituent present in all materials used in the study. In addition, RM is also characterized by minerals such as mullite ($Al_6Si_2O_{13}$) and bayerite ($Al(OH)_3$) (refer to Fig. 4.2a) while ZT prominently contains calcium aluminium silicate ($Ca_3Al_6Si_2O_{16}$) (refer to Fig. 4.2b). Similarly, FeT contain hematite (Fe_2O_3) as one of the principal minerals along with quartz (SiO_2). To determine the chemical composition of different materials, X-ray fluorescence spectrometer

(XRF) analysis is carried out through pressed pellet method using Panalytical Zetium XRF spectrometer.

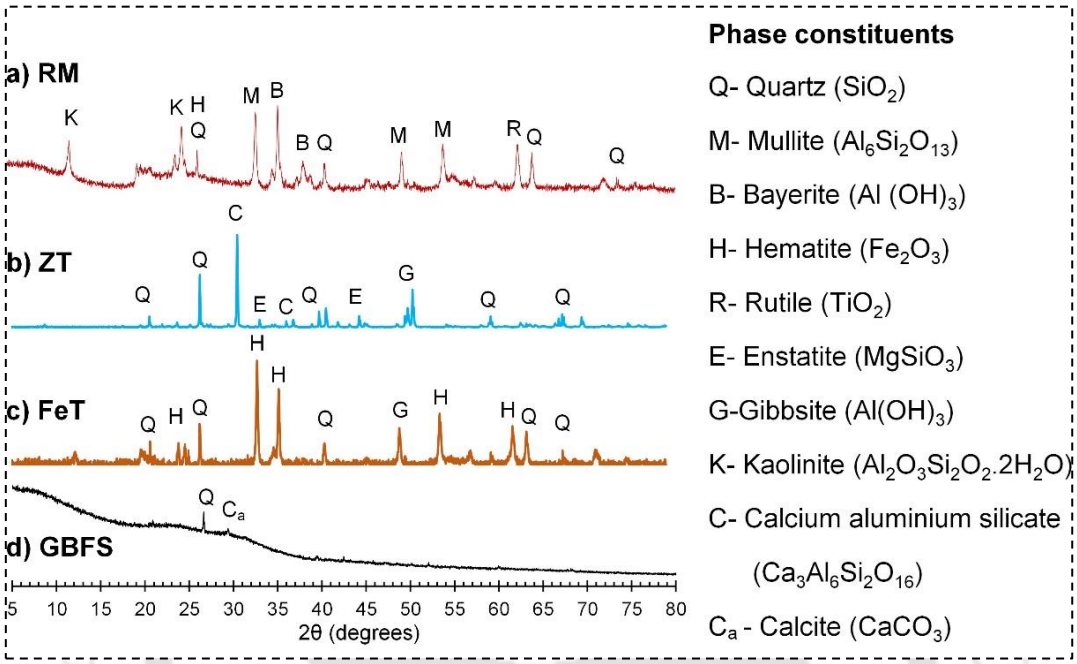

Fig. 4. 2 Results of XRD analysis showing the mineralogy of a) RM, b) ZT, c) FeT and d) GBFS

Table 4. 2 Chemical composition of various materials determined from XRF analysis

Major oxides (%)	RM	FeT	ZT	GBFS	PPC
SiO_2	36.12	29.73	57.25	33.15	26.60
Al_2O_3	23.90	25.56	8.72	17.67	7.38
Fe_2O_3	23.11	40.01	0.12	1.43	4.39
MnO	0.03	0.00	-	0.32	0.02
MgO	0.12	0.62	8.23	5.52	4.45
CaO	0.18	0.35	9.01	35.56	46.10
Na_2O	0.00	1.42	0.88	0.34	0.00
K_2O	0.14	1.15	2.32	0.62	0.58
TiO_2	2.67	0.86	-	0.66	0.59
P_2O_5	0.05	0.00	-	0.01	0.13
SO_3	0.02	-	0.02	0.02	2.52
ZnO	-	-	3.89	-	-

Table 4.2 presents the results of XRF analysis showcasing the weight proportions of major oxides present in RM, FeT and ZT. It can be noted from Table 4.2 that all MT (i.e. RM, FeT and ZT) contains a substantial amount of SiO_2 and Al_2O_3 which are the primary ingredients required in a geopolymer binder. Moreover, aside from SiO_2 and Al_2O_3, GBFS also contains a substantial proportion of CaO. Furthermore, it can be noted from Table 4.2 that PPC display a slightly reduced CaO content compared to ordinary Portland cement due to inclusion of pozzolanic material such as fly ash.

Figs. 4.3 (a-d) display the microstructure of various materials obtained from field emission scanning electron microscope (FESEM) (Manufacturer-Zeiss, model-Gemini). As shown in Fig. 4.3 (a-b), RM and FeT particles are irregular in shape with flake-like structure. On the other hand, ZT particles have cuboidal block-like structure (see Fig. 4.3c) while GBFS particles are irregular in shape with sharp edges (see Fig. 4.3d).

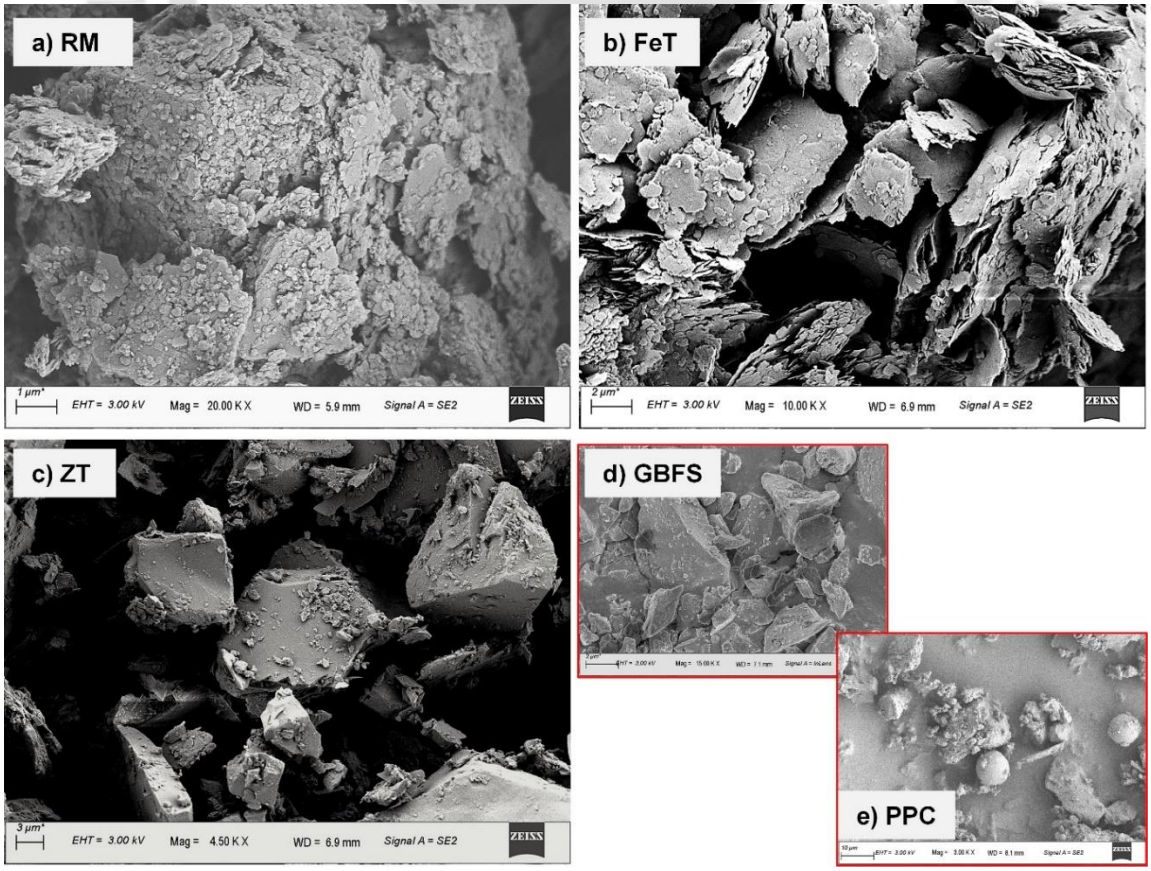

Fig. 4. 3 FESEM images of a) RM, b) FeT, c) ZT, d) GBFS, and PPC

4.2.4 Alkali activator

The function of alkali activators in geopolymerization is to dissolve reactive silicate and aluminate tetrahedra from aluminosilicate raw materials. The released Si- and Al- tetrahedra are polycondensed into oligomers, which further gets polymerized into synthetic aluminosilicate structures (Davidovits, 1991). Typically, NaOH, KOH, Na_2SiO_3 or a combination of these are employed for alkali activation. Among these, KOH has been observed to be the least effective in terms of improving strength and durability. On the other hand, both NaOH and Na_2SiO_3 are considered the most efficient alkali sources for alkali activation. Na_2SiO_3 has significantly better binding properties compared to NaOH and KOH, which provides greater strength and durability to geopolymer composites. Meanwhile, NaOH being a strong base, has a significantly higher dissolution efficiency which promotes the liberation of Si and Al units essential for geopolymerization. In terms of environmental sustainability, the use of Na_2SiO_3 is considered as more environmentally sustainable as it releases lesser CO_2 into the atmosphere compared to NaOH (Feng et al., 2024). However, Na_2SiO_3 is much costlier than NaOH as its production involves the melting of silica with Na_2CO_3 or NaOH, which is a more complex and energy-intensive process (McLellan et al., 2011). Based on the above discussion, NaOH with 97% purity (originally in pellet form) has been utilized as an alkali activator for the present study. NaOH solution is prepared by dissolving the required mass of NaOH pellets in deionised water to achieve a target concentration. To obtain the optimal concentration of NaOH for activation, solutions with 4 molarities namely; 2.5M, 5M, 7.5M and 10M are used in the current study. Prepared NaOH solutions are allowed to cool for at least 24 h before mixing it with RM. Since, the interaction of NaOH with water generates a lot of heat, this changes the kinetics of geopolymerization reaction. A higher temperature of NaOH solutions can lead to the quick setting of MT due to the faster reaction of NaOH with MT particles (Ismail et al., 2014; Miraki et al., 2022).

4.3 Compaction characteristics of RM, FeT and ZT

Compaction characteristics of tailings has a direct impact on the overall stability of TP embankments. To achieve the maximum shear strength and stiffness, tailings are compacted at their maximum dry unit weight (MDU) and optimum moisture content (OMC). Keeping this in view, the strength and durability of alkali activated RM are determined on the specimens compacted at their respective MDU and OMC. To obtain OMC and MDU of RM activated with different concentrations of NaOH solutions, mini compaction tests are performed following the procedure recommended by Sridharan and Sivapullaiah (2005). It is a known fact that MT exhibit greater dry density with NaOH solutions than with water due to its high lubricating capacity (Singh et al., 2023). However, to avoid the influence of this increased density on the mechanical, durability and hydraulic properties of MT, the compaction characteristics are determined with deionised water. To begin the compaction experiments, air-dried samples of RM, FeT and ZT are manually blended to ensure a uniform and consistent mixture. Following that, deionized water is added to the prepared blend and mixed meticulously for a duration of 5 minutes, ensuring the absence of any lumps. The prepared mixture is then compacted in a compaction mould in three distinct layers, each subjected to 36 blows with a 1 kg hammer. This procedure is repeated for 6 times by varying water content each time, to acquire the dry density values associated with different levels of water content.

Fig. 4.4 presents the outcomes of mini compaction tests regarding dry density and moisture content. It is evident from Fig. 4.4 that among all MT, FeT demonstrates the highest MDU followed by RM and ZT. The higher dry density of FeT can be attributed to its greater specific gravity (3.47) and larger coarse fraction (particle size > 0.075mm) compared to RM and ZT. Similarly, RM displays the highest OMC among all MT followed by ZT and FeT. Higher OMC of RM can be attributed to its higher water holding capacity and greater specific surface area

compared to ZT and FeT. Table 4.3 compiles the values of MDU and OMC for different MT employed in specimen preparation for various experiments.

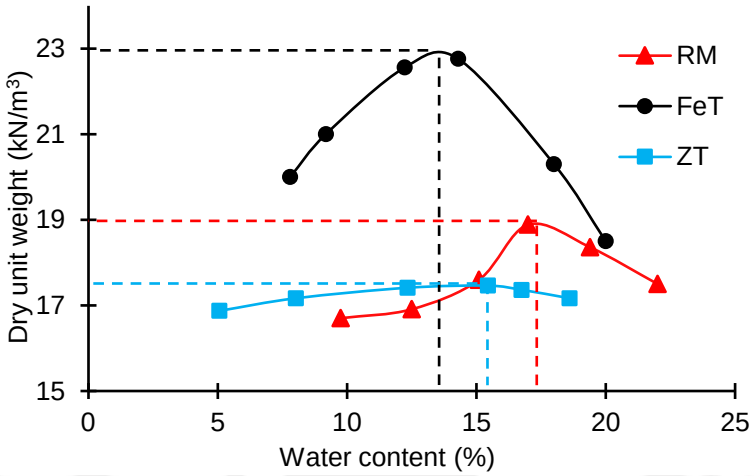

Fig. 4. 4 Compaction curve for RM, FeT and ZT

Table 4. 3 Dry unit weight and liquid alkali content used for various testing

Mix Type	Dry unit weight (kN/m^3)	Liquid alkali content (%)
RM	18.91	17.56
FeT	23.00	14.21
ZT	17.46	15.40

4.4 Mix proportion and sample preparation

In this study, three sets of samples are prepared for each test. The initial set of specimens is prepared by mixing bare MT with varying NaOH concentrations (i.e. 2.5M, 5M, 7.5M and 10M). To prepare the specimen, the oven-dried MT is hand mixed with different concentrations of NaOH solutions for 5 minutes until a uniform mixture is achieved. The quantity of dry MT and NaOH solutions is selected based on MDU and OMC obtained from mini compaction tests for respective MT. The prepared mixture is then utilized to make specimens for various experiments, the details of which will be discussed in subsequent subsections.

In the second set, GBFS is introduced as an additional precursor to enhance the strength and durability of FeT and ZT particularly at lower NaOH concentrations. To prepare the FeT-GBFS and ZT-GBFS specimens, the quantity of GBFS is set at 10% and 20% by dry weight of the mix, while the NaOH concentration is maintained at 2.5M. In the third set, specimens of MT are prepared using PPC. The proportion of PPC in the mix is set at 10%, which is the maximum amount used in any cement stabilized material. It should be noted here that for the current work, GBFS is employed to improve the strength and durability of ZT at lower NaOH concentrations. Therefore, only 2.5M NaOH solution is utilized to activate FeT and ZT mixtures to control the cost of geopolymer binder without compromising the strength and durability standards. Moreover, in the present study, GBFS is not utilized in the preparation of RM specimens as alkali activated RM alone is found to have sufficient strength and durability.

4.5 Experimental methodology

4.5.1 UCS tests

To examine the mechanical performance of geopolymer specimens, UCS tests are performed in compliance with ASTM D2166 (2006) using an automated testing machine with a load capacity of 50 kN. The rate of loading during the UCS tests is kept at 1.25 mm/minute as recommended by ASTM D2166 (2006). Specimens of length = 76 mm and diameter = 38 mm are prepared in a cylindrical mould by compacting different alkali activated MT mixtures at their respective MDU and OMC. After compaction, the specimens are retrieved out from the mould using a hydraulic extruder. Following that, prepared specimens are kept for curing under two distinct curing conditions before being UCS tested namely, a) ambient curing (AC), in which samples are kept under prevailing environmental conditions with temperature = 25 ± 7 ˚C and relative humidity = 80 ± 10%, and b) dry curing (DC), where specimens are kept in an oven at 50 ˚C throughout the curing period. These curing conditions replicate the diverse environmental circumstances encountered in most of the Indian subcontinent. AC conditions

mimic the current on-site conditions, while DC conditions replicate the highest temperatures observed in India. To investigate the effect of curing period on the strength development of geopolymer specimens, UCS tests are done after 3, 7, 14, and 28 days of curing. For each condition, at least three specimens are prepared and the average of the three values is reported as UCS of the specimen. Results of the UCS test are discussed in "Results and discussion section" later.

4.5.2 FESEM and EDS analysis

Microstructure of UCS tested geopolymer specimens are studied through a high performance FESEM (manufacturer-Zeiss, model-Gemini) instrument whereas elemental changes occurring during the geopolymerization reaction are traced through X-ray energy dispersive spectroscopy (EDS) analysis using FESEM coupled with an OXFORD spectroscopy device (manufacturer-Zeiss, model-Gemini). The samples for both FESEM and EDS testing are extracted from the geopolymer specimens that have already undergone UCS testing. These samples are oven-dried overnight at 60 ˚C to remove any moisture before being gold coated for image scanning.

4.5.3 DST tests

The stability of a TP is significantly influenced by the shear strength properties of material used in the construction of its embankments. In general, triaxial loading is considered as better laboratory tests for determining the shear characteristics of soil. However, in the present work, DST is utilized to determine the shear strength of geopolymer specimens since the stress conditions acting along the parts of failure surfaces of TP embankments are better replicated by direct shear test loading condition (Karim et al., 2023). Given that a major portions of TP embankments remain saturated throughout their design life, DST are performed under consolidated drained condition in accordance with ASTM D3080 (2011) standards. To carry out the test, specimens with dimensions 60 mm × 60 mm × 35 mm are compacted in a direct

shear box at MDU and OMC corresponding to each MT (as determined by mini compaction tests). After compaction, the specimens are extracted from the shear box with the help of hydraulic extruder and cured under AC for a period of 14 days. The 14-days curing period is selected based on the embankment-raising rate followed by the mining industries while constructing the TP (Singh et al., 2023). Following that, the cured specimens are saturated by immersing in water for at least 48 h. DST are performed on saturated specimens at shearing rate of 0.25 mm/minute under three vertical stresses of 50 kPa, 100 kPa and 150 kPa. The shear strength of stabilized ZT is calculated in terms of interparticle cohesion and friction angle utilizing Mohr-Coulomb failure criterion as given by equation 4.1.

$$\tau = c + \sigma \, tan\phi \tag{4.1}$$

where, τ = Shear strength (kPa), c = unit cohesion (kPa), σ = Normal stress (kPa), ϕ = Internal friction angle.

4.5.4 Durability tests

Since, the aim of the current study is to utilize different MT as TP embankment material, durability in such conditions is critical as these embankments are prone to weathering and abrasion caused by wind and water. The stabilized MT must be able to sustain these adverse environmental conditions at the site with respect to its strength and integrity. To replicate these adverse environmental conditions, durability tests are performed by exposing the specimens (with similar dimensions as used in UCS tests) to 12 cycles of alternate wetting and drying as specified by ASTM D559 (2015). Each cycle begins with immersing the specimens in water for 5 h followed by 42 h of oven drying at 60 ˚C (Turan et al., 2022). Following that, the specimens are brushed 18-20 times on the sides and 4-5 times on the ends. Finally, the loss of mass is reported in percentage as the ratio of total loss of weight (A) after 12 cycles of wetting and drying to the original oven-dried weight (B) of specimens as;

$$\text{Loss of mass, \%} = \frac{A}{B} \times 100 \quad (4.2)$$

where, A = Difference between the original oven-dried weight and the final oven-dried weight after 12 wetting and drying cycles. Further, B = Original oven-dried weight of specimens.

4.5.5 Permeability tests

The hydraulic conductivity of the material employed in embankment construction plays a vital role in determining the seepage path within a TP facility. Excessively high hydraulic conductivity can result in the ultimate failure of the TP, as it may lead to erosion of the downstream slope through excessive seepage. Hence, it is crucial to assess the permeability of stabilized MT material, ensuring its suitability as a material for TP embankments. The hydraulic conductivity of various geopolymer specimens is assessed using a fixed wall permeameter in accordance with ASTM D5856 (2015). A cylindrical mould with dimensions 25 mm × 25 mm is employed for the permeability tests ensuring that these dimensions significantly surpass the minimum requirement (i.e. 6 times the size of the largest particle of ZT) as recommended by ASTM D5856 (2015). The specimens for the permeability tests are prepared by compacting various MT mixtures within the mould in three layers at their respective MDU and OMC. The prepared specimens are then kept for curing under AC conditions for 14 days. Following this, the entire mould is submerged in water for a minimum of 24 h to achieve saturation and falling head permeability tests are performed until a stable flow is obtained. Before conducting the experiments, silica gel is applied at the interface between the permeameter and geopolymer specimens to prevent sidewall leakage. Three tests are conducted for each specimen, and the average of these three values is documented as the final hydraulic conductivity of the geopolymer specimen. Different sets of laboratory experiments performed in the current study are summarized in Fig. 4.5.

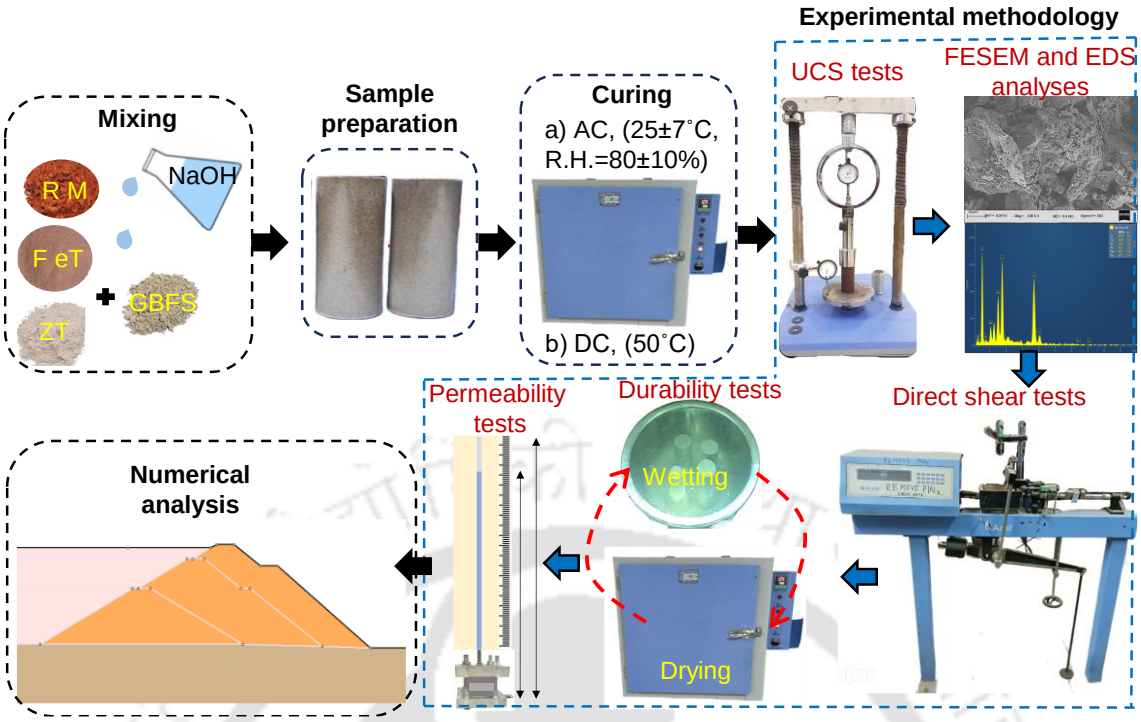

Fig. 4. 5 Experimental framework followed in the current study

4.6 Results and discussion

4.6.1 UCS results

Table 4.4 summarises the UCS values obtained for various MT specimens. It can be observed from Table 4.4 that irrespective of NaOH concentrations used for the activation, all alkali activated MT exhibit much higher compressive strength than their untreated counterparts. In addition, the strength development of stabilized MT is significantly affected by the MT type, curing conditions, curing period and alkali activator concentrations. The impact of each parameter on the UCS of different MT specimens is discussed in the subsequent subsections.

Table 4. 4 Summary of UCS tests for different MT specimens

MT type	NaOH concentration	UCS (MPa)							
		AC				DC			
		Curing period (days)				Curing period (days)			
		3	7	14	28	3	7	14	28
RM	Untreated	0.83	1.12	1.39	1.49	0.97	1.35	1.59	1.71
	2.5M	2.10	3.40	3.60	3.70	3.99	4.79	5.45	5.10
	5M	3.44	5.10	5.20	5.79	5.96	7.83	9.11	8.20
	7.5M	4.20	5.80	7.33	7.92	7.33	14.02	12.53	12.58
	10M	4.52	5.84	7.58	10.55	22.33	29.34	28.32	27.98
	PPC (10%)	3.84	4.49	6.13	6.75	-	-	-	-
FeT	Untreated	0.64	0.76	0.89	1.15	1.01	1.23	1.40	1.50
	2.5M	1.02	2.09	2.37	2.65	3.34	5.66	4.12	4.49
	5M	0.95	1.89	2.21	2.35	3.94	6.68	4.49	5.06
	7.5M	0.75	1.66	1.77	2.07	4.04	9.67	9.60	11.16
	10M	0.58	1.55	1.64	2.09	5.31	10.57	11.40	13.13
	GBFS (10%)-2.5M	3.99	4.25	5.17	6.22	-	-	-	-
	GBFS (20%)-2.5M	6.52	7.62	8.52	9.55	-	-	-	-
	PPC (10%)	3.39	3.56	3.84	4.12	-	-	-	-
ZT	Untreated	0.07	0.07	0.07	0.07	0.05	0.05	0.05	0.05
	2.5M	0.11	0.14	0.26	0.32	1.05	1.23	1.14	1.13
	5M	0.47	0.59	0.74	0.84	3.65	3.30	3.45	3.43
	7.5M	0.88	0.97	1.97	2.25	7.73	8.43	7.70	7.45
	10M	1.54	1.94	3.89	4.24	12.29	12.35	11.16	11.77
	GBFS (10%)-2.5M	2.75	3.36	4.07	4.42	-	-	-	-
	GBFS (20%)-2.5M	6.17	7.75	7.93	8.34	-	-	-	-
	PPC (10%)	1.79	1.85	2.09	2.17	-	-	-	-

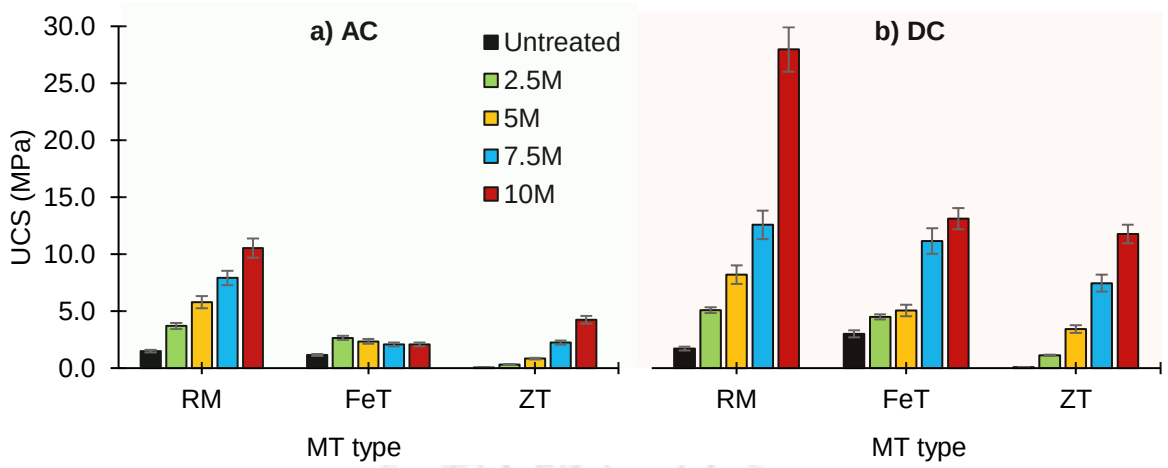

Fig. 4. 6 UCS of various MT specimens at 28 days of curing under a) AC conditions, and b) DC conditions

a) Effect of MT type

Irrespective of curing conditions and NaOH concentrations, the compressive strength of untreated MT is significantly enhanced by using alkali activation. For instance, the 28-day UCS of untreated RM, FeT, and ZT is substantially increased from 1.49 MPa, 1.15 MPa, and 0.07 MPa to 10.55 MPa, 2.65 MPa, and 4.24 MPa respectively, when activated with NaOH solution under AC curing conditions. This implies that RM displays the highest strength improvement among all MT during the geopolymerization process (refer to Fig. 4.6a-b). The higher strength development in RM specimens is due to the optimal ratio of SiO_2 and Al_2O_3 required for geopolymerization. It is widely acknowledged that the strength development in geopolymer specimens is negatively affected by both high SiO_2 /Al_2O_3 ratios (>4) and low SiO_2 /Al_2O_3 ratios (<0.5) (De Silva et al., 2007). As indicated by XRF results, the SiO_2 /Al_2O_3 ratio in RM is determined as 1.51 compared to 1.16 and 6.56 for FeT and ZT, respectively. Given that the SiO_2 /Al_2O_3 ratio is higher in RM than FeT, the specimens prepared from alkali activated RM exhibit a far superior strength improvement compared to those prepared with alkali activated FeT. On the other hand, ZT has a considerably high SiO_2 /Al_2O_3 ratio, which is undesirable for geopolymerization reactions (De Silva et al., 2007) indicating its lower effectiveness as a geopolymer binder compared to RM. Furthermore, the higher specific surface area of RM

(23.50 m^2/g) compared to FeT (12.85 m^2/g) and ZT (3.05 m^2/g) promotes the release of Si and Al during the dissolution phase owing to the greater interaction of SiO_2 and Al_2O_3 with NaOH solution (Dietel et al., 2017).This in turn results in the formation of a greater number of geopolymer gels contributing to higher UCS values in RM specimens.

Impact of GBFS on UCS of FeT and ZT: As evident from Figs. 4.6 (a-b), FeT and ZT specimens display significantly lower strength improvement compared to RM particularly at lower NaOH concentrations (i.e. molarity ≤ 5M) which may not be sufficient for their use as TP embankment material. Therefore, to further increase the compressive strength of FeT and ZT at lower NaOH concentrations, GBFS is used as a precursor to enhance the geopolymerization reaction. Fig. 4.7 displays the 28-day UCS of GBFS amended FeT and ZT specimens cured under AC conditions. It can be clearly seen from Fig. 4.7 that the compressive strength of both FeT and ZT is significantly enhanced by incorporating GBFS. For instance, the 28-day UCS of FeT activated with 2.5M NaOH rises from 2.65 MPa to 6.22 MPa and 9.55 MPa with the incorporation of 10% and 20% GBFS respectively. Similarly, the 28-day UCS of alkali-activated ZT improves from 0.32 MPa to 4.42 MPa and further to 8.34 MPa with the addition of 10% and 20% GBFS respectively. In addition to sufficient SiO_2 and Al_2O_3 fraction, GBFS also contains a high CaO content (i.e. 35.56 %) which influences the dissolution of aluminosilicates during geopolymerization. Ca^{+2} in GBFS raises the pH of the geopolymer matrix which promotes the dissolution of aluminosilicates during geopolymerization process (Canfield et al., 2014; Zhao et al., 2019). This results in the development of more geopolymer gels which contribute to the increased compressive strength of geopolymer specimens. Moreover, the high CaO content in GBFS enables the formation of C-S-H and C-A-S-H gel structures along with N-A-S-H gel structures (refer to equation 4.3 to 4.7) which provide additional strength to the geopolymer specimens (Chindaprasirt et al., 2012; Ghadir and Ranjbar, 2018).

$$CaSO_4, CaO \xrightarrow{H_2O} Ca^{+2} + SO_4^{-2} + OH^- \quad (4.3)$$

$$SiO_2 + Al_2O_3 \xrightarrow{OH^-} SiO_2(OH)_2^{-2} \text{ or } SiO(OH)_3^- + Al(OH)_4^- \quad (4.4)$$

$$Na^+ + SiO_2(OH)_2^{-2} \text{ or } SiO(OH)_3^- + Al(OH)_4^- \rightarrow NASH_{gel} \quad (4.5)$$

$$Ca^{+2} + SiO_2(OH)_2^{-2} \text{ or } SiO(OH)_3^- + Al(OH)_4^- \rightarrow CASH_{gel} \quad (4.6)$$

$$Ca^{+2} + SiO_2(OH)_2^{-2} \text{ or } SiO(OH)_3^- \rightarrow CSH_{gel} \quad (4.7)$$

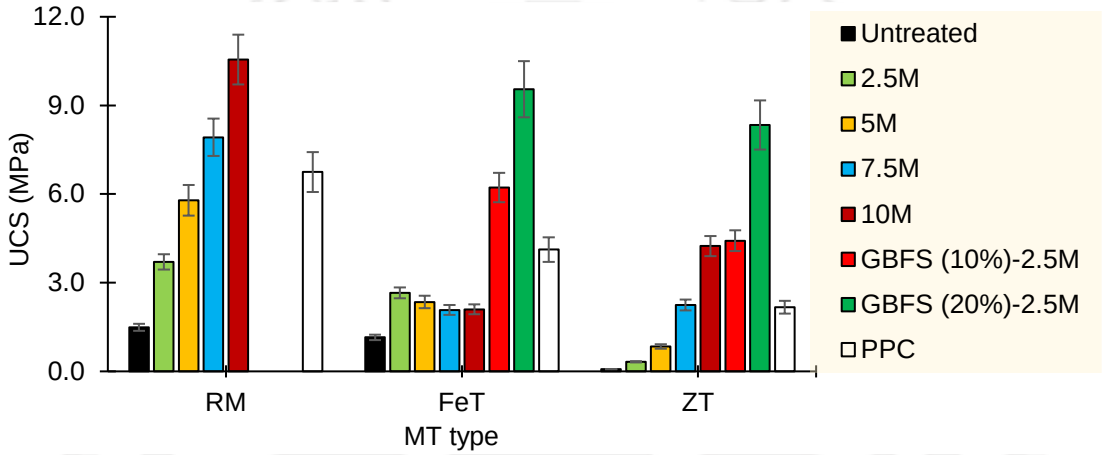

Fig. 4. 7 Comparison of 28-day UCS of different alkali activated MT specimens with PPC stabilized MT specimens

Fig. 4.7 also presents the 28-day UCS of MT stabilized with PPC. It is evident from the Fig. 4.7 that most of the alkali activated RM specimens show a UCS like that of PPC-stabilized RM. In contrast, alkali activated FeT and ZT specimens display considerably lower UCS compared to their PPC stabilized counterparts. However, the introduction of GBFS to FeT and ZT results in significantly higher UCS compared to PPC stabilized specimens. This suggests that alkali activation proves to be a more effective stabilization method for enhancing the UCS of MT when compared to cement stabilization.

b) Effect of curing conditions

The strength development in different alkali activated MT specimens is significantly influenced by the curing conditions employed. Specimens cured under DC conditions exhibit

significantly higher UCS values compared to those cured under AC conditions (refer to Figs. 4.6a-b). For instance, the 28-day UCS of RM specimen (activated with 10M NaOH) is found to be 27.98 MPa under DC conditions compared to 10.55 MPa under AC conditions. Likewise, the 28-day UCS of alkali activated FeT and ZT specimens (prepared with 10M NaOH solution) increases from 2.09 MPa and 4.24 MPa respectively under AC conditions to 13.13 MPa and 11.77 MPa under DC conditions. This indicates that the compressive strength of geopolymer specimens increases with increase in the curing temperature. Under DC conditions (i.e., at 50 ˚C), the movement of Na^+ and OH^- ions become more active resulting in the formation of highly dense Na^+ based aluminosilicates crystals (Sajan et al., 2021). Moreover, at higher curing temperatures, the polymerization reaction is more potent to convert 2D -Si-O-Al- chains into 3D -Si-O-Al- chains with stronger bonds (Sajan et al., 2021) which contributes to the higher compressive strength of geopolymer specimens.

Another possible reason for the higher compressive strength of various MT specimens under DC conditions compared to AC conditions can be attributed to the role of water in the geopolymerization process. In general, the geopolymer matrix comprises of two types of water i.e., structural water and residual water (Zuhua et al., 2009; Nath et al., 2016; Ghadir and Ranjbar, 2018; Park and Pour-Ghaz, 2018). Structural water, which takes an active participation in the geopolymerization process, provides a medium for the dissolution and hydrolysis of aluminosilicates and offers ion transfer (Ghadir and Ranjbar, 2018). In contrast, residual water is unfavourable for the geopolymerization as it retards the rate of dissolution and hydrolysis (Zuhua et al., 2009; Nath et al., 2016; Park and Pour-Ghaz, 2018). Because residual water cannot evaporate at low temperatures, its presence reduces the alkalinity of geopolymer matrix due to the dilution effects. This in turn decreases the rate of geopolymerization reaction during the dissolution and hydrolysis stages (Zuhua et al., 2009; Nath et al., 2016; Ghadir and Ranjbar, 2018; Park and Pour-Ghaz, 2018). Since the residual water is highest under AC conditions, a

fewer geopolymer gels are formed within the geopolymer matrix during the geopolymerization reaction (refer to Fig. 4.8a).

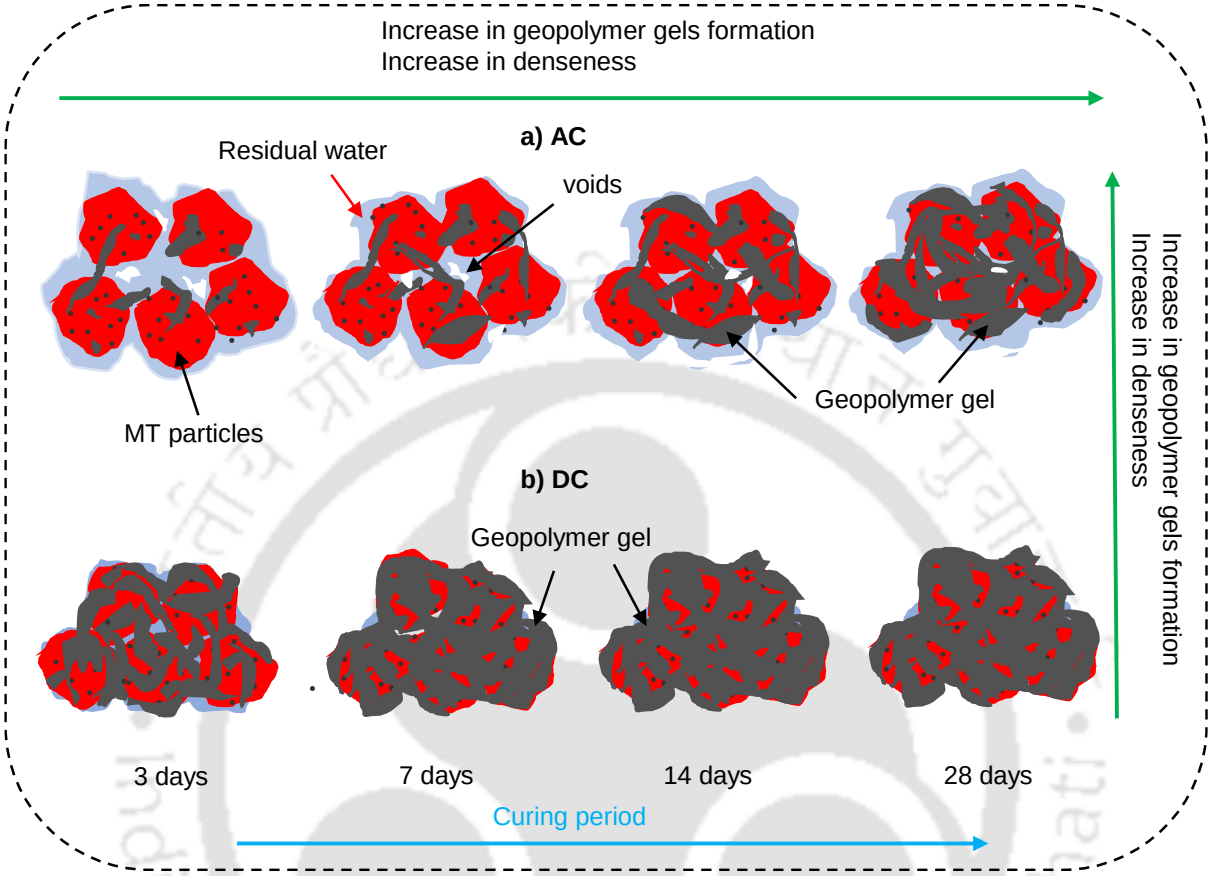

Fig. 4. 8 Illustration of geopolymer gel formation at different stages of curing under a) AC conditions and b) DC conditions

The limited formation of geopolymer gels under AC conditions hinders the development of a strong and compact structure, resulting in their lower UCS. On the contrary, under DC conditions, the amount of residual water decreases because of evaporation which in turn promotes the formation of a greater number of geopolymer gels (refer to Fig. 4.8b) owing to the increased alkalinity of RM specimens (Ghadir and Ranjbar, 2018). These geopolymer gels bind the MT particles together resulting in the formation of highly dense and compact structure which in turn increases the compressive strength of geopolymer specimens under DC specimens.

c) Effect of curing period

In addition to curing conditions, strength development in geopolymer specimens is also influenced by the curing period. Figs. 4.9 (a-b) display the UCS of various geopolymer specimens at different stages of curing under both AC and DC conditions. It can be noted from Fig. 4.9a that irrespective of the MT type and NaOH concentration, UCS of AC cured MT specimens increases gradually with increase in the curing time. Under AC conditions, the geopolymerization reaction proceeds at a slower pace owing to the existence of substantial residual water which hinders the dissolution and hydrolysis of aluminosilicates (Leung and Pheeraphan, 1995; Ghadir and Ranjbar, 2018). As a result, lesser quantities of geopolymer gels are formed under AC conditions during the initial stages of curing (refer to Fig. 4.8a). However, as the curing period increases, this residual water evaporates which accelerates the dissolution of SiO_2 and Al_2O_3 units facilitating the formation more geopolymer gels (see Fig. 4.8a). On the other hand, specimens cured under DC conditions show high early strength owing to the greater formation of geopolymer gels at elevated temperature i.e. at 50 ˚C (see Fig. 4.8b). The compressive strength of majority of MT specimens however ceases to increase after 7 days of curing displaying constant UCS values at 14 and 28 days as shown in Fig. 4.9b. This is because the majority of Na^+ and OH^- ions are consumed within 7 days of curing preventing the further geopolymerization even after a prolonged curing period. Additionally, the UCS of a few geopolymer specimens is observed to decrease slightly under DC conditions (refer to Fig. 4.9b) when subjected to a prolonged curing period of 28 days. This is due to the reason that high temperature curing induces microcracks within the geopolymer specimens due to excessive shrinkage and dehydration thereby reducing their compressive strength (Zuhua et al., 2009).

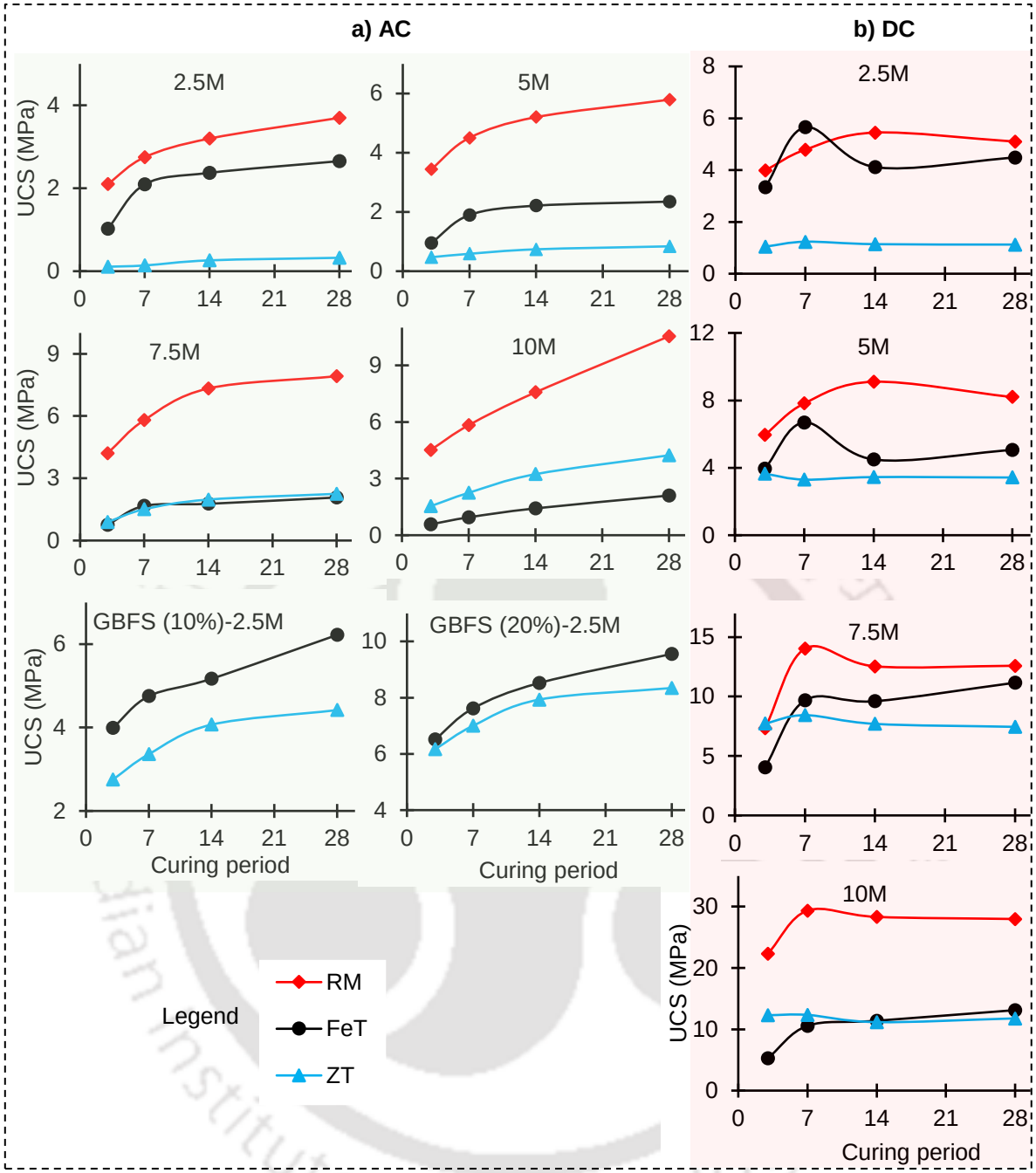

Fig. 4. 9 Variation of UCS with curing time for various MT specimens a) AC conditions, and b) DC conditions

d) Effect of alkali activator concentration

Mechanical performance of geopolymerized RM is also influenced by the concentration of NaOH solutions used for activation, as shown in Figs. 4.6 (a-b). It can be noted from Figs. 4.6 (a-b) that irrespective of curing conditions, the compressive strength of alkali activated RM and ZT specimens increases with increase in the concentration of alkali activator. For instance, the UCS of geopolymerized RM specimen is found to be highest for 10M NaOH whereas the

strength improvement is observed to be minimal with 2.5M NaOH solution. The reason for this can be attributed to the role of alkali concentration on the rate of dissolution/ leaching of Al^{+3} and Si^{+4} ions present in the aluminosilicate rich raw materials (Rattanasak and Chindaprasirt, 2009; Cristelo et al., 2013). The rate of dissolution of Al^{+3} and Si^{+4} ions increase with increase in the concentration of NaOH solution, resulting in early formation of $Si(OH)_4$, $Al(OH)_3$ and other aluminosilicate gels, which contributes to high compressive strength. In addition, the alkalinity of MT matrix increases with increasing NaOH concentrations, which facilitates the development of amorphous phase due to increased rate of geopolymerization (Rattanasak and Chindaprasirt, 2009; Cristelo et al., 2013).

Another explanation for the increased effectiveness of geopolymerization at higher NaOH concentrations can be related to the presence of residual water within the geopolymer matrix. At low NaOH concentrations, the geopolymer matrix contains a greater quantity of residual water, which inhibits the dissolution of aluminosilicates present in RM (Zuhua et al., 2009; Park and Pour-Ghaz, 2018). On the other hand, the presence of less residual water at higher concentrations of NaOH solution promotes the dissolution of alumina and silica due to increased alkalinity resulting in the formation of more reaction products (Zuhua et al., 2009; Park and Pour-Ghaz, 2018).

4.6.2 FESEM and EDS analysis

a) FESEM analysis

Structural changes occurring within the RM matrix during the geopolymerization process at micro level is examined using FESEM analysis. Figs. 4.10 (a-o) illustrates the FESEM images obtained for untreated, and alkali activated MT specimens after 28 days of curing period. Irrespective of activator concentrations, alkali activated MT specimens display more compact and denser matrix compared to untreated MT. As evident from Figs. 4.10 (a-c), untreated RM,

FeT and ZT display a relatively loose structure with open air void spaces within the MT matrix. On the other hand, a much denser and compact structure can be observed in various MT specimens activated with different concentrations of NaOH (refer to Figs. 15d-o). The reason for this can be attributed to the formation of new 3D structure of aluminosilicates during alkali activation process, which induces compactness to the geopolymer matrix.

Furthermore, with increase in the concentration of NaOH solutions geopolymer matrix become more compact and stronger (except for FeT specimens) (refer to Figs. 4.10d-o). This is due to the formation of more geopolymer gel (N-A-S-H) structures at higher concentrations of NaOH compared to lower NaOH concentrations. At high concentrations, a greater number of RM and ZT particles reacts with NaOH resulting in a higher dissolution of Al and Si. It can be clearly seen from Figs. 15 (d, f, g, i) that a lesser number of reaction products are formed within the geopolymer matrix at lower concentrations of NaOH (i.e. at 2.5M and 5M). As a result, these reaction products fail to provide sufficient strength and compactness to the geopolymer specimens. On the other hand, a greater number of N-A-S-H gel structures are formed at higher NaOH concentrations (i.e. 7.5M, 10M) as shown in Figs. 4.10 (j, l, m, o). These gel structures aids in developing a much compact and strong geopolymer matrix by filling the air voids which contribute to the higher compressive strength of RM and ZT specimens.

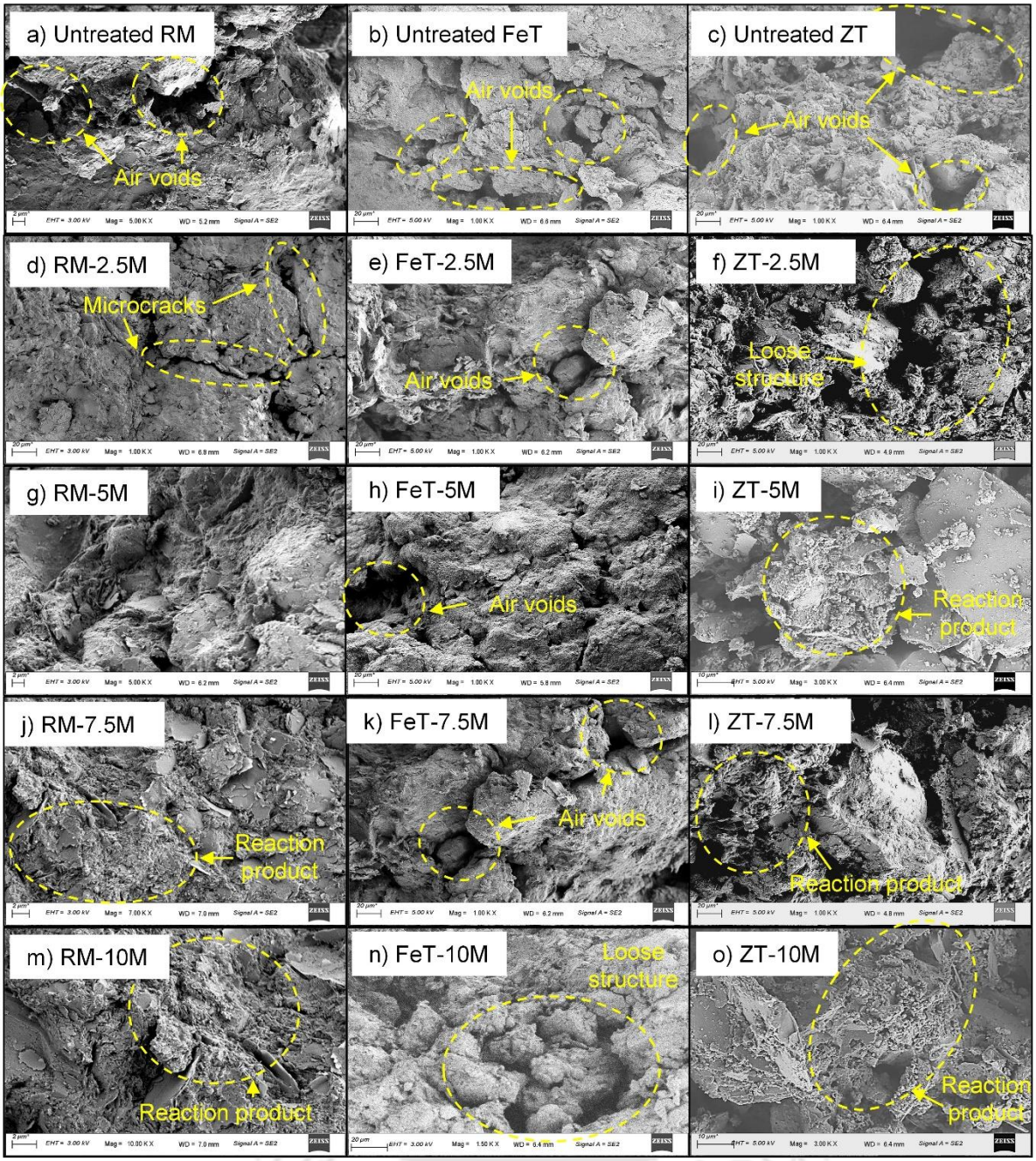

Fig. 4. 10 Microscopic images of different MT specimens a) untreated RM, b) untreated FeT, c) untreated ZT d) RM-2.5M, e) FeT-2.5M, f) ZT-2.5M, g) RM-5M, h) FeT-5M, i) ZT-5M, j) RM-7.5M, k) FeT-7.5M, l) ZT-7.5M, m) RM-10M, n) FeT-10M, and o) ZT-10M

Figs. 4.11 (a-d) show the FESEM images of FeT and ZT specimens stabilized with GBFS and 2.5M NaOH solution. It can be seen from Figs. 4.11 (a-d) that due to the presence of high CaO content in GBFS, both N-A-S-H and C-S-H gel structures are formed during the geopolymerization reaction which provides high compressive strength to the geopolymer specimens. Furthermore, a greater number of geopolymer gel is developed within the FeT and

ZT specimens prepared with 20 % GBFS in comparison to those prepared with 10 % GBFS. The formation of higher reaction products in specimens made with 20% GBFS contributes to their superior compressive strength over geopolymer specimens prepared with 10% GBFS (as evident from UCS values discussed in section 4.6.1).

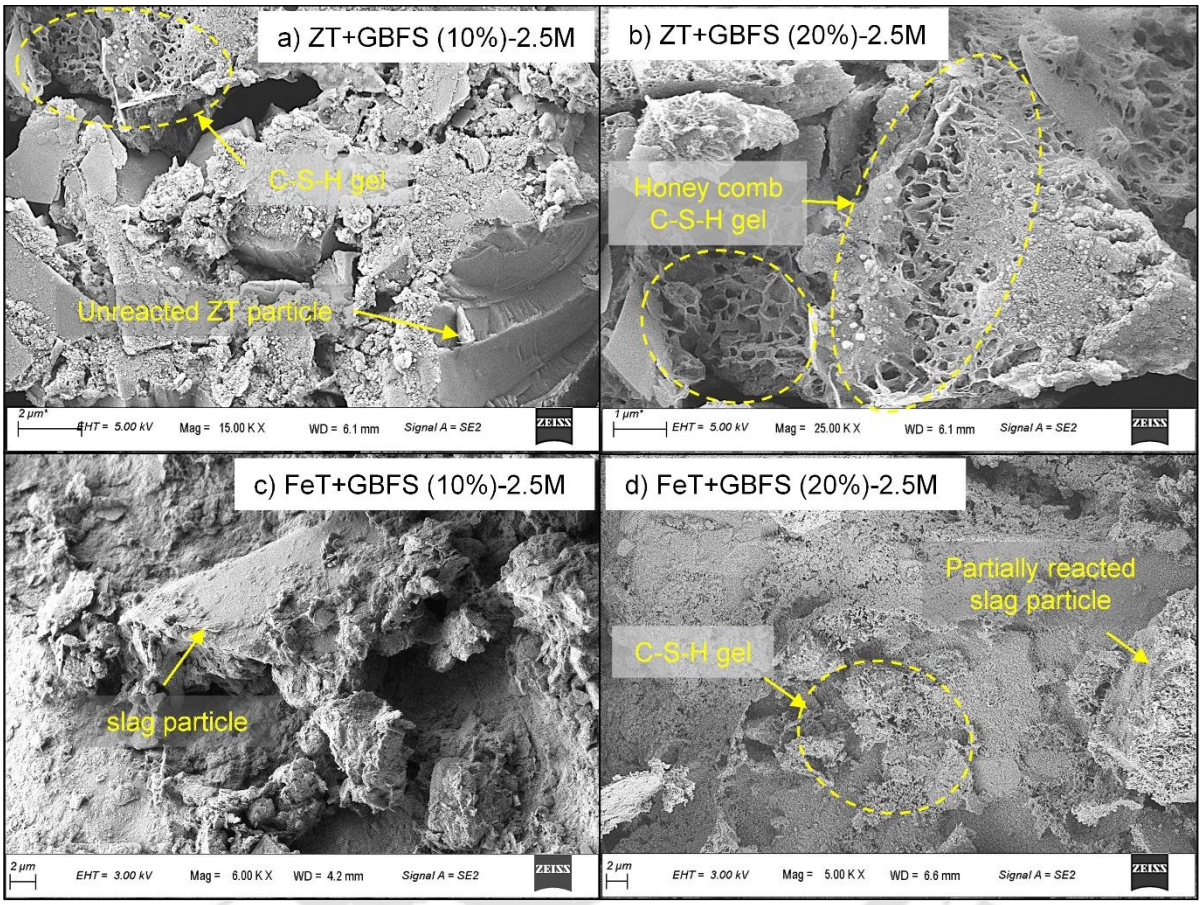

Fig. 4. 11 FESEM images of GBFS amended MT a) ZT+GBFS (10%)-2.5M, b) ZT+GBFS (20%)-2.5M, c) FeT+GBFS (10%)-2.5M, and d) FeT+GBFS (20%)-2.5M

b) EDS analysis

The overall effectiveness of geopolymerization is governed by the dissolution of aluminosilicates occurring during the activation phase. The dissolution of aluminosilicates during geopolymerization is better understood in terms of Si/Al, Na/Al and Ca/Si ratios which are determined from the results of EDS analysis. In general, the mechanical strength of geopolymer specimens increases with increasing Si/Al ratios indicating a higher dissolution of aluminosilicates during the activation phase (He et al., 2016; Silva et al., 2007). At higher Si/Al

ratios, -Si-O-Si- polymeric chains are predominately formed whereas -Si-O-Al- chains are more prevalent at lower Si/Al ratios. Since -Si-O-Si- bonds are stronger than -Si-O-Al- bonds, geopolymer specimens with higher Si/Al ratios are expected to exhibit greater compressive strength (He et al., 2016). Figs. 4.12 (a-l) present the results of EDS analysis performed on various geopolymer specimens in terms of the weight percentage of various elements (i.e. Si, Al, Na etc.). It can be noted from Figs. 4.12 (a-l) that Si/Al ratio increases with an increase in the concentrations of NaOH solution (except for FeT specimens) indicating a higher aluminosilicate dissolution. For instance, the Si/Al ratio in the ZT specimen activated with 2.5M NaOH is noted as 2.97 which increases to 3.12, 3.51 and 5.77 when 5M, 7.5M and 10M NaOH solutions are used for activation, respectively. This implies that more alumina and silica units are liberated at higher molarity of NaOH solutions contributing to the higher compressive strength of geopolymer specimens (as evident from the results of UCS tests discussed in section 4.6.1). It should be noted that the Si/Al ratio for FeT specimens is highest at 2.5M concentration which is quite understood as NaOH concentration beyond 2.5M fails to dissolve Si and Al units. As a result, highest strength is achieved by FeT specimens with 2.5M NaOH solution which is also evident from the UCS values.

Like Si/Al, increasing Na/Al indicates higher aluminosilicates dissolution owing to the increased alkalinity of the ZT matrix induced by additional Na^+ ions (He et al., 2016). For example, the Na/Al ratio in RM and ZT increases from 0.17 to 0.40 and 0.15 to 2.80 respectively when the concentration of NaOH solution is raised from 2.5M to 10M. Higher Na/Al ratios observed at higher NaOH concentrations can be attributed to the increased availability Na^+ and OH^- ions which raise the alkalinity of geopolymer matrix. This in turn enhances the liberation of aluminosilicates during the activation phase contributing to the increased compressive strength of geopolymer specimens.

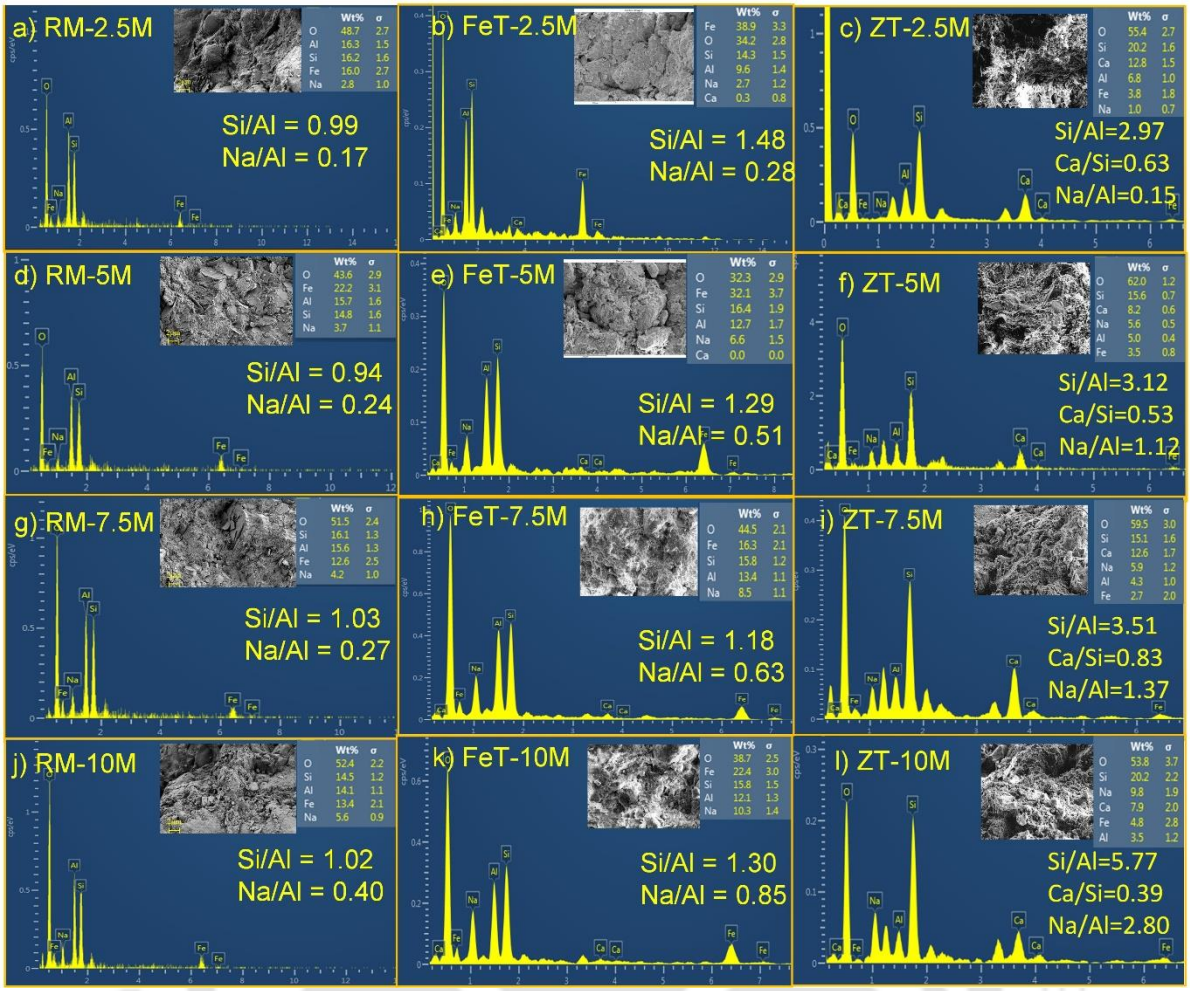

Fig. 4. 12 Results of EDS analysis for various MT specimens a) RM-2.5M, b) FeT-2.5M, c) ZT-2.5M, d) RM-5M, e) FeT-5M, f) ZT-5M, g) RM-7.5M, h) FeT-7.5M, i) ZT-7.5M, j) RM-10M, k) FeT-10M, and l) ZT-10M

Figs. 4.13 (a-d) illustrates the results of EDS analysis obtained for GBFS amended FeT and ZT specimens. It can be noted from Figs. 4.13 (a-d) that GBFS amended FeT and ZT specimens exhibit lower Si/Al and Na/Al ratios compared to those without GBFS incorporation. Although, the strength of geopolymer specimens is expected to decrease with decreasing Si/Al and Na/Al ratios, the compressive strength of GBFS amended MT specimens however increases even at reduced Si/Al and Na/Al ratios. The reason for this can be attributed to the higher impact of Ca/Si ratio on the strength development of geopolymer specimens than Si/Al and Na/Al ratios. Previous research has shown that an increase in the Ca/Si ratio increases the compressive strength of a geopolymer specimens (Yaghoubi et al., 2018). Similarly, in the current investigation geopolymer specimens with greater Ca/Si ratios are found to exhibit

higher compressive strength. For instance, Ca/Si ratios for ZT specimens amended with 10% and 20% GBFS are found to be 1.11 and 1.75, respectively which are substantially higher than the Ca/Si ratios obtained for all ZT specimens (refer to Figs. 4.12c, f, i, l). The higher Ca/Si ratio in ZT-GBFS specimens is attributable to the high CaO content of GBFS which introduces additional Ca^{+2} ions into the geopolymer matrix. As stated previously, the presence of Ca^{+2} ions increase the alkalinity of the geopolymer matrix (Zhao et al., 2019) which accelerates the dissolution of aluminosilicates resulting in the formation of more C/N-A-S-H gel structures. As a result, GBFS amended FeT and ZT specimens show higher compressive strength than other MT specimens (prepared with different NaOH concentrations) which is evident from the UCS values shown in Table 4.4.

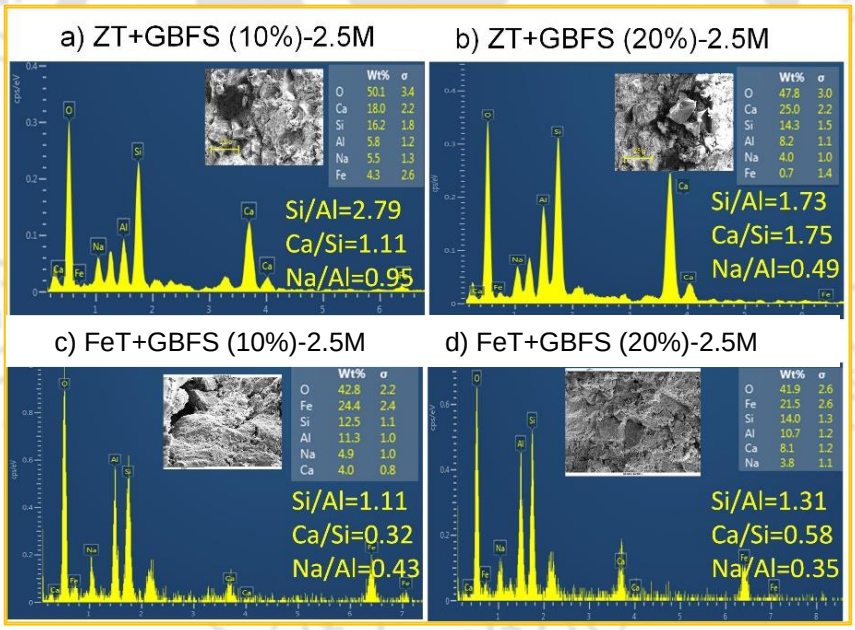

Fig. 4. 13 Results of EDS analysis for GBFS amended MT specimens a) ZT+GBFS (10%)-2.5M, b) ZT+GBFS (20%)-2.5M, c) FeT+GBFS (10%)-2.5M, and d) FeT+GBFS (20%)-2.5M

4.6.3 DST results

Figs. 4.14 (a-c) displays the results of DST for various MT specimens expressed in terms of shear stress vs shear displacement curves.

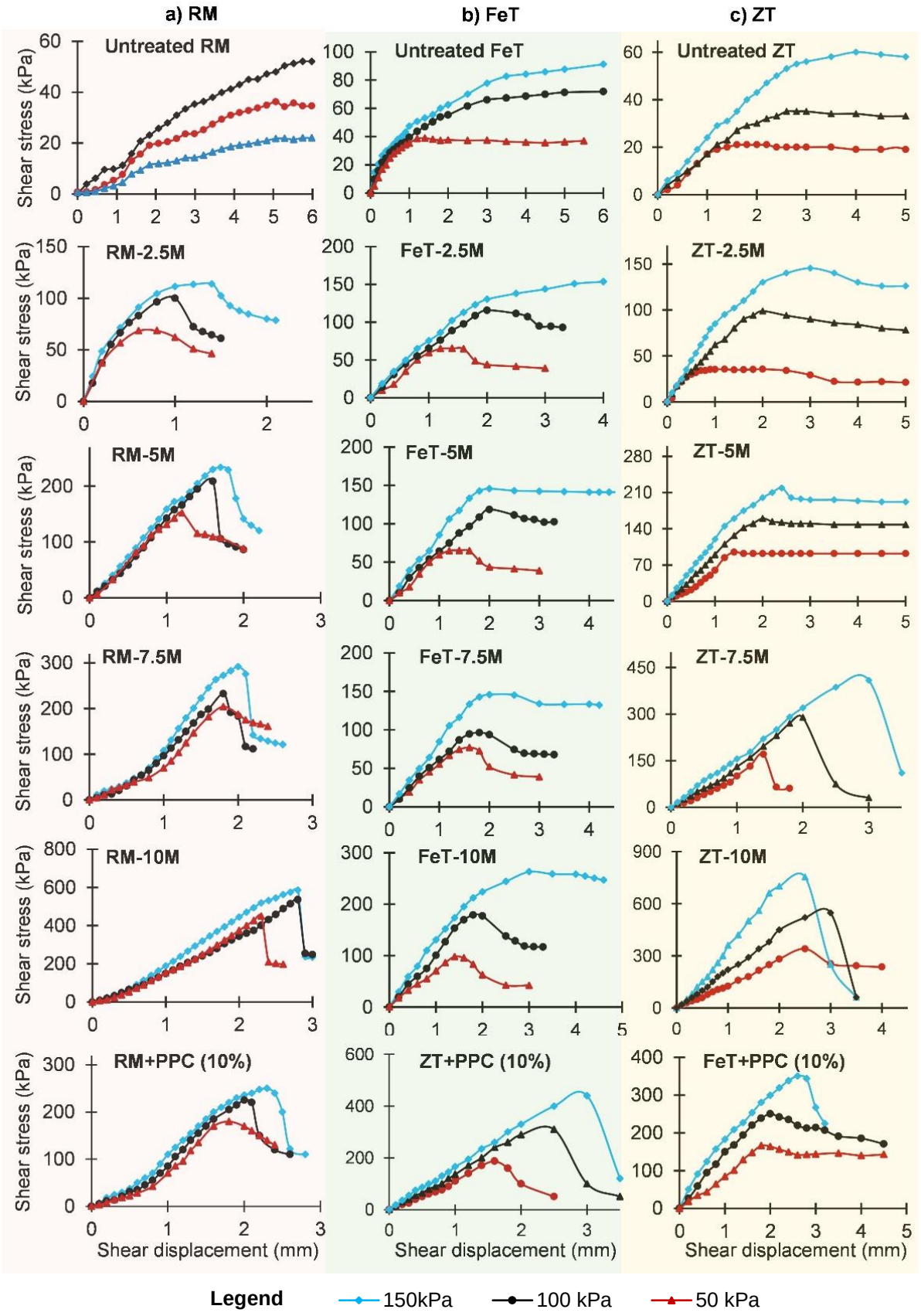

Fig. 4. 14 Shear stress vs shear displacement plots for various MT specimens under different confining pressure a) RM specimens, b) FeT specimens, and c) ZT specimens

Observations from Figs 4.14 (a-c) reveal that the shear stress vs shear displacement curves for untreated MT (i.e RM, FeT, and ZT) resemble those of typical contractive materials with no distinct peak on the stress-displacement curve. However, the nature of the stress-displacement curve undergoes significant changes when MT are activated with NaOH. As the concentration of NaOH increases, the shear behaviour of the geopolymer specimens shifts from loose to dense material showcasing a clear-cut peak on the shear stress vs shear displacement curve (refer to Figs 4.14a-c). Similarly, FeT and ZT specimens amended with GBFS experience a brittle failure displaying a distinct peak on the stress-displacement curve (refer to Figs 4.15a-b) indicating a compact and dense structure.

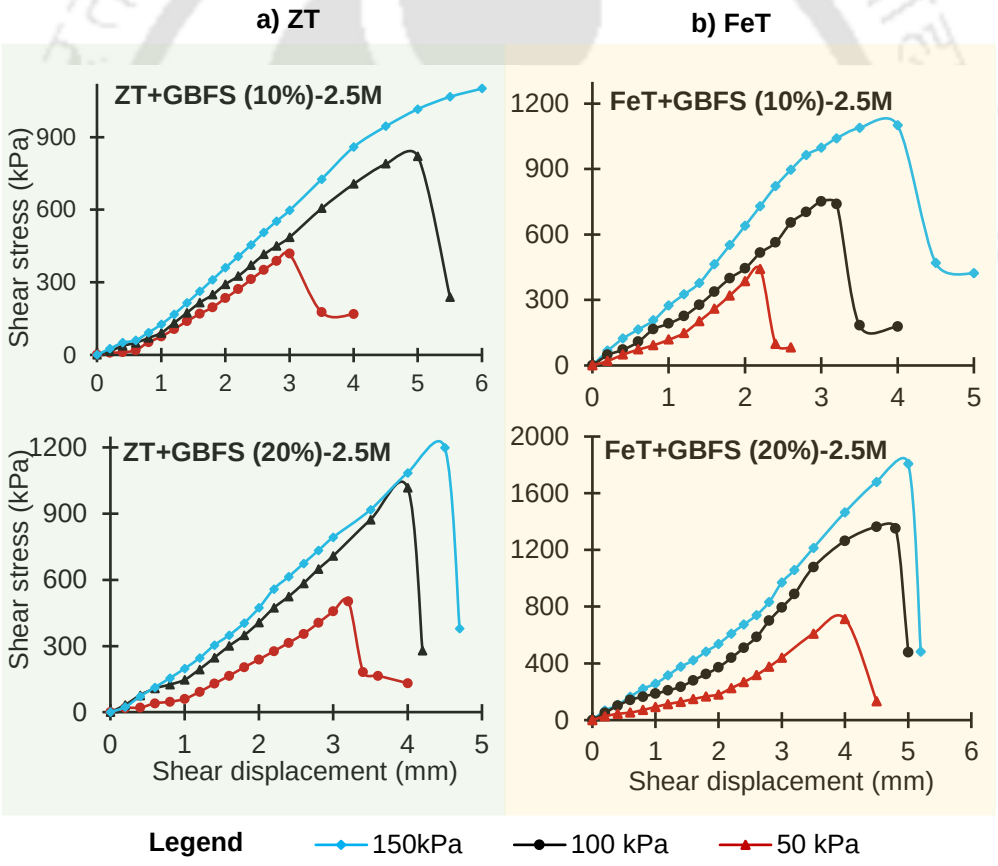

Fig. 4. 15 Shear stress vs shear displacement plots for GBFS amended MT specimens a) FeT specimens, and b) ZT specimens

To better comprehend the shear behaviour of geopolymer specimens, shear strength parameters i.e. c and ϕ of MT specimens are determined using the Mohr-Coulomb failure

criterion. Its noteworthy that *c* in a geomaterial is ascribed to the combination of matric suction, electrostatic attractions, cementation and adhesion due to compaction (Al-Shayea, 2001). Since DST are conducted under saturated conditions, the contribution of matric suction to the overall *c* will be zero. The ϕ, on the other hand, is a function of particle interlocking and normal stress acting on the failure shear plane (Al-Shayea, 2001; Ghadir et al., 2021).

a) Impact on interparticle cohesion, (*c*)

Fig. 4.16 presents the *c* values for various untreated and alkali-activated MT specimens obtained from DST. As depicted in Fig. 4.16, the interparticle *c* of all untreated MT (i.e. RM, FeT, and ZT) shows a substantial increase when activated with NaOH. Among all MT, RM demonstrates the most significant improvement in *c* through alkali activation followed by ZT and FeT. This trend can be attributed to the higher efficiency of geopolymerization in RM compared to FeT and ZT which results in the formation of a greater number of geopolymer gels. These geopolymer gels effectively bind the RM particles together increasing the cohesive forces between RM particles. On the other hand, alkali activated FeT exhibits a smaller increase in *c* values due to the limited formation of geopolymer gels during the geopolymerization process. Similar observations are also evident in alkali activated ZT specimens which also demonstrate a less pronounced improvement in interparticle *c* compared to RM.

In the case of alkali activated RM and ZT, specimens treated with higher concentrations of NaOH exhibit increased interparticle *c* compared to those treated with lower NaOH concentrations (as shown in Fig. 4.16). For instance, the interparticle *c* of untreated RM undergoes a notable rise from 15.36 kPa to 46.26 kPa, 110.89 kPa, 161.44 kPa, and 391.110 kPa upon activation with 2.5M, 5M, 7.5M, and 10M NaOH solutions, respectively. Similarly, the interparticle *c* of untreated ZT rises from 0 kPa to 6.29 kPa, 33.83 kPa, 51.09 kPa, and 133.91 kPa when activated with 2.5M, 5M, 7.5M, and 10M NaOH solutions, respectively. As discussed in section 4.6.1, higher NaOH concentrations lead to the formation of a greater

number of geopolymer gels which increases the interparticle adhesion between MT particles. However, the impact of increasing NaOH concentration on the interparticle *c* of FeT specimens is negligible with nearly constant *c* values observed across different NaOH concentrations (refer to Fig. 4.16).

As the improvement in *c* values is observed to be relatively lower (particularly at low NaOH concentration) for FeT and ZT specimen than RM. Therefore, to enhance the *c* values of FeT and ZT at lower NaOH concentrations, GBFS is incorporated as a precursor to increase the effectiveness of geopolymerization process. As evident from Fig. 4.16 that the interparticle *c* of FeT and ZT (activated with 2.5M) increases drastically from 12.6 kPa to 100 kPa and 6.29 kPa to 97.63 kPa, respectively with the addition of 10 % GBFS. Similarly, the c values for FeT and ZT activated with 2.5M NaOH increase sharply to 200.31 kPa and 209.52 kPa by the introduction of 20% GBFS. The reason for this increased interparticle *c* can be attributed to the coexistence of C-A-S-H/C-S-H and N-A-S-H gel structures in GBFS amended FeT and ZT which escalates the interparticle adhesion between FeT-GBFS and ZT-GBFS particles.

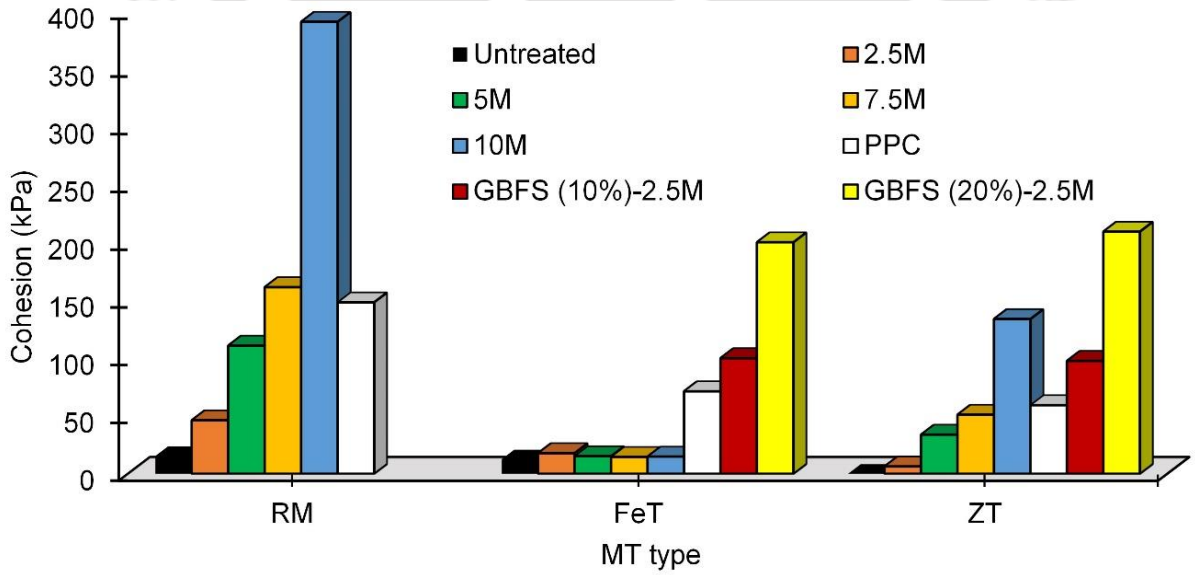

Fig. 4. 16 Interparticle cohesion for different MT specimens determined through DST using Mohr-Coulomb's failure criterion

b) Impact on internal friction angle, (ϕ)

Like interparticle *c*, the ϕ of untreated ZT is significantly enhanced by the alkali activation. The formation of 3D polymeric chains of aluminosilicates structures during geopolymerization improves the particle interlocking increasing the frictional resistance between two MT particles during shearing (Ghadir et al., 2021). As evident from Fig. 4.17, the value of ϕ increases with increasing molarity of NaOH solution employed during the activation phase. A high NaOH concentration facilitate the liberation of more Al and Si units to form new 3D networks of Na^+ based aluminosilicates oligomers which enhances the particle interlocking and consequently the ϕ. Furthermore, ZT specimens display the highest ϕ improvement among all MT followed by FeT and RM. For instance, the highest ϕ value for alkali activated ZT is found to be 76.38˚ compared to 52.85˚ and 43.71˚ for RM and FeT respectively. Since ZT contains higher coarser fraction compared to FeT and RM, a greater particle interlocking is achieved between ZT particles during alkali activation contributing to the increased ϕ values.

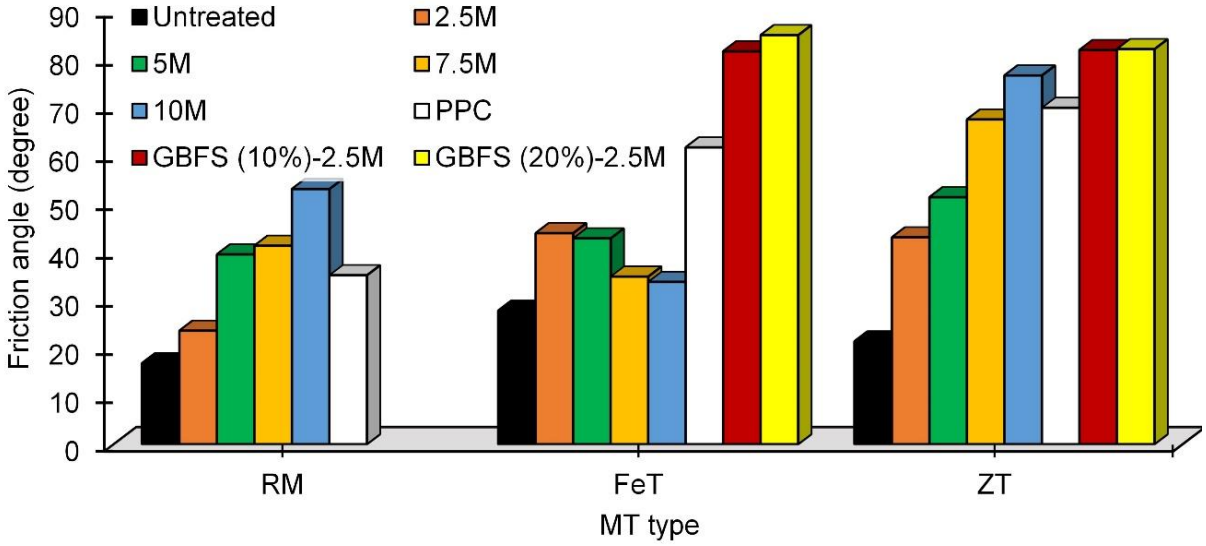

Fig. 4. 17 Internal friction angle values for different MT specimens determined from DST using Mohr-Coulomb's failure criterion

Furthermore, it is evident from Fig. 4.17 that the addition of GBFS significantly enhances the ϕ of both FeT and ZT. For instance, the ϕ of FeT and ZT activated with 2.5M

increases from 43.71˚ to 81.37˚ and 42.84˚ to 81.64˚ respectively when 10% GBFS is utilized as precursor material. This enhancement can be attributed to the presence of Ca^{+2} ions in GBFS which enhance the dissolution of aluminosilicates by raising the alkalinity of the geopolymer matrix (in addition to that raised by the 2.5M NaOH solution). Consequently, this leads to the formation of additional geopolymer gels. The polycondensation of these gels results in the agglomeration of MT particles thereby increasing particle interlocking and consequently the ϕ of geopolymer specimens. Similar findings have been also reported by other researchers (Al-Shayea, 2001; Ghadir et al., 2021).

4.6.4 Durability performance

Fig. 4.18 (a-b) displays the loss of mass (%) obtained after 12 cycles of alternate wetting and drying for untreated MT and other geopolymer specimens cured under AC and DC conditions. It can be noted from Fig. 4.18 (a-b) that all untreated MT show zero weathering resistance during alternate wetting and drying cycles with 100 % loss of mass. As evident from Figs. 4.19 (a-c) all untreated MT specimens disintegrate completely within 5 minutes of immersion in water. This indicates that untreated MT do not have sufficient strength and integrity to sustain extreme environmental conditions. However, the durability of untreated MT is improved significantly when activated with NaOH solutions. Moreover, the durability of geopolymer specimens is noted to be highly influenced by the MT type, curing conditions and the concentrations of NaOH solutions. Among all MT, alkali activated RM specimens display the least surface deterioration during the durability tests followed by ZT and FeT specimens (see Fig. 4.19a-c). This finding is further supported by the % loss in mass which is found to be lowest for RM specimens among all MT (see Fig. 4.18a-b). The enhanced durability of RM specimens can be readily understood given their superior strength and stiffness compared to ZT and FeT specimens as reflected in the UCS values discussed in section 4.6.1.

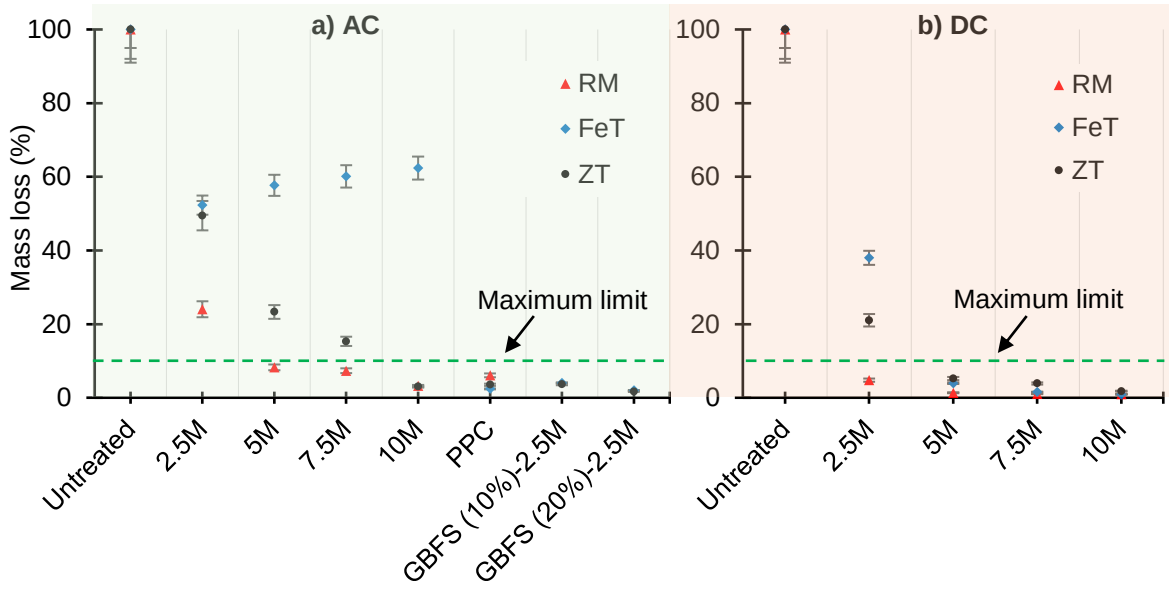

Fig. 4. 18 Loss of mass (%) observed after 12-wetting and drying cycles for various MT specimens cured under a) AC conditions, and b) DC conditions

Fig. 4. 19 Pictorial images of various MT specimens (cured under AC conditions) after durability tests a) RM specimens b) FeT specimens, and c) ZT specimens

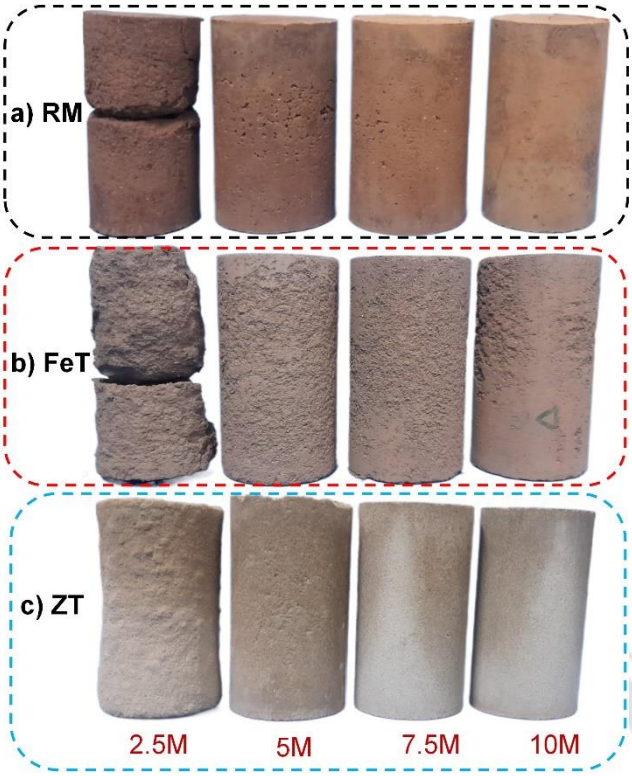

Fig. 4. 20 Pictorial images of various MT specimens (cured under DC conditions) after durability tests a) RM specimens b) FeT specimens, and c) ZT specimens

Furthermore, the durability tests reveal that specimens cured under DC conditions exhibit higher weathering resistance to alternate wetting and drying cycles in comparison to those cured under AC conditions. For example, the mass loss in RM, FeT and ZT specimens (after 12 wetting and drying cycles) activated with 5M NaOH solution is measured as 8.25%, 57.68%, and 23.30% respectively under AC conditions which reduces drastically to 1.33%, 3.93% and 5.21% under DC conditions. This improvement can be attributed to the more efficient geopolymerization reaction achieved under DC curing conditions which yields denser and stronger geopolymer specimens with superior weathering resistance.

Irrespective of the MT type and curing conditions, the durability of geopolymer specimens is noticed to increase with increasing concentrations of NaOH. Specimens activated with lower NaOH concentrations (i.e. Molarity ≤ 5M) exhibit far lesser surface disintegration (except for FeT specimens) during wetting and drying cycles compared to those activated with higher NaOH concentrations (see Figs. 4.19a-c and 4.20a-c). For instance, the % loss of mass

in AC cured RM and ZT specimens decreases drastically from 24.05% and 49.46% to 3.19% and 3.02%, respectively when the concentration of NaOH is increased from 2.5M to 10M. As previously emphasized, the higher NaOH concentration promotes the formation of additional geopolymer gels which enhances the strength and structural integrity of the MT specimens contributing to their improved durability performance. In general, most alkali-activated RM specimens meet the minimum durability requirement suggested by Jordi Bruschi et al. (2021) for stabilized embankment material. In contrast, most of FeT and ZT specimens, especially those activated with lower NaOH concentrations (Molarity ≤ 5M), fail to meet the durability criteria (loss in mass < 10%).

The addition of GBFS significantly enhances the weathering resistance of FeT and ZT specimens. In contrast to alkali activated FeT and ZT specimens, which show highly weathered and degraded surfaces, GBFS amended FeT and ZT specimens remain strong and intact throughout the durability tests with no discernible signs of weathering or surface deterioration (see Figs. 4.19b-c). This observation is further substantiated by the percentage loss of mass recorded after the conclusion of durability tests, which for ZT specimens decreases significantly from 49.46% to 1.03% and 0.61% by the incorporation of 10% and 20% GBFS, respectively. Likewise, the % loss of mass in FeT specimens decreases from 52.31% to 4.01% and 1.97% with the addition of 10% and 20% GBFS, respectively. As previously discussed, GBFS raises the alkalinity of the geopolymer matrix, expediting the dissolution of aluminosilicates during the activation phase and leading to the formation of additional N/C-A-S-H gel structures. These gel structures contribute to the increased compactness and density of the FeT and ZT matrix enhancing their resistance to weathering during wetting and drying cycles.

In general, the majority of alkali-activated RM specimens and GBFS-amended FeT and ZT specimens exhibit comparable or even superior weathering resistance compared to their

PPC counterparts (see Fig. 4.19a-c). This suggests that aside from providing sufficient strength, alkali-activated MT demonstrates good durability under challenging environmental conditions making them suitable for use as TP embankment material.

4.6.5 Permeability test results

Fig. 4.21 illustrates the hydraulic conductivity of various MT specimens obtained from permeability tests. It can be seen from Fig. 4.21 that RM has the lowest hydraulic conductivity among all MT followed by FeT and ZT which is expected considering RM contains the highest proportion of fine fractions. Irrespective of the MT type, the hydraulic conductivity of untreated MT is found to decrease significantly upon alkali activation (see Fig. 4.21). For instance, the hydraulic conductivity of untreated RM, FeT and ZT reduces from 1.38×10^{-8} cm/s, 8.70×10^{-7} cm/s and 1.20×10^{-5} cm/s to 2.89×10^{-11} cm/s, 8.20×10^{-8} cm/s and 1.67×10^{-7} cm/s respectively when activated with a 10M NaOH solution. Furthermore, the reduction in hydraulic conductivity is found to be more pronounced with higher concentrations of NaOH solution (see Fig. 4.21). Additionally, the incorporation of GBFS is observed to further decrease the hydraulic conductivity of FeT and ZT specimens (see Fig. 4.21). The reason for the reduced hydraulic conductivity of alkali activated MT specimens (compared to untreated specimens) is attributed to the formation of geopolymer gels during the geopolymerization process. As evident from Fig. 4.22, untreated MT consists of a substantial amount of air voids contributing to their higher hydraulic conductivity value. On the other hand, these air voids get plugged by the geopolymer gels formed during the geopolymerization process reducing the interconnectivity between them which in turn decreases the hydraulic conductivity of geopolymer specimens. It's worth noting that a lower hydraulic conductivity is preferable for materials intended for use in embankments as it aids in minimizing the seepage through the TP embankments.

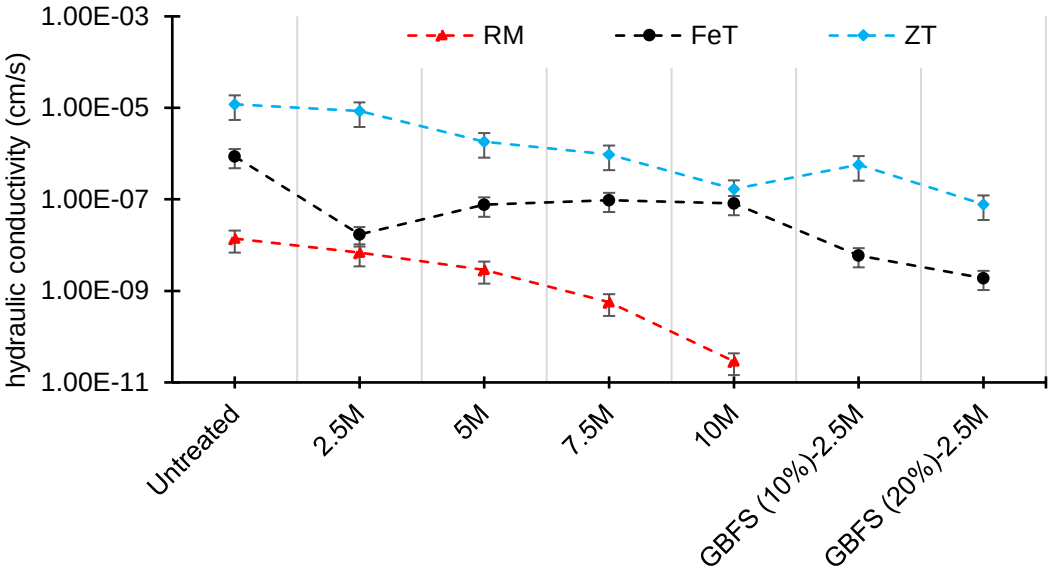

Fig. 4. 21 Hydraulic conductivity of different MT specimens

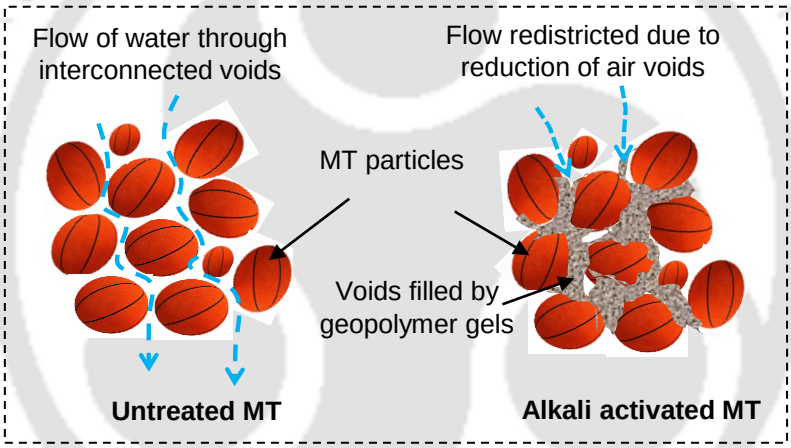

Fig. 4. 22 Illustration of mechanism accountable for the reduced hydraulic conductivity in alkali activated MT

4.6.6 Numerical analysis

To assess the potential of alkali-activated MT for use in TP embankment construction, a stability analysis is conducted on a TP previously examined in Chapter 3. This analysis is executed similarly to the procedures described in Chapter 3 focusing on steady-state flow conditions. Instead of using geosynthetic reinforcements and soil, alkali-activated MT is proposed for the construction of TP embankments. Fig. 4.23 illustrates the TP geometry used in the stability analysis highlighting both the actual materials employed on site and the alkali-activated materials considered for the numerical study. The strength and hydraulic properties

of tailings deposit and foundation soil are considered same as utilized for the numerical analysis performed in Chapter 3. Further, the shear strength parameters of embankment material (i.e. various alkali activated MT in this case) are varied based on the results of the DST discussed in section 4.6.3. The behaviour of embankment material, foundation soil and tailing deposit is assumed to be simulated using Mohr-Coulomb failure criterion. Furthermore, the slope of the linear component of the stress-strain curve obtained from the UCS tests is used to calculate Young's modulus (E) of various MT specimens (Zhang et al., 2013). The hydraulic conductivity of alkali activated MT employed for the construction of TP embankments is varied based on the results of permeability tests discussed previously in section 4.6.5. The engineering properties of various materials utilized in the numerical analysis are summarised in Table 4.5.

Fig. 4.24 presents the results of stability analysis in terms of critical SRF obtained at the end of the final construction of TP. It can be noted from Fig. 4.24 that critical SRF increases remarkably when alkali activated MT are used for the construction of TP embankments instead of untreated MT. Among all alkali activated MT, RM display the highest critical SRF values across all NaOH concentrations which is quite understood as it displays greater shear strength properties than other MT as discussed in section 4.6.3. Fig. 4.24 highlights that the majority of alkali-activated MT (excluding ZT-2.5M) exhibit higher SRF values compared to those derived from the actual materials employed in TP embankment construction. This suggests that instead of relying on natural soil and geosynthetic reinforcements alkali-activated MT can be leveraged for TP embankment construction. This alternative not only enhances stability but also proves to be more cost-effective as it involves utilizing on-site MT rather than relying on geosynthetic reinforcements and soil.

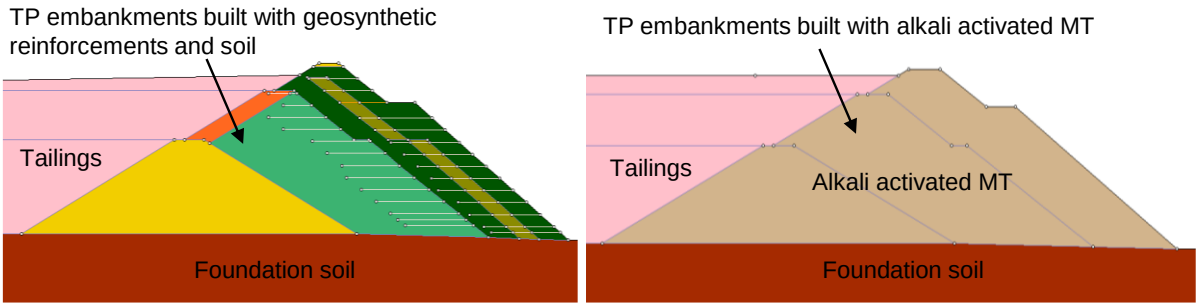

Fig. 4. 23 TP geometry used for numerical analysis

Table 4. 5 Values of input parameters for various materials used in the numerical analysis

Material	Unit weight (kN/m^3)	Young's Modulus, E (kPa)	Cohesion, c (kPa)	Friction angle, ϕ (degrees)	Hydraulic conductivity, k (m/s)
Settled tailings	20.00	12800	1	35	9.59×10^{-7}
Untreated RM	18.89	10000	15.36	16.76	1.38×10^{-10}
RM-2.5M	18.89	55000	46.26	23.5	6.89×10^{-11}
RM-5M	18.89	83333	110.89	39.31	2.89×10^{-11}
RM-7.5M	18.89	156862	161.44	41.1	5.63×10^{-12}
RM-10M	18.89	341463	391.11	52.85	2.89×10^{-13}
Untreated FeT	22.76	192493	12.6	27.65	8.7×10^{-9}
FeT-2.5M	22.76	515434	17.82	43.71	1.7×10^{-10}
FeT-5M	22.76	510000	15.2	42.63	7.6×10^{-10}
FeT-7.5M	22.76	384130	14.56	34.71	9.6×10^{-10}
FeT-10M	22.76	356956	14.81	33.61	8.2×10^{-10}
FeT-GBFS (10%)-2.5M	22.76	1123200	100	81.37	5.9×10^{-11}
FeT-GBFS (20%)-2.5M	22.76	1480217	200.32	84.73	1.9×10^{-11}
Untreated ZT	17.46	34634	0	21.3	1.20×10^{-7}
ZT-2.5M	17.46	171500	6.29	42.84	8.50×10^{-8}
ZT-5M	17.46	240065	33.83	51.15	1.81×10^{-8}
ZT-7.5M	17.46	480243	51.09	67.25	9.60×10^{-9}
ZT-10M	17.46	1088270	133.91	76.38	1.67×10^{-9}
ZT-GBFS (10%)-2.5M	17.46	993170	97.63	81.64	5.70×10^{-9}
ZT-GBFS (20%)-2.5M	17.46	2163970	209.30	81.83	7.81×10^{-10}

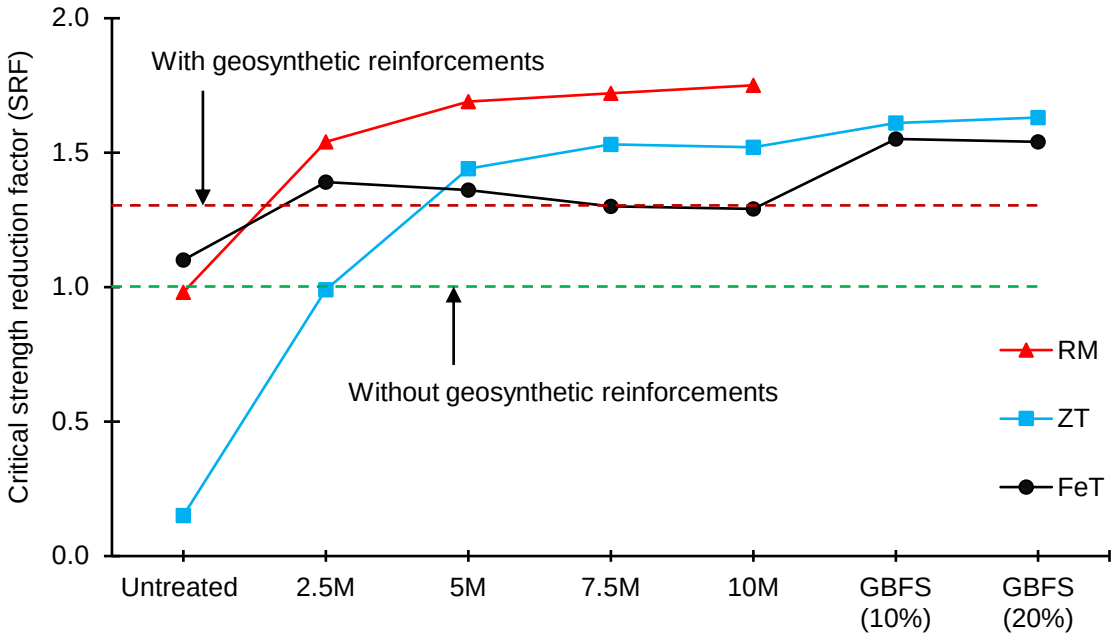

Fig. 4. 24 Critical SRF obtained for the TP embankment constructed with different alkali activated MT material

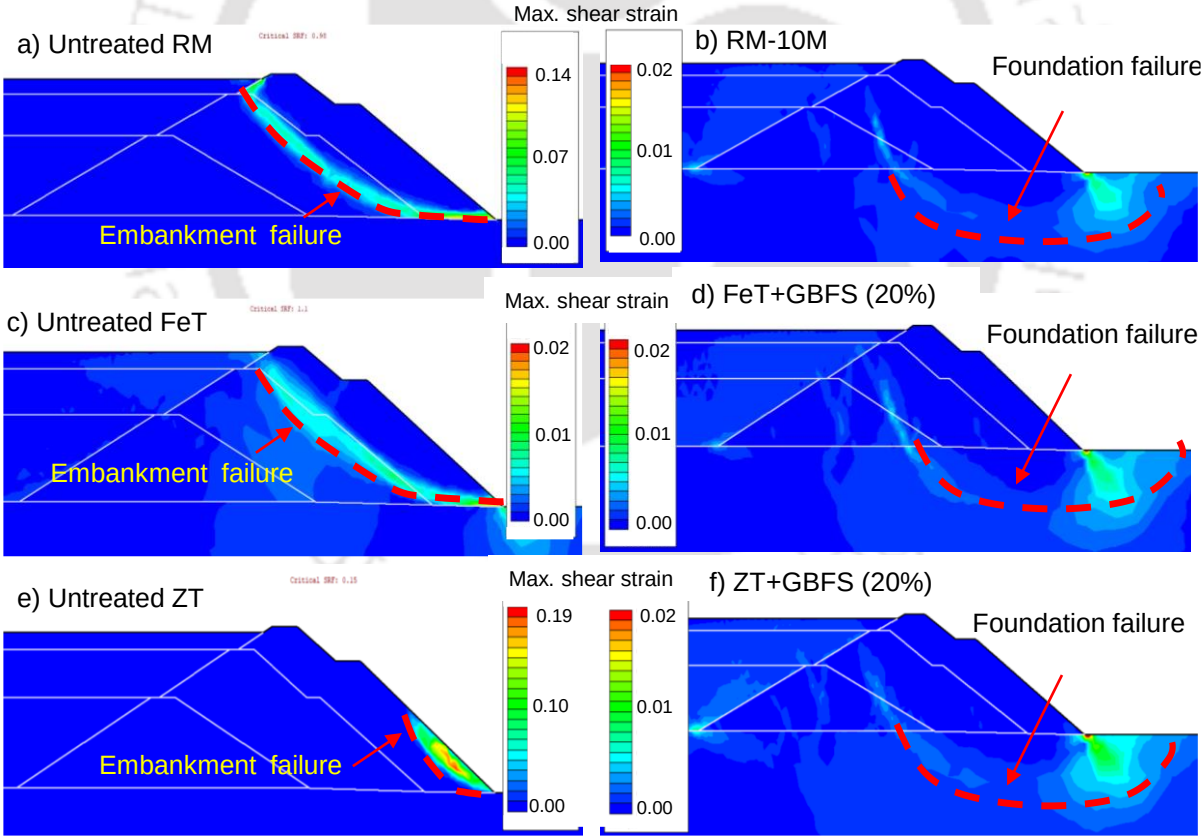

Fig. 4. 25 Contours of maximum shear strain indicating the modes of shear failure occurring within TP embankments built with a) a) untreated RM, b) RM-10M, c) untreated FeT, d) FeT+ GBFS (20%)-2.5M, e) untreated ZT, f) ZT+GBFS (20%)-2.5M

Figs. 4.25 (a-f) depict the contours of maximum shear strain, illustrating the failure surface patterns within TP embankments constructed using different alkali-activated MT. In the case of TP embankments built with untreated MT, the failure surface initiates from the toe of the embankments indicating toe failure (refer to Figs. 4.25 a, c, e). However, the pattern of failure surface changes when alkali activated MT are used in the construction of TP embankments. The failure of TP constructed with various alkali activated MT is primarily governed by the foundation soil indicating a base failure (refer to Figs. 4.25 b, d, f). Since the shear strength of alkali activated MT is substantially higher than foundation soil latter will fail before embankment material as shown in Figs. 4.25 (b, d, f). Overall, the results of the stability analysis indicate that alkali activated ZT has the potential to be used as TP embankment material.

4.7 Cost analysis

As mentioned previously, the embankments of TP can be built using either locally available soil or from stored tailings (EPA, 1994). However, the majority of MT lack the desired strength and durability characteristics required for an embankment material. Although the strength and integrity of tailings can be improved through cement stabilization, it is not considered an eco-friendly approach due to the release of greenhouse gases associated with cement production. On the other hand, apart from their high strength and durability properties, geopolymer binders are widely recognized for lower CO_2 emission than cement (Duxson et al., 2007). However, the cost of production for geopolymer binders can be relatively higher than for cement binders (McLellan et al., 2011). As a result, the overall effectiveness and practical implication of alkali activated MT as TP embankment material can be justified if its production cost is comparable or lesser than cement stabilized. This section provides a comparative cost analysis of TP embankments constructed with different alkali activated MT and cement (i.e. PPC) stabilized ZT. The analysis is conducted by evaluating the total cost incurred by various components for

the construction of 1 m^3 embankment. The quantity of NaOH consumed by geopolymer specimens is calculated based on the OMC and the concentration of NaOH solution used during its preparation. The amount of PPC required for ZT stabilization is considered as 10 % utilized in the current study as well as based on the work done by Ghadir and Ranjbar (2018). Table 4.5 presents the total estimated cost (in Indian rupees, ₹) consumed by different components involved in the construction of TP embankments which include the cost of raw materials, transportation cost, cost of handling, mixing and compaction etc. The total cost involved in the transportation, mixing, and compaction of different materials is sourced from the Rajasthan Public Works Department (Rajasthan PWD, 2019). The transportation cost is estimated based on the cost required to transport the raw material (i.e. NaOH/cement bags) from 20 km to the TP site. It should be noted that alkali activation of different MT only needs NaOH as a raw ingredient since both MT and GBFS are freely available at the mine site. However, a minimal cost for GBFS (i.e. ₹ 1/kg) is assumed in the current study in case of its unavailability on-site. Furthermore, the price of 1 bag of cement (i.e. 50 kg) is assumed as ₹ 400 based on the current market value while the cost of NaOH pellets is considered as ₹ 25/ kg.

It can be noted from Table 4.5 that the total production cost for various alkali activated MT prepared with lower concentrations of NaOH (i.e for 2.5M and 5M) is comparable or even lower than PPC stabilized MT. However, at higher NaOH concentrations (i.e molarity > 5M), the production cost for alkali activated MT increases significantly making them more expensive than their PPC stabilized counterparts. Based on the cost analysis, it is advantageous to employ alkali-activated MT prepared with lower NaOH concentrations for the construction of TP embankments. However, the majority of these MT (except for RM) fail to meet the strength and durability criteria (as discussed in sections 4.6.1 and 4.6.4) required for a TP embankment material.

Table 4. 6 Total production cost consumed (in ₹) by different components while constructing 1 m^3 of TP embankments

Components	MT type	2.5M	5M	7.5M	10M	GBFS (10%)-2.5M	GBFS (20%)-2.5M	PPC (10%)
Material cost		907.5	1815.0	2722.5	3630.0	-	-	1581.8
Transportation cost		5.1	10.2	15.3	20.4	-	-	27.7
Processing		200.0	200.0	200.0	200.0	-	-	0.0
Mixing	RM	670.2	670.2	670.2	670.2	-	-	670.2
Compaction		155.0	155.0	155.0	155.0	-	-	155.0
Total cost (₹)		**1937.8**	**2850.4**	**3763.0**	**4675.6**	**-**	**-**	**2434.7**
Material cost		833.3	1666.3	2499.3	3332.5	1067.8	1302.3	1876.2
Transportation cost		4.7	9.4	14.0	18.7	4.7	4.7	32.9
Processing		200.0	200.0	200.0	200.0	200.0	200.0	0.0
Mixing	FeT	670.2	670.2	670.2	670.2	670.2	670.2	670.2
Compaction		155.0	155.0	155.0	155.0	155.0	155.0	155.0
Total cost (₹)		**1863.1**	**2700.8**	**3538.5**	**4376.4**	**2097.7**	**2332.2**	**2734.4**
Material cost		685.3	1371.0	2056.3	2741.8	863.3	1041.3	1424.0
Transportation cost		3.9	7.7	11.6	15.4	3.9	3.9	25.0
Processing		200.0	200.0	200.0	200.0	200.0	200.0	0.0
Mixing	ZT	670.2	670.2	670.2	670.2	670.2	670.2	670.2
Compaction		155.0	155.0	155.0	155.0	155.0	155.0	155.0
Total cost (₹)		**1714.3**	**2403.9**	**3093.0**	**3782.4**	**1892.3**	**2070.3**	**2274.2**

The overall cost of MT specimens prepared with higher NaOH concentrations can be minimized using GBFS. As shown in Table 4.5, FeT and ZT specimens amended with GBFS exhibit a significantly lower production cost compared to their PPC counterparts. For example, the production cost for FeT amended with 10% GBFS is calculated as ₹ 2097, which is 23.2% less than the PPC stabilized FeT (i.e., ₹ 2734). Similarly, ZT specimens amended with 10%

GBFS show a 16.7% reduction in the production cost compared to PPC stabilized ZT. Likewise, the production cost for FeT and ZT specimens amended with 20% GBFS is noted to be 14.7% and 8.9% lower than their PPC stabilized counterparts. Overall, the addition of GBFS not only enhances the strength and durability of FeT and ZT specimens but it also reduces their production cost making them suitable for TP embankment application.

4.8 Summary

This study investigated the potential of ZT based geopolymer binder as embankment material for the construction of TP. A series of experiments are performed to investigate the strength and durability of geopolymer specimens prepared with different concentrations of NaOH solutions. The following major conclusions are drawn from the current study:

- The compressive strength of untreated MT (i.e. RM, FeT and ZT) is considerably improved through alkali-activation under AC and DC conditions respectively. Among all MT, RM exhibits the most substantial improvement in strength and durability when subjected to alkali activation owing to the superior effectiveness of geopolymerization compared to FeT and ZT. Furthermore, the rate of strength improvement is noticed to increase with increasing concentrations of NaOH solutions.
- The results of DST revealed that the shear strength of untreated MT can be significantly enhanced via alkali activation. The formation of Na^{+}/Ca^{+2} based aluminosilicate oligomers during geopolymerization increases both the interparticle adhesion and particle interlocking contributing to the enhanced interparticle c and ϕ values.
- Among all MT, RM display the highest weathering resistance against 12 alternate wetting and drying cycles compared to FeT and ZT. However, the weathering resistance of FeT and ZT specimens, particularly at lower NaOH concentrations (i.e. at 2.5M and 5M), is remarkably improved by the addition of GBFS.

- Hydraulic conductivity of untreated MT is reduced significantly when activated with NaOH solutions. Furthermore, the addition of GBFS in FeT and ZT results in the further reduction of hydraulic conductivity which is desirable for a TP embankment material.
- The production cost of alkali activated MT specimens are found to be comparable to those incurred by cement stabilized MT. However, these costs are significantly reduced when GBFS is utilized for the preparation of FeT and ZT based geopolymer binders.

Chapter 5

Utilization potential of red mud, iron tailings and zinc tailings as geopolymer binder in soil stabilization for sustainable road subgrade application

5.1 General

This chapter examines the utilization potential of three distinct MT viz.; RM, FeT, and ZT as geopolymer binders to stabilize the soil for road subgrade application. A series of UCS and California bearing ratio (CBR) tests are conducted to examine the mechanical response of soil stabilized with various MT-based geopolymers. While doing so, the effect of alkali activator concentration, curing conditions and curing period are also investigated. In addition, alternate wetting-drying tests are conducted to investigate the weathering resistance of stabilized soil specimens against extreme environmental conditions. Furthermore, permeability tests are also conducted to assess the hydraulic response of soil amended with MT-based geopolymers. Finally, leaching study is performed to examine the geo-environmental implications of the current study in terms of heavy metals concentration leached from the geopolymer specimens.

5.2 Material used

5.2.1 Soil, RM, FeT and ZT

The current study employs soil sourced from the Northeastern city of Guwahati, India along with three different types of MT i.e. RM, FeT and ZT. The basic geotechnical characterization of these MTs are previously discussed in section 4.2 of chapter 4. Similarly, the basic geotechnical characterization of soil follows a procedure like that used for the characterization of MT. Table 5.1 provides a summary of the basic geotechnical properties of soil, RM, FeT and ZT. It can be noted from Table 5.1 that soil has a lower specific gravity (2.67) compared to RM (2.94) and FeT (3.47). Fig. 5.1 displays the particle size distribution of various materials

utilized in the current study. Of all the materials, RM contains highest finer fraction (particle size > 0.075 mm) followed by soil, FeT and ZT (see Fig. 5.1). This trend is also reflected in the specific surface area measurements with RM having the highest value (23.50 m^2/g) followed by soil (19.21 m^2/g), FeT (12.85 m^2/g) and ZT (3.06 m^2/g). As per USCS (ASTM D2487, 2011), the soil, RM, and FeT fall under the category of CL, whereas ZT is classified as ML.

Table 5. 1 Basic geotechnical properties of soil, RM, FeT and ZT

Properties	**Soil**	**RM**	**FeT**	**ZT**
Specific gravity	2.67	2.94	3.47	2.65
Clay content (< 0.002 mm) %	19.05	30.22	17.41	13.01
Silt content (0.075 mm– 0.002 mm) %	51.03	57.38	37.68	73.56
Sand fraction (4.75 mm – 0.075 mm) %	29.81	12.40	44.91	13.43
Liquid limit (%)	38.51	40.30	31.37	23.45
Plastic limit (%)	15.14	18.85	19.05	Non-plastic
Plasticity Index (%)	23.37	21.45	12.32	Non-plastic
USCS classification	CL	CL	CL	ML
pH	8.20	10.40	8.58	8.60
Specific surface area, SSA (m^2/g)	19.21	23.50	12.85	3.06
Average pore diameter (nm)	9.44	15.72	12.27	8.24
Water holding capacity, WHC (%)	143.06	149.08	139.36	128.56

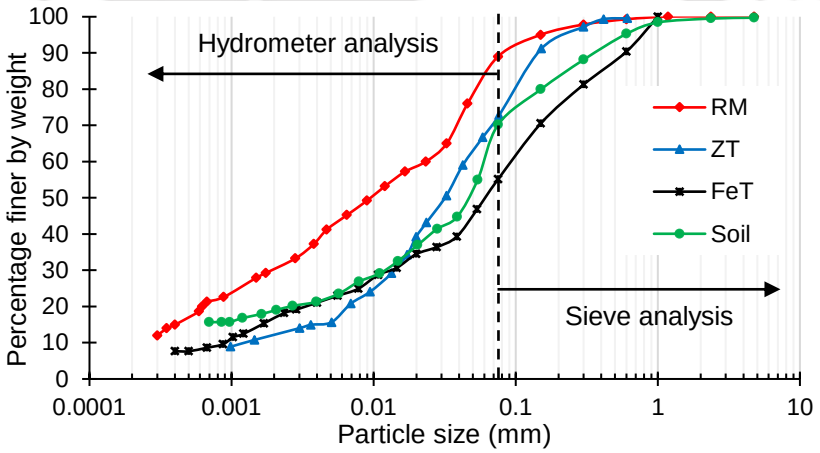

Fig. 5. 1 Particle size distribution curve for soil, RM, FeT and ZT

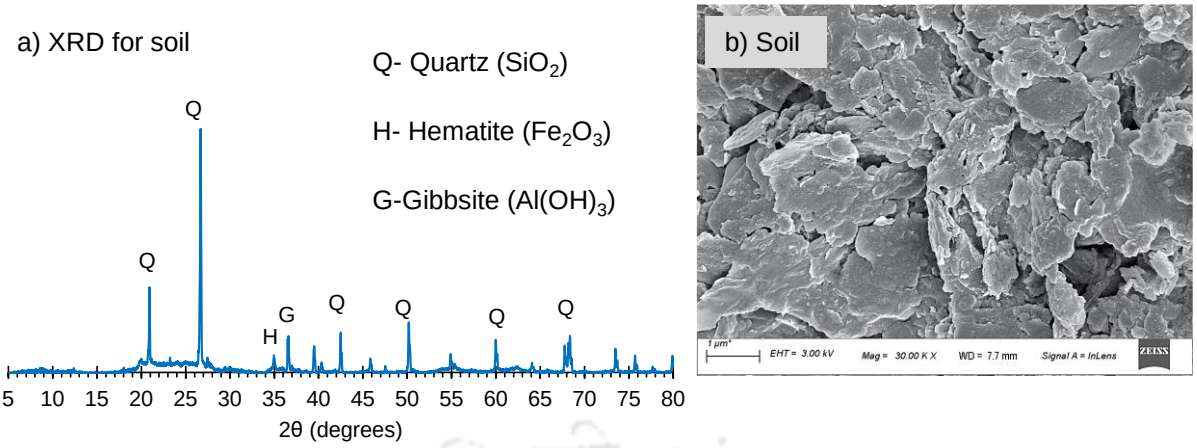

Fig. 5. 2 a) XRD pattern for soil, b) FESEM image of soil

Table 5. 2 Chemical composition of soil determined by XRF analysis

Major oxides (%)	SiO_2	Al_2O_3	Fe_2O_3	MnO	MgO	CaO	Na_2O	K_2O	TiO_2	P_2O_5	SO_3
Soil	51.76	14.97	6.00	0.12	0.73	0.11	0.08	2.68	0.74	0.04	0.04

Fig. 5.2a illustrates the mineralogical composition of the soil as determined through XRD analysis. It is clear from Fig. 5.2a that the soil predominantly consists of quartz mineral (SiO_2) with a noticeable peak of hematite (Fe_2O_3). This observation is further supported by analysing the chemical composition of the soil through XRF analysis, which reveals the presence of high SiO_2 content, as indicated in Table 5.2. The chemical composition of other materials i.e. RM, FeT, and ZT has been previously discussed in section 4.2.3 of chapter 4. Fig. 5.2b depicts the microstructure of the soil obtained from FESEM analysis illustrating its irregular shape with a flaky texture. A similar particle structure is also observed for RM and FeT as shown in Fig. 4.3, discussed in section 4.2.3 of chapter 4.

5.2.2 Alkali activator

NaOH is utilized as an alkali activator to initiate the dissolution of aluminosilicates during the geopolymerization reaction. It is sourced from the local market in pellet form with a purity of 97%. To prepare the NaOH solution, the required amount of NaOH pellets is dissolved in deionized water to achieve the desired concentration. For this study, NaOH solution

concentrations are maintained at 5M and 10M based on previous research on soil stabilization using MT geopolymers (Ghadir and Ranjbar, 2018). The prepared NaOH solutions are left to cool overnight before being mixed with different materials to prevent the rapid setting of soil mixtures (Ismail et al., 2014; Miraki et al., 2022).

5.3 Mix proportion and compaction characteristics of soil-MT blends

To stabilize the subgrade soil, it is typically recommended to keep the binder content below 30%. Therefore, in the present investigation, the content of MT to stabilize the subgrade soil is adjusted at 10%, 20% and 30%. The compaction characteristics of soil amended with RM, FeT and ZT are determined using mini-compaction mould following Sridharan and Sivapullaiah (2005). To begin the compaction experiments, the oven-dried samples of soil and MT are manually blended to ensure a uniform and consistent mixture. Following that the deionized water is added to the prepared blend and mixed meticulously for a duration of 5 minutes ensuring absence of any lumps. The prepared mixture is then compacted in a compaction mould in three distinct layers, each subjected to 36 blows with a 1 kg hammer. This procedure is repeated a minimum of 6 times by varying water content each time to acquire the dry density values associated with different levels of water content.

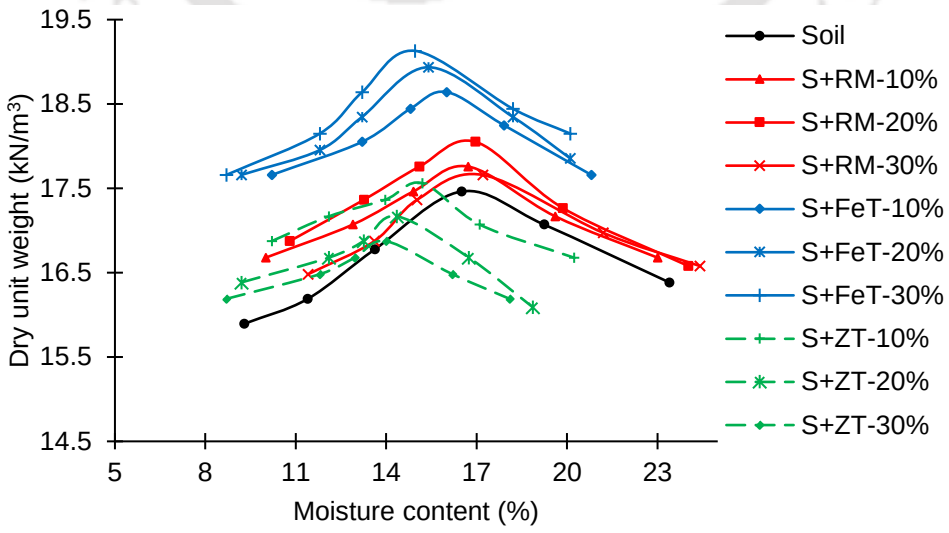

Fig. 5. 3 Compaction characteristics of soil amended with different MT

Fig. 5.3 presents the results of mini-compaction tests carried out on various soil-MT mixtures. The MDU of soil increases with increasing FeT content (refer to Fig. 5.3) which can be attributed to the higher specific gravity of FeT compared to soil. Consequently, the OMC of soil decreases as the FeT content increases, which can be associated with its low water holding capacity. Similarly, the MDU of soil shows an increasing trend with the addition of RM (refer to Fig. 5.3) owing to its greater specific gravity in comparison to soil. Moreover, the finer particles of RM occupy the available void spaces created by the soil particles leading to a denser structure. However, a slight decrease in MDU of the soil can be noticed when the RM content surpasses 20%. This decline can be attributed to the fact that the air voids are already filled by the initial 20% of RM and further addition of RM increases the air voids within the soil matrix. A similar pattern is also observed for soil-ZT mixtures where an increase in MDU is evident up to a ZT content of 10%. Increasing the ZT content beyond 10% leads to a decline in MDU and a subsequent reduction in the OMC. It must be highlighted here that the MDU of soil increases when the compaction tests are performed using NaOH solution instead of deionized water. The reason for this is attributed to enhanced lubrication ability of the NaOH solution (than water) which enables soil particles to adjust themselves in a denser structure during the compaction.

Keeping above discussion in view, constant values of MDU and OMC (corresponding to the lowest values observed for different soil-MT mixtures) are employed to minimize the influence of density variations on the strength and durability of geopolymer specimens (as shown in Table 5.3).

Table 5. 3 Dry unit weight and liquid alkali content used for sample preparation

Mix Type	Dry unit weight (kN/m^3)	Liquid alkali content (%)
S+RM	17.66	17.2
S+FeT	18.64	16.0
S+ZT	16.87	14.2

5.4 Experimental methodology

5.4.1 UCS tests

UCS tests are performed in compliance with ASTM D2166 (2006) on an automatic machine with a maximum load limit of 50 kN. To prepare the specimens for UCS tests, oven-dried samples of both soil and MT are amalgamated in three distinct ratios namely; 90:10, 80:20, and 70:30. After this, a specified amount of NaOH solution (with concentrations of 5M and 10M) is added to the soil-MT mixture and the entire amalgamation is thoroughly mixed to achieve a consistent blend. It is important to emphasize that the quantities of soil, MT and NaOH solution chosen for sample preparation are determined based on the MDU and OMC as discussed in section 5.2.3. The prepared mixture is thereafter compacted within a cylindrical mould to fabricate specimens of 38 mm diameter and 76 mm height. Before undergoing UCS testing, the specimens are cured for 3, 7 and 28 days under AC and DC conditions. Specimens in AC are placed in an ambient environment condition with an average temperature ranging from 25 ± 7 ˚C and relative humidity of 85 ± 10 % whereas in DC conditions, the specimens are cured in an oven at a constant temperature of 50 ˚C. At least three specimens are prepared for each UCS test to ensure the reliability and reproducibility of experimental data, and the average of three values is reported as the UCS of the specimen. Results obtained from the UCS tests are discussed later in the “Results and Discussion” section.

5.4.2 FESEM and EDS analysis

To understand the changes occurring within the geopolymer matrix during geopolymerization at microstructural and elemental level, FESEM and EDS analysis are performed respectively on selected geopolymer specimens. These analyses were carried out following the procedures outlined earlier in section 4.5.2 of chapter 4.

5.4.3 Durability tests

The material employed in pavement's subgrade construction should possess the capacity to endure harsh weather conditions caused by intense rainfall events and subsequent drying phases without experiencing significant erosion and disintegration. To assess the ability of stabilized material to withstand such demanding conditions, durability tests are conducted on geopolymer specimens (following 7 days of curing period) in compliance with ASTM D559 (2015). The complete procedure for conducting the durability tests has been previously outlined in section 4.5.4 of chapter 4. The results of these tests are reported in terms of the percentage loss in mass observed after the durability assessments.

5.4.4 CBR tests

To investigate the strength characteristics of subgrade soil, CBR tests are performed under soaked conditions following the guidelines outlined in ASTM D1883 (2021) and IS 2720-16 (1987). These tests are conducted only on those specimens which exhibit the least strength improvement during the UCS testing. The samples for CBR tests are prepared at the same MDU and OMC as used during the UCS testing. To prepare the specimen, the oven-dried samples of soil and MT are blended manually for 5 minutes with a known volume of NaOH solution. The prepared mixture is then compacted in three layers in a CBR mould at a standard Proctor energy level. Following this, the specimens are cured for 7 days in AC conditions. Once the curing process is completed, the specimens are immersed in water for at least 96 h. Finally,

the penetration test is carried out on a loading frame with load capacity of 50 kN maintaining a constant displacement rate of 1.25 mm/minute. The load values at 2.5 mm and 5 mm penetrations are recorded to calculate the CBR of the specimens. Each test is performed thrice to ensure the accuracy and the repeatability of experiments.

5.4.5 Permeability tests

Hydraulic conductivity of geopolymer specimens (which show highest compressive strength improvement during UCS tests) is determined using a fixed wall permeameter in accordance with ASTM D5856 (2015). The entire procedure for conducting the permeability tests has been already discussed in section 4.5.5 of chapter 4. These tests are conducted on those geopolymer specimens which are cured for 7 days. Each test is performed thrice and the average value obtained is reported as the hydraulic conductivity of that specimen.

5.4.6 Leaching tests

The stabilized material used for subgrade construction should not contribute to the toxicity resulting from the release of various heavy metals into surface water and groundwater sources. To evaluate the potential toxicity of soil treated with distinct MT-based geopolymers, toxicity characteristics leaching procedure (TCLP) tests are conducted in accordance with the USEPA 1311 method (USEPA, 1992). These tests are conducted on the specimens with the highest MT content as specimens containing higher MT content are more likely to leach higher concentration of toxic elements.

To prepare the sample for TCLP tests, 10 g of the specimen with particle size below 2 mm is mixed with 200 mg of extraction fluid (solution of acetic acid and deionized water). Following that, the solution containing extraction fluid and soil sample is shaken for 18 h before being filtered through a glass fibre filter. Finally, the concentration of leachate is

analysed using an atomic absorption spectrometer. Each mixture is subjected to three separate trials and the mean of these three values are considered as the concentrations of leached metals.

5.5 Results and discussion

5.5.1 UCS tests results

Table 5.4 summarises the results of UCS tests performed on various geopolymer specimens.

Table 5. 4 Summary of UCS values (MPa) obtained for different soil-MT mixtures

Sample type	MT content (%)	NaOH concentration	AC			DC		
			Curing period (days)			Curing period (days)		
			3	7	28	3	7	28
S+RM	10	5M	1.12	2.21	3.71	7.97	10.45	9.56
S+FeT			1.62	1.86	4.12	13.62	13.96	14.01
S+ZT			0.76	0.81	1.81	4.68	4.14	3.96
S+RM	10	10M	2.20	2.82	3.82	19.2	23.07	24.62
S+FeT			2.53	4.65	5.09	17.08	21.27	20.36
S+ZT			1.33	1.93	3.78	9.72	10.29	10.35
S+RM	20	5M	1.52	2.77	4.99	10.55	10.50	11.29
S+FeT			0.81	1.06	2.68	10.66	10.83	10.92
S+ZT			0.24	0.49	1.79	4.46	4.01	3.81
S+RM	20	10M	2.97	3.51	5.24	24.01	25.42	30.86
S+FeT			2.02	3.32	4.44	16.34	18.44	18.45
S+ZT			1.41	1.94	2.8	8.06	8.06	7.87
S+RM	30	5M	1.25	2.82	4.81	10.35	10.5	10.84
S+FeT			0.74	0.76	2.24	7.20	6.58	6.50
S+ZT			0.41	0.44	1.55	3.13	3.13	3.01
S+RM	30	10M	3.53	4.14	5.12	21.14	25.17	26.42
S+FeT			1.11	1.94	2.79	13.62	13.23	13.10
S+ZT			1.20	1.51	1.81	6.40	5.62	5.50

It can be noted from Table 5.4 that the compressive strength of soil is significantly enhanced using MT-based geopolymers. This enhancement is attributed to the distinctive interaction between soil and MT geopolymers during the geopolymerization process. Geopolymers, being inorganic polymers, exhibit a distinct interaction with soil particles compared to that with organic polymers. During activation, the NaOH solution liberates amorphous silica and alumina from MT precursors (or from the soil itself), leading to the formation of cementitious compounds with a chain network of -Si-O-Al- or -Si-O-Si- units. These cementitious gels tie the soil particles together leading to a much denser soil matrix (refer to Fig. 5.4) which contributes to increase in UCS of soil-MT system. However, the potency of geopolymer gel formation in the soil-MT system is contingent upon various factors including the concentrations of amorphous silica and alumina in MT and soil, the type of MT, concentrations of alkali activator, and the curing conditions. The effect of these parameters on the compressive strength of soil is discussed in the following sections.

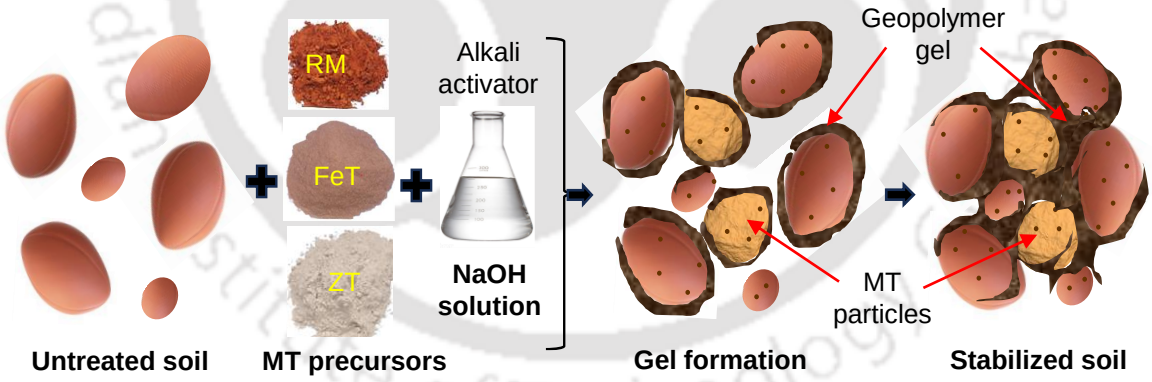

Fig. 5. 4 Illustration of soil-MT based geopolymer interactions during geopolymerization process

a) Effect of MT type

Figs. 5.5 (a-b) illustrate that the 28-day compressive strength of soil treated with various MT based geopolymers cured under AC and DC conditions respectively. It can be clearly seen from Figs. 5.5 (a-b) that the compressive strength of soil is substantially enhanced using RM, FeT and ZT geopolymers. Regardless of the curing conditions and activator concentrations, RM

stands out as the most effective geopolymer binder among all the MT followed by FeT and ZT. For example, the 28-day UCS of soil is improved by 1325.71% from 0.35 MPa to 4.99 MPa when stabilized with RM based geopolymer binder. In contrast, the 28-day UCS of soil treated with FeT and ZT based geopolymers is enhanced from 0.35 MPa to 4.12 MPa and 1.81 MPa respectively. The optimal ratio of SiO_2 and Al_2O_3 required for geopolymerization contributes to the greater effectiveness of RM (as a geopolymer binder) in comparison to FeT and ZT. It is widely acknowledged that the strength enhancement of geopolymer specimens is negatively affected by both high SiO_2 /Al_2O_3 ratios (>4) and low SiO_2 /Al_2O_3 ratios (<0.5) (De Silva et al., 2007). As indicated by XRF results, the SiO_2 / Al_2O_3 ratio in RM is measured as 1.51 in comparison to 1.16 and 6.56 for FeT and ZT respectively. Given that the SiO_2 /Al_2O_3 ratio in RM is slightly higher than FeT, soil stabilized with RM-based geopolymers exhibits a marginally superior strength improvement.

On the other hand, ZT has a considerably high SiO_2 /Al_2O_3 ratio, which is undesirable for geopolymerization reactions (De Silva et al., 2007) indicating its ineffectiveness as a geopolymer binder. Furthermore, the higher effectiveness of RM as a geopolymer binder compared to other MT may also be attributable to its high specific surface area. Since the specific surface area of (23.50 m^2/g) is relatively higher than FeT (12.85 m^2/g) and ZT (3.05 m^2/g), a greater amount of Si and Al are released during the dissolution phase. This is because a greater amount of SiO_2 and Al_2O_3 interacts with NaOH at higher specific surface area (Dietel et al., 2017), which leads to the formation of a greater number of reaction products (see Figs 5.6a-c). This in turn makes the soil-RM geopolymer matrix more compact and denser (refer to Figs 5.6a-c), contributing to its high compressive strength.

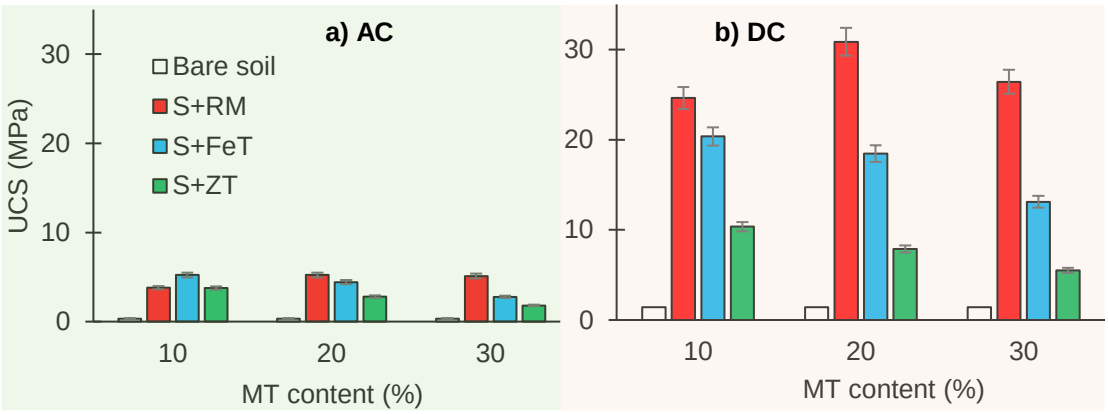

Fig. 5. 5 28-day UCS of soil stabilized with various MT based geopolymer under a) AC, and b) DC conditions

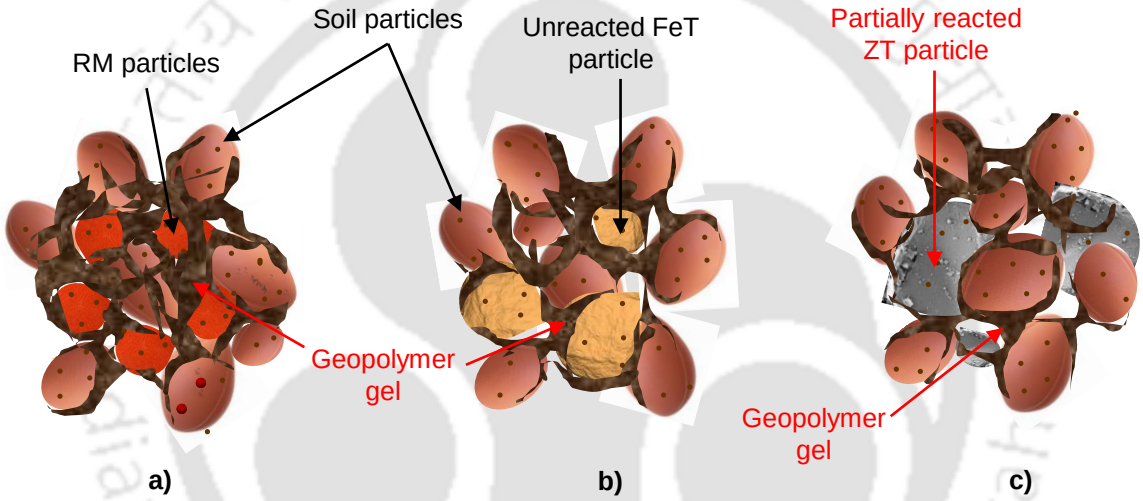

Fig. 5. 6 Illustration of geopolymer gel formed in various soil-MT mixtures a) S+RM, b) S+FeT, and c) S+ZT

b) Effect of curing environment

Regardless of MT type, geopolymer specimens display a far better strength improvement under DC conditions as compared to AC conditions (refer to Figs. 5.5a-b). At higher temperatures (i.e. under DC conditions), the movement of Na^+ and OH^- becomes more active resulting in greater SiO_2 and Al_2O_3 dissolution (Sajan et al., 2021). This results in the development of a greater number of Na^+ based aluminosilicate oligomers increasing the UCS of soil-MT mixtures. Moreover, at elevated temperatures, the polymerization reaction becomes more effective in transforming 2D polymeric chains into 3D polymeric chains with a more robust structural integrity (Sajan et al., 2021). In addition, higher curing temperatures have

been observed to enhance the overall pore volume and surface area of the soil matrix making the geopolymerization reaction more vigorous (Leung and Pheeraphan, 1995). Alternately, under DC conditions, there is a reduced presence of residual water within the soil matrix compared to AC conditions, which elevates the alkalinity of the soil matrix. This in turn accelerates the overall rate of geopolymerization reaction thereby enhancing the compressive strength of the geopolymer specimens (Ghadir and Ranjbar, 2018).

c) Influence of MT fraction

The strength enhancement in geopolymer specimens is also affected by the quantity of MT employed in their preparation. In the case of RM stabilized soil, the highest strength improvement is achieved at 20% RM content irrespective of the alkali activator concentration. This is due to the reason that a higher quantity of reaction products is formed when the soil-RM matrix contains 20% RM content, resulting in a denser structure. However, at 30% RM content, NaOH solution is found to be insufficient to dissolve all SiO_2 and Al_2O_3 units resulting in the development of fewer Na^+ based aluminosilicates polymeric chains (compared to 20% RM). On the other hand, the highest strength improvement of soil is attained at MT content of 10% when it is stabilized with FeT and ZT geopolymers. Increasing FeT and ZT content beyond 10% is observed to have an adverse impact on the UCS of stabilized soil specimens. The reason for this can be attributed to the reduction in SiO_2/ Al_2O_3 ratios as FeT content is increased from 10% to 30%. For instance, the SiO_2/ Al_2O_3 ratio in soil-FeT mixtures decreases from 3.09 to 2.48 when FeT content is increased from 10% to 30%. At lower SiO_2/ Al_2O_3 ratios, fewer geopolymer gels are formed owing to lesser dissolution of Si ions. In contrast, the SiO_2/ Al_2O_3 ratios in soil-ZT mixtures become too high (> 4) when the ZT content exceeds 10%. This high ratio results in the reduced formation of aluminosilicate networks leading to the lower compressive strength of soil-ZT mixtures.

d) Effect of activator concentration

Figs. 5.7 (a-b) display the variation of UCS of various geopolymer specimens with NaOH concentrations and curing conditions.

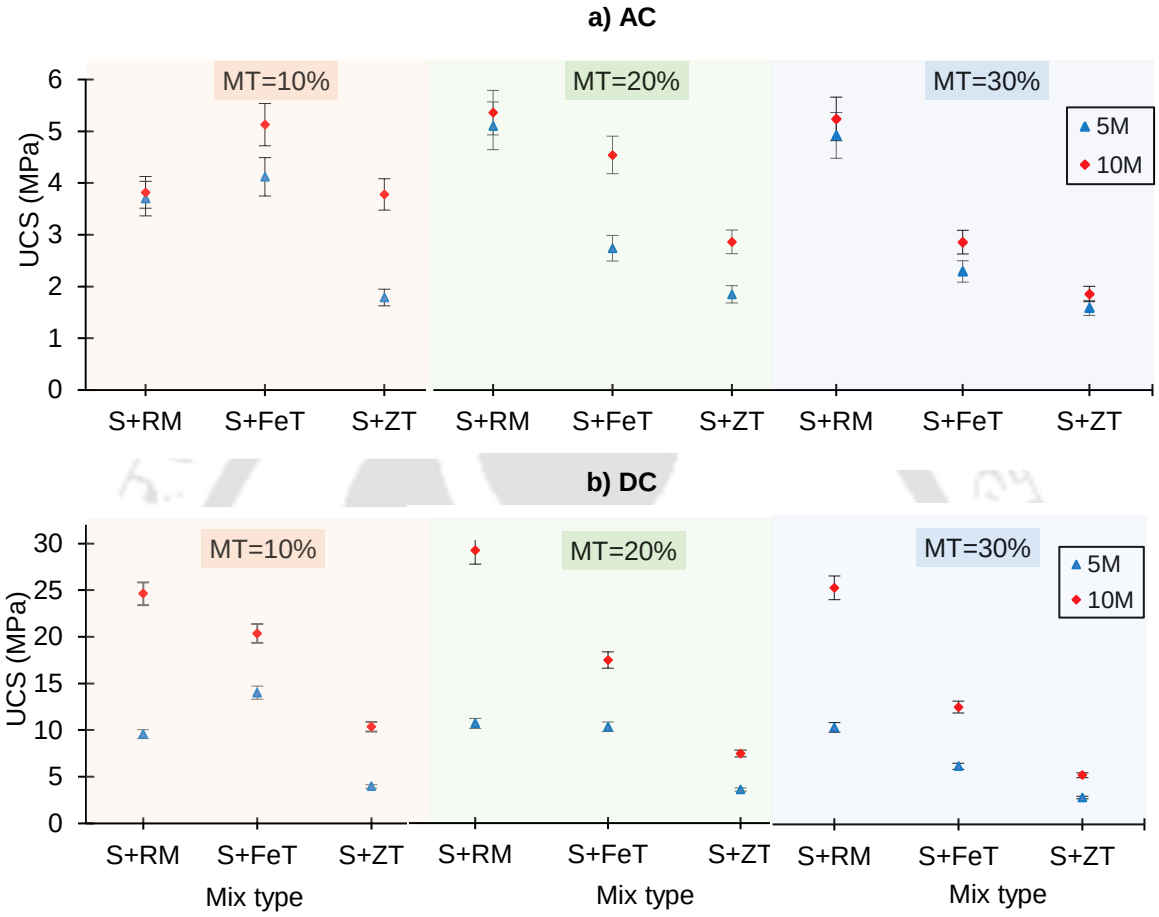

Fig. 5. 7 Variation of 28-day UCS with varying NaOH concentrations under a) AC conditions, and b) DC conditions

It is evident from Figs. 5.7 (a-b) that irrespective of the MT type and curing conditions, the UCS of soil increases significantly when the concentration of NaOH is raised from 5M to 10M. Higher concentration of NaOH solution accelerates the dissolution of SiO_2 and Al_2O_3 units facilitating the development of more aluminosilicates networks comprising of $Al(OH)_3$ and $Si(OH)_4$ units (Leung and Pheeraphan, 1995). As illustrated by Figs. 5.8 (a-b), a greater number of geopolymer gels are formed within the soil matrix when 10M NaOH solution is employed for the activation purpose as compared to 5M NaOH solution. These gel structure

fills most empty spaces within the geopolymer matrix (see Figs. 5.8a-b) enhancing the compressive strength of geopolymer samples. Furthermore, at lower NaOH concentration (i.e. 5M), geopolymer matrix contains a greater amount of residual water which hinders the dissolution of aluminosilicate during the activation phase (Ghadir and Ranjbar, 2018). On the other hand, the presence of lesser amount of residual water at higher NaOH concentrations (e.g., 10M) facilitates the dissolution of aluminosilicate units (due to the increased alkalinity). This leads to the formation of more geopolymer gels (in comparison to that formed with 5M NaOH), ultimately contributing to the enhanced UCS of geopolymer specimens.

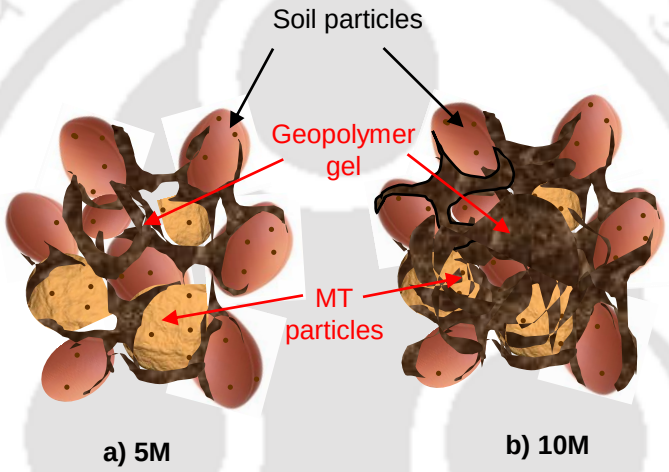

Fig. 5. 8 Illustration of geopolymer gel formed in various soil-MT mixtures with a) 5M NaOH, b) 10M NaOH

e) Effect of curing period

The time required for subgrade preparation largely hinges on how long it takes for the subgrade material to gain a desired level of compressive strength. In such situations, the duration of curing has a significant influence on the strength improvement of soil stabilized with MT based geopolymers. Figs. 5.9 (a-b) display the UCS of various geopolymer specimens at different stages of curing under both AC and DC conditions respectively. It can be noted from Fig. 5.9a that the UCS of geopolymer specimens cured under AC conditions increases substantially with increase in the curing time. In AC conditions, the geopolymerization reaction proceeds at a slower pace owing to the existence of substantial residual water which hinders the dissolution

and hydrolysis of aluminosilicates (Ghadir and Ranjbar, 2018). As the curing period increases, this residual water evaporates, which accelerates the dissolution of more SiO_2 and Al_2O_3 units. In contrast, specimens exposed to DC conditions show a negligible increase in compressive strength with an increasing curing period. As evident from Fig. 5.9b, all geopolymer specimens gain most of their compressive strength during the early stage of curing (3 days in this case). This implies that the majority of the geopolymerization process (under DC conditions) is completed within the curing period of 3 days due to the faster consumption of Na^+ and OH^- at elevated temperatures.

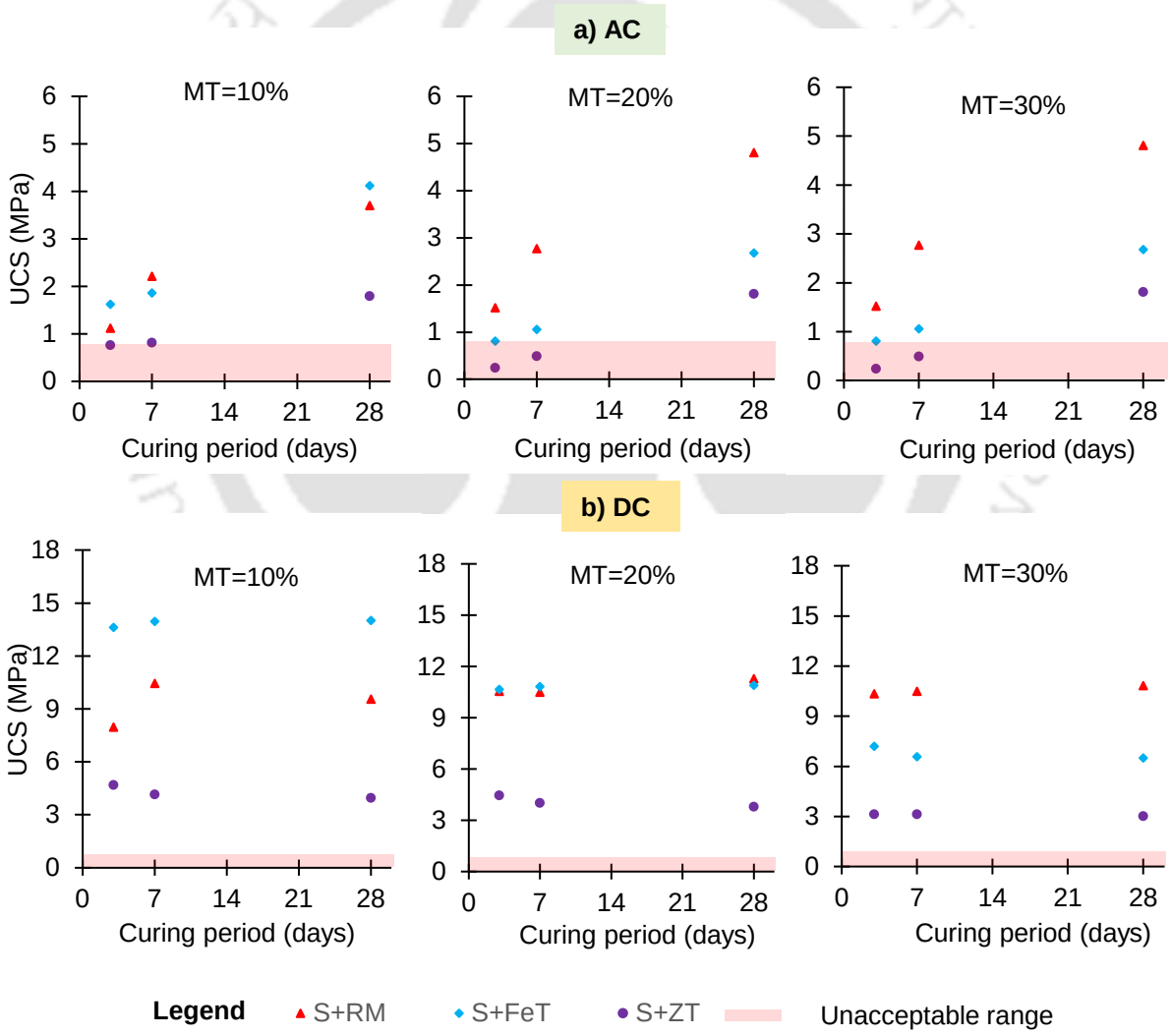

Fig. 5. 9 Variation of UCS in different soil-MT mixes with curing period under a) AC conditions and b) DC conditions

Furthermore, some geopolymer specimens exhibit a slight decrease in UCS (refer to Fig. 5.9b) following an extended curing period of 28 days at 50°C. This reduction in UCS is attributed to the formation of microcracks within the geopolymer matrix due to excessive shrinkage and hydration induced by oven curing (Zuhua et al., 2009). It can be noted from Fig. 5.9 that each DC cured geopolymer specimen satisfies the minimum strength criteria of 7-day UCS > 0.75 MPa recommended by IRC SP-72 (2015) for road subgrade material. In contrast, only RM and FeT treated soil specimens can satisfy the 7-day strength criteria under AC conditions. It should be noted that ZT stabilized specimens require extended curing of 28 days to satisfy the minimum strength criteria, which can hamper the construction time if used in highways or expressways projects. In such scenarios, the utilization of ZT-based geopolymers in subgrade construction may be best suited for village or low-traffic roads where the longer curing period of 28 days can be permitted to achieve the desired compressive strength.

5.5.2 FESEM and EDS results

Figs. 5.10 (a-f) display FESEM images of selected geopolymer specimens which exhibit the highest strength improvement among all MT geopolymers. As evident from Figs. 5.10 (a-b), there is a notable increase in the quantity of geopolymer gels in the RM stabilized soil when the molarity of NaOH solution is raised from 5M to 10M. These gel structures effectively fill the voids resulting in a more compact and denser geopolymer matrix (see Fig. 5.10b), which enhances the UCS of soil specimens. Similar observations are also apparent in case of soil stabilized with FeT and ZT geopolymers. As evident from Figs. 5.10 (c, e), a lesser quantity of geopolymer gels along with a substantial amount of air voids are noticeable within the FeT and ZT stabilized soil matrix when 5M NaOH is employed for activation. On the other hand, a greater formation of reaction products (i.e. geopolymer gels) is evident (refer to Figs. 5.10d, f) when 10M NaOH is employed for activation, resulting in fewer air voids and a more densely packed geopolymer matrix. In a nutshell, the FESEM analysis clearly indicates that RM stabilized soil forms a significantly denser geopolymer matrix with fewer air voids, followed by FeT and ZT treated soil.

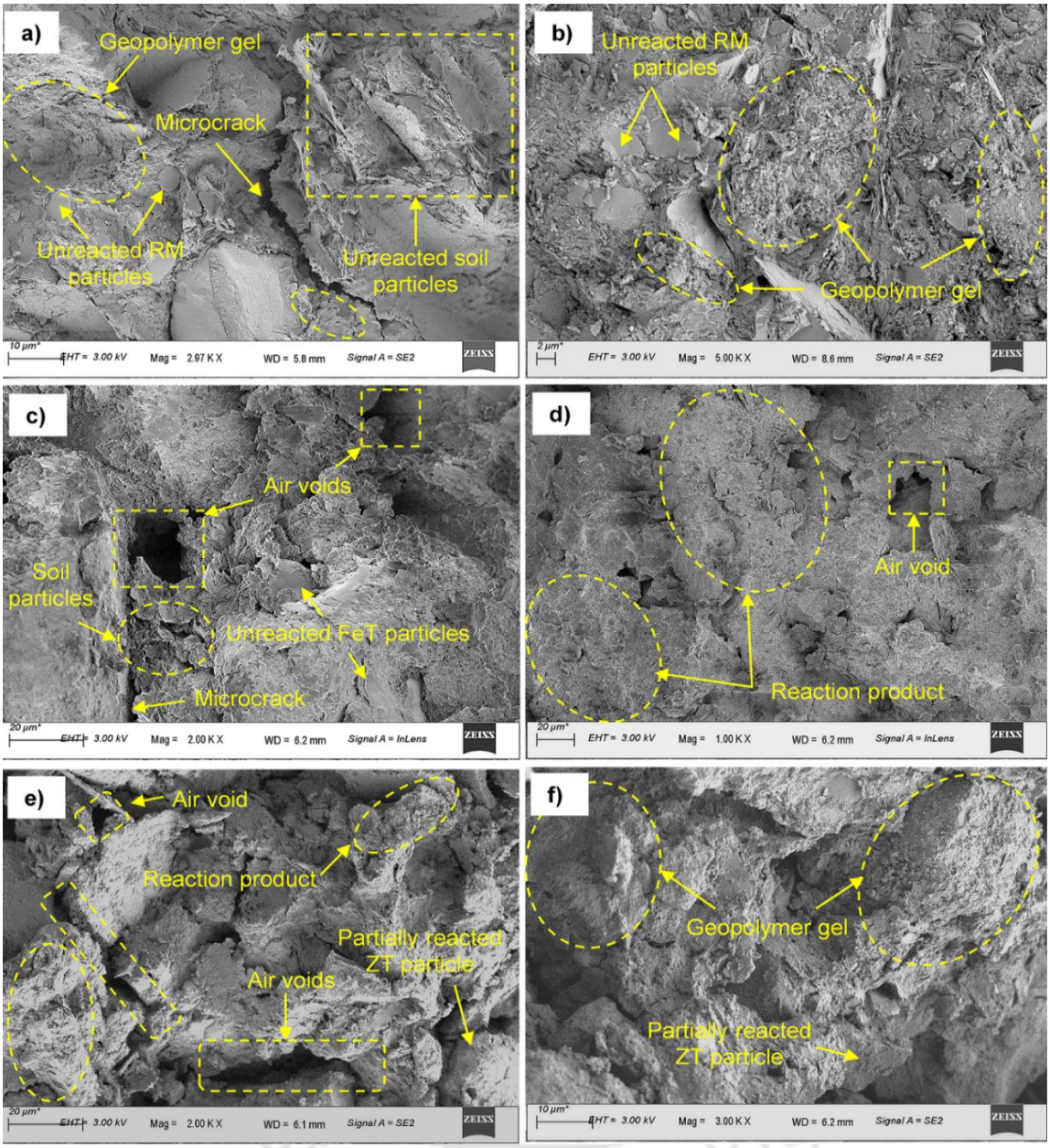

Fig. 5. 10 FESEM images of soil-MT mattrix: a) S+RM (20%)-5M, b) S+RM (20%)-10M, c) S+FeT (10%)-5M, d) S+FeT (10%)-10M, e) S+ZT (10%)-5M and f) S+ZT (10%)-10M

To gain a deeper understanding of the dissolution efficiency of aluminosilicate components, it is essential to analyse elemental composition of the geopolymer matrix through EDS analysis. Figs. 5.11 (a-d) display the results of EDS analysis performed on selected geopolymer specimens which exhibit the highest compressive strength. As shown in Figs. 5.11 (a-d), untreated soil has the least Si/Al ratio (i.e. 1.55) as compared to MT treated soil.

Furthermore, soil amended with RM geopolymer displays the highest Si/Al ratio (1.93) among all geopolymer specimens followed by FeT (Si/Al= 1.73) and ZT (Si/Al= 1.65) stabilized soil. This indicates that the release of Al and Si during the dissolution phase is more pronounced in RM-stabilized soil as compared to soil treated with FeT and ZT-based geopolymers. Furthermore, higher Si/Al ratios predominantly result in the formation of more -Si-O-Si- polymeric chains, which possess greater bond strength compared to -Si-O-Al- bonds formed at lower Si/Al ratios (He et al., 2016). It is worth noting that higher Si/Al and Na/Al ratios signify a more extensive dissolution of aluminosilicates which impart high compressive strength to the geopolymer specimens (due to the formation of more geopolymer gels) (He et al., 2016). Due to this reason, soil stabilized with RM geopolymers exhibits a higher strength improvement compared to FeT and ZT stabilized soil.

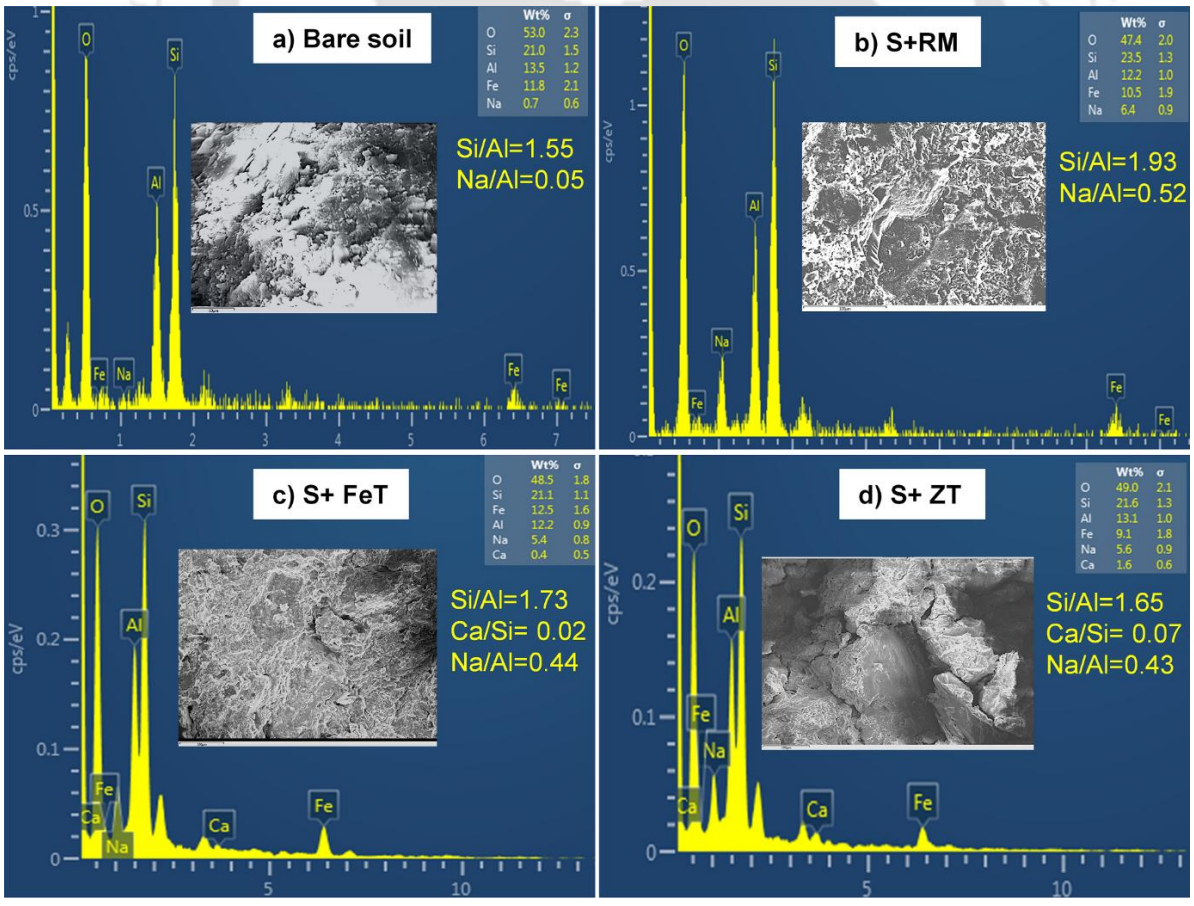

Fig. 5. 11 Results of EDS analysis for soil-MT mixes with highest UCS: a) bare soil b) S+RM (20%)-5M c) S+FeT (10%)-5M, and d) S+FeT (10%)-5M

5.5.3 Durability performance

Figs. 5.12 (a-f) and 5.13 (a-f) show the images of various geopolymer specimens following the completion of 12 alternate wetting-drying cycles. In addition, Figs. 5.14 (a-c) also display the loss of mass (%) recorded for various geopolymer specimens at the end of the durability tests. Irrespective of the MT Type, curing conditions, and activator concentrations, all geopolymer specimens remain structurally intact (after the commencement of durability tests) displaying minimal surface erosion or degradation (see Figs. 5.12a-f and 5.13a-f). On the other hand, specimens of untreated soil disintegrate completely within just 5 minutes of immersion in water during the first wetting cycle. These observations are further corroborated by the loss of mass measured after the conclusion of durability tests. It can be noted from Figs. 5.14 (a-c) that all geopolymer specimens display minimal mass loss during the durability tests. Furthermore, the mass loss in geopolymer specimens is affected by several factors including the types of MT used for soil stabilization, curing conditions and alkali activator concentration. Soil stabilized with RM geopolymers exhibits the highest weathering resistance to 12 alternate wetting and drying cycles followed by FeT and ZT stabilized soil. As evident from Figs. 5.12 (a-c), geopolymer specimens prepared with RM remain completely intact throughout the durability test showing no significant surface erosion. On the other hand, FeT and ZT stabilized specimens show a notable surface degradation indicating a lower resistance to weathering compared to the RM stabilized specimens.

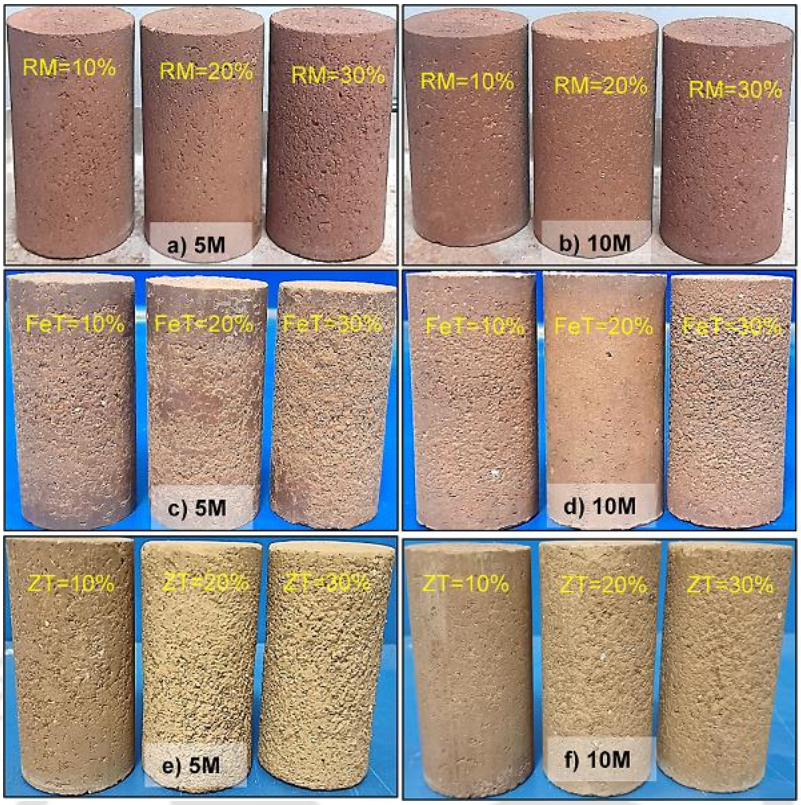

Fig. 5. 12 Images of various specimens cured under AC conditions (for 7 days) after durability tests: a) S+RM-5M, b) S+RM-10M, c) S+FeT-5M, d) S+FeT-10M, e) S+ZT-5M, f) S+ZT-10M

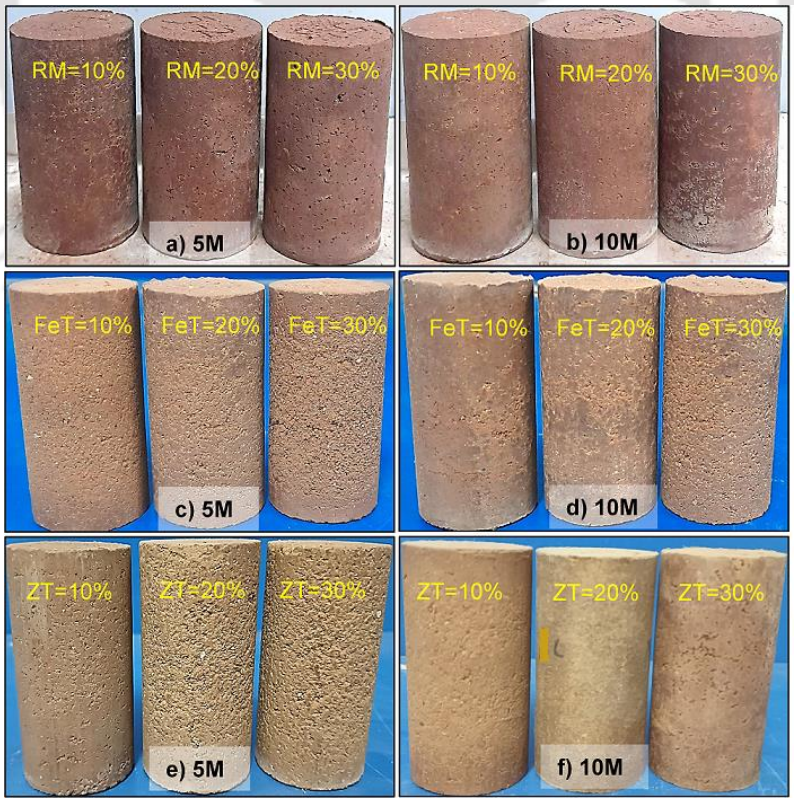

Fig. 5. 13 Images of various specimens cured under DC conditions (for 7 days) after durability tests: a) S+RM-5M, b) S+RM-10M, c) S+FeT-5M, d) S+FeT-10M, e) S+ZT-5M, f) S+ZT-10M

Above observations are further substantiated by examining the mass loss for various geopolymer specimens as illustrated in Figs. 5.14 (a-c). It is evident from Figs. 5.14 (a-c) that regardless of the curing conditions and alkali activator concentration used, RM-stabilized specimens exhibit the lowest mass loss on wetting and drying followed by FeT and ZT-stabilized specimens. Due to the formation of a greater quantity of geopolymer gels in RM-stabilized soil in comparison to FeT and ZT-stabilized soil, a stronger and denser geopolymer matrix is created imparting additional durability to the specimens. Furthermore, it is found that geopolymer specimens kept under DC environment exhibit a far better resistance to weathering and surface erosion (refer to Figs. 5.12a-f) as compared to AC cured specimens (Figs. 5.13a-f). This is because the geopolymer matrix displays a greater strength and structural integrity at elevated temperatures contributing to their enhanced durability.

Regardless of the MT type used and the curing conditions applied, geopolymer specimens made with 10M NaOH solution display significantly lesser surface degradation (Figs. 5.12b, d, f and 5.13b, d, f) and mass loss as compared to those prepared with 5M NaOH (Figs. 5.12a, c, e and 5.13a, c, e). This is due to the reason that the release of Al and Si (during the dissolution phase) is higher at 10M NaOH concentration resulting in the development of more reaction products. These reaction products impart added structural integrity to the soil specimens contributing to the enhanced durability of geopolymer specimens. Nonetheless, the loss of mass for all geopolymer specimens following the durability testing remains well below the prescribed threshold limit of 14% as recommended by IRC: SP-89 (2018) for subgrade material. Overall, it can be concluded that soil stabilized with various MT based geopolymers meets the durability standards specified in IRC: SP-89 (2018) validating its suitability as subgrade material.

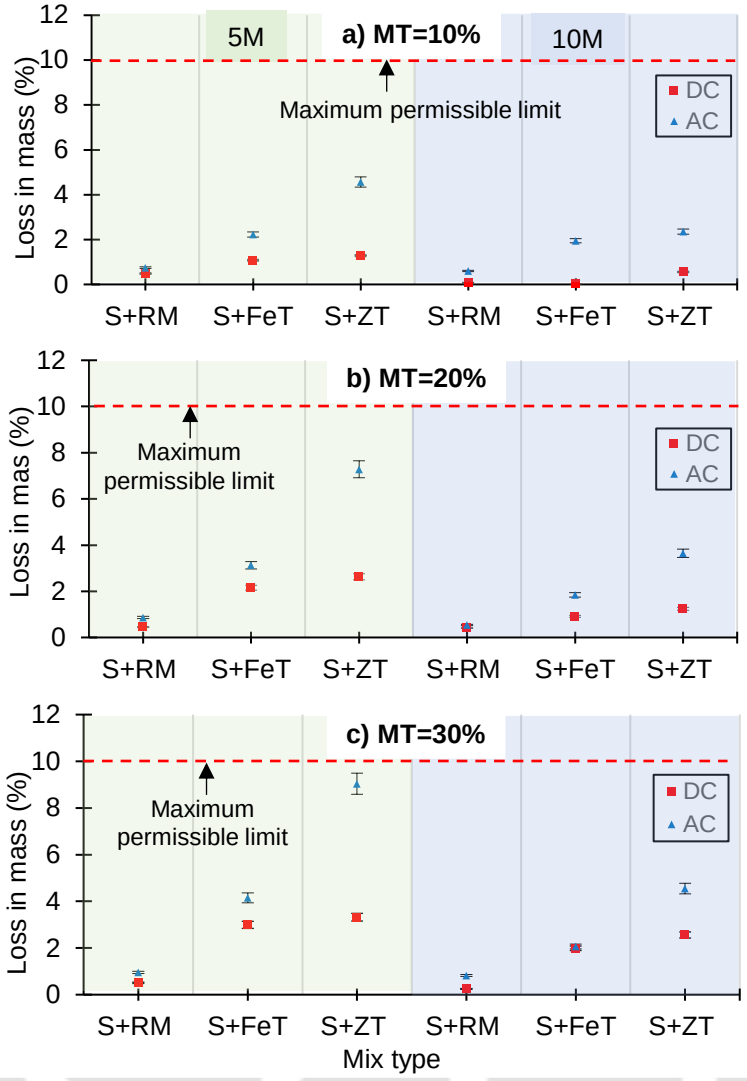

Fig. 5. 14 Loss in mass after 12 alternate cycles of wetting and drying for soil specimens prepared with MT content of a) 10%, b) 20%, and c) 30%

5.5.4 CBR results

Fig. 5.15 displays the results of soaked CBR tests conducted on selected geopolymer specimens having the least compressive strength (i.e. soil amended with 30% MT and 5M NaOH solution) among all soil-MT mixtures. It is evident from Fig. 5.15 that untreated soil has a soaked CBR value of 2.87% which is well below the minimum CBR of 5% as recommended by IRC: SP-72 (2015) for a subgrade material. This indicates that untreated soil has insufficient strength for its use as subgrade material. However, the strength of soil is enhanced significantly when it is stabilized with different MT-based geopolymers. As evident from Fig. 5.15, the soaked

CBR of soil increases from 2.87% to 75.6%, 55.60% and 45.37% when RM, FeT, and ZT-based geopolymers are employed for its stabilization, respectively. These CBR values comfortably exceed the minimum CBR value (5%) specified by IRC: SP-72 (2015) indicating the suitability of MT-stabilized soil for subgrade construction.

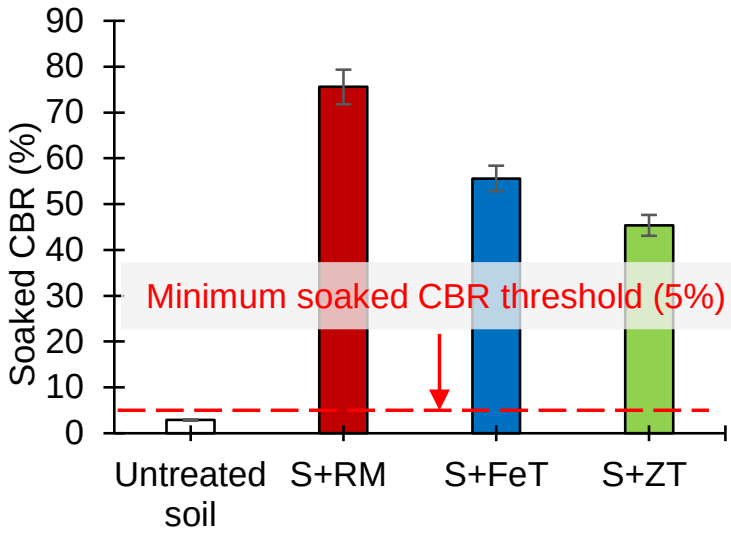

Fig. 5. 15 Results of soaked CBR tests for soil-MT mixes with least UCS value

5.5.5 Permeability test results

Fig. 5.16 presents the coefficient of hydraulic conductivity of soil treated with different MT-based geopolymers. It can be noted from Fig. 5.16 that the hydraulic conductivity of soil decreases from 10^{-7}cm/s to 10^{-9} cm/s (a reduction of two orders of magnitude) with the application of MT-based geopolymers. Moreover, specimens treated with RM-based geopolymers exhibits the least hydraulic conductivity closely followed by the soil treated with FeT and ZT-based geopolymers. The lower hydraulic conductivity of soil stabilized with MT-based geopolymers (as compared to untreated soil) is attributable to the development of geopolymer gels structures during the geopolymerization reaction which effectively plugs the empty void spaces present within the soil matrix (see Fig. 5.17a-b). Apart from filling the air voids, these geopolymer gels also reduce the interconnections between the air voids restricting the flow of water (Onyia et al., 2021).

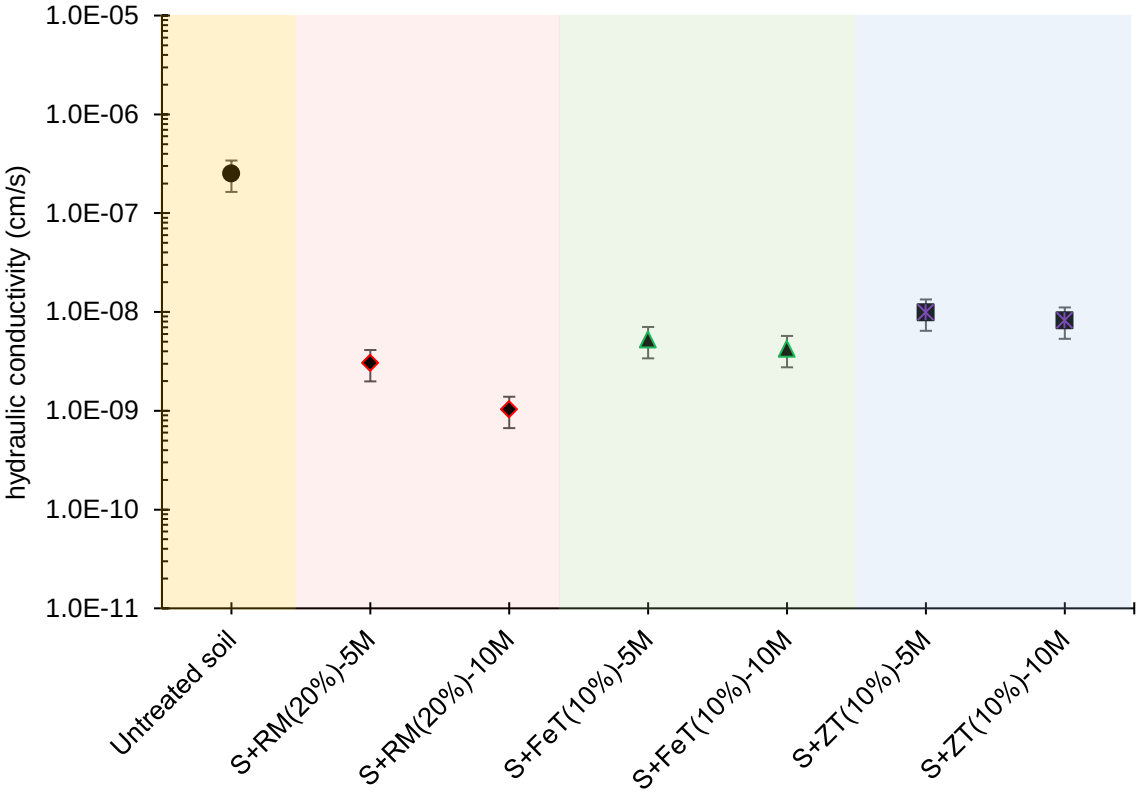

Fig. 5. 16 Hydraulic conductivity of soil treated with different MT- based geopolymers

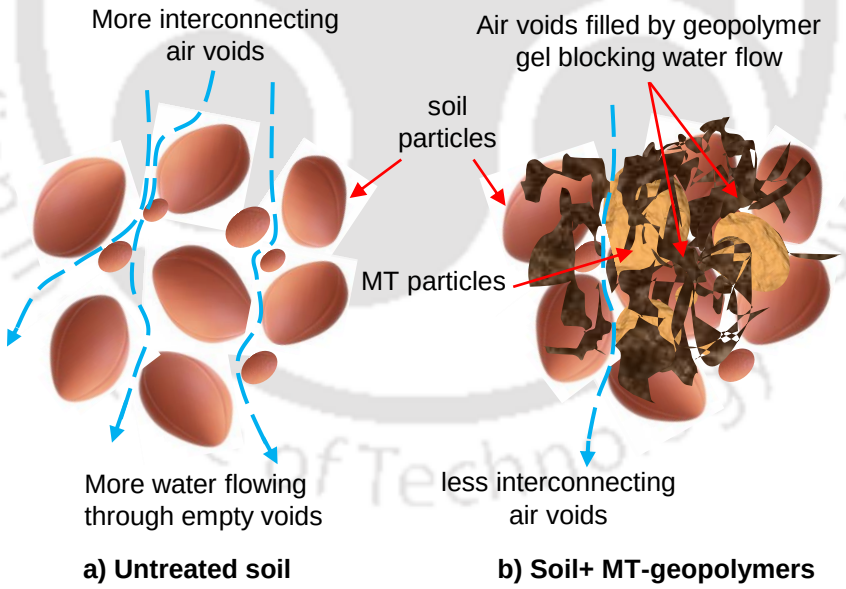

Fig. 5. 17 Illustration showing mechanism controlling the hydraulic conductivity in a) untreated soil b) soil treated with MT-based geopolymers

5.5.6 Toxicity characteristics of geopolymer specimens

Table 5.5 summarises the concentrations of heavy metals leachate determined from the TCLP tests.

Table 5. 5 Toxicity characteristics of alkali activated soil specimens with maximum MT content (i.e. 30%)

Analytes	S+RM (5M) (g/ml)	S+RM (10M) (g/ml)	S+FeT (5M) (g/ml)	S+FeT (10M) (g/ml)	S+ZT (5M) (g/ml)	S+ZT (10M) (g/ml)	USEPA limits for hazardous waste (g/ml)
Zn	0.049	0.058	0.054	0.025	0.583	0.456	25.00
Pb	ND*	0.030	0.030	ND*	0.90	0.740	5.00
Cd	0.013	0.008	0.023	0.010	0.054	0.054	1.00
Cu	0.037	0.000	0.037	0.028	0.010	0.010	25.0
Fe	0.049	0.000	0.121	0.000	0.009	0.006	0.30
Cr	0.312	0.269	0.235	0.209	0.252	0.152	5.00
Ni	0.030	0.000	0.002	0.000	ND*	0.010	25.0
Mn	0.610	0.540	0.790	0.710	1.24	1.06	10.0

*Not detected

It is evident from Table 5.5 that the concentrations of various heavy metals (such as Pd, Cr, Zn, Fe etc.) in the leachate are well below the regulatory limits established by the USEPA. Furthermore, specimens activated with 10M NaOH are noticed to leach a lower concentration of heavy metals (see Table 5.5) in comparison to those prepared with 5M NaOH solution. This indicates that the heavy metals encapsulation capacity of geopolymer specimens is higher at higher alkali activator concentrations. The exposure of aluminosilicate materials to high alkaline conditions during alkali activation results in the creation of various oligomeric and polymeric structures composed of diverse aluminate and silicate species. These structures serve as a crucial catalyst in promoting the sustained progression of polycondensation reactions efficiently capturing and immobilizing various heavy metals through a physical binding

mechanism (Taki et al., 2020). Hence, it can be concluded that the application of MT-based geopolymers in subgrade construction does not pose any environmental risks concerning groundwater contamination due to the leaching of heavy metals. Overall, geopolymers derived from MT not only enhance the strength and durability of soil but also mitigate the potential harm associated with MT by ensuring their safe disposal.

5.6 Summary

In this chapter, the feasibility of three distinct MT i.e., RM, FeT, and ZT as geopolymer binders for their potential use for soil stabilization in road subgrade applications is investigated. A comprehensive series of experiments are performed including UCS tests, CBR tests, FESEM analysis, EDS analysis, alternate wetting and drying tests and TCLP tests to examine the strength, durability and toxicity level of different combinations of soil-MT mixtures. Following conclusions can be drawn from the current study:

- Among all MT, RM is found to be the most efficient geopolymer binder followed by FeT and ZT. In contrast to AC conditions, geopolymer specimens show higher strength improvement under DC conditions due to faster rate of geopolymerization reaction at elevated temperatures. Moreover, a greater strength increase in geopolymer specimens is noticed when the concentration of NaOH solution is increased from 5M to 10M.
- The soaked CBR of soil shows a substantial increase with the utilization of RM, FeT and ZT-based geopolymer binders. Overall, based on the UCS and CBR tests, soil stabilized with different MT-based geopolymers satisfy the minimum strength criteria (i.e. UCS > 0.75 MPa and soaked CBR > 5%) outlined in Indian Road Congress guidelines.
- The durability of soil is significantly enhanced using different MT-based geopolymers. Furthermore, specimens cured in DC conditions exhibit far better weathering resistance to alternate wetting-drying cycles than AC cured specimens. Overall, the mass loss of all

geopolymer specimens meet the minimum durability criteria (i.e. mass loss < 14%) outlined by Indian Road Congress for the subgrade material.

- The hydraulic conductivity of soil is significantly reduced by two orders of magnitude from 10^{-7} cm/s to 10^{-9} cm/s due to the application of MT-based geopolymers. This reduction is attributed to the development of geopolymer gels which effectively plug most air voids leading to the reduced hydraulic conductivity.
- Results of TCLP tests demonstrate that the concentrations of heavy metals in leachate extracted from geopolymer specimens lie within the regulatory limits established by the USEPA.

Chapter 6

Utilization potential of alkali activated MT as paste backfills for underground mine stopes

6.1 General

This chapter presents a comparative study on the utilization potential of three different alkali activated MT viz. RM, FeT, and ZT as paste backfill for underground mine stopes. A series of laboratory experiments are conducted to examine the UCS, flowability, setting and shrinkage characteristics of various alkali activated paste backfills (AAPB). While doing so, the effect of varying water to solid (w/s) ratios, curing period and the alkali activator concentration are investigated. To further improve the strength, shrinkage and setting performance of AAPB mixtures, GBFS is used as a precursor to accelerate the geopolymerization reaction. Finally, an approximate cost analysis is also presented to demonstrate the applicability of various AAPB as an alternative to conventional CPB made from PPC.

6.2 Materials used

6.2.1 RM, FeT, ZT, GBFS and PPC

The materials used in this study include RM, FeT, ZT, GBFS and PPC. Various engineering properties of these materials have been already discussed in detail in section 4.2 of chapter 4 and will not be discussed here again.

6.2.2 Alkali activator

In this study, NaOH in pellet form with a purity of 97% is utilized as an alkali activator. To prepare NaOH solutions, the required mass of NaOH pellets is dissolved in deionized water to achieve the desired concentration. For the current study, the concentrations of NaOH solution are set at 1M and 2M following work by Ouffa et al. (2022). Prepared NaOH solutions are

allowed to cool for at least 24 h to avoid the quick setting of materials during the mixing operation.

6.3 Slurry preparation

In this chapter, 4 types of paste backfill are prepared for each MT (i.e. for RM, FeT and ZT). First set of paste backfills (untreated paste backfill, UPB) are prepared by mixing the oven-dried MT with deionised water (excluding any binder or alkali activator). In the second set, paste backfills are prepared by mixing the dry weight of MT with the alkali activator solution (i.e NaOH solution). Finally, AAPB are prepared by the inclusion of GBFS (10% by weight) to improve the strength and workability of paste backfills. It is important to emphasize that the quantity of GBFS is set at a minimum of 10% to ensure that the maximum amount of MT can be utilized in backfill preparation. To explore the impact of w/s ratios on various properties of paste backfills, slurries are prepared at varying w/s ratios. For RM based paste backfills, the w/s ratios are varied as 0.40 (71% solid content), 0.50 (67% solid content) and 0.60 (62% solid content) while for FeT-derived AAPB the w/s ratios are fixed at 0.30 (77% solid content), 0.35 (74% solid content), and 0.40 (71% solid content). Similarly, the w/s ratios for ZT based paste backfills are set at 0.25, 0.30, and 0.35 which corresponds to a solid content of 80%, 77% and 74% respectively. These ratios are selected based on the preliminary trials performed keeping in mind the workability of slurries required for their conveyance to the underground cavities. The fourth set of paste backfill, which serves as a reference mix (referred to as CPB in this study), is prepared by mixing 10% of PPC with MT. The w/s ratios for CPB prepared from RM, FeT, and ZT are maintained at 0.50, 0.35, and 0.30 respectively in accordance with workability requirements.

6.4 Experimental methodology

6.4.1 UCS tests

To prepare the specimens for UCS testing, the CPB slurry is poured into poly vinyl chloride (PVC) mould of dimensions diameter, d = 35 mm and length, l = 75 mm. Before pouring, the moulds are adequately lubricated with oil, and the lower end is sealed with transparent tape to uphold an undrained condition. During the slurry pouring process, moulds are gently tapped by hand gently to eliminate any entrapped air in the backfill paste. Following this, specimens are cured for 7 days and 28 days in a temperature-controlled room with temperature = 25 ± 2 ˚C and relative humidity = 80 ± 5%. These curing conditions replicate the environmental conditions encountered in underground mine stopes (Yilmaz et al., 2015; Niroshan et al., 2017). Once the curing period is over, the specimens are demoulded from the PVC moulds and trimmed to prepare UCS samples with dimensions of approximately 35 mm in diameter and 70 mm in length, maintaining an aspect ratio (l/d) of 2 (ASTM D2166, 2006). Triplicate specimens are prepared for each mix and the average of three tests is considered as the UCS of paste backfill. The UCS tests are conducted on an automatic machine with maximum load limit of 50 kN at a constant deformation rate of 1.25 mm/minute (Xu et al., 2020). The entire experimental framework followed in the current study is illustrated in Fig. 6.1.

6.4.2 FESEM and EDS analyses

To better understand the microstructural properties of AAPB matrix and to relate these properties with UCS, FESEM studies are done on specimens that have previously undergone through strength testing. In addition, EDS analysis is also performed to identify the phase compositions of reaction products formed during the geopolymerization reaction. Before undergoing FESEM and EDS analysis, the specimens are oven-dried overnight at a temperature of 60 ˚C.

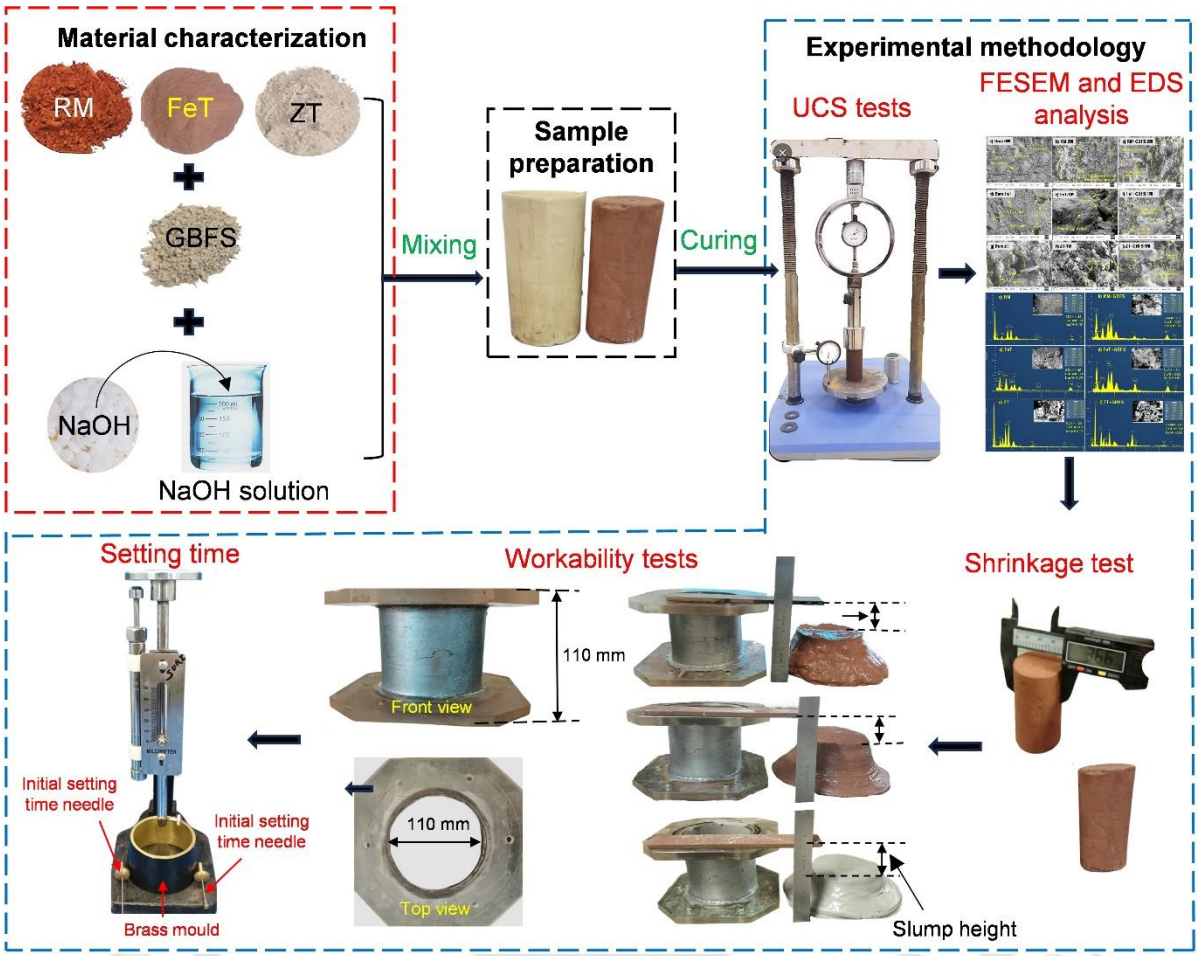

Fig. 6. 1 Experimental framework followed in the current study

6.4.3 Drying shrinkage tests

The specimens for shrinkage tests are prepared following a procedure like that employed for UCS testing. Various paste backfill slurries are poured into PVC moulds (closed at one end) measuring 35 mm in diameter and 75 mm in length (Omidi et al., 1996). While placing the slurry, gentle tapping is applied to the closed end of the mould to eliminate entrapped air within the paste backfill. Subsequently, the prepared specimens are sealed in plastic bags and allowed to cure at room temperature for 24 h to achieve a certain level of hardness. Following this, the specimens are extruded out from the mould and kept for curing for 7 days and 28 days in controlled environment with temperature = 25 ± 2 ˚C and relative humidity = 80 ± 5%. Following the curing period, dimensions of cylindrical specimens are measured using a vernier calliper with a least count 0.01 mm. The diameter measurements are taken at the top, bottom,

and middle portions of the specimens and the average value is recorded as the final diameter of the shrunken specimens. Similarly, the height of the specimens is measured at three points across the diameter and the average value is documented as the final height of the specimen. Finally, the volumetric shrinkage of AAPB specimens at the different stages of curing is calculated using the following expression;

$$Volumetric\ shrinkage, V_s(\%) = \frac{V_i - V_f}{V_i} \times 100 \quad (6.1)$$

Where, V_i = initial volume of specimen = internal volume of PVC mould, V_f = final measured volume of cured specimen.

6.4.4 Slump tests

The workability of cement concrete and MT mixes is generally assessed using a truncated slump cone with dimension of 100 mm (top diameter) × 200 mm (bottom diameter) × 300 mm (height) (ASTM C143, 2020). However, in this study, the workability of AAPB is evaluated utilizing a hollow cylindrical mould with dimensions 110 mm (diameter) × 110 mm (height). This cylindrical mould can accurately reproduce the results of standardized slump cone while minimizing the volume of material required for the experiments (Niroshan et al., 2018; Sadrossadat et al., 2020). To start the experiments, the mould is filled to the brim with freshly prepared paste and the top surface is levelled using a spatula. Following this, the mould is lifted vertically at a gradual pace and the slump height is measured from the top of the cylindrical mould to the midpoint of slumped surface (see Fig. 6.1). To ensure accuracy, a minimum of three sets of experiments are conducted for each mix and the average value is adopted as the slump height. In general, an optimal slump height of around 190 mm, as established by the standardized slump cone, is sought for the efficient conveyance of paste backfills from the surface to underground mine stopes (Xu et al., 2020). This translates to an approximate value

of 40 mm when measured using the corresponding hollow cylindrical mould as proposed by various researchers (Niroshan et al., 2018; Cavusoglu et al., 2021).

6.4.5 Setting time tests

Setting time is the time required by a paste backfill to attain a desired level of stiffness. This time includes both initial setting (IST) and final setting time (FST). In this study, the IST and FST of paste backfills are determined using the Vicat's apparatus in accordance with ASTM C191 (2021). The IST and FST of the paste backfill are determined by gently lowering the IST Vicat needle (with a diameter of 1 mm) and the FST Vicat needle (with an annular collar of 5 mm diameter) onto the surface of the AAPB placed in the Vicat mould. The needles are allowed to penetrate the paste under their own weight. The time interval measured from the point of addition of water (or NaOH solution) to the backfill material until the needle ceases to pierce the paste to a depth of 5 mm from the bottom of the mould, is recorded as the IST. Similarly, the duration from the introduction of water to the moment when the annular collar no longer leaves an impression on the surface of the paste backfill is noted as the FST. The results of setting time tests are discussed in the next section.

6.5 Results and discussion

6.5.1 UCS tests results

Figs. 6.2 (a-c) present the results of UCS tests conducted on various paste backfill specimens prepared from RM, FeT and ZT. It can be noted from Figs. 6.2 (a-c) that irrespective of MT type and w/s ratios, the UCS of UPB prepared from RM, FeT and ZT is significantly enhanced through alkali activation. Among all specimens, paste backfills derived from RM exhibit the highest strength improvement compared to FeT and ZT based paste backfills. To illustrate, the 28-day UCS of UPB prepared with RM is increased from 1.24 MPa to 4.26 MPa through alkali activation using NaOH as an alkali activator. Similarly, the 28-day UCS of UPB derived from

ZT is enhanced from 0.10 MPa to 0.81 MPa using NaOH solution. This increase in UCS can be ascribed to the development of geopolymer gels formed during the alkali activation process which effectively bind the MT particles together enhancing the compressive strength of AAPB derived from RM and ZT. Contrastingly, activation of FeT derived backfills with NaOH solutions does not yield a substantial strength improvement. The reason for this can be attributed to the relatively low proportion of SiO_2, Al_2O_3 and CaO in FeT which are the prime ingredients required for alkali activation. As a result, a lower amount of geopolymer gels is formed during the geopolymerization process owing to the limited availability of SiO_2 and Al_2O_3 which reduces the dissolution of Si and Al ions.

To further improve the UCS of AAPB, GBFS (10% by dry weight) is incorporated into RM, FeT and ZT during the preparation of AAPB specimens. As evident from Figs. 6.2 (b-c), inclusion of GBFS significantly boost the UCS of FeT and ZT derived AAPB. For instance, the 28-day UCS of FeT based AAPB is increased by 167% from 1.05 MPa to 2.80 MPa with the addition of GBFS. Similarly, the UCS of ZT derived AAPB exhibit a remarkable 340% increase from 0.81 MPa to 3.57 MPa with the incorporation of GBFS. The addition of GBFS to MT increases the availability of free SiO_2, Al_2O_3 and CaO promoting the dissolution of Al, Si and Ca during the activation phase. This leads to the formation of a greater number of reaction products contributing to the enhanced compressive strength of the paste backfill specimens. The elucidation of this phenomenon is further supported by FESEM and EDS analyses discussed in subsequent sections. In general, at a specified w/s ratio, the majority of AAPB exhibits higher UCS values when compared to their counterpart CPB prepared with PPC. This implies that AAPB display far better strength performance than CPB making them suitable for mine stopes.

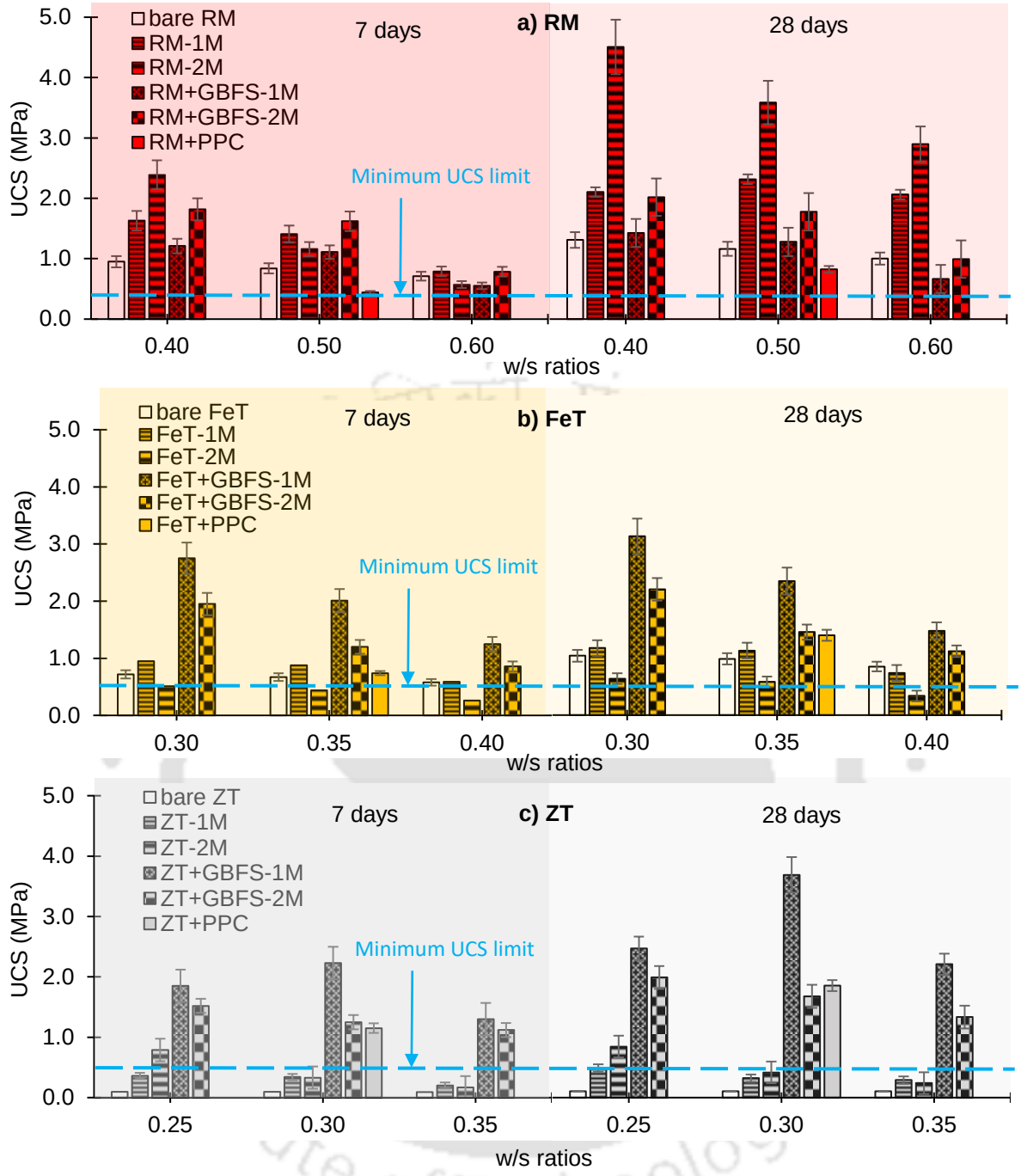

Fig. 6. 2 UCS of various AAPB mixtures with varying w/s ratios a) RM paste backfills, b) FeT paste backfills, and c) ZT paste backfills

a) Effect of w/s ratios

The UCS of AAPB is significantly influenced by the w/s ratio employed in the preparation of paste backfill specimens. It is important to highlight that each MT necessitates a distinct w/s ratio for paste backfill preparation. Among all paste, RM based paste backfills requires the highest water content followed by FeT and ZT based backfills. This higher water demand for

RM is attributed to its greater SSA allowing a larger number of water/activator molecules to adhere to the surface of the RM particles. On the contrary, the SSA of FeT and ZT is significantly lesser as compared to RM resulting in the consumption of a reduced amount of water for slurry preparation. It can be seen from Figs. 6.2 (a-c) that irrespective of alkali activator concentration, the UCS of AAPB experiences a notable decrease increasing w/s ratios. For instance, RM based AAPB exhibit the highest UCS of 4.26 MPa at w/s = 0.40 which decreases to 3.39 MPa and 2.74 MPa at w/s ratios of 0.50 and 0.60 respectively (refer to Fig. 6.2a). Similarly, the peak compressive strength in FeT derived AAPB is achieved at w/s = 0.30 which reduces as the w/s ratio is raised to 0.35 and 0.40 (refer to Fig. 6.2b). At low w/s ratios (i.e high solid content), paste backfill contains a higher quantity of MT particles with fewer pore spaces. These voids are effectively occupied by the reaction products formed during the geopolymerization reactions fostering the bonds between MT particles (see Fig. 6.3a) (Yin et al., 2012; Li et al., 2020; Hou et al., 2022). Consequently, this results in a dense and compact structure of the paste backfill, contributing to elevated mechanical strength. In contrast, a greater number of pores exist within the paste backfill matrix at high w/s ratios (i.e. less solid content) which reaction products fail to plug completely resulting in reduced compressive strength (Hou et al., 2022). It's worth noting that in case of AAPB prepared from ZT+GBFS, a higher UCS is observed at w/s = 0.30 instead of w/s = 0.25. This discrepancy is attributed to the fact that the NaOH solution corresponding to w/s = 0.25 is insufficient to dissolve SiO_2 and Al_2O_3 leading to the formation of fewer reaction products which fails to effectively fill the pore spaces within the paste backfill. Conversely, the higher UCS of ZT+GBFS AAPB at w/s = 0.30 can be attributed to the formation of a higher quantity of reaction products which bind the solid particles together and effectively plug the pore spaces (refer to Fig. 6.3b).

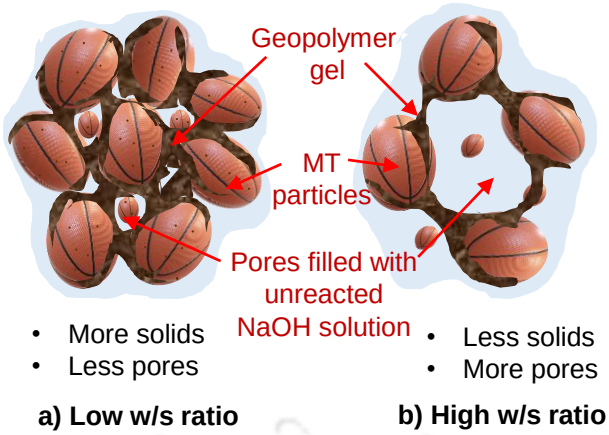

Fig. 6. 3 Arrangement of solid particles in AAPB at a) low w/s ratio, and b) high w/s ratio

b) Effect of alkali activator concentration

At a given w/s ratio, the UCS of RM derived AAPB increases as the concentration of NaOH solution increases from 1M to 2M (see Fig. 6.2a). The increase in NaOH concentration facilitates a more extensive dissolution of SiO_2 and Al_2O_3 within RM resulting in the formation of additional geopolymer gel structures. These gel structures adeptly fill the pores and densify the paste backfill matrix contributing to enhanced UCS values. However, the UCS of AAPB prepared with FeT and ZT decreases as the concentration of NaOH solution is increased from 1M to 2M (see Figs. 6.2b-c). Since the combined proportion of SiO_2 and Al_2O_3 in FeT and ZT is substantially lower than in RM, a low concentration of NaOH (i.e. 1M) is sufficient to liberate the majority of Si and Al ions. The use of a higher concentration of NaOH solution leaves unreacted NaOH behind, which adversely affects the UCS. Additionally, the heightened alkalinity of the 2M NaOH solution facilitates the rapid dissolution of aluminosilicates, leading to the prompt formation of corresponding geopolymer gels. These reaction products stick to the surface of unreacted MT (or GBFS) particles hindering the further dissolution of aluminosilicates (Tuyan et al., 2018). Moreover, the excess Na^+ ions induce brittleness to the geopolymer matrix which have a detrimental impact on the quality of binding products and consequently on the compressive strength (Bonder et al., 2011).

6.5.2 FESEM and EDS results

Figs. 6.4 (a-j) display the FESEM images of various paste backfills prepared from RM, FeT, and ZT following a 28-day curing period. It can be noted from Figs. 6.4 (a, d, g), the solid particles in all UPB are visibly loosely arranged contributing to their lower UCS. However, in the case of AAPB, some of these air voids are filled by the geopolymer gels formed during the reaction of NaOH with the aluminosilicate source (i.e., RM, FeT, and ZT) as illustrated in Figs. 6.4 (b, e, h). Moreover, with the addition of GBFS, a coexistence of C-A-S-H and N-A-S-H gel structures is observed effectively plugging most air voids within the paste backfill matrix (refer to Figs. 6.4c, f, i). This results in the development of a compact and dense structural framework within the matrix of paste backfills contributing to the higher compressive strength of AAPB prepared with GBFS.

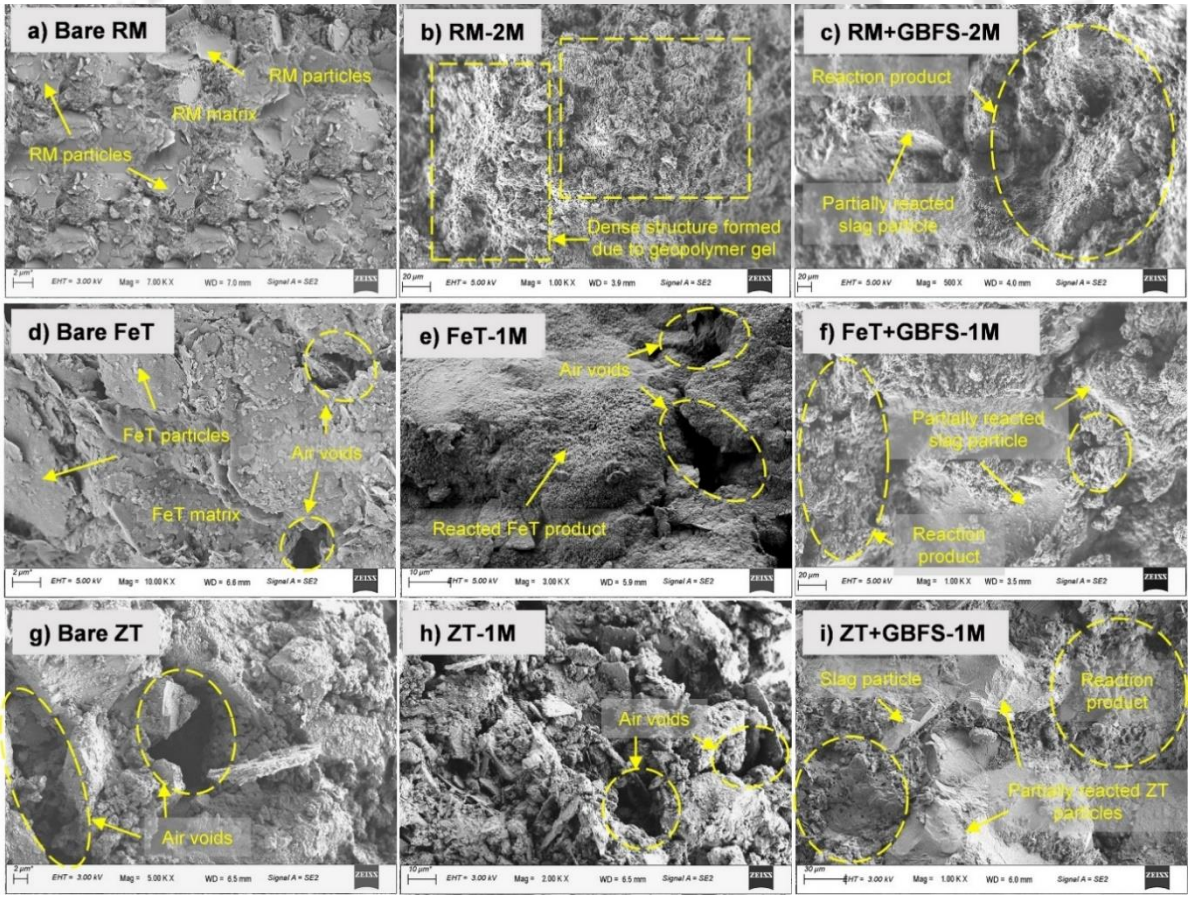

Fig. 6. 4 Microscopic images of AAPB mixtures after 28 days of curing a) bare RM, b) RM-2M, c) RM+GBFS-2M, d) bare FeT, e) FeT-1M, f) FeT+GBFS-1M, g) bare ZT, h) ZT-1M, and i) ZT+GBFS-1M

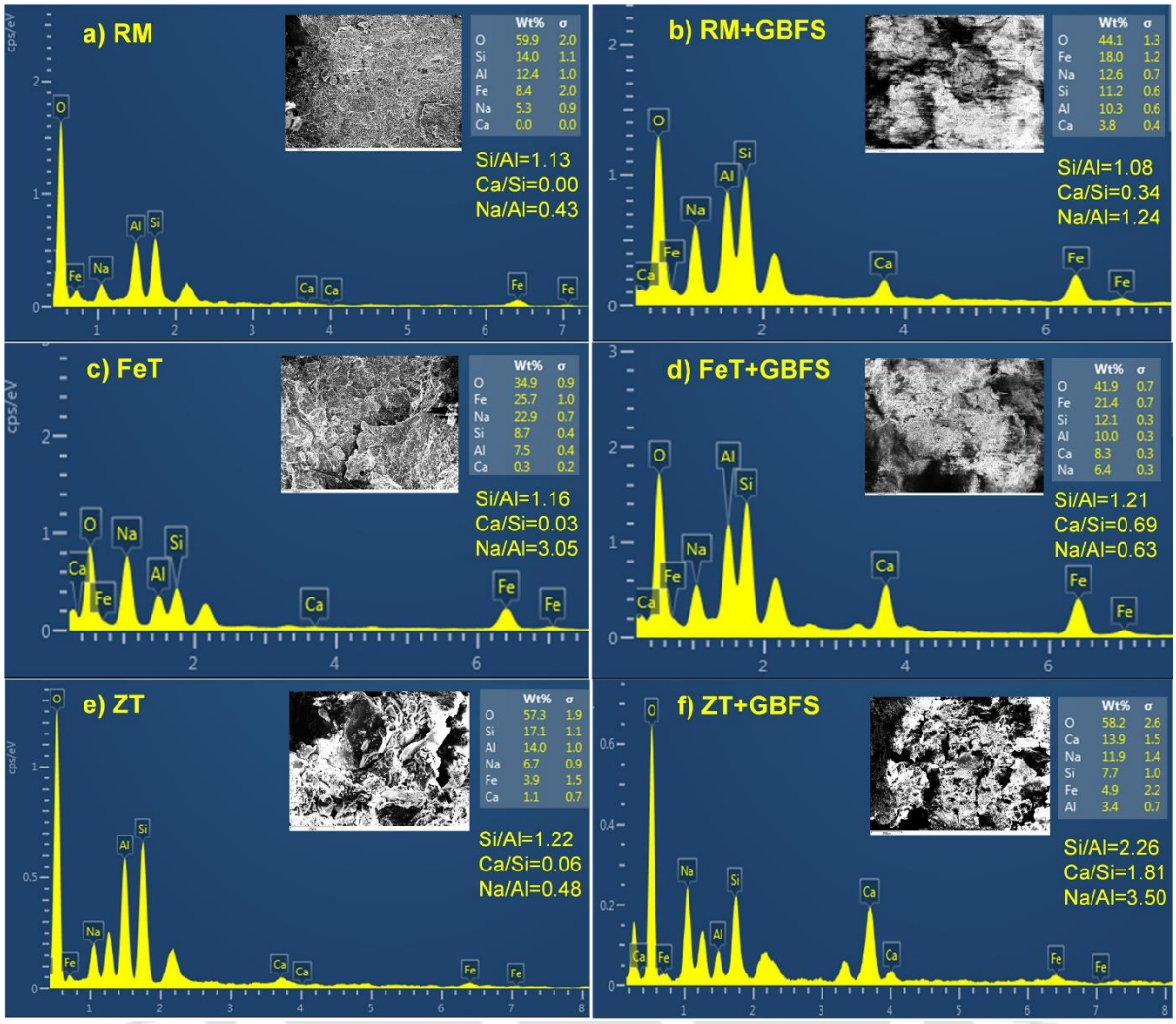

Fig. 6. 5 Results of EDS analysis for different AAPB mixtures after 28 days of curing a) RM, b) RM+ GBFS, c) FeT, d) FeT+ GBFS, e) ZT, f) ZT+GBFS

The efficacy of geopolymerization is highly dependent on the effectiveness of SiO_2 and Al_2O_3 dissolution which can be analysed through EDS analysis. Figs. 6.5 (a-e) present the results of EDS analysis performed on AAPB specimens which display the highest strength improvement. Generally, the compressive strength of the geopolymer matrix tends to increase with higher Si/Al, Ca/Si, and Na/Al ratios (Yaghoubi et al., 2018; Singh et al., 2023). This is attributed to the fact that a larger number of -Si-O-Si bonds are established at higher Si/Al, which are considerably stronger than the -Si-O-Al- bonds formed at lower Si/Al (He et al., 2016). It can be noted from Figs. 6.5 (a-b) that Si/Al is higher for RM based AAAPB in comparison to RM+GBFS paste backfill indicating a higher dissolution of SiO_2 and Al_2O_3

which contributes to their higher UCS values. However, it's noteworthy that although the Ca/Si ratio in RM+GBFS paste backfill is higher than in RM based AAPB, it also exhibits an excessively high Na/Al ratio, signifying non-reactive NaOH that adversely affects the compressive strength of specimens (Singh et al., 2023). On the other hand, both Si/Al and Ca/Si ratios are significantly higher in FeT+GBFS and ZT+GBFS paste backfills indicating a greater dissolution of SiO_2 and Al_2O_3. This leads to the greater formation of geopolymer gel structures during the dissolution process contributing to the higher UCS of FeT+GBFS and ZT+GBFS backfills compared to FeT and ZT based AAPB (as indicated by Figs. 6.2b-c).

6.5.3 Shrinkage results

Figs. 6.6 (a-c) display the V_s observed in various paste backfills. It is evident from these figures that at a given w/s ratio and curing period, the V_s in all UPB specimens is significantly reduced by alkali activation. For instance, at w/s =0.40, the V_s of paste backfills (after 28 days curing) prepared from RM reduces from 60.43% to 20.53% when activated with NaOH solution. Similar trends are also observed in paste backfills derived from FeT and ZT, where a notable decrease in void ratios is noted when NaOH solution is employed in the preparation of the paste backfill. Furthermore, irrespective of the MT type and w/s ratio, all AAPB specimens prepared with 1M NaOH solution consistently exhibit higher V_s in comparison to those prepared with 2M NaOH solutions. This is because addition of NaOH reduces the surface tension of pore solution and act as a shrinkage reducing admixture. As a result, capillary pressure is reduced which inhibit the contraction of solid particles during the drying process leading to lower V_s (Scherer et al., 2015). Furthermore, the V_s of all paste backfill specimens increases with an increase in the w/s ratio. This is due to the reason that a higher loss of water takes place at higher w/s ratio due to the increased availability of water for evaporation which reduces the volume of specimens upon drying/curing process.

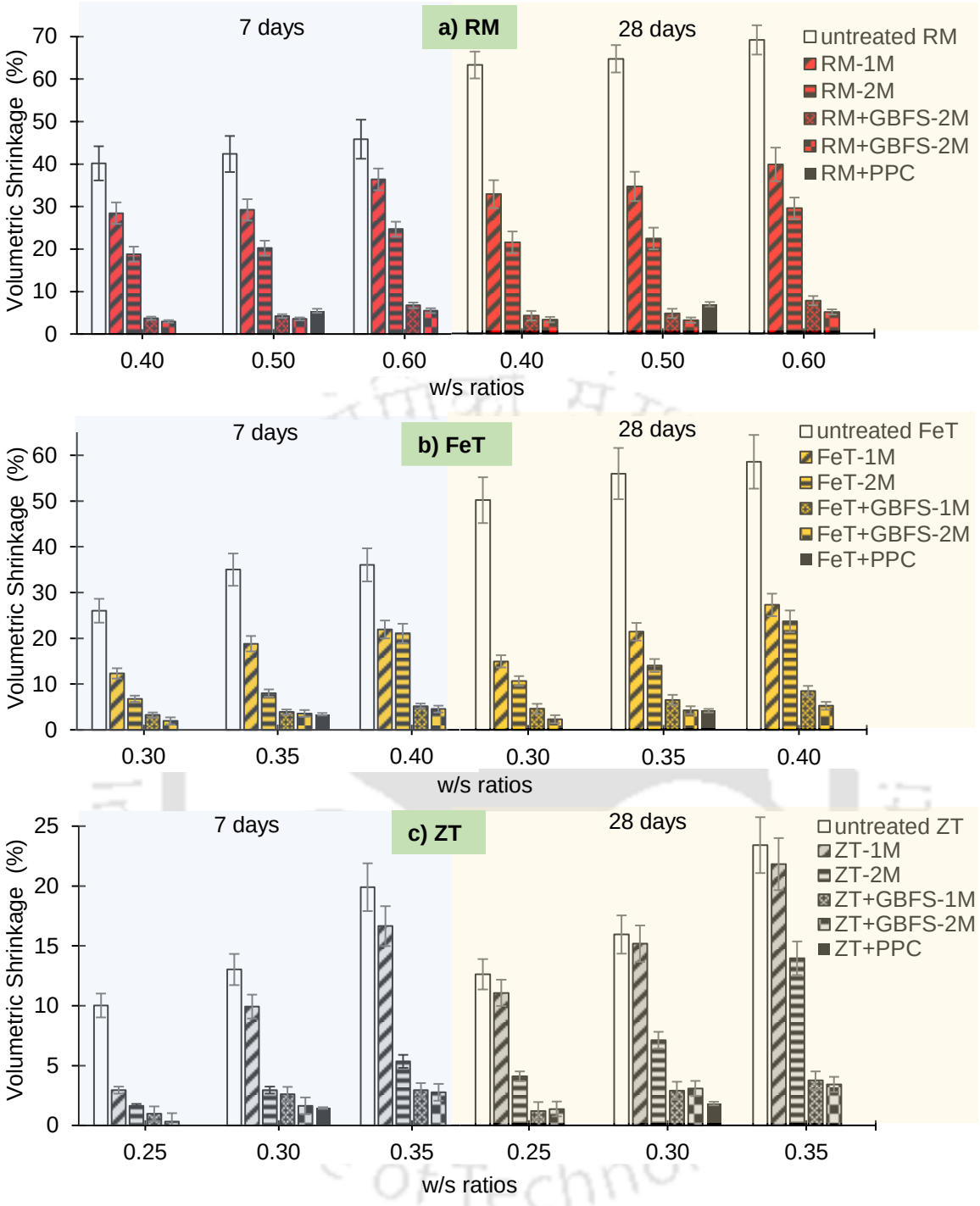

Fig. 6. 6 Volumetric shrinkage measured at different stages of curing a) RM paste backfills b) FeT paste backfills and c) ZT paste backfills

It can be further noticed from Figs. 6.6 (a-c) that the V_s of various paste backfills is significantly reduced by the addition of GBFS. The addition of GBFS results in the formation of additional C-A-S-H and C-S-H gel which effectively fills the majority of capillary pores. This transforms the existing macropores within the paste backfill matrix into mesopores

thereby decreasing capillary pressure and ultimately reducing the drying shrinkage (Yusuf et al., 2014; Scherer et al., 2015). Overall, the V_s of paste backfills derived from RM, FeT and ZT decreases from 60.43% to 3.11%, 49.35% to 2.29% and 12.03% to 1.31%, respectively by the use of GBFS and NaOH solution. The higher V_s in RM paste backfills can be attributed to the higher water content employed in their preparation resulting in a greater loss of water through evaporation. Furthermore, RM contains higher fine fraction (i.e. particle size < 0.002 mm) than FeT and ZT which contributes to higher capillary pressure causing more V_s in paste backfill specimens. It is important to highlight that all AAPB prepared with GBFS show comparable or even lesser V_s shrinkage compared to their CPB counterparts as evident from Figs. 6.6 (a-c). This indicates that AAPB amended with GBFS exhibit satisfactory shrinkage performance making them a viable substitute for CPB.

6.5.4 Slump tests

Figs. 6.7 (a-c) display the results of slump test performed on various AAPB. It is evident from these figures that the workability of paste backfills is significantly influenced by w/s ratio, MT type, and alkali activator concentration. Irrespective of the MT type and alkali activator concentrations, the workability of AAPB increases with an increase in w/s ratio. For instance, the slump height for RM derived AAPB (prepared with 1M NaOH) exhibit an 87% increase from 41 mm to 77 mm as the w/s ratio is increased from 0.40 to 0.60. On a similar note, the workability of FeT and ZT based AAPB increases from 43 mm to 76 mm and 40 mm to 95 mm as the w/s ratio changes from 0.30 to 0.40 and 0.25 to 0.35 respectively. A higher water content implies a lower concentration of solids within the paste backfill indicating a greater interparticle distance (Jiang et al., 2019). This allows the solid particles to slide more easily past one another during shearing as the interparticle friction is reduced due to the presence of water acting as a lubricant between the solid particles. Furthermore, regardless of the MT type, the workability of paste backfills is significantly influenced by the concentrations of NaOH

solution employed for their preparation. Paste backfill prepared with 2M NaOH are found to exhibit higher workability in comparison to those prepared with 1M NaOH solution. This is because NaOH solution exhibits a greater lubrication effect at higher concentrations which not only facilitate the readjustment of solid particles during shearing but also impart a more dispersive nature to the paste (Jiang et al., 2019).

At a given w/s ratio and alkali activator concentration, paste backfills prepared from RM exhibit the lowest slump value compared to those prepared from FeT and ZT. Given that the water adsorption capacity of RM is the highest among all MT (as evidenced by water holding values), a larger quantity of water is needed to adequately lubricate the RM particles. Additionally, the higher clay fraction in RM leads to an increased number of collisions and frictional resistance between the tailings particles reducing the workability of paste backfills (Ke et al., 2015). On the other hand, ZT has a lower fine fraction and higher coarser fraction than other MT which contributes to higher workability of ZT derived paste backfills. Another potential factor contributing to the higher workability of ZT-derived paste backfills can be attributed to the morphology of ZT particles. ZT particles possess a 3D cuboidal structure (refer to Fig. 6.7c) allowing them to easily roll down through each other during shearing. On the contrary, the irregular and flaky nature of RM and FeT particles (refer to Figs. 6.7b-c) impart higher frictional resistance during shearing reducing the flowability of paste backfills. Overall, the workability of all AAPB exceeds the minimum value of 39 mm (corresponding to 190 mm determined from standard slump cone) (Xu et al., 2020; Jiang et al., 2023). However, it is advisable to use paste backfill with sufficiently high workability/flowability in mine backfilling to minimize the overall cost of pumping.

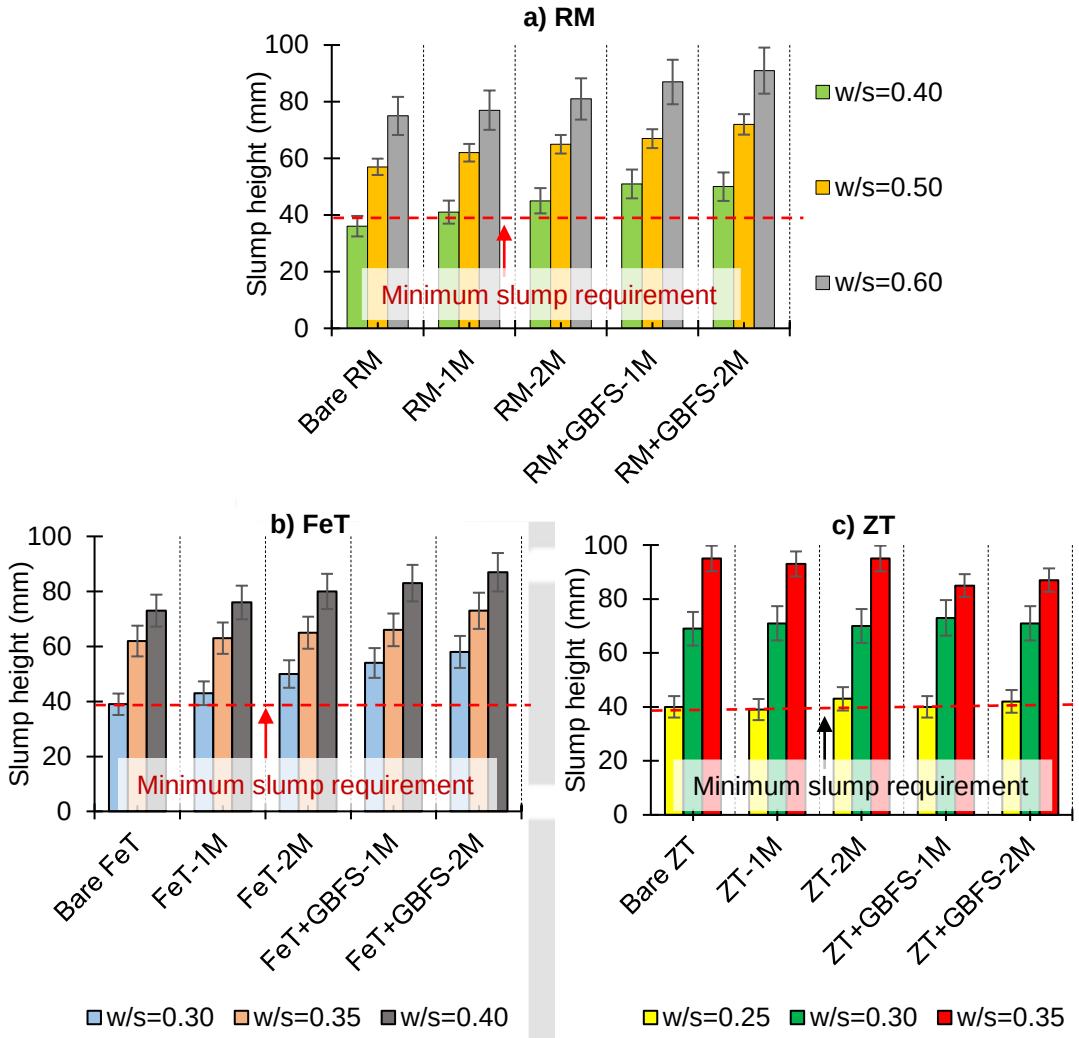

Fig. 6. 7 Measured slump height for a) RM AAPB, b) FeT AAPB, and c) ZT AAPB

6.5.5 Setting test results

Figs. 6.8 (a-b) display the setting time (both IST and FST) observed for various paste backfills. It can be noted from Figs. 6.8 (a-b) that the addition of GBFS results in a substantial decrease in the setting time of AAPB. For instance, IST of RM derived AAPB prepared with 2M NaOH (at w/s = 0.40) is reduced from 267 h to 11 h with the addition of 10% GBFS. Similarly, the IST of FeT and ZT derived AAPB (at w/s = 0.30) decreases from 151 h to 5 h and 14 h to 1.5 h, respectively when GBFS is introduced to the paste backfill. Similar trends are also observed in the context of FST of AAPB, where a substantial reduction in FST is noted with the inclusion of GBFS (refer to Fig. 6.8b). This reduction in setting time can be attributed to the high CaO content present in GBFS which plays a crucial role in controlling the setting properties of paste

backfills. The presence of Ca^{+2} enhances the rate of liberation of free Si and Al ions (due to the increased alkalinity) resulting in the rapid formation of C-A-S-H gels (Nath and Sarker, 2014; Cao et al., 2018). It is widely acknowledged that C-A-S-H structures condense at a faster rate compared to N-A-S-H gel contributing to the early setting of paste backfills prepared with GBFS (Nath and Sarker, 2014; Chen et al., 2018).

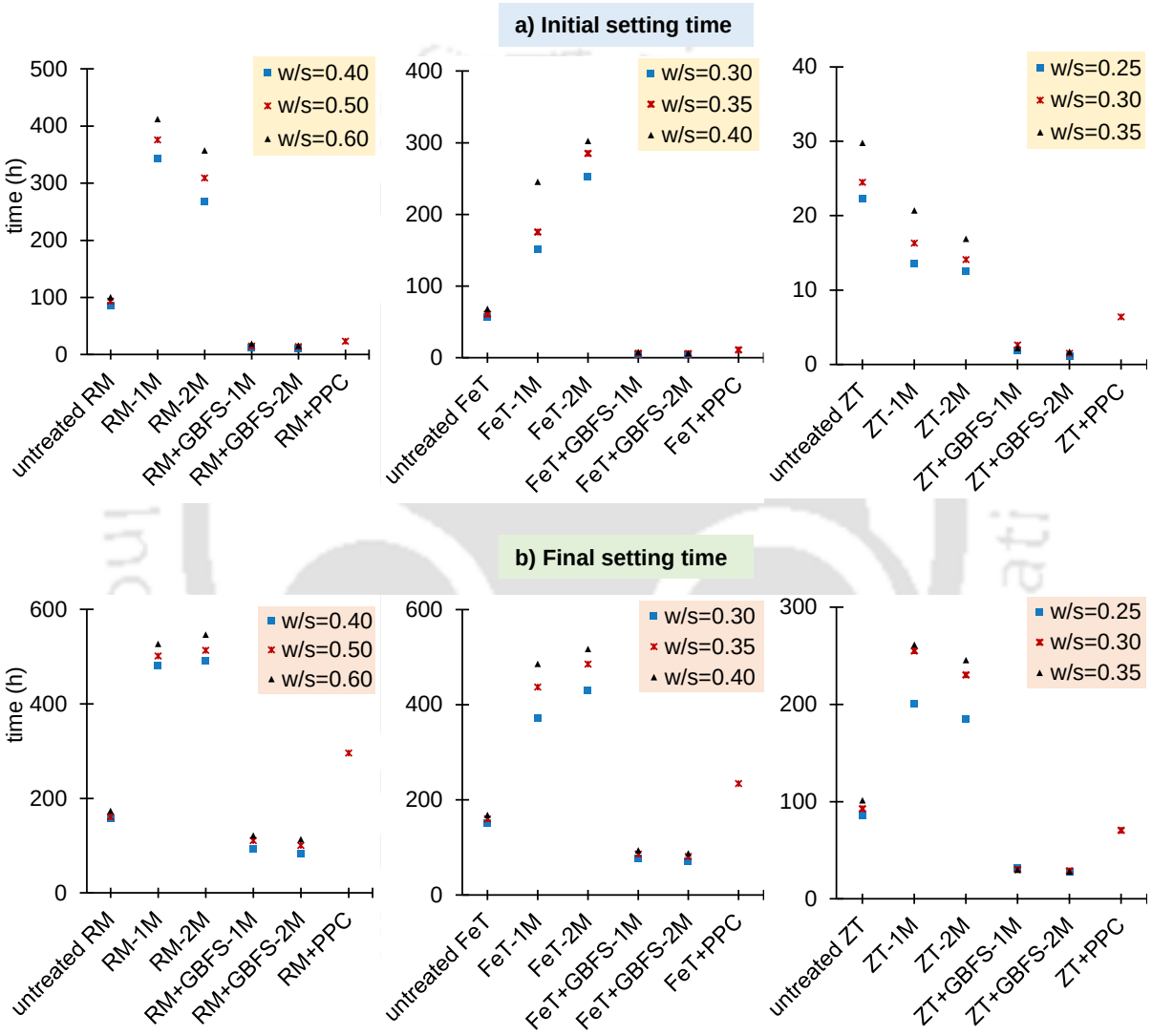

Fig. 6. 8 Setting time for various AAPB mixtures a) IST, and b) FST

Overall, ZT+GBFS AAPB exhibits the shortest IST (1.1 h) and FST (27.5 h) among all paste backfills while RM+GBFS AAPB displays the longest IST (11 h) and FST (83.5 h). The presence of notable CaO content in ZT (as evident from XRF results) increases the overall CaO fraction in ZT+GBFS paste backfills. As highlighted earlier, a higher CaO accelerates the rate

of geopolymerization reaction contributing to the rapid hardening of paste backfills. It is important to observe that all AAPB amended with GBFS display lower IST and FST compared to their CPB counterparts made from PPC (refer to Figs. 6.8a-b), indicating their superior setting performance. Typically, an IST ranging from 2.5 h to 3 h is considered suitable for mine backfilling operation with high production rates (Cavusoglu, 2021). In this study, only ZT+GBFS could satisfy the IST criteria making it suitable for mines with a need for faster metal extraction rates. In case of RM and FeT based AAPB, the addition of appropriate admixtures is necessary to further reduce the IST and FST before being implemented at mine site with high production rates. Nevertheless, these pastes can find application in mine sites where metal extraction occurs at a slower pace and there is no urgent need for rapid filling of mine stopes.

6.6 Cost analysis

The AAPB employed for the mine backfilling should have economic advantages compared to CPB prepared with PPC. To assess the cost-effectiveness of AAPB in comparison to traditional CPB, the total cost incurred in preparing one ton of paste backfill is calculated. The total cost for AAPB includes the expenses for NaOH, the processing costs involved in the preparation of NaOH solution, and the transportation cost. The costs of NaOH and PPC are considered based on the prevailing market prices, while the processing and transportation costs are obtained from Yang et al. (2022). Table 6.1 summarizes the total cost incurred in the preparation of various AAPB and traditional CPB. The findings from Table 6.1 indicate that the maximum production costs for AAPB prepared from RM, FeT, and ZT are ₹ 1120, 880, and 820, respectively, whereas the production cost of PPC-derived CPB is calculated as ₹ 900. This implies that irrespective of w/s ratio, AAPB prepared from FeT and ZT are economical advantageous compared to conventional CPB which can reduce the overall cost of mine backfilling. On the

other hand, only the RM derived AAPB prepared with w/s = 0.40 are found to be economical for mine backfilling.

Table 6.2 provides a summary of the design criteria adhered to by various paste backfills taking into account their strength, shrinkage, workability, setting, and cost characteristics. It can be inferred from Table 6.2 that FeT+GBFS and ZT+GBFS paste backfills meet all the design criteria required for mine backfilling. In contrary, RM-derived AAPB only satisfies the strength, shrinkage, and workability criteria, falling short on the setting and cost criteria. Therefore, the addition of suitable rapid-setting admixtures or extra GBFS may be necessary for RM-derived AAPB to meet the setting and cost requirements for mine backfilling.

Table 6. 1 Total estimated cost consumed by various AAPB per ton of paste

AAPB type	**w/s ratio**	**Material cost/ton, ₹ (NaOH/cement)**	**Transportation cost/ton (₹)**	**Processing cost/ton (₹)**	**Total cost/ton (₹)**
RM/RM+GBFS	0.40	480	100	300	880
RM/RM+GBFS	0.50	600	100	300	1000
RM/RM+GBFS	0.60	720	100	300	1120
FeT/FeT+GBFS	0.30	360	100	300	760
FeT/FeT+GBFS	0.35	420	100	300	820
FeT/FeT+GBFS	0.40	480	100	300	880
ZT/ZT+GBFS	0.25	300	100	300	700
ZT/ZT+GBFS	0.30	360	100	300	760
ZT/ZT+GBFS	0.35	420	100	300	820
CPB	**-**	**800**	**100**	**0**	**900**

Table 6. 2 Summary of AAPB satisfying various design criteria required for mine backfilling

AAPB	w/s ratio	UCS criteria	Shrinkage criteria	Workability criteria	Setting criteria	Cost criteria
RM	0.40	✓	×	✓	×	✓
	0.50	✓	×	✓	×	×
	0.60	✓	×	✓	×	×
RM+GBFS	0.40	✓	✓	✓	×	✓
	0.50	✓	✓	✓	×	×
	0.60	✓	×	✓	×	×
FeT	0.30	✓	×	✓	×	✓
	0.35	✓	×	✓	×	✓
	0.40	✓	×	✓	×	✓
FeT+GBFS	0.30	✓	✓	✓	✓	✓
	0.35	✓	✓	✓	✓	✓
	0.40	✓	×	✓	✓	✓
ZT	0.25	×	✓	✓	×	✓
	0.30	×	×	✓	×	✓
	0.35	×	×	✓	×	✓
ZT+GBFS	0.25	✓	✓	✓	✓	✓
	0.30	✓	✓	✓	✓	✓
	0.35	✓	✓	✓	✓	✓

6.7 Summary

This chapter explores the utilization of three different MT i.e. RM, FeT and ZT as paste backfill by the use of alkali activation technique. A series of laboratory experiments are performed to examine the strength, shrinkage, flowability, and setting characteristics of AAPB derived from various MT materials. While doing so, the effect of w/s ratios and the alkali activator concentrations is also investigated. Following major conclusion are drawn from the current study:

- Compressive strength of UPB is significantly enhanced through alkali activation. Of all AAPB, paste backfills derived from RM exhibit the highest 28-day UCS followed by the FeT and ZT derived AAPB. Furthermore, higher UCS is achieved under lower w/s ratio compared to higher w/s ratio. Moreover, the introduction of GBFS leads to a noteworthy enhancement in the 28-day UCS of AAPB attributed to the coexistence of both C-A-S-H and N-A-S-H gel structures, providing additional strength to the paste backfill.
- Regardless of the AAPB type and w/s ratio, the V_s of paste backfills is substantially reduced by the use of GBFS. Inclusion of GBFS to paste backfills facilitates the formation of a higher quantity of geopolymer gels which reduces the capillary pores within the paste backfill. This in turn reduces the magnitude of capillary pressure resulting in the decreased contraction of solid particles.
- Among all paste backfills, AAPB prepared from ZT exhibit the highest flowability followed by those prepared from FeT and RM. In addition, higher w/s ratios result in an increased workability of AAPB which is attributed to the enhanced lubrication of tailings particles. In general, all AAPB fulfil the minimum workability criteria necessary for the pipe transportation of paste backfills to mine stopes.
- Of all paste backfills, ZT derived AAPB display the shortest IST and FST followed by FeT and RM derived AAPB. Furthermore, the addition of GBFS significantly reduces the IST and FST of AAPB. The notable presence of CaO in GBFS facilitates the formation of C-A-S-H gel which is responsible for the rapid hardening of GBFS amended AAPB.
- In general, the majority of the AAPB examined in the current work display comparable or even better strength, shrinkage, and setting performance compared to their CPB counterparts prepared with PPC. This implies that AAPB derived from RM, FeT and ZT can serve as a viable alternative to conventional CPB for backfilling the underground mine cavities.

Chapter 7

Conclusions, limitations, and future scope of current study

7.1 Conclusions

Following major conclusions are drawn from the current thesis:

- Stability of TP is significantly influenced by the rate at which its embankments are raised during height raising operations. Higher embankment raising rates results in the development of higher EPWP, particularly beneath the raised embankment, which reduces the overall stability of TP.
- The strength of MT can be significantly improved through alkali activation for their use as TP embankment material. For instance, the 28-day UCS of untreated RM, FeT, and ZT is significantly enhanced from 1.49 MPa to 10.55 MPa, 1.15 MPa to 2.65 MPa, and 0.07 MPa to 4.24 MPa respectively through alkali activation. Similarly, the c of untreated RM, FeT, and ZT is increased by 25 times, 16 times, and 33 times respectively, while the ϕ of untreated RM, FeT, and ZT displays increases of 3 times, 3 times, and 3.8 times, respectively following alkali activation.
- The durability of raw RM, ZT, and FeT is considerably enhanced following alkali activation with the percentage loss in mass after 12 cycles of alternate wetting and drying reducing from 100% to 3.02%, 2.01%, and 1.62% respectively.
- Furthermore, the strength and durability of MT specimens are significantly influenced by the concentration of alkali activator and the curing conditions utilized. Raising NaOH concentrations and elevating curing temperatures increases the efficacy of geopolymerization reaction thereby enhancing the strength and durability of MT specimens.

- Based on strength, durability, and permeability criteria, alkali-activated RM is found to be the most suitable material for TP embankment construction followed by FeT and ZT. However, the production cost for alkali-activated RM is found to be the highest among all MT due to the increased requirement of NaOH solution. Additionally, the incorporation of GBFS not only enhances the strength and durability properties of FeT and ZT specimens but also results in lower production costs compared to RM specimens. Overall, the cost of optimized RM, FeT, and ZT specimens is found to be comparable to or even lower than that of their PPC counterparts indicating their suitability as TP embankment materials.
- Among all the MT, RM is found to be the most effective geopolymer binder for soil stabilization exhibiting a 7-day UCS of 3.51 MPa compared to 3.32 MPa and 1.93 MPa for soil stabilized with FeT and ZT respectively. Similarly, the soaked CBR of untreated soil is enhanced from 2.87% to 75.60%, 55.60%, and 45.37% using RM, FeT, and ZT geopolymers respectively.
- The use of RM, FeT, and ZT geopolymers significantly improves the weathering resistance of untreated soil reducing mass loss from 100% to 0.60%, 1.96%, and 2.35% respectively, after 12 wetting-drying cycles. In general, soil stabilized with various MT geopolymers meets the strength and durability criteria of IRC SP-72 (2015) required for road subgrade applications.
- Of all AAPB, Paste backfills derived from RM exhibit the highest 28-day UCS (i.e. 4.26 MPa) followed by those derived from ZT (3.57 MPa) and FeT (2.80 MPa) exceeding the minimum strength (i.e. 0.50 MPa) required for mine backfill materials. Furthermore, it is found that the V_s of RM, FeT, and ZT paste backfills is drastically reduced from 60.43% to 3.11%, 49.35% to 2.29%, and 12.03% to 1.31% respectively by using NaOH solution and GBFS.

- Of all paste backfills, ZT derived AAPB display the shortest IST (1.1 h) and FST (27.5 h) followed by FeT and RM derived AAPB. Furthermore, the addition of GBFS is found to reduce both the IST and FST of AAPB which could help in maintaining the construction timeline as per industry requirements.
- Paste backfills made from ZT are the most cost-effective with a production cost of ₹ 760 compared to ₹ 820 for FeT and ₹ 1000 for RM. Furthermore, the production cost of ZT and FeT derived AAPB is found to be 15.5% and 4.4% lower compared to CPB (i.e. ₹ 800). In general, AAPB derived from RM, FeT and ZT can serve as a viable alternative to conventional CPB for backfilling the underground mine cavities.
- Among the various applications of alkali-activated MT explored in the present thesis, its use as embankment material and mine backfill material appears to be more economically viable. This is primarily because both of these applications require large quantities of MT, leading to substantial consumption and consequently reducing the necessity for storing MT in TP.
- Overall, alkali activation offers a holistic solution that considers both technical performance and environmental sustainability. By providing comparable performance to cement stabilization methods while offering environmental benefits, alkali-activated MT presents a compelling alternative for various engineering applications contributing to more sustainable construction practices.

7.2 Practical implications/field implementations

The findings of this study can be applied by the mining industry to implement MT geopolymers for constructing TP embankments in the field. Implementing these geopolymers involves several key steps, from material preparation to field application. Fig. 7.1 illustrates various steps that can be followed to construct TP embankments using MT geopolymers. Furthermore, Fig. 7.2 display the step-by-step procedure which can be adopted at site to stabilize the subgrade soil with various MT geopolymers. In general, this study provides various design criteria and optimized design mixes that can be adopted for their respective field applications.

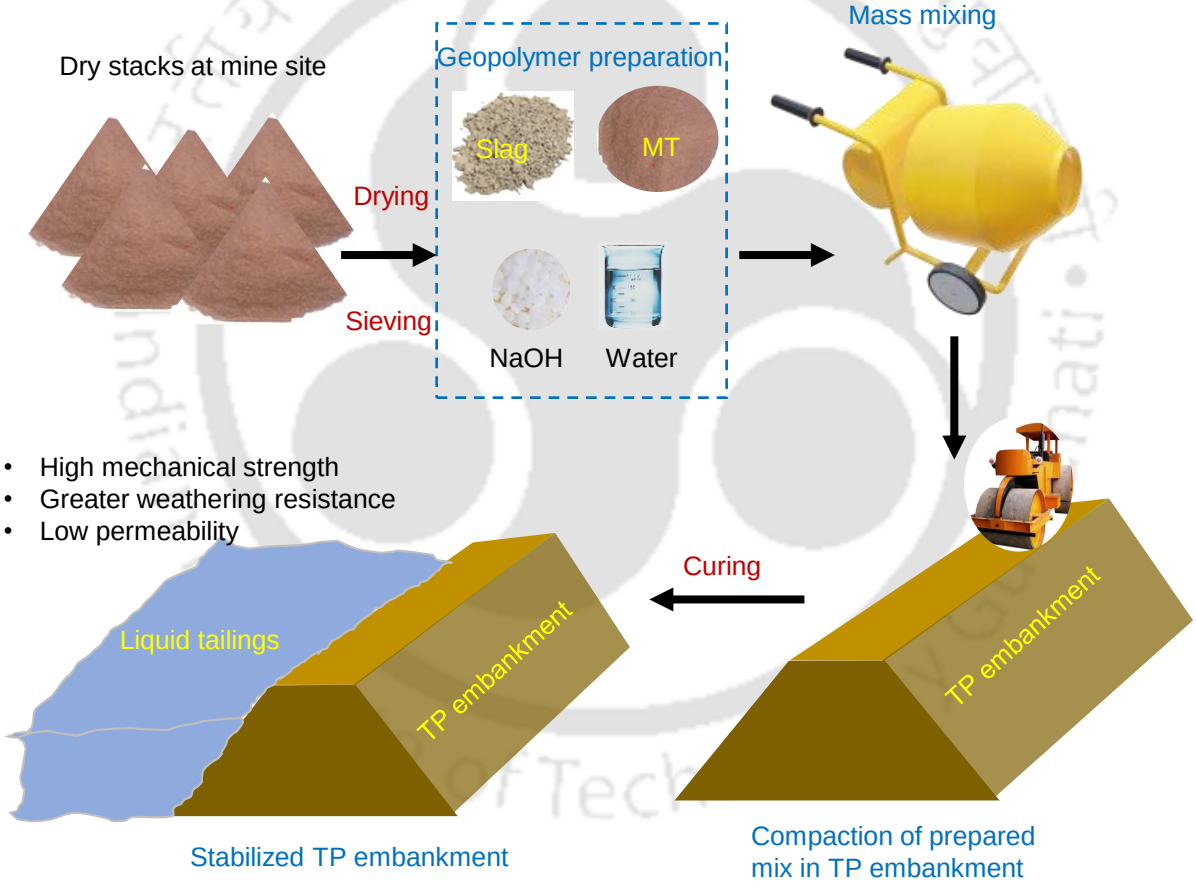

Fig. 7. 1 Illustration of field implementation of MT geopolymers in TP construction

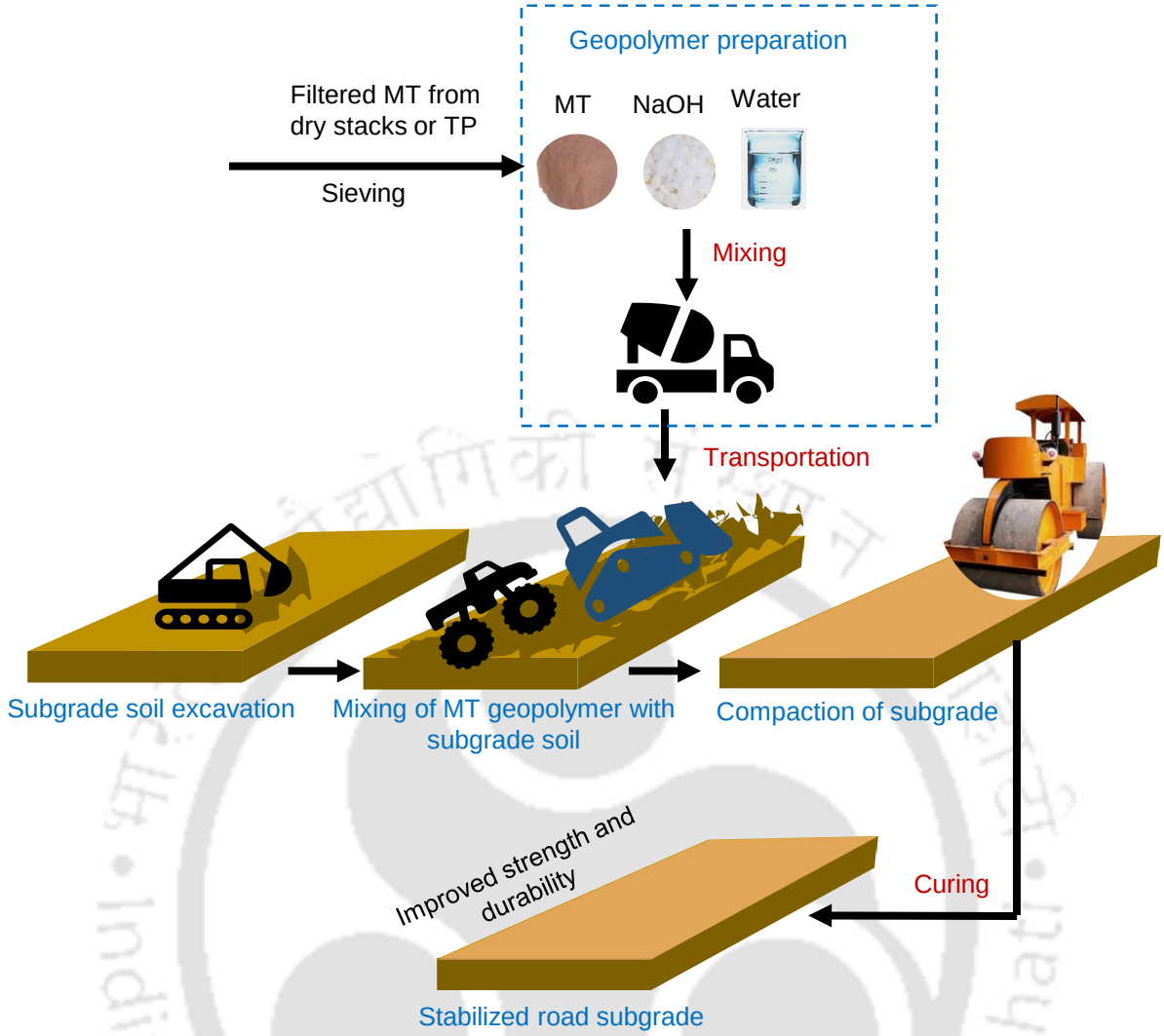

Fig. 7. 2 Illustration of field implementation of MT geopolymers in stabilizing road subgrade soil

7.3 Limitations of current study

Following are some limitations associated with the current study:

- The current study does not consider the influence of variations in the hydraulic conductivities of MT and embankment material on the development of EPWP during height-raising operations. However, this factor has a direct influence on the overall stability of TP especially those constructed with U/S type TP.
- In this study, only the Mohr-Coulomb constitutive law is exclusively employed to model the behaviour of embankment material and tailings. Other constitutive models, such as the

Cam Clay model or NorSand model etc. could be utilized to simulate the behaviour of tailings material more accurately.

- The present study is constrained to a solitary soil type. Future research should involve diverse soil types to enhance the broader applicability of the results obtained from the current study.
- The alkali activation conducted in the present study is restricted to the utilization of NaOH as the alkali activator. Subsequent research should explore the application of alternative alkali activators such as KOH and Na_2SiO_3 in the geopolymerization process.
- The current study is confined to laboratory-scale experiments investigating the diverse utilization potential of alkali-activated MT. Conducting pilot-scale studies is essential to gain a deeper understanding of the applicability of alkali-activated MT in real-world field applications.

7.4 Future scope

Some possible future scopes of this study are outlined below:

- The influence of particle size of different MT on the efficacy of alkali activation can be incorporated in the future study.
- Durability of alkali activated MT under freezing and thawing conditions can be performed to assess their applicability in colder regions.
- Further investigation into the rheology of AAPB is necessary, particularly through the determination of yield stress, to accurately evaluate their flowability for pipe transport.
- Consolidation behaviour of AAPB can be further explored to examine the time dependent settlement which is crucial for a mine backfill material.
- A comprehensive life cycle analysis of various MT geopolymers is necessary to evaluate their environmental impact.

List of publications

Journals:

1. Singh, S., Kumar, A., and Sitharam, T. G. (2024). Experimental study on strength, durability, hydraulic and toxicity characteristics of soil stabilized with mine tailings based geopolymers for sustainable road subgrade application. **Construction and Building Materials, 414, 134894.** ***(I.F.-7.4).***
2. Singh, S., Kumar, A., and Sitharam, T. G. (2023). Investigating the strength and durability properties of alkali activated red mud for tailings pond embankment material. **Geomechanics for Energy and the Environment, 36, 100500.** ***(I.F.-5.1).***
3. Singh, S., Kumar, A., and Sitharam, T. G. (2023). Stability assessment of a tailings pond considering the effect of staged construction and embankment raising rate: a numerical study. **Mining, Metallurgy and Exploration, 1-19.** ***(I.F.-1.9).***
4. Singh, S., Kumar, A., and Sitharam, T. G. (2023). Stability investigation of embankments of a tailings pond for its dry closure: an Indian case study. **Sādhanā, 48(2), 1-22.** ***(I.F.-1.6).***
5. Singh, S., Kumar, A., and Sitharam, T. G. Strength and durability enhancement of zinc tailings via alkali activation for tailings pond embankment application. **Under review.**
6. Singh, S., Kumar, A., and Sitharam, T. G. Strength, shrinkage, flowability and setting performance of mine tailings-based alkali activated paste backfills for mine stopes: a comparative study. **Under review.**
7. Singh, S., Kumar, A., and Sitharam, T. G. Investigating the utilization potential of iron tailings-slag based geopolymers for TP embankment applications. **Under review.**
8. A critical review on the utilization of mine tailings geopolymers for various field applications: current uses and future directions. **Under preparation**.

List of publications

Conferences:

1. Singh, S., Kumar, A., and Sitharam, T. G. (2023). Effect of red mud-based geopolymer binder on the strength development of clayey soil. 9th International Conference on Environmental Geotechnics (ICEG), Chania, Greece.
2. Singh, S., Kumar, A., and Sitharam, T. G. (2021). Stability investigation of embankments of a tailings pond with varying embankment raising rate. Tailings and Mine Waste (TMW). University of Alberta, Geotechnical Centre, Canada.
3. Singh, S., Kumar, A., and Sitharam, T. G. (2021). Effect of embankment raising rate and beach widths on the stability of embankments for the tailings pond. In proceedings of 8th Young Indian Geotechnical Engineers Conference, Chennai chapter, Oct. 21-23.

Book chapters:

1. Singh, S., Kumar, A., and Sitharam, T. G. (2021). A comparative study on the stability analysis of tailings pond embankments under transient and steady-state seepage conditions. In Indian Geotechnical Conference (pp. 357-368). Springer Singapore.
2. Singh, S., Kumar, A., and Sitharam, T. G. (2022). Stability analysis of tailings dam using finite element approach and conventional limit equilibrium approach. In Stability of Slopes and Underground Excavations: Proceedings of Indian Geotechnical Conference 2020 Volume 3 (pp. 91-103). Springer Singapore.

References

1. Ahmari, S., & Zhang, L. (2012). Production of eco-friendly bricks from copper mine tailings through geopolymerization. *Construction and Building Materials*, *29*, 323-331.
2. Akinyemi, B. A., Alaba, P. A., & Rashedi, A. (2022). Selected performance of alkali-activated mine tailings as cementitious composites: A review. *Journal of Building Engineering*, *50*, 104154.
3. Anirudh, M., Rekha, K. S., Venkatesh, C., & Nerella, R. (2021). Characterization of red mud-based cement mortar; mechanical and microstructure studies. *Materials Today: Proceedings, 43,* 1587-1591.
4. Arunachalam, K. P., Avudaiappan, S., Maureira, N., Garcia Filho, F. D. C., Monteiro, S. N., Batista, I. D., & de Azevedo, A. R. (2023). Innovative use of copper mine tailing as an additive in cement mortar. *Journal of Materials Research and Technology*.
5. ASTM C143-20 (2020). Standard test method for slump of hydraulic-cement concrete 1, ASTM International, West Conshohocken, PA.
6. ASTM C191-21 (2021). Standard test methods for time of setting of hydraulic cement by Vicat needle 1, ASTM International, West Conshohocken, PA.
7. ASTM D 5322 (2017). Standard practice for laboratory immersion procedures for evaluating the chemical resistance of geosynthetics to liquids, ASTM International, West Conshohocken, PA.
8. ASTM D1883 (2021). Standard test method for California bearing ratio (CBR) of laboratory compacted soils, ASTM International, West Conshohocken, PA.
9. ASTM D2166, 2006. Standard test method for unconfined compressive strength of cohesive soil. ASTM International, West Conshohocken, PA.
10. ASTM D2487, 2011. Standard practice for classification of soils for engineering purposes (unified soil classification system). ASTM International, West Conshohocken, PA.

11. ASTM D3080, 2011. Standard test method for direct shear test of soils under consolidated drained conditions. ASTM International, West Conshohocken, PA.
12. ASTM D559, 2015. Standard test methods for wetting and drying compacted of soil-cement mixtures. ASTM International, West Conshohocken, PA.
13. ASTM D-5856 (2015). Standard test method for measurement of hydraulic conductivity of porous material using a rigid-wall, compaction mold permeameter 1, ASTM International, West Conshohocken, PA.
14. ASTM D5856, 2015. Standard test method for measurement of hydraulic conductivity of porous material using a rigid-wall, compaction-mold permeameter 1. ASTM International, West Conshohocken, PA.
15. ASTM D7928-21, 2021. Standard test method for particle-size distribution (gradation) of fine-grained soils using the sedimentation (hydrometer) analysis. ASTM International, West Conshohocken, PA.
16. Berg, R. R., Christopher, B. R., & Samtani, N. C. (2009). *Design and construction of mechanically stabilized earth walls and reinforced soil slopes*. US Department of Transportation, Federal Highway Administration, National Highway Institute.
17. Biot, M. A. (1941). General theory of three-dimensional consolidation. *Journal of Applied Physics*, *12*(2), 155-164.
18. Bishop, A. W. (1959). The principles of effective stress. *Teknisk Ukeblad* 106(39): 859–863.
19. Bondar, D., Lynsdale, C. J., Milestone, N. B., Hassani, N., & Ramezanianpour, A. A. (2011). Effect of type, form, and dosage of activators on strength of alkali-activated natural pozzolans. *Cement and Concrete Composites*, *33*(2), 251-260.
20. Canfield, G. M., Eichler, J., Griffith, K., & Hearn, J. D. (2014). The role of calcium in blended fly ash geopolymers. *Journal of Materials Science*, *49*, 5922-5933.

21. Cao, Y. F., Tao, Z., Pan, Z., & Wuhrer, R. (2018). Effect of calcium aluminate cement on geopolymer concrete cured at ambient temperature. *Construction and Building Materials*, *191*, 242-252.

22. Cavusoglu, I., Yilmaz, E., & Yilmaz, A. O. (2021). Sodium silicate effect on setting properties, strength behavior and microstructure of cemented coal fly ash backfill. *Powder Technology*, *384*, 17-28.

23. Chandra, K. S., Krishnaiah, S., Reddy, N. G., Hossiney, N., & Peng, L. (2021). Strength development of geopolymer composites made from red mud–fly ash as a subgrade material in road construction. *Journal of Hazardous, Toxic, and Radioactive Waste*, *25*(1), 04020068.

24. Chen, X., Sutrisno, A., & Struble, L. J. (2018). Effects of calcium on setting mechanism of metakaolin-based geopolymer. *Journal of the American Ceramic Society*, *101*(2), 957-968.

25. Cheng, Y., Huang, F., Li, W., Liu, R., Li, G., & Wei, J. (2016). Test research on the effects of mechanochemically activated iron tailings on the compressive strength of concrete. *Construction and Building Materials, 118,* 164-170.

26. Chindaprasirt, P., De Silva, P., Sagoe-Crentsil, K., & Hanjitsuwan, S. (2012). Effect of SiO 2 and Al 2 O 3 on the setting and hardening of high calcium fly ash-based geopolymer systems. *Journal of Materials Science*, *47*, 4876-4883.

27. Cihangir, F., Ercikdi, B., Kesimal, A., Deveci, H., & Erdemir, F. (2015). Paste backfill of high-sulphide mill tailings using alkali-activated blast furnace slag: Effect of activator nature, concentration and slag properties. *Minerals engineering*, *83*, 117-127.

28. Coulibaly, Y., Belem, T., & Cheng, L. (2017). Numerical analysis and geophysical monitoring for stability assessment of the Northwest tailings dam at Westwood Mine. *International Journal of Mining Science and Technology*, *27*(4), 701-710.

29. Cristelo, N., Glendinning, S., Fernandes, L., & Pinto, A. T. (2013). Effects of alkaline-activated fly ash and Portland cement on soft soil stabilisation. *Acta Geotechnica*, *8*, 395-405.

30. Das, S. K., Kumar, S., & Ramachandrarao, P. (2000). Exploitation of iron ore tailing for the development of ceramic tiles. *Waste Management*, *20*(8), 725-729.

31. Davidovits, J. (1991). Geopolymers: inorganic polymeric new materials. *Journal of Thermal Analysis and calorimetry*, *37*(8), 1633-1656.

32. Davies, M., 2001. Impounded mine tailings: what are the failures telling us? Can. Min. Metall. Bull. 94, 53‑59.

33. De Silva, P., Sagoe-Crenstil, K., & Sirivivatnanon, V. (2007). Kinetics of geopolymerization: Role of Al_2O_3 and SiO_2. *Cement and Concrete Research*, *37*(4), 512-518.

34. Demir, F., & Derun, E. M. (2019). Modelling and optimization of gold mine tailings based geopolymer by using response surface method and its application in Pb2+ removal. *Journal of Cleaner Production*, *237*, 117766.

35. Dietel, J., Warr, L. N., Bertmer, M., Steudel, A., Grathoff, G. H., & Emmerich, K. (2017). The importance of specific surface area in the geopolymerization of heated illitic clay. *Applied Clay Science*, *139*, 99-107.

36. do Carmo, F. F., Kamino, L. H. Y., Junior, R. T., de Campos, I. C., do Carmo, F. F., Silvino, G., ... & Pinto, C. E. F. (2017). Fundão tailings dam failures: the environment tragedy of the largest technological disaster of Brazilian mining in global context. *Perspectives in Ecology and Conservation*, *15*(3), 145-151.

37. Do, T. M., Laue, J., Mattsson, H., & Jia, Q. (2021). Numerical analysis of an upstream tailings dam subjected to pond filling rates. *Applied Sciences*, *11*(13), 6044.

38. Du, C., Tao, H., & Yi, F. (2024). Seepage stability analysis of geogrid reinforced tailings dam. *Scientific Reports, 14(1)*, 1814.

39. Duan, N., Fan, W., Changbo, Z., Chunlei, Z., & Hongbing, Y. (2010). Analysis of pollution materials generated from electrolytic manganese industries in China. *Resources, Conservation and Recycling*, *54*(8), 506-511.

40. Duan, P., Yan, C., Zhou, W., & Ren, D. (2016). Development of fly ash and iron ore tailing based porous geopolymer for removal of Cu (II) from wastewater. *Ceramics International*, *42*(12), 13507-13518.

41. Duxson, P., Fernández-Jiménez, A., Provis, J. L., Lukey, G. C., Palomo, A., & van Deventer, J. S. (2007). Geopolymer technology: the current state of the art. *Journal of Materials Science*, *42*, 2917-2933.

42. EPA, 1994. *Technical report on design and evaluation of tailings dams*. Office of United State Environmental Protection Agency, Washington D.C.

43. Ercikdi, B., Kesimal, A., Cihangir, F., Deveci, H., & Alp, İ. (2009). Cemented paste backfill of sulphide-rich tailings: Importance of binder type and dosage. *Cement and Concrete Composites*, *31*(4), 268-274.

44. Etim, R. K., Eberemu, A. O., & Osinubi, K. J. (2017). Stabilization of black cotton soil with lime and iron ore tailings admixture. *Transportation Geotechnics*, *10*, 85-95.

45. Falayi, T., & Ikotun, B. D. (2021). A comparison between ferrochrome slag and gold mine tailings based geopolymers as adsorbents for heavy metals in aqueous solutions: Analyzing reusability and sustainability. *Korean Journal of Chemical Engineering*, *38*(4), 816-825.

46. Ferreira, I. C., Galery, R., Henriques, A. B., de Carvalho Teixeira, A. P., Prates, C. D., Lima, A. S., & Souza Filho, I. R. (2022). Reuse of iron ore tailings for production of metakaolin-based geopolymers. *Journal of Materials Research and Technology*, *18*, 4194-4200.

47. Fontes, W. C., de Carvalho, J. M. F., Andrade, L. C., Segadães, A. M., & Peixoto, R. A. (2019). Assessment of the use potential of iron ore tailings in the manufacture of ceramic tiles: From tailings-dams to "brown porcelain". *Construction and Building Materials, 206,* 111-121.

48. Fredlund, D. G., & Rahardjo, H. (1993). *Soil mechanics for unsaturated soils*. John Wiley & Sons.

49. Ghadir, P., & Ranjbar, N. (2018). Clayey soil stabilization using geopolymer and Portland cement. *Construction and Building Materials*, *188*, 361-371.

50. Gordon, R. B. (2002). Production residues in copper technological cycles. *Resources, Conservation and Recycling*, *36*(2), 87-106.

51. Gou, M., Zhou, L., & Then, N. W. Y. (2019). Utilization of tailings in cement and concrete: A review. *Science and Engineering of Composite Materials, 26(1),* 449-464.

52. Gupta, C., & Prasad, A. (2018). Strength and durability of lime-treated jarosite waste exposed to freeze and thaw. *Journal of Cold Regions Engineering*, *32*(1), 04017025.

53. Hajjaji, W., Andrejkovičová, S., Zanelli, C., Alshaaer, M., Dondi, M., Labrincha, J. A., & Rocha, F. (2013). Composition and technological properties of geopolymers based on metakaolin and red mud. *Materials & Design (1980-2015)*, *52*, 648-654.

54. Hassan, A., Arif, M., & Shariq, M. (2019). Use of geopolymer concrete for a cleaner and sustainable environment–A review of mechanical properties and microstructure. *Journal of Cleaner Production*, *223*, 704-728.

55. He, P., Wang, M., Fu, S., Jia, D., Yan, S., Yuan, J., ... & Zhou, Y. (2016). Effects of Si/Al ratio on the structure and properties of metakaolin based geopolymer. *Ceramics international*, *42*(13), 14416-14422.

56. Hendershot, W. H., Lalande, H., & Duquette, M. (1993). Soil reaction and exchangeable acidity. *Soil sampling and methods of analysis*, *2*.

57. Hou, C., Yang, L., Li, L., & Yan, B. (2022). Mechanical characteristics and stress evolution of cemented paste backfill: effect of curing time, solid content, and binder content. *Frontiers in Materials*, *8*, 812402.

58. Hou, D., Wu, D., Wang, X., Gao, S., Yu, R., Li, M., ... & Wang, Y. (2021). Sustainable use of red mud in ultra-high performance concrete (UHPC): Design and performance evaluation. *Cement and Concrete Composites, 115,* 103862.

59. Hoy, M., Horpibulsuk, S., & Arulrajah, A. (2016). Strength development of recycled asphalt pavement–fly ash geopolymer as a road construction material. *Construction and Building Materials*, *117*, 209-219.

60. Hu, L., Wu, H., Zhang, L., Zhang, P., & Wen, Q. (2017). Geotechnical properties of mine tailings. *Journal of Materials in Civil Engineering*, *29*(2), 04016220.

61. Huang, S., Pi, Z., Cai, C., & Li, H. (2023). Utilization of high-sulfur iron ore tailings in cement mortar by considering the influence of curing temperature and tailing content. *Journal of Building Engineering, 74,* 106826.

62. IRC: SP-72 (2015). Guidelines for the design of flexible pavements for low volume rural roads, *Indian Road Congresss*, New Delhi.

63. IRC: SP-89 (2018). Guidelines for the design of stabilized pavements (Part II), *Indian Roads Congress,* New Delhi.

64. IS 14739 (1999). Geotextiles- method for determination of creep. *Bureau of Indian Standard*, New Delhi.

65. IS 1893 (2002). Criteria for earthquake resistant design of structures. *Bureau of Indian Standards, Part*, *1*.

66. IS 2720-16 (1987). Methods of test for soils, Part 16: Laboratory determination of CBR, *Bureau of Indian Standards,* New Delhi.

67. IS 7894 (1975). Code of practice for the stability analysis of the earth dams. *Bureau of Indian Standards,* New Delhi.

68. Ismail, I., Bernal, S. A., Provis, J. L., San Nicolas, R., Hamdan, S., & van Deventer, J. S. (2014). Modification of phase evolution in alkali-activated blast furnace slag by the incorporation of fly ash. *Cement and Concrete Composites*, *45*, 125-135.

69. Jiang, H., Qi, Z., Yilmaz, E., Han, J., Qiu, J., & Dong, C. (2019). Effectiveness of alkali-activated slag as alternative binder on workability and early age compressive strength of cemented paste backfills. *Construction and Building Materials*, *218*, 689-700.

70. Jiang, H., Ren, L., Gu, X., Zheng, J., & Cui, L. (2023). Synergistic effect of activator nature and curing temperature on time-dependent rheological behavior of cemented paste backfill containing alkali-activated slag. *Environmental Science and Pollution Research*, *30*(5), 12857-12871.

71. Jiang, H., Ren, L., Zhang, Q., Zheng, J., & Cui, L. (2022). Strength and microstructural evolution of alkali-activated slag-based cemented paste backfill: Coupled effects of activator composition and temperature. *Powder Technology*, *401*, 117322.

72. Justo, J. L., Morales-Esteban, A., Justo, E., Jiménez-Cantizano, F. A., Durand, P., & Vázquez-Boza, M. (2019). The dry closure of the Almagrera tailings dam: detailed modelling, monitoring results and environmental aspects. *Bulletin of Engineering Geology and the Environment*, *78*, 3175-3189.

73. Kang, X., Gan, Y., Chen, R., & Zhang, C. (2021). Sustainable eco-friendly bricks from slate tailings through geopolymerization: synthesis and characterization analysis. *Construction and Building Materials*, *278*, 122337.

74. Karim, M. E., Rahman, M. M., Karim, M. R., Fourie, A. B., & Reid, D. (2023). Characteristics of Copper Tailings in Direct Simple Shearing: A Critical State

Approach. *Journal of Geotechnical and Geoenvironmental Engineering, 149(5),* 04023018.

75. Kastiukas, G., Zhou, X., & Castro-Gomes, J. (2017). Preparation conditions for the synthesis of alkali-activated binders using tungsten mining waste. *Journal of Materials in Civil Engineering*, *29*(10), 04017181.
76. Ke, X., Hou, H., Zhou, M., Wang, Y., & Zhou, X. (2015). Effect of particle gradation on properties of fresh and hardened cemented paste backfill. *Construction and Building Materials*, *96*, 378-382.
77. Kiventerä, J., Perumal, P., Yliniemi, J., & Illikainen, M. (2020). Mine tailings as a raw material in alkali activation: A review. *International Journal of Minerals, Metallurgy and Materials*, *27*, 1009-1020.
78. Koerner, R. M., Martin, J. P., & Koerner, G. R. (1986). Shear strength parameters between geomembranes and cohesive soils. *Geotextiles and Geomembranes*, *4*(1), 21-30.
79. Kong, L., Xie, S., Wang, C., & Wang, L. (2023). Effect of Iron Tailings as Fine Aggregate and Mineral Admixture on Strength and Microstructure of Cement Mortar. *International Journal of Concrete Structures and Materials, 17(1),* 24.
80. Kossoff, D., Dubbin, W. E., Alfredsson, M., Edwards, S. J., Macklin, M. G., & Hudson-Edwards, K. A. (2014). Mine tailings dams: Characteristics, failure, environmental impacts, and remediation. *Applied Geochemistry*, *51*, 229-245.
81. Krahn, J. (2003). The 2001 RM Hardy Lecture: The limits of limit equilibrium analyses. *Canadian Geotechnical Journal, 40(3),* 643-660.
82. Kuranchie, F. A., Shukla, S. K., & Habibi, D. (2016). Utilisation of iron ore mine tailings for the production of geopolymer bricks. *International Journal of Mining, Reclamation and Environment*, *30*(2), 92-114.

83. Kuranchie, F. A., Shukla, S. K., Habibi, D., & Mohyeddin, A. (2015). Utilisation of iron ore tailings as aggregates in concrete. *Cogent Engineering, 2(1),* 1083137.

84. Leung, C. K., & Pheeraphan, T. (1995). Very high early strength of microwave cured concrete. *Cement and Concrete Research*, *25*(1), 136-146.

85. Li, J., Yilmaz, E., & Cao, S. (2020). Influence of solid content, cement/tailings ratio, and curing time on rheology and strength of cemented tailings backfill. *Minerals*, *10*(10), 922.

86. Li, Q., Ma, G., & Lu, Y. (2023). An Experimental and Theoretical Study on the Tailings Dam with Geotextile Bags. *Sustainability, 15(6),* 4768.

87. Li, Y., Min, X., Ke, Y., Liu, D., & Tang, C. (2019). Preparation of red mud-based geopolymer materials from MSWI fly ash and red mud by mechanical activation. *Waste Management*, *83*, 202-208.

88. Liu, Q., Cui, M., Li, X., Wang, J., Wang, Z., Li, L., & Lyu, X. (2022). Alkali-hydrothermal activation of mine tailings to prepare one-part geopolymer: Activation mechanism, workability, strength, and hydration reaction. *Ceramics International*, *48*(20), 30407-30417.

89. Liu, R. X., & Poon, C. S. (2016). Utilization of red mud derived from bauxite in self-compacting concrete. *Journal of cleaner production, 112,* 384-391.

90. Luo, L., Li, K., Fu, W., Liu, C., & Yang, S. (2020). Preparation, characteristics and mechanisms of the composite sintered bricks produced from shale, sewage sludge, coal gangue powder and iron ore tailings. *Construction and Building Materials, 232,* 117250.

91. Luo, L., Zhang, Y., Bao, S., & Chen, T. (2016). Utilization of iron ore tailings as raw material for Portland cement clinker production. *Advances in Materials Science and Engineering*.

92. Lyu, Z., Chai, J., Xu, Z., Qin, Y., & Cao, J. (2019). A comprehensive review on reasons for tailings dam failures based on case history. *Advances in Civil Engineering*, *2019*, 1-18.

93. Manjarrez, L., & Zhang, L. (2018). Utilization of copper mine tailings as road base construction material through geopolymerization. *Journal of Materials in Civil Engineering*, *30*(9), 04018201.

94. Manjarrez, L., Nikvar-Hassani, A., Shadnia, R., & Zhang, L. (2019). Experimental study of geopolymer binder synthesized with copper mine tailings and low-calcium copper slag. *Journal of Materials in Civil Engineering*, *31*(8), 04019156.

95. McLellan, B. C., Williams, R. P., Lay, J., Van Riessen, A., & Corder, G. D. (2011). Costs and carbon emissions for geopolymer pastes in comparison to ordinary portland cement. *Journal of Cleaner Production*, *19*(9-10), 1080-1090.

96. Miraki, H., Shariatmadari, N., Ghadir, P., Jahandari, S., Tao, Z., & Siddique, R. (2022). Clayey soil stabilization using alkali-activated volcanic ash and slag. *Journal of Rock Mechanics and Geotechnical Engineering*, *14*(2), 576-591.

97. Mualem, Y. (1976). A new model for predicting the hydraulic conductivity of unsaturated porous media. *Water Resources Research*, *12*(3), 513-522.

98. Mukiza, E., Zhang, L., Liu, X., & Zhang, N. (2019). Utilization of red mud in road base and subgrade materials: A review. *Resources, Conservation and Recycling*, *141*, 187-199.

99. Naeini, M., & Akhtarpour, A. (2018). Numerical analysis of seismic stability of a high centerline tailings dam. *Soil Dynamics and Earthquake Engineering*, *107*, 179-194.

100. Nath, P., & Sarker, P. K. (2014). Effect of GGBFS on setting, workability and early strength properties of fly ash geopolymer concrete cured in ambient condition. *Construction and Building Materials*, *66*, 163-171.

101. Nath, S. K., Maitra, S., Mukherjee, S., & Kumar, S. (2016). Microstructural and morphological evolution of fly ash based geopolymers. *Construction and Building Materials*, *111*, 758-765.

102. Nigam, S. K., Sinha, A. K., & Madan, S. K. (2023). Characterisation of stabilised red mud waste material for road infrastructure. *Materials Today: Proceedings*, *93*, 41-46.

103. Niroshan, N., Sivakugan, N., & Veenstra, R. L. (2017). Laboratory study on strength development in cemented paste backfills. *Journal of Materials in Civil Engineering*, *29*(7), 04017027.

104. Niroshan, N., Sivakugan, N., & Veenstra, R. L. (2018). Flow characteristics of cemented paste backfill. *Geotechnical and Geological Engineering*, *36*(4), 2261-2272.

105. Niu, H., Helser, J., Corfe, I. J., Kuva, J., Butcher, A. R., Cappuyns, V., ... & Illikainen, M. (2022). Incorporation of bioleached sulfidic mine tailings in one-part alkali-activated blast furnace slag mortar. *Construction and Building Materials*, *333*, 127195.

106. Nwonu, D. C. (2021). Exploring soil geopolymer technology in soft ground improvement: A brief excursion. *Arabian Journal of Geosciences*, *14*(6), 460.

107. Omidi, G. H., Prasad, T. V., Thomas, J. C., & Brown, K. W. (1996). The influence of amendments on the volumetric shrinkage and integrity of compacted clay soils used in landfill liners. *Water, Air, and Soil Pollution*, *86*, 263-274.

108. Onyia, M. E., Agunwamba, J. C., & Nwonu, D. C. (2021). Hydraulic conductivity behaviour of expansive soil geopolymer binders. *Arabian Journal of Geosciences*, *14*, 1-16.

109. Ormann, L., Zardari, M. A., Mattsson, H., Bjelkevik, A., & Knutsson, S. (2013). Numerical analysis of strengthening by rockfill embankments on an upstream tailings dam. *Canadian Geotechnical Journal*, *50*(4), 391-399.

110. Ouffa, N., Benzaazoua, M., Belem, T., Trauchessec, R., & Lecomte, A. (2020). Alkaline dissolution potential of aluminosilicate minerals for the geosynthesis of mine paste backfill. *Materials Today Communications*, *24*, 101221.

111. Park, S., & Pour-Ghaz, M. (2018). What is the role of water in the geopolymerization of metakaolin?. *Construction and Building Materials*, *182*, 360-370.

112. Patwa, D., Chandra, A., Ravi, K., & Sreedeep, S. (2021). Influence of biochar particle size fractions on thermal and mechanical properties of biochar-amended soil. *Journal of Materials in Civil Engineering*, *33*(9), 04021236.

113. Qi, C., & Fourie, A. (2019). Cemented paste backfill for mineral tailings management: Review and future perspectives. *Minerals Engineering*, *144*, 106025.

114. Qin, J., Zheng, J., & Li, L. (2021). Experimental study of the shrinkage behavior of cemented paste backfill. *Journal of Rock Mechanics and Geotechnical Engineering*, *13*(3), 545-554.

115. Rajasthan P.W.D., 2019) Basic schedule of rates. Public Work Department, Government of Rajasthan, India.

116. Rattanasak, U., & Chindaprasirt, P. (2009). Influence of NaOH solution on the synthesis of fly ash geopolymer. *Minerals Engineering*, *22*(12), 1073-1078.

117. Rocscience, Inc. RS2 Version 11.003 (2020). *Finite element analysis for excavations and slopes.* Toronto, Ontario, Canada.

118. Saad, B., & Mitri, H. (2011). Hydromechanical analysis of upstream tailings disposal facilities. *Journal of Geotechnical and Geoenvironmental Engineering*, *137*(1), 27-42.

119. Sadrossadat, E., Basarir, H., Luo, G., Karrech, A., Durham, R., Fourie, A., & Elchalakani, M. (2020). Multi-objective mixture design of cemented paste backfill using particle swarm optimisation algorithm. *Minerals Engineering*, *153*, 106385.

120. Sajan, P., Jiang, T., Lau, C., Tan, G., & Ng, K. (2021). Combined effect of curing temperature, curing period and alkaline concentration on the mechanical properties of fly ash-based geopolymer. *Cleaner Materials*, *1*, 100002.

121. Scherer, G. W. (2015). Drying, shrinkage, and cracking of cementitious materials. *Transport in Porous Media*, *110*, 311-331.

122. Shanmugasundaram, V., & Shanmugam, B. (2023). Application of cement treated magnesite mine tailings as subgrade. *Construction and Building Materials*, *365*, 130064.

123. Sharath, B. P., Shivaprasad, K. N., Athikkal, M. M., & Das, B. B. (2018, October). Some studies on sustainable utilization of iron ore tailing (IOT) as fine aggregates in fly ash based geopolymer mortar. In *IOP conference series: materials science and engineering* (Vol. 431, No. 9, p. 092010). IOP Publishing.

124. Singh, S., Aswath, M. U., & Ranganath, R. V. (2020). Performance assessment of bricks and prisms: Red mud based geopolymer composite. *Journal of Building Engineering*, *32*, 101462.

125. Sinha, A. K., Havanagi, V. G., Sreekantan, P. G., & Chandra, S. (2022). Geotechnical characterisation of zinc tailing waste material for road construction. *Geomechanics and Geoengineering*, *17*(6), 1984-2004.

126. Sitharam, T. G., & Hegde, A. (2017). Stability analysis of rock-fill tailing dam: an Indian case study. *International Journal of Geotechnical Engineering*, *11*(4), 332-342.

127. Smith, I. M., Griffiths, D. V., & Margetts, L. (2013). *Programming the finite element method*. John Wiley & Sons.

128. Sridharan, A., & Sivapullaiah, P. V. (2005). Mini compaction test apparatus for fine grained soils. *ASTM Geotechnical Testing Journal*, *28*(3), 7.

129. Taki, K., Mukherjee, S., Patel, A. K., & Kumar, M. (2020). Reappraisal review on geopolymer: A new era of aluminosilicate binder for metal immobilization. *Environmental Nanotechnology, Monitoring & Management*, *14*, 100345.

130. Tang, W. C., Wang, Z., Liu, Y., & Cui, H. Z. (2018). Influence of red mud on fresh and hardened properties of self-compacting concrete. *Construction and Building Materials, 178,* 288-300.

131. Thompson, B. D., Bawden, W. F., & Grabinsky, M. W. (2012). In situ measurements of cemented paste backfill at the Cayeli Mine. *Canadian Geotechnical Journal*, *49*(7), 755-772.

132. Tuyan, M., Andiç-Çakir, Ö., & Ramyar, K. (2018). Effect of alkali activator concentration and curing condition on strength and microstructure of waste clay brick powder-based geopolymer. *Composites Part B: Engineering*, *135*, 242-252.

133. USEPA (1992). Toxicity characteristics leaching procedure, *United States Environmental Protection Agency.*

134. Van Genuchten, M. T. (1980). A closed-form equation for predicting the hydraulic conductivity of unsaturated soils. *Soil science society of America journal*, *44*(5), 892-898.

135. Vick S.G., Viotti C.B., Watts B.D., 2016. Fundão tailings dam review panel report on the immediate causes of the failure of the Fundão dam.

136. Vick, S. G. (1990). *Planning, design, and analysis of tailings dams*. BiTech Publishers Ltd.

137. Vogel, T., Van Genuchten, M. T., & Cislerova, M. (2000). Effect of the shape of the soil hydraulic functions near saturation on variably-saturated flow predictions. *Advances in Water Resources*, *24*(2), 133-144.

138. Wan, Q., Rao, F., Song, S., & Zhang, Y. (2019). Immobilization forms of ZnO in the solidification/stabilization (S/S) of a zinc mine tailing through geopolymerization. *Journal of Materials Research and Technology,* 8(6), 5728-5735.

139. Wang, C., Harbottle, D., Liu, Q., & Xu, Z. (2014). Current state of fine mineral tailings treatment: A critical review on theory and practice. *Minerals Engineering*, *58*, 113-131.

140. Wang, W., Chen, W., Liu, H., & Han, C. (2018). Recycling of waste red mud for production of ceramic floor tile with high strength and lightweight. *Journal of Alloys and Compounds*, 748, 876-881.

141. Wei, Z., Yin, G., Li, G., Wang, J. G., Wan, L., & Shen, L. (2009). Reinforced terraced fields method for fine tailings disposal. *Minerals Engineering, 22(12),* 1053-1059.

142. Wei, Z., Zhao, J., Wang, W., Yang, Y., Zhuang, S., Lu, T., & Hou, Z. (2021). Utilizing gold mine tailings to produce sintered bricks. *Construction and Building Materials, 282,* 122655.

143. Weishi, L., Guoyuan, L., Ya, X., & Qifei, H. (2018). The properties and formation mechanisms of eco-friendly brick building materials fabricated from low-silicon iron ore tailings. *Journal of Cleaner Production, 204,* 685-692.

144. Wu, S., Liu, Y., Southam, G., Nguyen, T. A., Konhauser, K. O., You, F., ... & Huang, L. (2023). Ecological engineering of iron ore tailings into useable soils for sustainable rehabilitation. *iScience*.

145. Xu, W., Tian, M., & Li, Q. (2020). Time-dependent rheological properties and mechanical performance of fresh cemented tailings backfill containing flocculants. *Minerals Engineering*, *145*, 106064.

146. Yaghoubi, M., Arulrajah, A., Disfani, M. M., Horpibulsuk, S., Bo, M. W., & Darmawan, S. (2018). Effects of industrial by-product based geopolymers on the strength development of a soft soil. *Soils and Foundations*, *58*(3), 716-728.

147. Yang, F., Wu, F., Yang, B., Li, L., & Gao, Q. (2022). Preparation and performance of composite activated slag-based binder for cemented paste backfill. *Chemosphere*, *309*, 136649.

148. Yang, Y., Wei, Z., Cao, G., Yang, Y., Wang, H., Zhuang, S., & Lu, T. (2019). A case study on utilizing geotextile tubes for tailings dams construction in China. *Geotextiles and Geomembranes, 47(2),* 187-192.

149. Yilmaz, E., Belem, T., & Benzaazoua, M. (2014). Effects of curing and stress conditions on hydromechanical, geotechnical and geochemical properties of cemented paste backfill. *Engineering Geology*, *168*, 23-37.

150. Yilmaz, E., Belem, T., & Benzaazoua, M. (2015). Specimen size effect on strength behavior of cemented paste backfills subjected to different placement conditions. *Engineering Geology*, *185*, 52-62.

151. Yilmaz, E., Belem, T., Bussière, B., Mbonimpa, M., & Benzaazoua, M. (2015). Curing time effect on consolidation behaviour of cemented paste backfill containing different cement types and contents. *Construction and Building Materials*, *75*, 99-111.

152. Yin, G., Li, G., Wei, Z., Wan, L., Shui, G., & Jing, X. (2011). Stability analysis of a copper tailings dam via laboratory model tests: A Chinese case study. *Minerals Engineering, 24(2),* 122-130.

153. Yin, S., Wu, A., Hu, K., Wang, Y., & Zhang, Y. (2012). The effect of solid components on the rheological and mechanical properties of cemented paste backfill. *Minerals Engineering*, *35*, 61-66.

154. Yin, S., Yan, Z., Chen, X., & Wang, L. (2022). Effect of fly-ash as fine aggregate on the workability and mechanical properties of cemented paste backfill. *Case Studies in Construction Materials*, *16*, e01039.

155. Yin, S., Zhou, Y., Wang, L., Pan, J., & Kou, Y. (2022). Setting, bleeding, and hardening strength properties of coarse aggregate backfill slurry. *Case Studies in Construction Materials*, *17*, e01667.

156. Yliniemi, Paiva, Ferreira, Tiainen, & Illikainen. (2017). Development and incorporation of lightweight waste-based geopolymer aggregates in mortar and concrete. *Construction and Building Materials*, *131*, 784-792.

157. Yusuf, M. O., Johari, M. A. M., Ahmad, Z. A., & Maslehuddin, M. (2014). Shrinkage and strength of alkaline activated ground steel slag/ultrafine palm oil fuel ash pastes and mortars. *Materials & Design*, *63*, 710-718.

158. Zandarín, M. T., Oldecop, L. A., Rodríguez, R., & Zabala, F. (2009). The role of capillary water in the stability of tailing dams. *Engineering Geology, 105(1-2),* 108-118.

159. Zhang, C., Chai, J., Cao, J., Xu, Z., Qin, Y., & Lv, Z. (2020). Numerical simulation of seepage and stability of tailings dams: a case study in Lixi, China. *Water*, *12*(3), 742.

160. Zhang, J., Provis, J. L., Feng, D., & van Deventer, J. S. (2008). Geopolymers for immobilization of Cr^{6+}, Cd^{2+}, and Pb^{2+}. *Journal of Hazardous Materials*, *157*(2-3), 587-598.

161. Zhang, M., El-Korchi, T., Zhang, G., Liang, J., & Tao, M. (2014). Synthesis factors affecting mechanical properties, microstructure, and chemical composition of red mud–fly ash based geopolymers. *Fuel*, *134*, 315-325.

162. Zhao, X., Liu, C., Zuo, L., Wang, L., Zhu, Q., & Wang, M. (2019). Investigation into the effect of calcium on the existence form of geopolymerized gel product of fly ash based geopolymers. *Cement and Concrete Composites*, *103*, 279-292.

163. Zhuang, X. Y., Chen, L., Komarneni, S., Zhou, C. H., Tong, D. S., Yang, H. M., ... & Wang, H. (2016). Fly ash-based geopolymer: clean production, properties and applications. *Journal of Cleaner Production*, *125*, 253-267.

164. Zuhua, Z., Xiao, Y., Huajun, Z., & Yue, C. (2009). Role of water in the synthesis of calcined kaolin-based geopolymer. *Applied Clay Science*, *43*(2), 218-223.